SYSTEMATIC INVESTIGATION ON THE GROWTH OF ONE-DIMENSIONAL WURTZITE NANOSTRUCTURES

A Dissertation
Presented to
The Academic Faculty

by

Christopher Ma

In Partial Fulfillment
of the Requirements for the Degree
Doctor of Philosophy in the
School of Materials Science & Engineering

Georgia Institute of Technology
August 2005

SYSTEMATIC INVESTIGATION ON THE GFROWTH OF ONE-DIMENSIONAL WURTZITE NANOSTRUCTURES

Approved by:

Dr. Zhong Lin Wang, Advisor
School of Materials Science & Engineering
Georgia Institute of Technology

Dr. Samuel Graham
School of Mechanical Engineering
Georgia Institute of Technology

Dr. C.P. Wong
School of Materials Science & Engineering
Georgia Institute of Technology

Dr. Chris Summers
School of Materials Science & Engineering
Georgia Institute of Technology

Dr. Rina Tannenbaum
School of Materials Science & Engineering
Georgia Institute of Technology

Date Approved: July 14, 2005

ACKNOWLEDGEMENTS

I would like to express my thanks to my advisor, Dr. Z.L. Wang, for allowing me to grow, albeit painfully at times, into the self-propelled researcher and scientist that I am today. I would also like to thank my committee members: Dr. C.P. Wong, Dr. Rina Tannenbaum, Dr. Samuel Graham, and Dr. Chris Summers. I could not have undertaken the research for this thesis if not for Will Hughes and Brent Buchine who challenged and pushed me during times when I most needed and least wanted it. Many thanks are also due to the rest of my research group, namely Xudong Wang, Daniel Moore, and Puxian Gao.

A dissertation such as this is more than just five years of experiments, graphs, and tables translated into a few pages of comprehensible English. It is the summation of influence from people who have not or will not set foot in the Love Building. It's through my mother's stubbornness and high expectations that I was never allowed to give up. My Uncle Larry's work ethic, which has been converted from manual to mental labor, pulled me through the six months of 90 hour work weeks. If not for my Tía Angie and Tío Jose, I would have never survived my childhood, let alone Iowa winters, if not for their love and charity.

Dr. Steve Feller and Dr. Mario Affatigato of Coe College were the first to see my potential and stopped me from squandering it. This, of course, was balanced by my interactions with the Boyz of First Armstrong who gave me the depth, the scope, and the perseverance to plod ahead, even at the most humbling moments. For nearly twenty years, George Ebert has been a best friend and confidant, and I am grateful to have such a

constant, strong, and humorous influence in my life. While he might not have had much to do with this thesis, he certainly had quite a bit to do with me.

Most importantly, my wife. Thank you for teaching vowels other than “I”.

This project was supported by the National Science Foundation, the Georgia Institute of Technology Molecular Design Institute, under prime contract N00014-95-1-1116 from the Office of Naval Research

TABLE OF CONTENTS

LIST OF TABLES

LIST OF FIGURES

SUMMARY

The past decade has seen the rapid emergence of a new material class known as nanomaterials. One-dimensional nanostructures, in particular, have garnered a tremendous amount of attention due to their possible applications. Yet the underlying mechanisms controlling the one-dimensional nanostructure growth are still not well understood. If nanoscience is to have a significant impact in the scientific community, then investigations into these structures must delve deeper than simply reporting a newly observed morphology or physical property. This thesis gives a systematic investigation into the growth of one-dimensional nanostructures of select II-VI compounds with the wurtzite crystal structure. Two process parameters are systematically altered to observe how each affects deposition. The results of which may give a further understanding into the formation of one nanostructure over another, as well as experimental parameters for optimizing the growth of particular CdSe nanomaterials. A statistical analysis will be conducted on the experimental data to quantitatively determine the variability and robustness of the experimental setup and process. The information complied from this extensive investigation will yield a more complete understanding of the experimental setup and how improvements may be made to reduce variability, increase yield, and gain insight into the mechanisms controlling this class of materials. In short, this body of work seeks to gain more control over the growth of one-dimensional nanostructures.

CHAPTER I

INTRODUCTION

Nanotechnology is an important initiative in science and technology in the 21st century. All mainstreaming aside, nanotechnology has become a dominant player in the scientific arena. This field explores materials and their properties when at least one dimension is in the range of one to one hundred nanometers in length, a size regime referred to as the nanoscale. Materials at this scale may consist only of a few atoms or molecules clustered together. At the nanoscale, quantum confinement effects begin to dictate a material's properties. What makes these nanomaterials so interesting, and what has led to the explosion of research in this field, is that these materials can exhibit significantly enhanced and altered properties as they experience quantum confinement in one, two, or three dimensions.

Research in this field will likely provide some of the most exciting breakthroughs in technology. The ability to work with atoms at the nanoscale, and with atomic precision, promises to open new areas of technological development. The size-dependent luminescent properties of quantum dots and ultra-high strength of carbon nanotubes are just two of the nanomaterial properties that gave gained notoriety over the past decade. However, this does not begin to break the surface of the vast and interesting structures and properties that nanoscience has discovered. This field is envisioned to change almost everything about how we manufacture and approach technology. Nanomaterials research has already garnered interest from field effect transistors (FET's) for smaller, lighter, and

faster electronic devices, biological labeling for early detection of cancer, and even opened new fields like spintronics.

However, nanoscience and nanotechnology are still in their infancy. The basic concepts that govern this field are not fully understood and need to be further explored. In fact, a bulk of the research in this field aims to make the next big discovery in novel properties, unique structures, or commercial device fabrication using these nanostructures. Yet if nanoscience and technology is ever to make a meaningful impact in the scientific community and the world at large, the fundamental concepts and theories that govern this unique class of materials must be uncovered.

When research in this field began, it was sufficient enough to report a new nanostructure or a new physical property observed at the nanoscale. In those days, emphasis was placed on discovery of the next nano-phenomenon. I believe that time has passed. It is not enough to present eye-catching scanning electron microscope (SEM) images or tantalizing transmission electron microscope (TEM) images. Simply showing measurements of a new property and casting it under the umbrella of "quantum confinement effects" will no longer suffice. Research must be more focused and probe into the mechanisms controlling the properties and growth of these unique structures. We must look harder to understand these amazing discoveries; we must investigate, measure, and model, but most importantly we *must* be able to predict.

In an attempt to help bridge this deficiency, the research described in this thesis focuses on the mechanisms controlling the growth of a specific group of II-VI semiconducting one-dimensional nanostructures. Synthesized through a thermal evaporation process, the most commonly received structures were nanobelts and

nanosaws and were therefore the centerpiece of the investigation. The goal was to systematically investigate the experimental parameters that affected the morphology and structure/property relation of these nanomaterials. The first report of the nanobelt structure was in early 2001. The reported materials used to synthesize the nanobelt structure were ZnO, CdO, In_2O_3, $Ga2_{O3}$, and SnO_2. These materials are all transparent conducting oxides covering a large spectrum of elemental groups (II-VI, III-VI, and IV-V) with at least five different types of crystallographic structures. My focus was strictly on the non-oxide II-VI semiconductors (ZnS, ZnSe, ZnTe, CdS, CdSe, and CdTe). Each of the semiconductors in this group has a stable or metastable wurtzite crystal structure with an associated piezoelectric phenomenon. Examining all of the II-VI semiconductors would prove to be a daunting task, therefore my focus was on ZnS and CdSe, with the bulk of the research being conducted on CdSe nanomaterials. These particular materials were chosen both for their extensive research, which provided insight into the semiconductors' properties, and for their possible applications in optoelectronics.

It was the focus of this work to gain precise control over the design of the materials involved, including positioning/patterning, dimensionality, physical properties, and, most importantly (at least in the scope of this thesis), morphology. Manipulation of materials on this scale could potentially provide the ability to tailor many properties to suit specific criteria.

Positioning and patterning is essentially growing a nanostructure from a specific site or in a specific pattern. This plays an important role in the eventual incorporation of these structures into device fabrication as it provides an ease of manipulation. Researchers have successfully aligned nanowires by using a variety of different methods.

While positioning and patterning research has made significant progress, controlling properties at the nanoscale has proven to be difficult. One of the greatest aspects of nanotechnology is that changing the size of a material by only a few nanometers can have a significant impact on the properties of the material. Conversely, this one of the greatest detriments to nanotechnology, as a deviation in size of a material by only a few nanometers can have a significant impact on the material's properties.

In this way, there is a direct correlation between dimensionality and physical properties. For example, as further explained later in this thesis, variance in size of quantum dots of only four nanometers can shift their luminescence from red to blue. One can imagine from this illustration that the precision required to control dimensionality within a few nanometers or less has been, up to this point, an arduous – yet equally significant – task.

The primary focus of this thesis will be about morphology, the structure and form. My goal is to understand the mechanism which determines the morphology of these structures. If I can understand the mechanism, I can control the morphology. If I can control the morphology, I can control certain physical properties of the material. Even when chemically identical, structures can have different physical properties. For instance, there is an associate dipole moment across a ZnO. Nanobelt can have multiple growth directions, one of which maximizes the dipole moment across the belt.. Zinc oxide nanowires, which can only be grown in one direction, have a significantly weaker dipole moments. Because of the inherent non-centrosymmetric nature of wurtzite crystal structure, the dipole moment creates a piezoelectric effect in this II-VI semiconducting material. This will be discussed at great lengths later in this dissertation.

All of the above characteristics require having an understanding of the growth mechanism that dictates whether we synthesize nanobelts, nanosaws/nanocombs, or nanowires. In the current synthesis set-up, there is little we can do to manage the exact size or morphology of the nanostructures. Typical synthesis runs will have a range of sizes and morphologies within a narrow region of deposition.

The ultimate goal of this thesis is understand what role each of the synthesis parameters plays in impacting the morphology and structure/property relation of the II-VI semiconducting nanostructures. To reduce the variability of the size and morphology within a given run, a series of systematic studies were carried out in order to investigate what impact specific synthesis parameters, namely pressure and temperature, has on this group of nanomaterials. If successful, the ramifications of fully understanding and exerting precise control over these nanomaterials will allow a higher level of selectivity, more control over dimensionality and type of morphology, easier manipulation, and, hopefully, the eventually implementation of these structures into a device.

CHAPTER II

II-VI SEMICONDUCTING NANOBELTS

For decades, II-VI semiconducting materials have attracted a tremendous amount of attention for their possible application in optoelectronics. With direct bandgaps that range from as low as 1.475 eV for CdTe[1] to as high as 3.68eV for ZnS[2], this group of materials seem ideal for optoelectronic application since optical absorption and emission process occur to first order in direct-gap systems, making these materials extremely useful as both photonic detectors and emitters. With the large range of bandgap energies, these materials could be used to detect radiation from the far infrared to the ultraviolet portion of the spectrum.

It is apparent that the next logical step is to investigate the II-VI semiconductors at the nanoscale. There has already been research conducted on zero-dimensional nanostructures correlating a strong size dependency on the band structure[3,4]. When CdSe is only a few nanometers in size, the band structure becomes discrete energy levels that can emit light in a range of different wavelength as the size of the CdSe in altered. Nanobelts, above all other nanostructures offer the unique capability to investigate quantum confinement in only one dimension. Other one-dimensional nanostructures, like nanowires and nanotubes, have their entire cross-section in the nano-regime owing to their circular shape. However, the rectangular cross-section of the nanobelts allows us to study a nanostructure where only the thickness is in the range where quantum confinement effects govern the physical properties.

2.1: The Evolution from Dots to Belts

It is a common misconception that nanomaterials are a recent discovery. They are found throughout the natural world – certain bacteria[5] have magnetic nanoparticles which help provide a sense of direction, some reptiles have nano-sized cilia that act as tiny suction cups, allowing them to adhere to surface[6] (see Figure 2.1). While Mother Nature

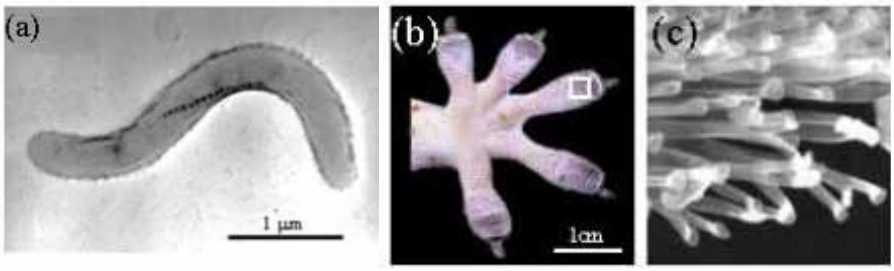

Figure 2. 2: (a)Image of magnetic bacterium, Magnetospirillum Magneticum. (b) Image of a gecko's foot, and (c) image of a cilla from box area in (b).

had billions of years to perfect her craft, there is evidence that reveals nanomaterials were being used thousands of years ago in ancient China. Figure 2.2 is an image of an ancient Chinese vase. The decorative red paint on this vase looks basic enough, however upon a much, much closer investigation, one discovers that the color actually consists of

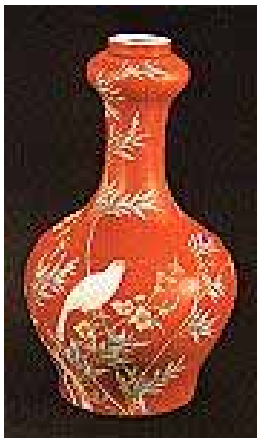

Figure 2. 1: Ancient Chinese vase.

nanometer-sized gold particles. How is this possible? It has been determined that when gold is significantly reduced in size, it no longer has the yellowish-metallic appearance we often associate with it; rather, it can appear red – among other colors – depending on the size of the particle[7].

This then begs the question, if the Chinese were able to apply nanomaterials to their everyday life thousands of years ago, why are we just now utilizing this apparently ancient technology?

Until the advent of electron microscopy techniques, materials within the nanoscale were virtually undetectable. Imaging a material optically requires that it be at least as large as the wavelength of visible light (400-700nm). The nano-regime is much smaller than this. With electron microscopes, we are able to observe what was previously unobservable: a new dimension of the known world. The wavelength of typical electron beam, or e-beam, can range from 0.173Å for a typical 5kV scanning electron microscope (SEM) to 0.0087 Å for a 1000kV transmission electron microscope (TEM)[8]. Some of these microscopes even have the power to distinguish individual atoms, giving us the ability to discover and investigate this entirely new class of materials.

2.1.1: Quantum Dots

The first aspect of nanoscience to gain notoriety was the novel properties of quantum dots (QDs). Quantum dots are semiconductors that have all three dimensions in the nanoscale and for this reason they are referred to as zero-dimensional (0D) structures. Discovered in the late 1980's, these nanostructures demonstrated a physical property phenomenon that had never before been seen; scientists could modify the luminescent

and electronic properties by simply changing the size of the QD. To fully understand the mechanism behind this phenomenon and its importance, we must first examine a few principles of quantum mechanics.

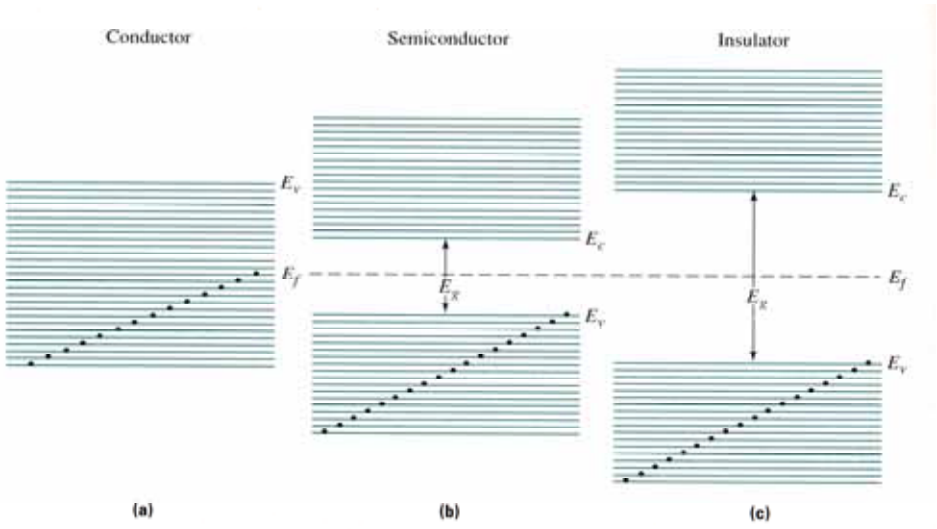

Figure 2. 3: Energy band structure of (a) a conductor, (b) a semiconductor, and (c) an insulator.

Quantum mechanics tells us that in a single atom only certain discrete energy levels area allowed. If two identical atoms are held at large distances from one another, a given electron will have the exact same energy in each atom. However, as those two atoms are brought closer to one another, quantum mechanics places a restriction on them called the Pauli exclusion principle, which states that no two electrons with the same spin can have the same energy. When a large number of atoms are brought together to form a solid, the discrete energy levels of the individual atoms spread into continuous energy bands in order to compensate for the restriction imposed by the Pauli exclusion principle. The energy band structure of a solid, shown in Figure 2.3 for various solids, directly affects the electronic and optical properties of a material. These properties are inherent to the bulk material and can only be altered by adding constituents to the system. The

phenomenon that garnered quantum dots so much attention within the scientific community was how the optical and electronic properties could be precisely tuned not by adding dopants but by merely changing the size of the dots. What was thought to be inherent to a material was actually transformed when examined in the nanoscale.

As dimensionality of a material decreases to the nanoscale, quantum confinement effects begin to occur. Quantum confinement effects occur when a material is smaller than the bulk exciton Bohr radius[9]. This reduction in size restricts each atoms' movement, resulting in the aforementioned discrete energy levels, and thus the differences in material properties. One can liken quantum confinement to the rules of a football game. In American football, the playing field is one hundred yards long and forty yards wide with eleven players on each team. There are associated sets of rules that accompany this game in order for it to progress. Now imagine if the field were shrunk to one-tenth of its original size, keeping the number of players the same. The players on that field would no longer have the ability to move as freely as they did before, and, as a result, there would have to be a corresponding change in the rules for the game to continue. Analogously, if instead of players there were atoms, and if instead of a field here was a material, and the material was reduced down to the nanoscale, then the atoms or electrons in that material would be confined and unable to move freely. The rules that governed the material would have to change, resulting in different physical properties.

As is the case of quantum dots, these quantum confinement effects can have a significant impact on the physical properties of a material. Figure 2.4 illustrates the size-dependent optical properties of cadmium selenide (CdSe) quantum dots. In the image, each vial is filled with a solution of monodispersed QDs with the particle size getting

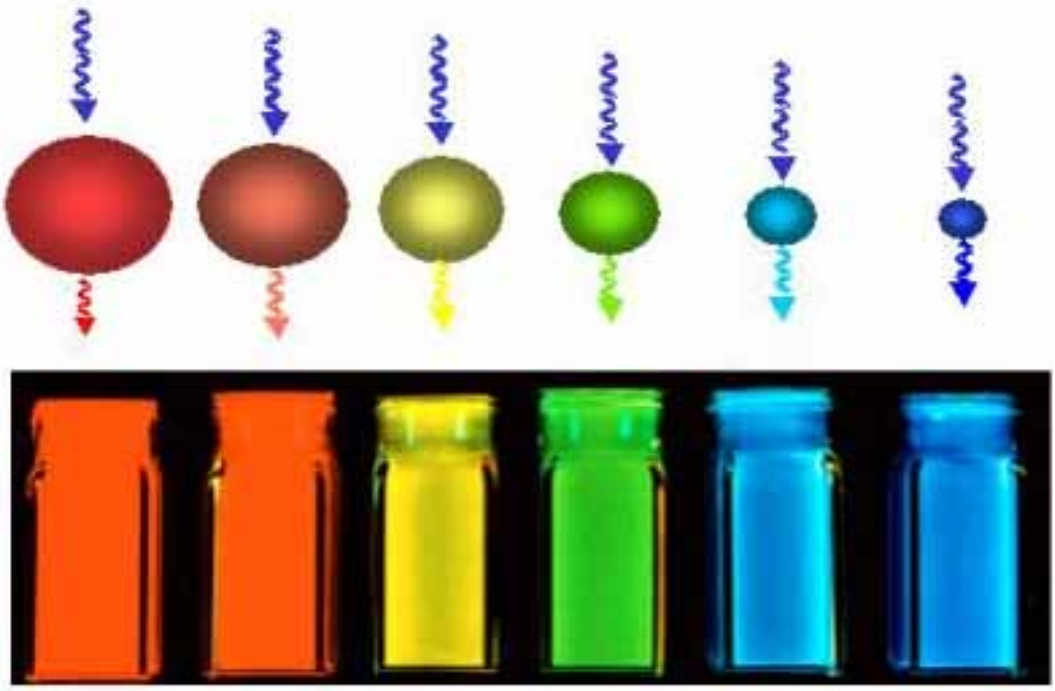

Figure 2.4: Various solutions of monodispersed cadmium selenide quantum dots.

progressively smaller as we move from left to right. This image illustrates the changing optical properties of the material as the dimensionality is altered.

What determines the specific optical properties of a nanomaterial? Brus *et al.*[10], and then later his coworkers from Bell Labs Alvisatos *et al.*[11], Murray *et al.*[12], and Bawendi *et al*[13]., were some of the first scientists to discover the direct relationship between the quantum confinement of 0D cadmium selenide nanostructures and an induced higher energy shift in the electronic band structure. They were able to demonstrate that as CdSe was reduced in one, two, and three dimensions to the nanoscale, the energy bands reconfigured to look more like the discrete energy levels of individual atoms. Because of this, quantum dots are often referred to as artificial atoms.

More specifically, as the size of the quantum dot approaches the bulk exciton Bohr radius, the motion of electrons within the solid becomes confined. This confinement reconfigures the band structure, giving way to discrete energy levels instead

of energy bands[14]. It is at this point that the electronic and optical properties become size dependent. A decrease of a few nanometers in size results in a shift of the energy levels to higher values[15] (see Figure 2.5).

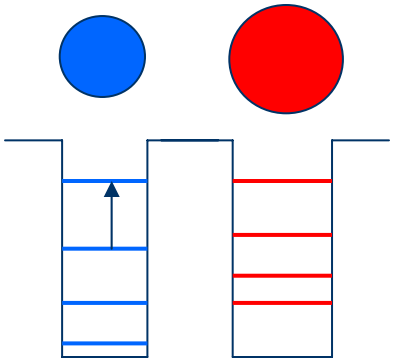

Figure 2. 5: Diagram depicting induced energy shift with dimensionality change.

This unique characteristic of quantum dots offers promising applications within technology. Some of the more prevalent research being conducted investigates quantum dots for use both in computing[16] and biological imaging[17] applications, with each of these applications utilizing different attributes of the quantum dots. Biological labeling hopes to exploit the luminescent properties, which would entail attaching a functional group to the surface of a QD[18,19]. This functional group would preferentially bind itself to a specified organism, cell, or even protein once injected into a system. The QDs are then forced to luminesce or fluoresce[20] allowing scientists or doctors to detect and trace biological targets throughout the body. Quantum dots offer the advantages of being significantly brighter and vastly more resistant to photobleaching than the organic dyes, which are currently being used for biological labeling[21]. The information gained from such research can be used toward further understanding how the human body works as well as possible early detection for certain cancers. Figure 2.6 depicts two live mice.

Both mice have been injected with equal amounts of a QD-prostate-specific membrane antigen Ab conjugate. The mouse on the right is harbored with C4-2 tumor xenografts. The orange-red fluorescence indicates a prostate tumor growing in the mouse on the right. The mouse on the left is the control subject- a healthy mouse with no tumor- and shows no localized fluorescence signal. This suggests that indeed the functional groups are binding to site-specific locations.

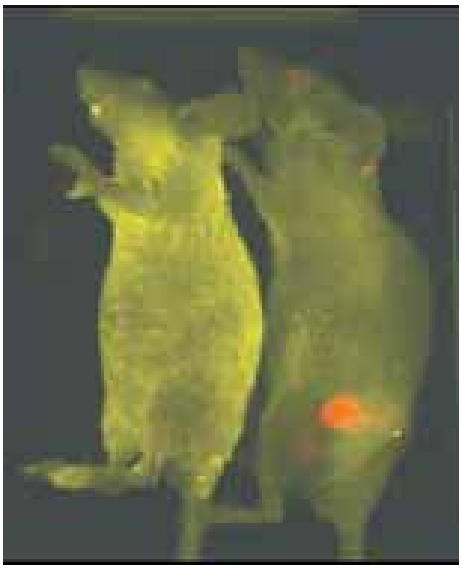

Figure 2. 6: Image of two mice injected with quantum dots functionalized with a site-specific antigen.

While biological labeling exploits the interesting luminescent properties of QDs, quantum computing makes use of their unique electronic properties. Quantum computers promise to enable immense computing power in systems based on units of information called qubits, which are similar to the binary bits in today's classical computers. Today's computers work by representing information as a series of ones and zeros, or binary digits called “bits”. This code is relayed by transistors, which are minute switches that

can either be on or off, representing a one or a zero, respectively. While conventional computers use binary code, quantum computers would function on ternary code, consisting of not only 1 and 0, but also 1 and 0 simultaneously. This ternary system is based on the quantum mechanical phenomenon of "superposition". This phenomenon states that an electron can exist in two places or in two states at the same time. That means computers based on quantum physics would have quantum bits, or "qubits", that can exist in both the on and off states simultaneously, making it possible for them to process information much faster than conventional computers. As you string together more and more qubits, the computing power grows exponentially[22]. By linking two qubits together, you can work with four values at the same time. Three qubits can work with eight values, and so on. If you can link up to 40 qubits, you could work with more than a trillion values simultaneously. Quantum computing is more than just making computer processors faster, it an entirely new way of computing.

Excitement aside, there are obstacles science must overcome before we have quantum computing or biological labeling introduced into our everyday lives. In the case of biological labeling, biocompatibility is an enormous problem for quantum dots[23]. The most heavily research quantum dot material, cadmium selenide, is believed to have carcinogenic effects. Researchers have gone to great lengths to solve this problem of toxicity by encasing the QDs in biocompatible shells[24,25], which has been met with some success. There is also an issue of synthesizing a monodispersed solution of quantum dots[26]. Because small changes in size have such dramatic effects on properties, a tremendous amount of precision must be attained in order to ensure that the QDs are consistent in dimension.

Although the particular problems facing QDs in biological labeling are not relevant for quantum computing, it also has substantial hurdles to overcome. One of the largest obstacles is simply detecting the qubit value of the QD – whether it's a 1, a 0 or a 1/0. Quantum dots are very sensitive to their environment. So sensitive, in fact, that the act of measuring the value a qubit has at a particular moment can alter its value and destroy its information. While some research groups have developed an unobtrusive nuclear magnetic resonance (NMR) technique for measuring qubits[27,28], it is impractical and too expensive to be economically feasible for consumer use. In addition to this, errors can arise as a direct result of decoherence, or the tendency of a qubit to decay from a given quantum state into an incoherent state as it interacts, or entangles, with the state of the environment[29]. These interactions between the environment and qubits are unavoidable, and induce the breakdown of information stored in the quantum computer, and thus errors in computation.

2.1.2: Carbon Nanotubes

It was in the early 1990's that Iijima burst onto the scene with his discovery of a one-dimensional nanostructure, the carbon nanotube[30]. One-dimensional nanostructures are materials that have only one dimension within the nano-regime. Carbon nanotubes are tube-like structures that may be grown to lengths of several centimeters[31], but their cross-sections are only a few nanometers thick. These nanostructures are made up of a hexagonal network of carbon atoms forming a crystalline graphite sheet. This sheet is "rolled up" seamlessly to form tubular structures. If these tubes are "rolled" together so that the ends of the carbon sheet meet, then the carbon nanotube is referred to as a single

wall nanotube (SWNT). If, however, the tubular structure is made up of a few layers of

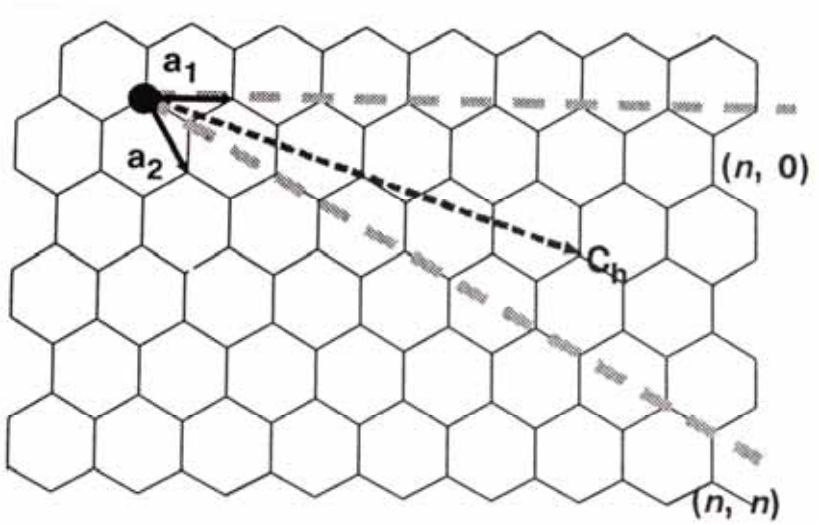

Figure 2. 7: Schematic of a two-dimensional grapheme sheet illustrating lattice vectors $\hat{a}_1$ and $\hat{a}_2$ and chiral vector $C_h=n\hat{a}_1+m\hat{a}_2$.

graphite, then the structure is referred to as a multiple wall nanotube (MWNT).

Other differences among nanotubes exist beyond being a SWNT or MWNT. The chirality, or the direction the nanotubes are rolled, has a significant impact on the physical properties[32,33]. There are three distinct types of nanotubes based on their chirality: armchair, zig-zag, and chiral nanotubes. To understand the differences in these nanotubes, we must first examine the chiral vector and the chiral angle. The chiral vector is defined as $C_h=n\hat{a}_1+m\hat{a}_2$, where $\hat{a}_1$ and $\hat{a}_2$ are unit vectors and n and m are integers. The chiral angle, θ, is measured relative to $\hat{a}_1$. Figure 2.7 illustrates the concept of a chiral vector and chiral angle on a two-dimensional carbon hexagonal lattice. Armchair nanotubes are formed when $n = m$ and the chiral angle is 30°. The moniker "armchair" is derived from the pattern the carbon lattice makes when "rolled" this way. The same holds true for the zigzag nanotubes, which are formed when either *n* or *m* are zero and the

chiral angle is 0°. All other nanotubes, with chiral angles between 0° and 30°, are known as chiral nanotubes. Figure 2.8 moves past a two-dimensional analysis and depicts a three-dimensional view of each type of carbon nanotubes. Understanding the chirality is important since it is directly correlated to the electronic conductivity of the nanotubes. If

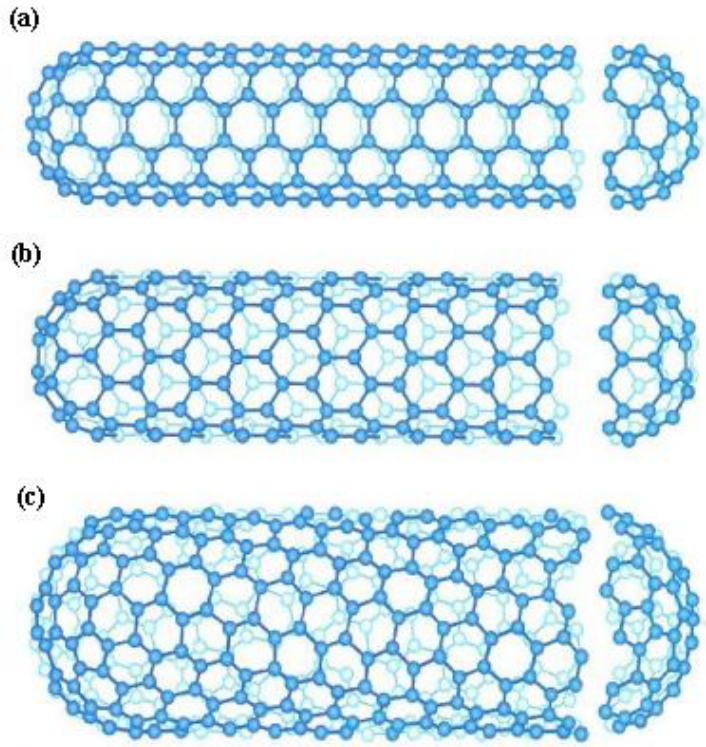

Figure 2. 8: Schematic of three-dimensional carbon nanotubes in the (a) armchair, (b) zigzag, and (c) chiral configurations.

a carbon nanotube has the armchair configuration, then its electronic conduction closely resembles that of a metal[32]. Conversely, the zigzag configuration tends to have the same electronic properties as a semiconductor, whereby electrons must overcome a bandgap in order to enter the conduction band[32]. It is these metallic-conducting nanotubes that provide the most interesting applications in the field of electronics.

In particular, one of the most intriguing properties associated with metallic-conducting nanotubes is ballistic conduction[34,35]. Ballistic conduction is an electronic

transport phenomenon that has no energy dissipation[34] and quantized conduction. Consequently, to observe ballistic conduction in a carbon nanotube, it must have armchair chirality. The impact of having electronic components that display quantized conduction and generate no heat would be significant for electronic packaging. To date, the electronic packaging industry is rapidly approaching the limits of current technology as miniaturization crowds more and more components with increasingly fine feature size into an ever-shrinking device. Some view carbon nanotubes as having the potential to be the next breakthrough in computer technology.

However, nanotubes are not limited to novel conducting properties. Carbon nanotubes have been shown to have Young's moduli and tensile strength values far greater than that of diamond[37,38]. To understand these values we must first delve into the bonding characteristics of carbon. Carbon can arrange itself as a hexagonal network of carbon atoms that form sheets, which are stacked on one another (graphite), or arrange itself into a tetragonal configuration (diamond). In the hexagonal configuration, carbon forms sp^2 bonds with its neighboring carbon atoms, while the tetragonal form produces sp^3 carbon bonds[39]. The bond strength for graphite's sp^2 bond and diamond's sp^3 bond are 430kJ·mol^{-1} and 350kJ·mol^{-1}, respectively[40]. Initially, it seems counterintuitive that a material used as a lubricant would have a higher bond energy than one of the hardest materials on earth. The reason why is that the strong sp^2 bond only occurs between carbon atoms within the same graphite sheet. The sheets themselves are loosely bonded together, making them easy to "peel off" or cleave. It is this inter-sheet bonding that gives rise to the soft quality of graphite, not the strong intra-sheet sp^2 bonds.

Carbon nanotubes are graphite sheets that have been seamlessly rolled together and are made up of this strong sp^2 bond. As several studies have discovered (both theoretically[41,42] and experimentally[43,44]), this bonding nature gives rise to amazing mechanical properties. How does one test the mechanical strength for something that is only a few nanometers thick? Conventional measurement techniques are unrealistic for something of such dimensions. To circumvent this problem of dimensionality, researchers had to develop a variety of new techniques for isolating and measuring the properties of a single nanostructure[45,46,47]. One such investigation involved using an in-

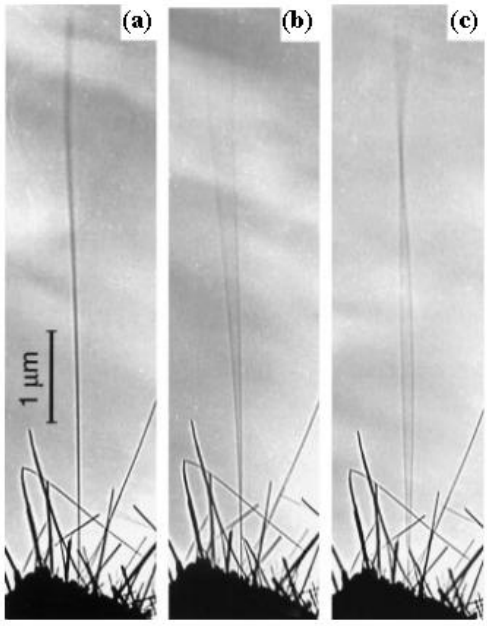

Figure 2. 9: A nanotube's response to an applied AC potential (a) no potential, (b) resonance on the fundamental mode, and (c) resonance in the second harmonic[47].

situ TEM experiment, whereby a stage holder was fabricated to allow an individual nanotube to be electrically excited into resonance[48] (see Figure 2.9). The resonating nanotube could then be treated as a cantilevered beam in resonance governed by the theories of classical dynamics. By measuring a few values and knowing material

constants, a value for the bending modulus of an individual nanotube can be calculated. This particular study revealed an indirect relationship with the bending modulus of a nanotube and the tube diameter. Values ranged from 1TPa for the smallest diameter tube (8nm) to 0.1TPa for the largest diameter tube (40nm). The bending modulus can be related back to the Young's modulus for a solid. In fact, several previous investigations have reported measuring the Young's modulus for SWNT to be around 1TPa[49,50,51]. Additionally, scientists have measured the tensile strength for nanotubes which were reported to be 30GPa. It is possible that the lack of defects in an individual carbon nanotube is what accounts for these incredibly high values. When a material becomes increasingly smaller, it becomes thermodynamically less stable for dislocations and other line defects to exist within them. However, it should be noted much more research must be conducted before defect concentration can be directly linked to the carbon nanotube's strength values.

Having exceptional mechanical properties, like bending to extreme angles (~180˚) without fracture[52,53] (see Figure 2.10) and high tensile strength, makes carbon nanotubes

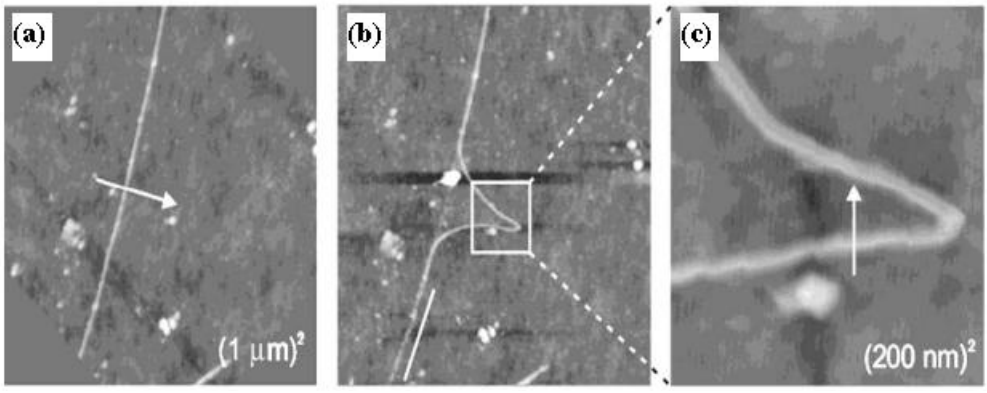

Figure 2. 10: Images of a carbon nanotube being manipulated by an AFM[51].

candidates for the next generation of superstrong fibers for use as mechanical

reinforcement in composites, polymers, or other building materials. There was even an idea of using carbon nanotubes to build an elevator that went into space.

However with all its fantastic electronic and mechanical properties, there are still substantial obstacles to overcome before nanotubes are used commercially. Cost is a huge obstacle inhibiting nanotubes use in large-scale construction applications. Currently companies like Carbon Technologies Inc. are selling single wall carbon nanotubes at prices ranging $375 per gram for low purity to $2000 per gram for high purity samples. Attempting to build an entire structure using nanotubes as a constituent in any building material would raise the cost to astronomical heights with the current market being what it is.

Yet it is not just the mechanical properties that have difficulties to overcome. As explained previously, the electronic properties like ballistic conduction are contingent on the chirality of the nanotube. If the electronic properties of these nanostructures are to be used in a commercial application, then nanoscientists must be able to exhibit some control over the chirality. In all of the current techniques for nanotube synthesis there is always a mixture of metallic (armchair) or semiconducting (zigzag) nanotubes. Since control during synthesis cannot yet be achieved, attempts to separate the two types of conducting nanotubes post-synthesis are being made. This effort has been met with some success. A group in Germany reported a technique they used to successfully separate metallic conducting nanotubes from semiconducting ones[54]. This technique involved dispersing nanotubes into a solution and using alternating current dielectric phoresis to essentially sieve the metallic tubes from the semiconducting tubes. However in their study they were only able recover around 100pg of metallic tubes. Though this process

could be scaled up, an inherent problem plaguing this technique was bundling of the nanotubes. During growth, nanotubes can bunch and coil together to form nanotube fibers. If the bundles or fibers are a mix of metallic and semiconducting nanotubes, then effectiveness of the dielectric phoresis is greatly inhibited. Without the ability to control the electronic structure with some amount of precision, the use of these nanotubes in electronics will be unlikely.

This desire to implement nanostructure into device fabrication represents a shift from a top down to a bottom up approach. Top down refers to the conventional miniaturization of silicon electronics. The current computer industry is built upon using methods for making smaller and smaller device features through high precision lithography. However, this top down approach has already begun to push the limits of current technology and may be unable to reach the deep nanometer regime (1-10nm). Conversely, the bottom up approach utilizes nanostructures as building blocks to fabricate devices from the atomic level up. But, like the top down approach, fabricating a device from the bottom up also has severe limitations. Current technology can use tools like atomic force microscopy (AFM) to place individual nanostructures at specific sites[55]. However, this process is clumsy and time-consuming; manipulating a large number of nanostructures to make a complex working device would take an almost infinite amount of time with the current methods we have at our disposal. For this reason, researchers have been trying to create self-assembled architectures of nanostructures[56] as well as attempting to develop better e-beam lithography techniques. If these methods prove successful, then they would bring nanotechnology one step closer to an economical and efficient fabrication process.

In recent years, research into nanotubes has begun to dwindle. But due to both the promise and shortcomings of carbon nanotubes and quantum dots, interest into the overall field of nanoscience has continued to grow since their discovery. These structures helped bring a huge influx of attention, both scientifically and economically, into this field and allowed researchers the freedom to investigate other material systems and structures.

2.1.3: Nanowires

With the outpouring of research, the door was thrown wide open for an entirely new aspect of nanoscience and technology. It wasn't long before different types of one-, two-, and three-dimensional nanostructures and materials were being synthesized and studied. One particular nanostructure, the silicon nanowire, quickly developed considerable momentum as "the next big thing" in nanoscience. It was a logical progression that shifted focus from carbon nanotubes to silicon nanowires and nanorods. The nanotubes made a lot of people stand up and notice the huge potential for nanotechnology in the computing and electronics industry. Since silicon is the basis of all computing and electronic technology, the move into silicon nanostructures was a natural and inevitable evolution.

Just as nanotubes are considered one-dimensional nanostructures because only their cross-sections are in the nanoscale, so are nanowires and nanorods. However where nanowires and nanorods diverge from nanotubes is in the geometry of their cross-sections. Nanotubes are hollow; nanowires and nanorods have solid cores. Furthermore, what separates the nanowire from the nanorod is the relationship between the length and

the cross-section. For a nanowire, the cross-section is so small in comparison to its length that it s usually considered negligible, i.e. nanowires are extremely long and very thin. A nanorod, on the other hand, has its cross-section and length roughly within an order of magnitude of each other, i.e. the rod is short and thick. Most scientists within the nano-community consider nanorods to be a short nanowire, and therefore a subgroup of this nanostructure. As such, the rest of this thesis will refer only to the larger class of materials, nanowires, even when speaking of nanorods.

Nanowires have been successfully synthesized out of several different materials[57,58,59,60], but similarly to QDs, one particular nanowire material attracted the most attention. In the late 1990's, research in nanowires was dominated by silicon. The synthesis technique used at the time was physical vapor deposition. In this technique, a source material, usually high purity silicon[61] or silicon dioxide[62] was sublimated and the vapor was transported to a cool zone where it redeposited in the form of silicon nanowires. One of the immediate benefits of silicon nanowires over nanotubes was the electronic structure. Whereas nanotubes were either metallic or semiconducting, depending on the chirality, silicon nanowires were always semiconducting in nature[63]. This characteristic immediately allowed nanowires to bypass one of the more substantial roadblocks that impeded the implementation of carbon nanotubes into electronic applications - there was no need to separate the metallic-conductors and semiconductors.

Although diverting this pitfall, there were still significant hurdles necessary for silicon nanowires to overcome. By nature, silicon is an oxygen-hungry material. Whenever silicon is in an oxidizing atmosphere, such as air, an unavoidable passivating silicon dioxide (SiO_2) layer is formed at the surface. This is true for bulk silicon and

silicon nanowires. A silicon nanowire with be encased in a sheath amorphous SiO_2 (see Figure 2.11) as soon as it is exposed to an oxygen atmosphere[64,65]. This has implications in the conduction of the silicon nanowire, because, unlike silicon, silicon dioxide is electrically insulating.

This passivating oxide layer is not the only conduction problem facing silicon nanowires. Extensive TEM studies reveal that silicon nanowires are sometimes made of

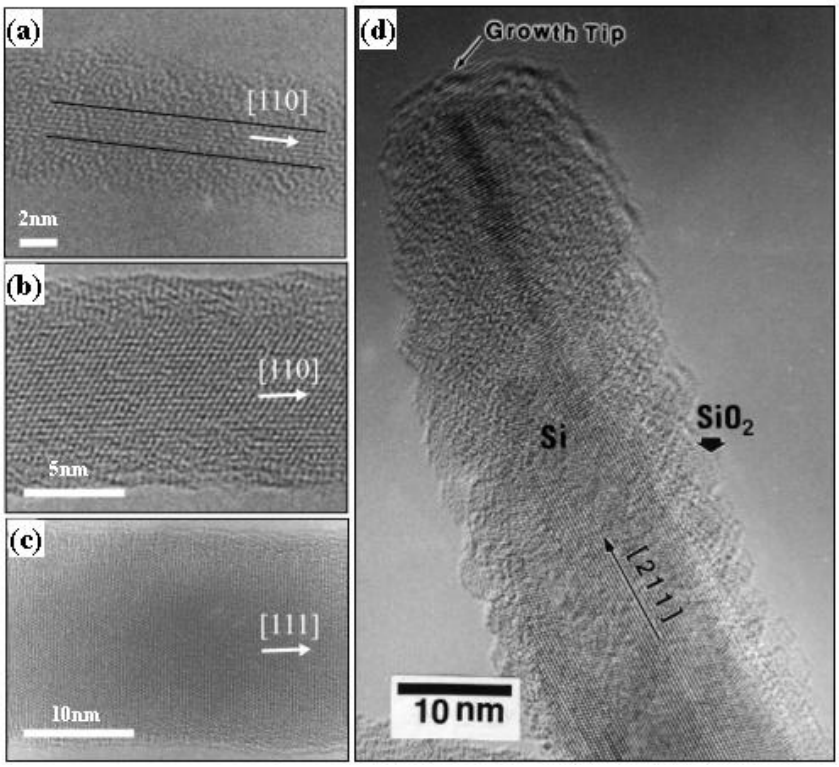

Figure 2. 11: High-resolution TEM images of (a) 6.7nm, (b) 10.7nm, and 20.6nm diameter silicon nanowires[67] grown by the dissociation of SiH_4. TEM image (d) of silicon nanowires[63] grown by the sublimation of SiO.

polycrystalline cores[66] and typically have dislocations or defects incorporated into the nanostructure[67]. In the ideal case of electron transport, a material should be single-crystal and defect-free. The boundaries in polycrystalline materials, as well as any dislocations that are present, serve as possible scattering events in a material. Scattering events

impede electrons from moving through the material and thus hinder electronic conduction. That is why defects, polycrystallinity, and the SiO_2 sheath present problems in the electronic conduction of silicon nanowires.

To combat these issues, researchers looked to alternate methods of synthesis. Charles Lieber was the front-runner of this movement and played a major role in the uncovering of a fundamental mechanism that controls the growth of these nanostructures. Instead of employing a physical vapor deposition (PVD) technique, his group at Harvard used a chemical vapor deposition (CVD) method for synthesizing single crystal-silicon nanowires[68]. This CVD process differed from the PVD technique in that a silane (SiH_4) gas was used as a source. This source dissociated into silicon and hydrogen gas. Molten metal particles, such as gold, were placed in the reaction chamber to act as preferential nucleation site. The growth of the nanostructure is controlled by the vapor-liquid-solid mechanism[69,] which will be discussed in much further detail later in this dissertation.

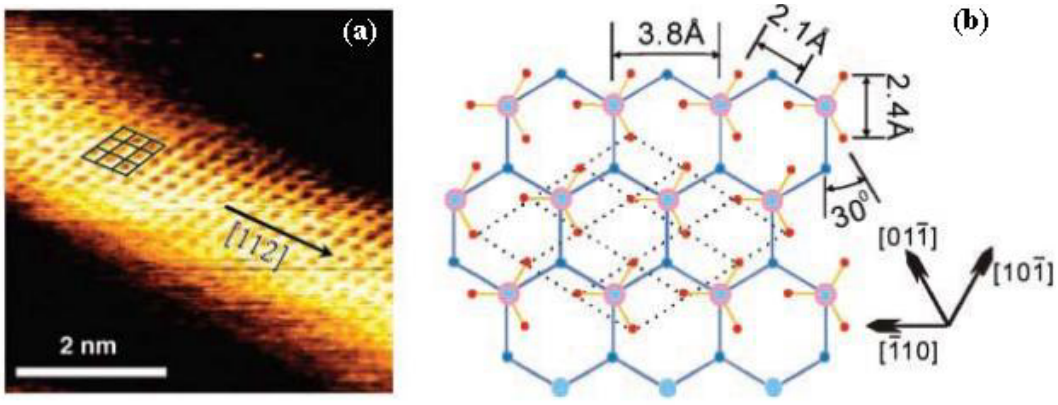

Figure 2. 12: STM image and schematic of a silicon nanowire[69] after hydrofluoric acid treatment (a) STM image of the Si (111) facet, with wire axis along the [112] direction. (b) schematic view of SiH_3 on Si (111). Red and large blue dots represent the H atoms and Si atoms in the SiH_3 radical, respectively. Small blue dots represent Si (111) atoms in the layer below.

This new growth technique drastically decreased the dislocation concentration in the wires and consistently produced single-crystal nanowires[68].

However, despite having single-crystal silicon cores and far fewer defects than the PVD-grown silicon nanowires, these CVD-grown silicon nanowires still had a SiO_2 sheaths surrounding them. A post-synthesis technique involving a treatment of hydrofluoric acid must be performed on the wires in order to etch away the SiO_2 layer. This etching process leaves behind a hydrogen-terminated surface[70] (see Figure 2.12). This new surface is chemically inert, disallowing the reformation of the amorphous sheath. It should be noted that hydrofluoric acid is a dangerous and toxic chemical requiring special precautions necessary for its safe handling.

Research began to shift to other materials in search of a one-dimensional nanostructure that would not form an amorphous layer at the surface. By the end of 2000, single crystal nanowires of group III-V and II-VI semiconductors were successfully synthesized via a vapor-liquid-solid mechanism[71]. Unlike its silicon predecessor, nanowires made from III-V or II-VI materials did not grow an amorphous sheath.

And so it happened with the synthesis of nanostructures - as the types of materials expanded, so did the synthesis techniques. Not only were nanowires being made through CVD and PVD methods, but also through solution-based synthesis[72] and laser ablation[73], both which allowed more complex chemistries - like ternary systems - to be successfully synthesized. The development of these various synthesis techniques allowed researchers the ability to exert more and more control over the dimensionality, morphology, and overall quality of nanomaterials. As was the case with quantum dots, small changes in the size of the nanostructure could result in large changes in the physical properties. The

ability to fabricate high quality nanowires with well-defined and monodispersed diameters would permit scientists to systematically investigate the effects of quantum confinement. Once the properties are understood, devices can be tailored to accommodate those properties for device applications.

In the first half of 2001, Lieber *et al.* published two reports on the successful fabrication of nanoscale electronic[63] and sensing devices[74]. In these reports, nanowires were used as fundamental building blocks, representing some of the first working devices to demonstrate the capability to build devices from nanowires using the bottom up approach. The first report demonstrated three different device configurations that mimicked a passive diode, an active bipolar transistor, and a complementary inverter. The second report gave detailed functionalizing the surface of a nanowire to selectively detect specific biological or chemical species. These two papers were just a few of the reports that signaled a shift to come in nanoscience and technology away from synthesis and into device fabrication.

2.1d: Transparent Conducting Oxide Nanobelts

Due to the novel properties of nanotubes and successful fabrication of simple devices with nanowires, the landscape of research of nanotechnology in the early part of the twenty-first century was dominated by these two morphologies. Yet change again was soon to come.

A group at the Georgia Institute of Technology, led by Dr. ZL Wang, was interested in synthesizing nanostructures out of transparent conducting oxides. This group of materials, ZnO, In_2O_3, Ga_2O_3, SnO_2, and CdO, demonstrated a tremendous

variety of differing properties when doped with the correct constituents[75] (see Table 2.1). Dr. Wang recognized the potential this group of materials had in nanotechnology - particularly, tin-doped indium oxide[76], the transparent conducting oxide used in the majority of flat panel display applications. A $15 billion dollar a year industry, flat panel displays were forecast to almost double by 2005, thus the potential for more widespread applications, as well as future funding[77].

Table 2. 1: List of properties the transparent conducting oxides can exhibit when doped[75].

Choice of Transparent Conductors	
Property	**Material**
Highest transparency	ZnO:F
Highest conductivity	In_2O_3:Sn
Lowest plasmon frequency	ZnO:F, SnO_2:F
Highest plasmon frequency	In_2O_3:Sn
Highest work function	SnO_2:F
Lowest work function	ZnO:F
Best thermal stability	SnO_2:F
Best mechanical stability	SnO_2:F
Best chemical stability	SnO_2:F
Easiest to etch	ZnO:F
Best resistance to H plasmons	ZnO:F
Least toxic	ZnO:F, SnO_2:F
Lowest cost	SnO_2:F

Dr. Wang's researchers saw the possible applications in nanotechnology if the transparent conducting oxides could be made into nanostructures. Therefore they set out on the task of fabricating nanostructures from these materials through a PVD technique by way of a thermal evaporation of a transparent conducting oxide source. What they hoped to get were nanowires, what they actually got was a remarkable new nanostructure that would change the face of nanoscience and technology. This new one-dimensional nanostructure was completely faceted, defect-free, and had geometry similar to that of a belt or ribbon, thus leading to the moniker, "nanobelts". In early 2001, Science

magazine, one of the more prestigious scientific journals, published Dr. Wang's report citing the first observations of this new nanostructure[78].

Although this first report of nanobelts was only a brief paper, the scientific community immediately took notice. A testament to this was an article published in 2003 by Science Watch, a group that documents the impact of papers. In it, the article stated that the paper published in Science just two years earlier by Dr. Wang was the second-most cited nanoscience paper in all of chemistry[79]. This tiny structure started a storm of research, and soon there was a flood of papers using these nanostructures in devices such as lasers[80] and gas sensors[81], as well as new materials made into nanobelts[82,83,84].

2.2: Characteristics of a Nanobelt

From the onset of their discovery, there was immediate discussion as to whether nanobelts were a subclass of the already-established nanowires (like nanorods) or a class of nanostructures all their own. As stated previously in this dissertation, the only difference between a nanorod and a nanowire is the ratio between the cross-section and the length of the structures. While nanobelts share this high ratio between length and cross-section, their faceted morphology defines not only their appearance, but certain physical properties as well. Nanowires and nanorods, however different in length, have the same physical properties. Just as some wouldn't consider nanotubes to be hollow nanowires due to the difference in physical properties, nanowires and nanobelts must also be distinguished from each other. When a material, like ZnO, is made into either a nanowire or a nanobelt, there are distinct properties associated with the nanobelt that are

not present in nanowires. For this reason, nanobelts must be considered their own independent class.

The high aspect ratio (width to thickness) and rectangular cross-section are just two of the defining characteristics of a nanobelt. Although single-crystallinity and low defect concentration are not intuitively a prerequisite for nanobelt structures, these two characteristics are permanently linked with them. (For instance, if a polycrystalline nanobelt were to be synthesized, it would be necessary to describe it as such, to avoid confusion). The reason for these particular designations may be the juxtaposition of silicon nanowires and metal oxide nanobelts. As stated previously, during the early days of silicon nanowire synthesis, nanowires were either polycrystalline or single crystals that were riddled with defects like dislocations[85,86]. Contrastingly, nanobelts, as they were discovered, were always single-crystalline and typically were dislocation-free, thereby making these characteristics synonymous with nanobelts[78].

Before the discovery of nanobelts, all other one-dimensional nanostructures were either irregular in shape or had rounded surfaces. Nanobelts, in sharp contrast, have clear and distinct edges at the points where their facets intersected and these faceted surfaces are defined by specific crystallographic planes. For instance, ZnO has a wurtzite crystal structure with a fast growth direction in the <0001>. If a nanobelt is promoted to grow along this direction, then the surface facets of that nanobelt will be comprised of the $\pm(2\bar{1}\bar{1}0)$ and $\pm(01\bar{1}0)$ crystallographic planes. It is this faceted nature that gives rise to the physical characteristic that most distinguishes a nanobelt has from all other morphologies: its rectangular cross-section.

It is this rectangular cross-section and ultra-long lengths (up to a few millimeters) that led Dr. Wang to don the name, "nanobelts", to these structures. As nanobelts have facets, there is also the aspect of width to consider – something that nanowires and nanotubes, being circular in cross-section, are without. A nanobelt's width may vary along its length if a catalyst is used during synthesis, but its thickness has been observed to remain constant, regardless of the material[87]. Figure 2.13 is a collection of images taken from the now well-known 2001 Science paper. From these images, the nanobelts demonstrate a high flexibility without fracture despite being a ceramic oxide material.

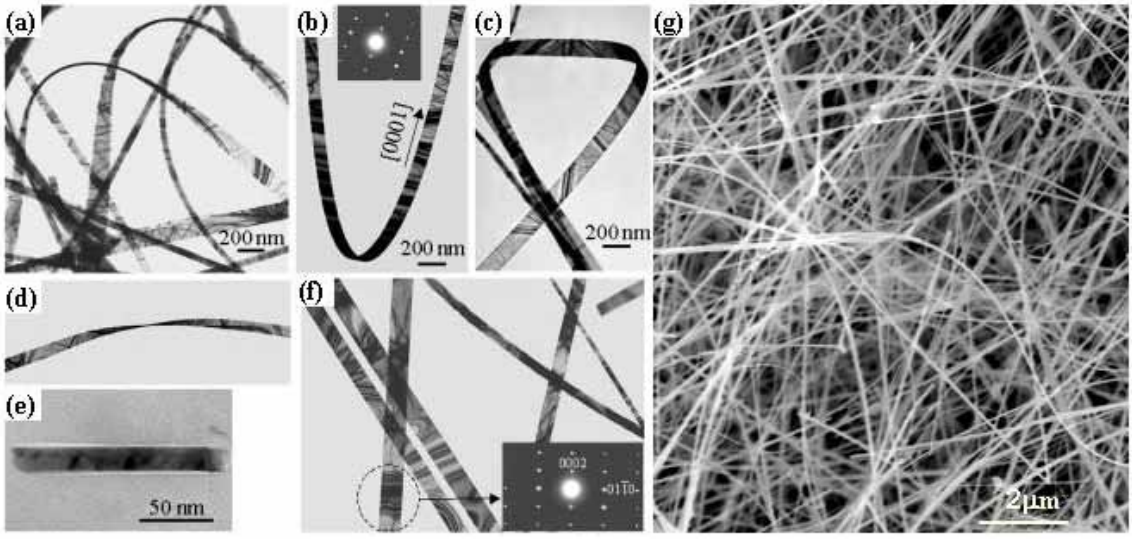

Figure 2. 13: SEM and TEM images of ZnO nanobelts from the first publishes report observing the structure[78].

Many have postulated that it is the high aspect ratio (width to thickness) that gives the nanobelts these properties. For ZnO, the aspect ratio on average was measured to be ~9, but it will vary for each nanobelt material[78].

To recap, nanobelts are defined by a faceted morphology that is comprised of well-defined crystallographic planes. These planes serve to form a rectangular cross-

section with uniform thickness through the entirety of its length. These one-dimensional nanostructures are also defined as being single-crystalline and virtually dislocation-free.

2.3: II-VI Semiconductors

For over a decade, II-VI semiconductors have attracted growing interest owing to their possible application in optoelectronics. The wide band gap II-VI semiconductors are efficient emitters in the blue to UV spectral range and are likely candidates to replace materials like GaN in light emitting laser diodes[88]. Despite some similarities, each of the II-VI semiconductors demonstrate their own unique and novel physical properties. ZnS has a band gap energy of 3.6 eV[2], displays a high refractive index[89], and a high transmittance in the visible range[90,91], making this material a strong candidate for use in optoelectronic devices. However what makes this material so intriguing is its various luminescent properties. ZnS not only exhibits photoluminescence[92], but also acousticluminescence[93], triboluminescence[94], electroluminescence[95], and thermoluminescence[96], lending the material to promising applications in flat panel display, sensors, and lasers. CdTe and ZnSe have direct band gaps of 1.4eV[1] and 2.8eV[97], respectively. CdTe has a high optical absorption coefficient making it ideal for investigation in solar cells and other photoelectric devices[98], while ZnSe could potentially be used in short wavelength lasers[99].

The nanostructures of II-VI semiconductors may exhibits some unique properties. Duan *et al*[100] have shown that CdS nanowires function as Fabry-Perot optical cavities and used these nanowires as electrically driven lasers. As stated before, CdSe is the most extensively studied quantum nanostructures material due to it strong size-tunable

properties, and possible applications for this material include laser diodes[101], nanosensing[102], and biological labeling[80]. Recently Alivisatos *et al.* demonstrated that CdSe nanorods can have up to 100% polarized luminescence and could be used as nano-emitters or high resolution detectors of polarized light[103].

2.3.1: Crystallographic Structure of II-VI Semiconductors

In the broadest sense, the II-VI semiconductors include all compounds formed from elements of the group II and group VI of the periodic table. By definition this encompasses the oxides, sulfides, selenides, and tellurides of beryllium, magnesium, zinc, cadmium, and mercury. However there has been a significantly less amount of research conducted on the chalcogenides of beryllium and magnesium, as well as cadmium and mercury oxide. Therefore, the focus of this and the subsequent section will be narrowed to the sulphides, selenides, and tellurides of zinc and cadmium. This is a natural cutoff within the II-VI compounds since all of the compounds in this restricted II-VI grouping takes one of two crystal structures in the bulk material, zinc blend or wurtzite.

Despite the zinc blend crystal structure being cubic and the wurtzite crystal structure being hexagonal, the two structures do share some commonalities. The combination of the group II elements with the group VI elements give as an average of four valence electrons per atom. If there is a preference for the electrons to be shared rather then transferred between atoms, then the II-VI atoms within the compound will tend to form tetrahedral coordination[104]. A tetrahedral lattice site in a compound AB is one where each A atom is surrounded symmetrically by four nearest neighboring B atoms. In order for this to occur, the B atoms must sit on the corners of the tetrahedron

with the A atom placed in the center of the geometric figure. Within the AB compound the A and B sites are identical in relation to their tetrahedral nature. There are two possible combinations for forming the tetrahedral sites that are relevant to the II-VI compounds. The first possible formation, illustrated in Figure 2.14a, configures the two tetrahedra interpenetrating each other with the base triangles parallel and lined normal to one another. This configuration corresponds to the wurtzite crystal structure. Figure

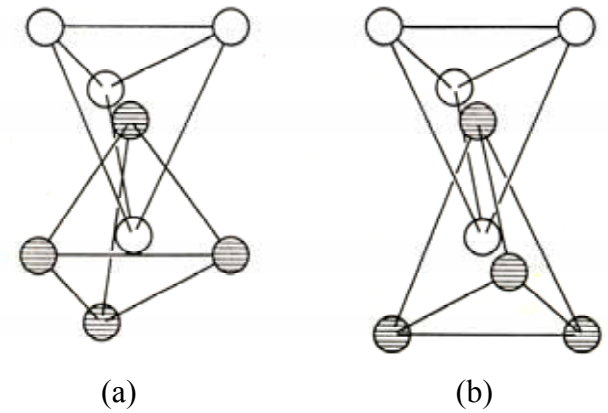

Figure 2. 14: Tetrahedra configurations for the II-VI compounds corresponding to the (a) wurtzite and (b) zinc blend crystal structure.

2.14b depicts a similar configuration, but rotates the bases 60º, while still keeping the bases parallel. This yields the cubic zinc blend crystal structure. The wurtzite structure is in the hexagonal crystal class and consists of two interpenetrating close-packed hexagonal lattices as illustrated in Figure 2.15. A common characteristic all II-VI semiconductors share is a propensity to form into the wurtzite crystal structure given the right conditions.

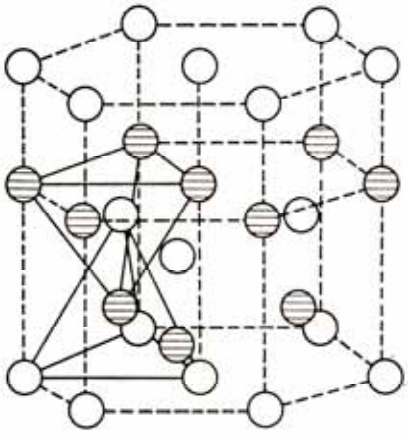

Figure 2. 15: Schematic demonstrating how the interpenetrating tetrahedra form the wurtzite crystal structure.

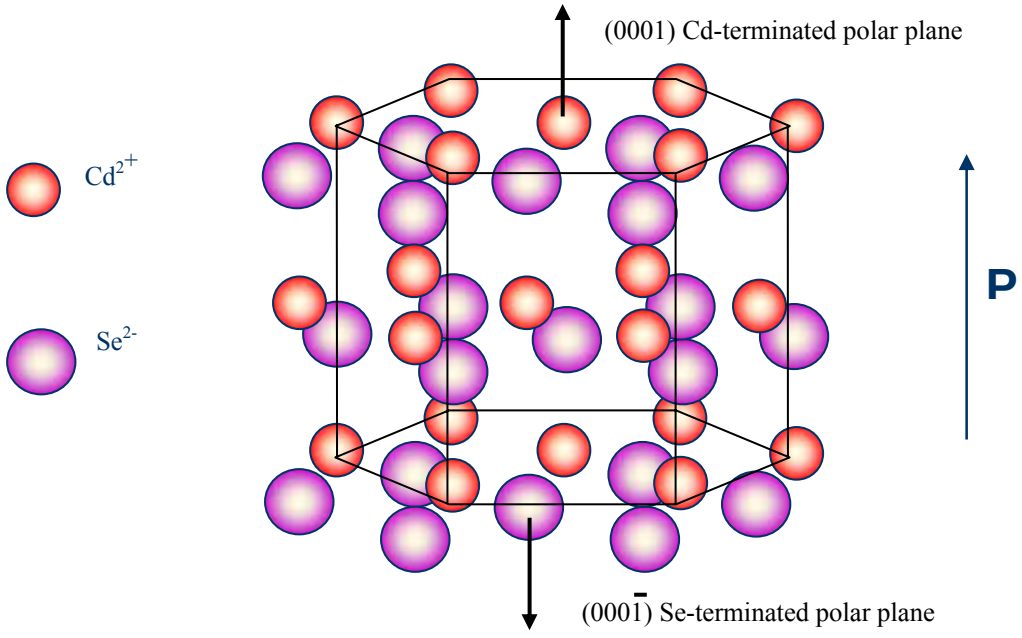

Figure 2. 16: Schematic of the cadmium selenide wurtzite crystal structure.

We now use CdSe as an example to illustrate specific structural characteristics of wurtzite. To do this, we view the CdSe crystal structure in terms of a number of alternating planes composed of the tetrahedrally coordinated Se^{2-} and Cd^{2+} ions, stacked alternatively along the *c*-axis (Figure 2.16). The tetrahedral coordination in CdSe results in non-central symmetric structure. *This will become of great importance in the next section.* Another important characteristic of CdSe is the polar surfaces. The most common polar surface is the basal plane. The oppositely charged ions produce positively charged Cd-(0001) and negatively charged Se-$(000\bar{1})$ polar surfaces, resulting in a normal dipole moment and spontaneous polarization along the *c*-axis as well as a divergence in surface energy. Structurally, CdSe has three-types of fast growth directions: $<2\bar{1}\,\bar{1}\,0>$ ($\pm[2\bar{1}\,\bar{1}\,0]$, $\pm[\bar{1}\,2\bar{1}\,0]$, $\pm[\bar{1}\,\bar{1}\,20]$); $<01\bar{1}0>$ ($\pm[01\bar{1}0]$, $\pm[10\bar{1}0]$, $\pm[1\bar{1}00]$); and $\pm[0001]$. Together with the polar surfaces due to atomic termination, CdSe exhibits a wide range of novel structures by tuning the growth rates along these directions.

2.4: Advantages of Nanobelts

With more established one-dimensional nanostructures already being investigated, what possible utility could the nanobelt structure offer over more heavily researched structures like nanotubes and nanowires? The answer is quite simple - nanobelts lack many of the disadvantages from which the other structures suffer, while still offering other unique attributes, namely consistent semiconducting properties, no risk of oxide sheaths, multiple growth directions, and faceted morphology.

As was extensively discussed previously, the electronic properties of carbon nanotubes are based on the chirality of the individual structure. Yet research into carbon nanotubes face a fundamental issue with the inability to control the chirality of this structure. With no viable synthesis technique available for making only semiconducting or only metallic conducting nanotubes and with current methods for separating the two types of nanotubes post-synthesis being too primitive and unrealistic for industry use, carbon nanotubes may go the way of high temperature superconductors. Herein lies one of the advantages of nanobelts over carbon nanotubes. The conduction characteristic of a nanobelt do not appear to have a large dependence on growth direction like nanotubes; all of the nanobelts that have been studied have demonstrated semiconducting electronic properties[105]. Despite lacking the novel electronic property of ballistic conduction, nanobelts should still display quantum confinement effects in the thickness direction of the belt. Regardless, the consistent electronic configuration of the nanobelts bypasses a major obstacle impeding the implementation of nanotubes into large-scale device fabrication. Therefore, until the problems associated with chirality are solved, nanobelts

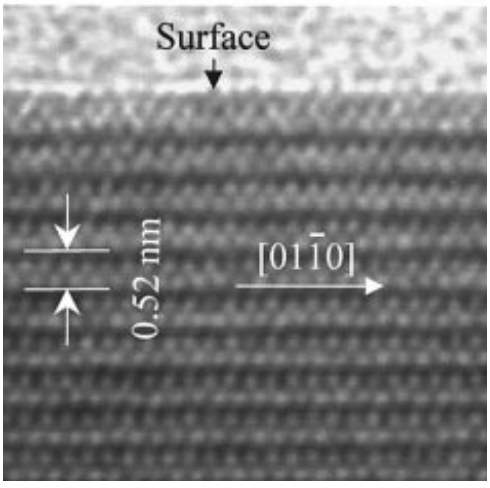

Figure 2. 17: High resolution TEM image of the surface of a ZnO nanobelt[77].

offer a significant advantage over carbon nanotubes for the use in large-scale electronics.

Not only do nanobelts sidestep nanotubes' issue of chirality, they also evade the problem of forming an oxide sheath that the silicon nanowires suffer from. Figure 2.17 is a high resolution TEM image of the surface of a ZnO nanobelts. A quick examination of the image reveals the absence of an amorphous or polycrystalline sheath. Additionally, the nanobelts can be grown to have perfect crystallinity and no dislocation, both of which can have an adverse effect on the conduction properties of a material. In short, nanobelts are more pure than silicon nanowires and do not require a post-synthesis treatment with a toxic chemical in order to realize its electronic conduction potential.

Despite the aforementioned advantages of nanobelts, the largest disparity between nanobelts and other one-dimensional nanostructures is without doubt the possibility for nanobelts to be grown in multiple directions and the faceted morphology of the structures. It is these factors that allow nanobelts to exhibit a wider range of enhanced properties than if a chemically identical structure were to be synthesized in a wire- or tube-like form. For instance, one such structure-property relationship is the observed piezoelectric effect in ZnO. This is a material property and not indicative of a particular nanostructure. However, the nanostructure *does* have a role in how large of a piezoelectric effect can be observed.

2.4.1: Multiple Growth Directions

Unlike chemically identical nanostructures, the nanobelts have been observed to grow in multiple growth directions[106]. The various possible growth directions directly

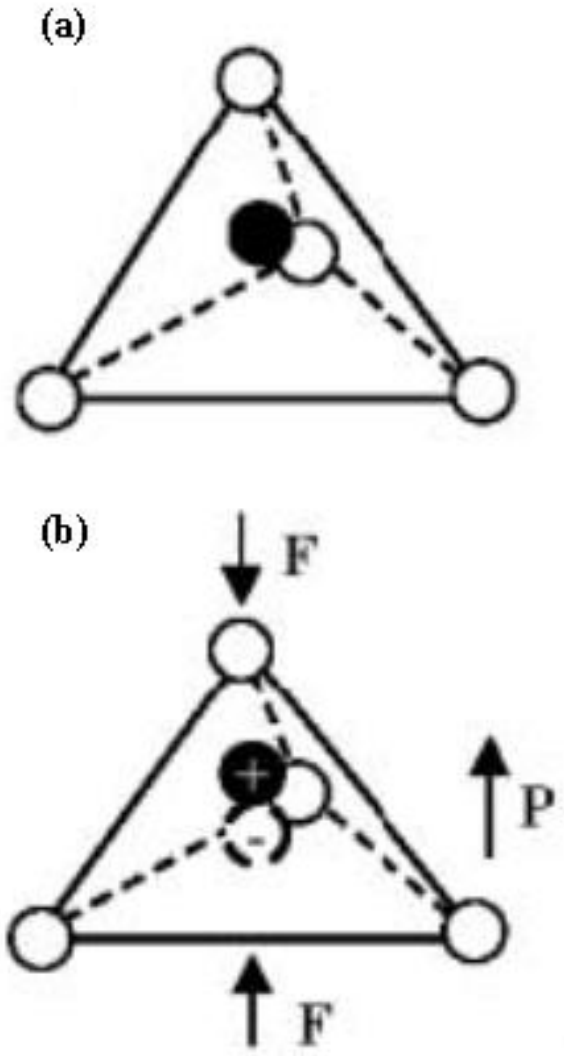

Figure 2. 18: Schematic of (a) tertahedral configuration of a II-VI compound and (b) force being applied along the corner direction of the tetrahedron.

affects the crystallographic planes that comprise the surface facets of the belts. This has its largest impact in regards to the piezoelectric effect observed in the nanobelts.

Due to the intrinsic asymmetric nature of the wurtzite crystal structure of the II-VI compounds, all of these materials can exhibit a piezoelectric phenomenon. Piezoelectricity is a consequence of an atomic-scale polarization. To further understand the piezoelectricity, we again examine the AB tetrahedral configuration discussed in the above section. For this particular case, let us assume that the ion in the center position is the cation, which is surrounded by four anions (Figure 2.18). The center of gravity of the negative charge is at the center of the tetrahedron. When a pressure is exerted on the crystal along the corner direction of the tetrahedron, the geometry of the figure will be distorted and the center of the gravity of the negative charge will no longer coincide with the position of the central atoms. The result will be an electric dipole moment occurring parallel to the direction of force being exerted. If all the tetrahedra in the crystal are oriented in the same direction, then the crystal will have a macroscopic dipole, and thus the two opposite faces of the crystal will have opposite charges.

The piezoelectricity refers to a reversible process in which a crystal elongates or contracts once it is positioned in an electric field. Crystals can only be piezoelectric if they are non-centrosymmetric to ensure the non-compensation among the dipoles created by the tetrahedral. The piezoelectric effect can convert a mechanical stress into an electrical response or vice versa.

Due to the nature of the crystal structure of ZnO, the piezoelectric phenomenon is anisotropic. This effect is largest along the c-axis, the <0001>, of zinc oxide's wurtzite crystal structure. There is one key parameters which is necessary to observe a strong

electromechanical response from ZnO nanostructures, the distance between the surface basal planes, d_b, to be small. By decreasing the distance between the surface ±(0001), the magnitude of the dipole across the structure will increase yielding a larger piezoelectric effect. Nanobelts, on the other hand, can be promoted to grow along the <0001>, $<2\bar{1}\bar{1}0>$, and $<01\bar{1}0>$, depending on the synthesis parameters[107]. Figure 2.19 is a schematic of three different nanobelts with different growth directions and their corresponding surface facets. If a nanobelt's major growth direction is the $<2\bar{1}\bar{1}0>$, then the top and bottom surfaces of the nanobelts are the ±(0001) planes (see Figure 2.19c), and the dipole moment would be running across the thickness of the nanobelt. The effective piezoelectric coefficient (d_{33}) of a single ZnO nanobelt has been measured using a piezoresponse force microscopy (PFM) technique[108]. Values for d_{33} were measured for a (0001) polar surface-dominated zinc oxide nanobelt and found to be dependent on frequency. The measurements gave d_{33} values ranging from 14.3 pmV^{-1} to 26.7 pm V^{-1}, which are much larger than that of the bulk (0001) ZnO value of 9.93 pm V^{-1}. This nanobelt configuration minimizes d_b and demonstrates the largest piezoelectric

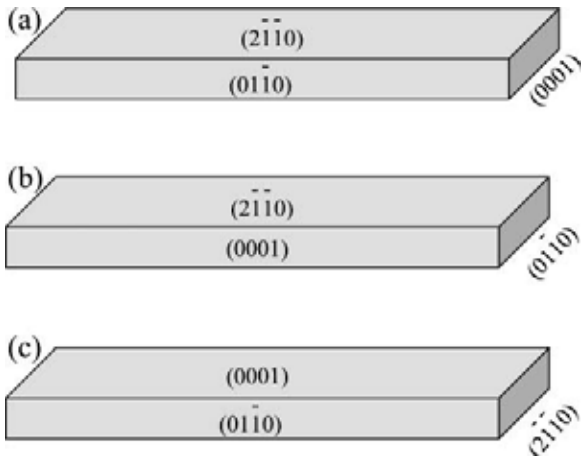

Figure 2. 19: Schematic illustrating the three possible growth directions for ZnO, (a) <0001>, b) $<01\bar{1}0>$, and c) $<2\bar{1}\bar{1}0>$.

effect of the three different growth directions[108]. This piezoelectric phenomenon could be used for a variety of different electro-mechanical coupling device applications.

To date, all of the ZnO nanowires that have been reported grow along the <0001>[109,110]. As a result the piezoelectric effect is along the longitudinal axis of the wire. Since wires are typically long in comparison to their cross-section, then the value for d_b is large and the associated piezoelectric effect would be weak. The electromechanical response for a ZnO nanowire would be equivalent to a nanobelt with the major growth direction being <0001>, which is significantly smaller than $<2\bar{1}\,\bar{1}0>$ grown-nanobelts. It is the ability to change the growth direction, thereby altering the piezoelectric coefficient of the nanobelts. This gives these structures a significant competitive advantage over the other 1D nanostructures in electromechanical coupling devices.

2.4.2: Faceted Morphology

The multiple growth directions are not the only factor controlling the physical properties and potential applications of the nanobelts. The geometric structure of the nanobelts also has a large impact in the properties of the nanobelts, specifically the flat surface facets that define the belt. Researchers have used nanowires in possible lasing applications by optically pumping light through an aligned array of nanowires[111]. If the nanowires have faceted ends, then they can act as mirrors that define a Fabry-Perot cavity[100]. The faceted ends trap in the light as it propagates along the longitudinal axis of the wire. The structure of the nanobelts offer an advantage of having facets not just at the end but also making up the cross-section of the belts. This completely faceted structure

should allow more light to be trapped within the nanostructure. Zapien *et al*[80] have taken one of the first steps in this direction by studying ZnS nanobelts as room temperature lasers using a photoluminescence technique, whereby a 266 nm laser was used as an excitation source. Zapien measured the threshold pumping power to be 45 kW/cm^2 and that it is possible to have an individual ZnS nanobelt to begin lasing at a power density as low as 9 kW/cm^2. This measured value for threshold pumping is similar to results published earlier using ZnO nanowires as lasers[109].

Trapping of light makes the nanobelts not only good structures for nanolasers, but excellent candidates for waveguide applications. Waveguides operates by using a material property called the index of refraction to not allow light to transmit out of the material at certain angles, essentially trapping the light. Initial research into using nanobelts as waveguides has yielded some promising results[112] (see Figure 2.20). The nanobelt can act as a rectangular box of mirrors that reflects the light down its axis.

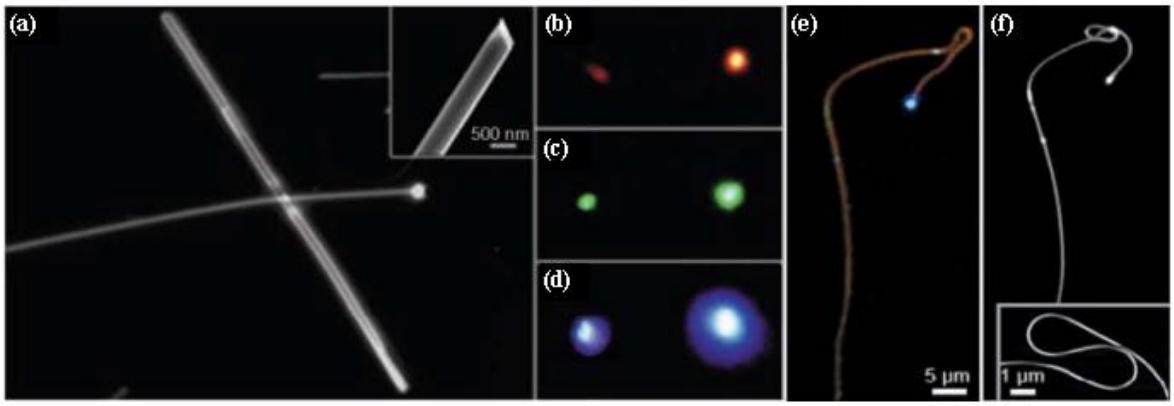

Figure 2. 20: (a) Magnified dark-field photoluminescence view of the right end, with the laser focused on the left end. A wide (~1µm) belt lies across the belt of interest. (Inset) A SEM image of the right terminus of the nanobelts, showing its rectangular cross section. (b to d) Digital images of the guided emission during nonresonant excitation with monochromatic red, green, and blue light, respectively. The leftmost emission spot, caused by scattering at the belt-belt junction.. Optical images of the emission end of a long nanobelts showing the minimal effect of curvature on waveguiding. (e) A true-color photograph taken after crafting a single bend. (f) A black-and-white dark-field PL image captured after an S turn was completed. Blue light is guided around both 1µm radii curves. An SEM image (inset) resolves the bent geometry[112].

Researchers have demonstrated that physical manipulation of the nanobelts into complex orientations with high curvature results in minimal effect on the loss of light within waveguide. This is due to the nature of the morphology. It is because of the completely faceted nature of the nanobelts that the optical properties, independent of material, demonstrate such promise in the field of optics or optoelectronics.

Having specific crystallographic planes serving as surface facets can be a distinct advantage, particularly for functionalization or selectivity of absorbed chemical/biological species. This is of great importance for sensing applications. For several years, researchers have investigated using nanostructures as chemical sensors. Their size and large surface-to-volume ratio allow them to detect extremely small changes in concentration. One of the largest obstacles standing in the way of these ultra-sensitive devices is selectivity. Selectivity can be thought of as identifying a specific species amongst the presence of many other different species. A chemical sensor relies on a change or occurrence of an electrical signal induced by the presence of some chemical species. This electrical signal can be indicative of a change in the surface concentration of donors/acceptors, as is the case for semiconducting oxide sensors, or a net change in mass, as is the case for piezoelectric sensors[113]. However the changes associated with electric signal is indiscriminate of chemical species. To increase the selectivity, functional groups have been attached to the surface of nanostructures. The functional groups act as filters, only bonding with specific chemical or biological species. When a specified species interacts with the functional group, the necessary electrical signal occurs.

A variety of groups have already demonstrated the ability to attach functional groups to the surface of different nanostructures. Where the nanobelts offer a competitive advantage is in the preferential attachment of certain species to specific crystallographic structures. A group from the University of Texas has demonstrated the preferential binding of a specific peptide to the (100) plane of gallium arsenide (GaAs) over the (111) Ga-terminated and (111) As-terminated faces of GaAs[114]. If this observed phenomenon can be further exploited, then the three different crystallographic facets that comprise the surface of the nanobelts can each be functionalized by a different group, allowing a nanobelt sensing device to sense multiple species. This multi-sensing process is not as applicable to carbon nanotubes or silicon nanowires, where there are no distinct surface planes to attach a variety of different functional groups to.

Thus far, four of the II-VI semiconductors have been successfully synthesized into a belt-like morphology. The principles that governed the devices illustrated above can be equivalently applied to all of the 1D II-VI nanostructures. The faceted surfaces of the nanobelts give advantages over other 1D nanostructures. For the case of waveguides, the facets act as reflective mirrors, trapping light in all three directions not just in the axial direction. By selecting particular surfaces of the ionic wurtzite structure, the material can exhibit a strong piezoelectric effect for use in electromechanical devices such as nanoactuators as well demonstrate the potential for preferential adherence of different functional groups to the various crystallographic facets. It is obvious from the initial research already conducted on this group of materials that they show potential for significant impact in the field of nanoscience and technology. It is of the utmost

importance that we continue to investigate these materials to further understand their structure-property relations and incorporate these structures into devices.

CHAPTER III

METHODOLOGY

The thrust of this dissertation focuses on the controlled synthesis on one-dimensional nanostructures. Since the field of nanoscience and technology is so new, there are still many fundamental questions that have yet to be answered regarding synthesis. Like the field of metallurgy, it appears that theories and models regarding synthesis of nanostructures will come through empirical studies. My goal is to better understand the synthesis setup used to grow our nanostructures and improve upon the precision and control we can exert over the entire range of material systems currently being researched.

Because many of the results I attain may be indicative of the experimental setup, I will begin this chapter with a section that details the specific equipment utilized for the entirety of my work. This will be followed by an explanation of different growth mechanisms employed and end with a section that meticulously describe the exact procedures implemented to synthesize our one-dimensional nanostructure.

3.1: Synthesis Setup

The nanostructures to be reviewed in this dissertation were synthesized by a physical vapor deposition (PVD) process by way of a thermal evaporation technique. In principle, the thermal evaporation technique is a simple process in which condensed or powder source material is vaporized at elevated temperatures and then the resultant vapor phase(s) condenses under certain conditions (temperature, pressure, atmosphere, substrate, etc.) to form a desired product. A process involving physical vapor deposition describes

the solidification of a vapor, in this case vapor created through thermally evaporating a II-VI compound source, directly onto a surface. This direct deposition implies that no chemical reactions are permitted to occur either in the vapor or with the vapor and the surface to be deposited on. If a chemical reaction does occur, then the process is not PVD, but rather a chemical vapor deposition (CVD) process.

The furnace system used throughout the entirety of my work was comprised of two components: the furnace and the vacuum system. A schematic of the entire system is given in Figure 3.1. A Thermolyne 79300 single zone split tube furnace was used to carry out all of the synthesis. Exposed heating element coils embedded into a ceramic fiber insulation provided the furnace with the capability of heating up to 1200 ˚C in only 20 minutes. The heating rate of the furnace was controlled by a C1 programmable controller. The C1 is a digital program controller with one stored program of eight segments. Each segments of the program consisted of three parts: a ramp rate (ranging from 1 ˚C/min to 60 ˚C/min), a temperature set point (ranging from 100˚C to 1200˚C), and a dwell time (ranging from 0.1 min to 999.9 min). An alumina (Al_2O_3) tube measuring 30” in length and having a 1.75” outer diameter and 1.50” inner diameter was placed inside the tube furnace. With the furnace measuring only 24” in length, the Al_2O_3 tube protruded from the furnace six inches on either side. Three-inch tube collars lay at the open end of the tube furnace and the alumina tube was placed across the furnace, supported by the collars. Because of the disparity in size of the alumina tube and tube collars, a large gap existed between the tube and collars, allowing cool air to travel inside furnace. The importance and effects of this gap will be discussed later in section 3.3.1.

Figure 3. 1: Schematic of furnace setup.

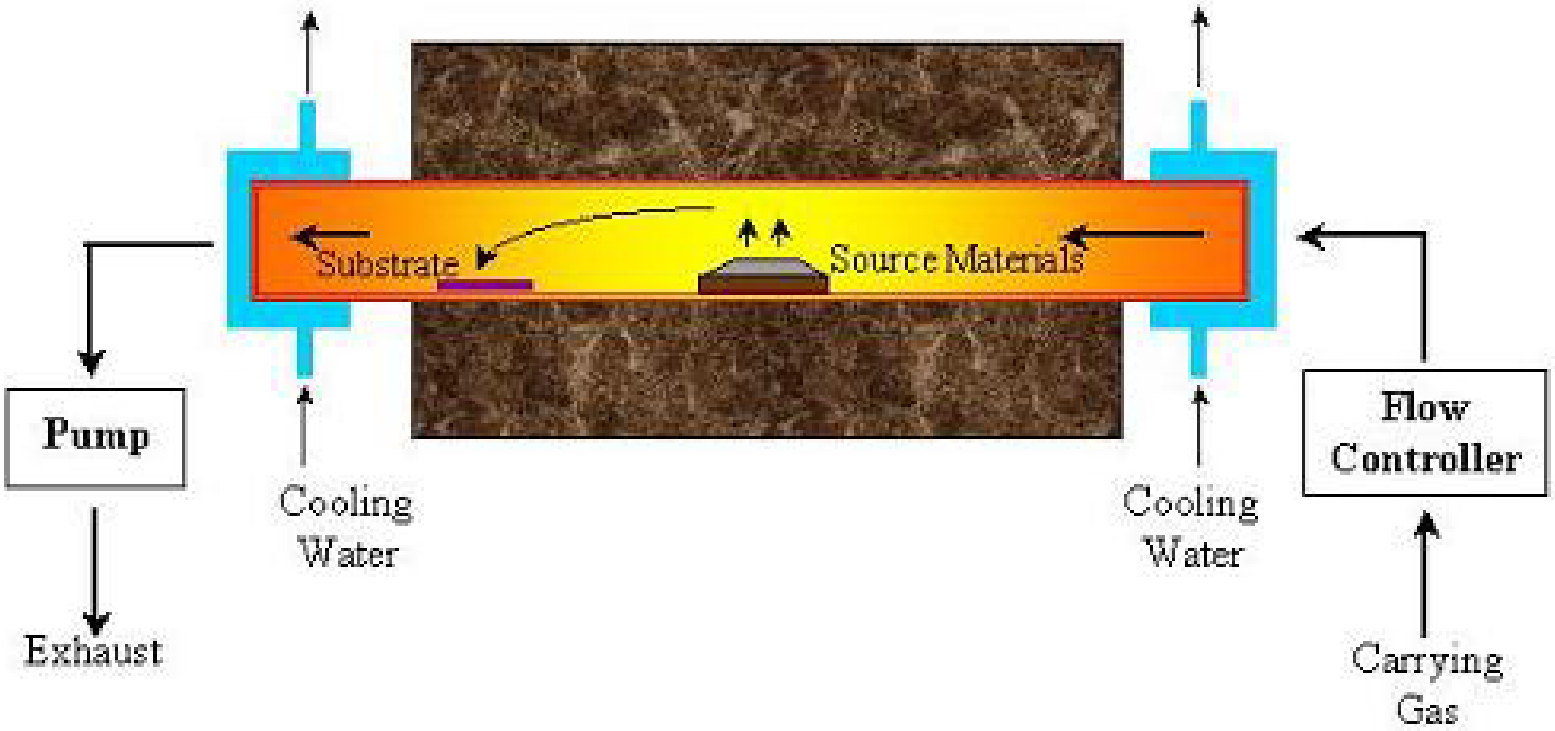

The vacuum system had three distinct functions: evacuating the chamber for synthesis, monitoring and controlling the pressure in the synthesis chamber, and introducing a carrier gas into the system. A BOC Edwards RV8 Hydrocarbon rotary vacuum pump was used to purge the system of oxygen. The mechanical pump was rated to pull gas at a rate of 8.0 m^3/h with an ultimate vacuum of $2x10^{-3}$ mbar. Despite excess oxygen content having an adverse effect on deposition[115], this machinery was sufficient for our needs. The mechanical pump was connected to the synthesis chamber through a series of aluminum tube segments of t-bars, cross bars, and one of the water-cooled end gaps. Figure 3.2 is a schematic of the entire vacuum system. The two end caps, one connected to the pressure system and the other connected to the mass flow controller, were placed at the ends of the alumina tube. Rubber O-rings coated with vacuum grease positioned between the alumina tube and end caps deform as they are compressed between the tube and the caps, sealing the vacuum and furnace systems together. The pump was then turned on, beginning the evacuation process.

The second function of the vacuum system, monitoring the pressure, was achieved through using two analog gauges. The first was a BOC Edwards analog Pirani vacuum gauge series 500 (see Figure 3.2). This gauge monitors lower pressures ranging from 100-10^{-3} mbar. Typically this gauge is only used to observe the system pressure during the evacuation process. The bulk of synthesis is conducted at higher pressure ranges, and for that reason a BOC Edwards analog dial vacuum gauge series CG16K is used to monitor the system pressure during synthesis. This dial gauge measures pressures from 1000 to a 20 mbar in increments of 20mbar. However, this system must not only monitor the chamber

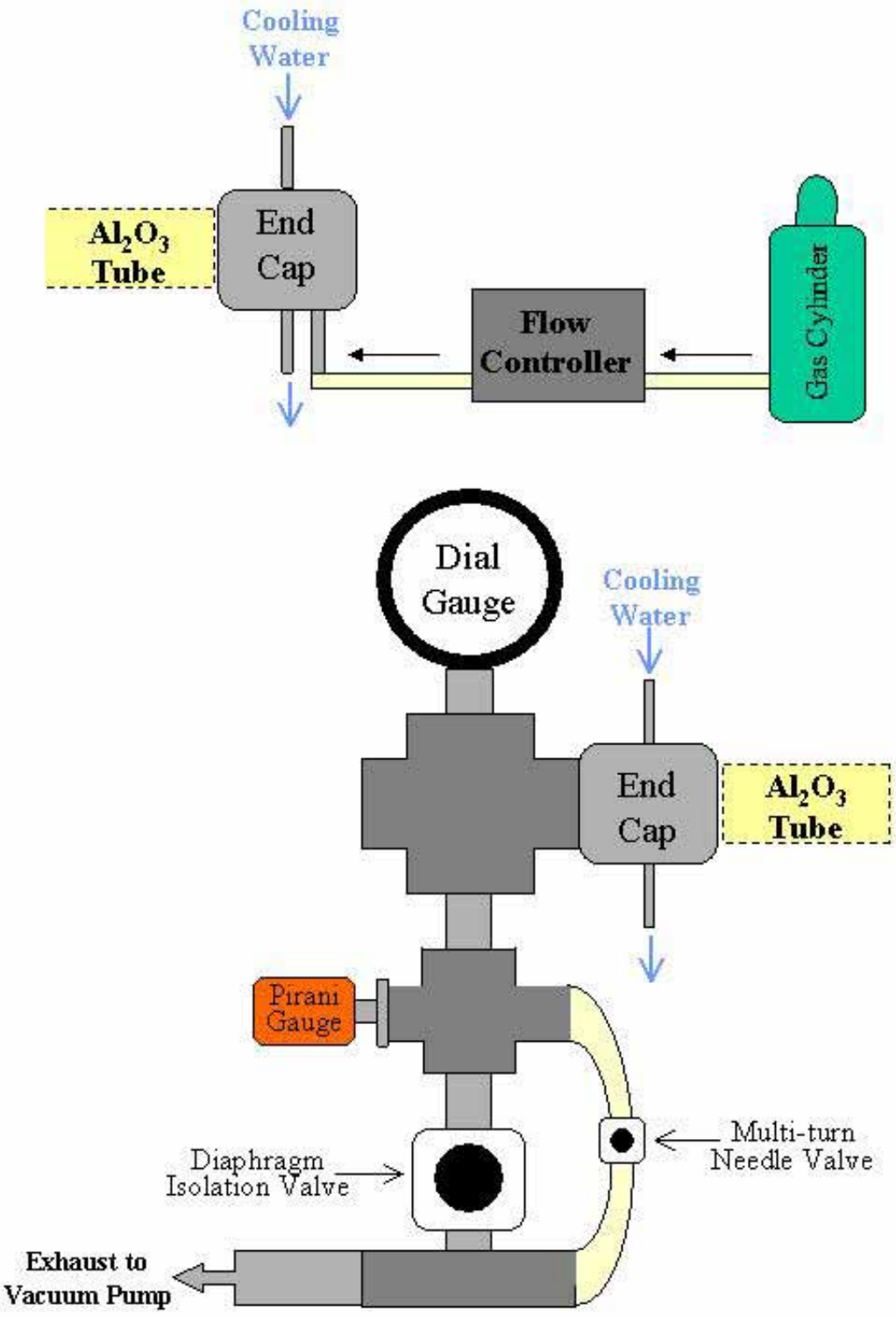

Figure 3. 2: Schematic of vacuum system.

pressure, it must be able manipulate it. Two valves are incorporated into the vacuum system in order to control the system pressure with coarse and fine adjustments. The coarse valve is a BOC Edwards diaphragm isolation valve. The primary purpose of this valve was to open the system to the mechanical pump and purge the chamber. The fine adjustable valve, a Cole-Palmer multi-turn needle valve, was used during synthesis to make small adjustments to pressure.

The last function of the vacuum system was to introduce a carrier gas into the system. An inert nitrogen gas was first sent through an Aalborg N_2 mass flow controller in order to regulate the flow of gas running through the chamber (see Figure 3.2). The flow controller could send N_2 through at a rate ranging from 0-200 standard cubic centimeters (sccm) ±0.1. Once a flow rate was selected and the carrier gas sent through the flow controller, it entered the chamber through one of the end caps via 3/8" plastic tubing connected from the flow controller to the water-cooled end gap.

These are the two major components of our experimental setup. The experimental procedure and methodology for synthesis will be detailed in section 3.3.

3.2: Growth Mechanisms

Though nanostructures can be formed through a variety of synthesis techniques, thermal evaporation has proven effective in synthesizing numerous types of nanostructures. There are two primary growth mechanisms that are widely accepted amongst the one-dimensional nanostructure synthesis community. They are the vapor-solid (VS) process and the vapor-liquid-solid (VLS)[116] process. These two mechanisms are the dominant theories for 1D nanomaterials growth. Each of these mechanisms has

been employed in the work of this dissertation, with the bulk being the VLS growth. As such, the following sections will describe each mechanism, as well as a secondary growth mechanism observed in the morphology of II-VI nanostructures.

3.2.1: Vapor-Solid (VS) Growth

Not much is known about this growth mechanism. Vapor-solid growth is a catalyst-free process whereby deposition occurs when vapor condenses to form a solid. In our particular set up, the sublimated vapor created by heating the source powder is transported via a nitrogen carrier gas to cooler regions within the furnace. When the vapor reaches a temperature zone where solidification is energetically favorable, the vapor may deposit forming a nanostructure.

It should be noted that ultimately it is still unclear if the vapor solidifies in transit or if the vapor directly deposits onto the substrate before forming the nanostructure. In-situ experiments to observe solidification during VS growth is extremely difficult and has several logistical problems to overcome before any definitive answer can be made. However, intuitively if the vapor solidified in transit to form one-dimensional nanostructures, it seems likely that this type of growth would then be observed in conjunction with VLS growth, a site-specific growth process.

It is more likely that "self-catalytic" behavior aids the growth of these structures once the initial deposition occurs. Structures observed via scanning electron microscope (SEM) seem to confirm this theory. Figure 3.3 is a schematic of a proposed VS growth of one-dimensional nanostructures whereby the vapor solidifies directly onto the substrate. Figure 3.3a illustrates the vapor as it reaches a region within the furnace where

it solidification is favorable. The vapor then can solidify, forming a small crystal on the substrate (see Figure 3.3b). This crystal can now act as a "seed" to promote further deposition of the local vapor (see Figure 3.3c). Depending on the size of the "seed" crystal, multiple nanostructures can grow, creating a weed-like growth (see Figure 3.3d).

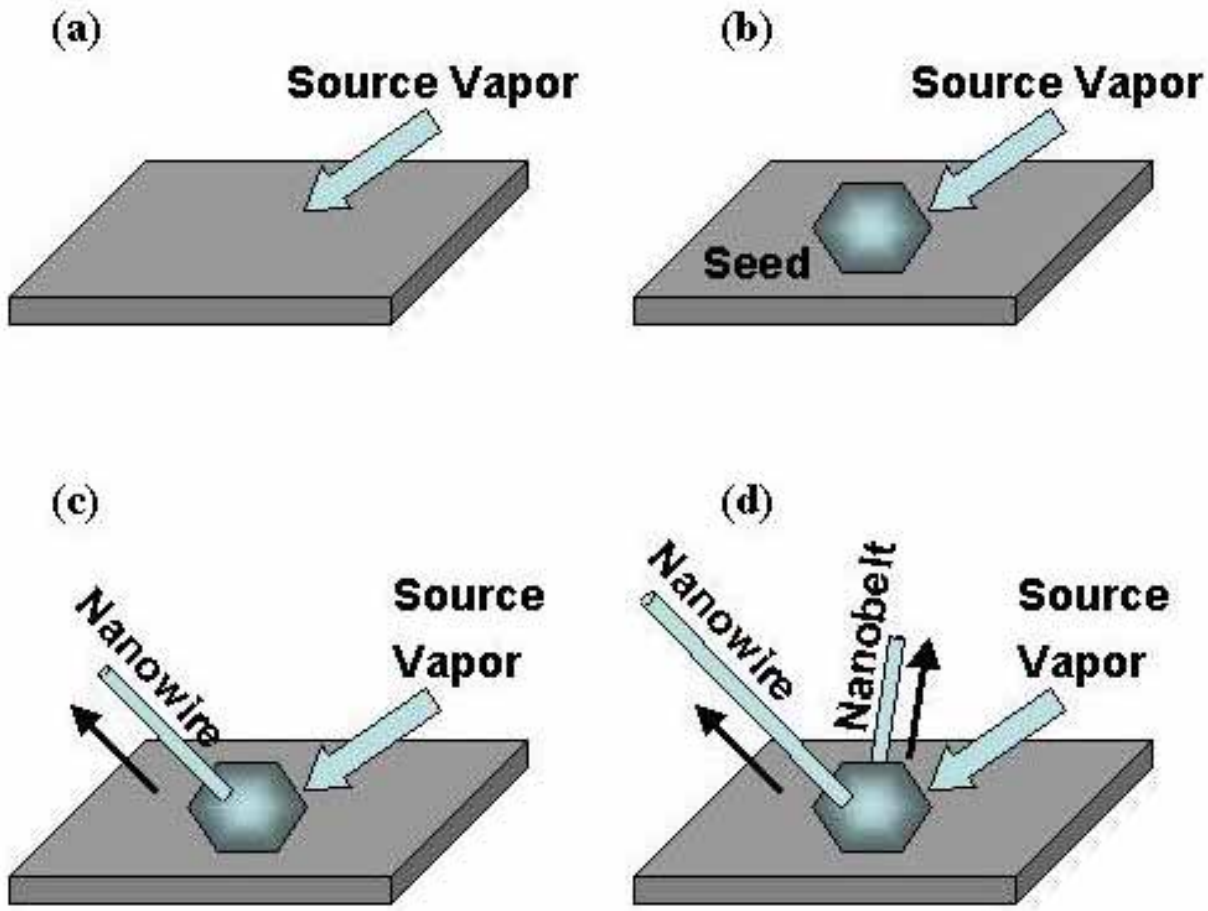

Figure 3.3: Schematic Schematic illustrating the various stages of the vapor-solid growth.

3.2.2: Vapor-Liquid-Solid (VLS) Growth

The VLS growth mechanism was first proposed by Wagner and Ellis[116] in 1964 for silicon whisker growth, and later adapted to one-dimensional nanostructure growth by

Morales and Lieber[117]. Unlike VS growth, in-situ TEM experiments[118] have been conducted to observe the growth mechanism (see Figure 3.4). In particular for one-

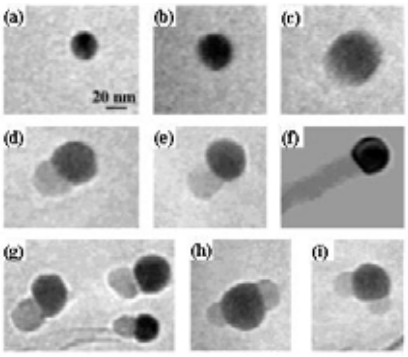

Figure 3.4: TEM images of VLS growth Error! Bookmark not defined.**.**

dimensional nanostructures, the VLS process works in a straightforward manner. Typically, a low melting point metal is selected as catalytic material. Metal nanoparticles are dispersed onto a substrate via solution dispersion, thermal evaporation, or sputtering. Gold was the primary catalyst used throughout this dissertation and will therefore serve as the catalyst for this example. As the gold particle is heated, the metal forms a molten liquid droplet (see Figure 3.5a). Vapor from the sublimating source material is transported by the carrier gas to the catalyst. Vapor then begins to be diffuse into the metal catalyst, forming a liquid alloy (see Figure 3.5b). As more and more vapor is incorporated into the catalyst, eventually the concentration of the vapor material exceeds the solubility of the metal particle. At this point, the supersaturated catalyst precipitates out a solid (see Figure 3.5c). This process of supersaturation and precipitation continues until the growth temperature drops below the eutectic temperature of the particle or the

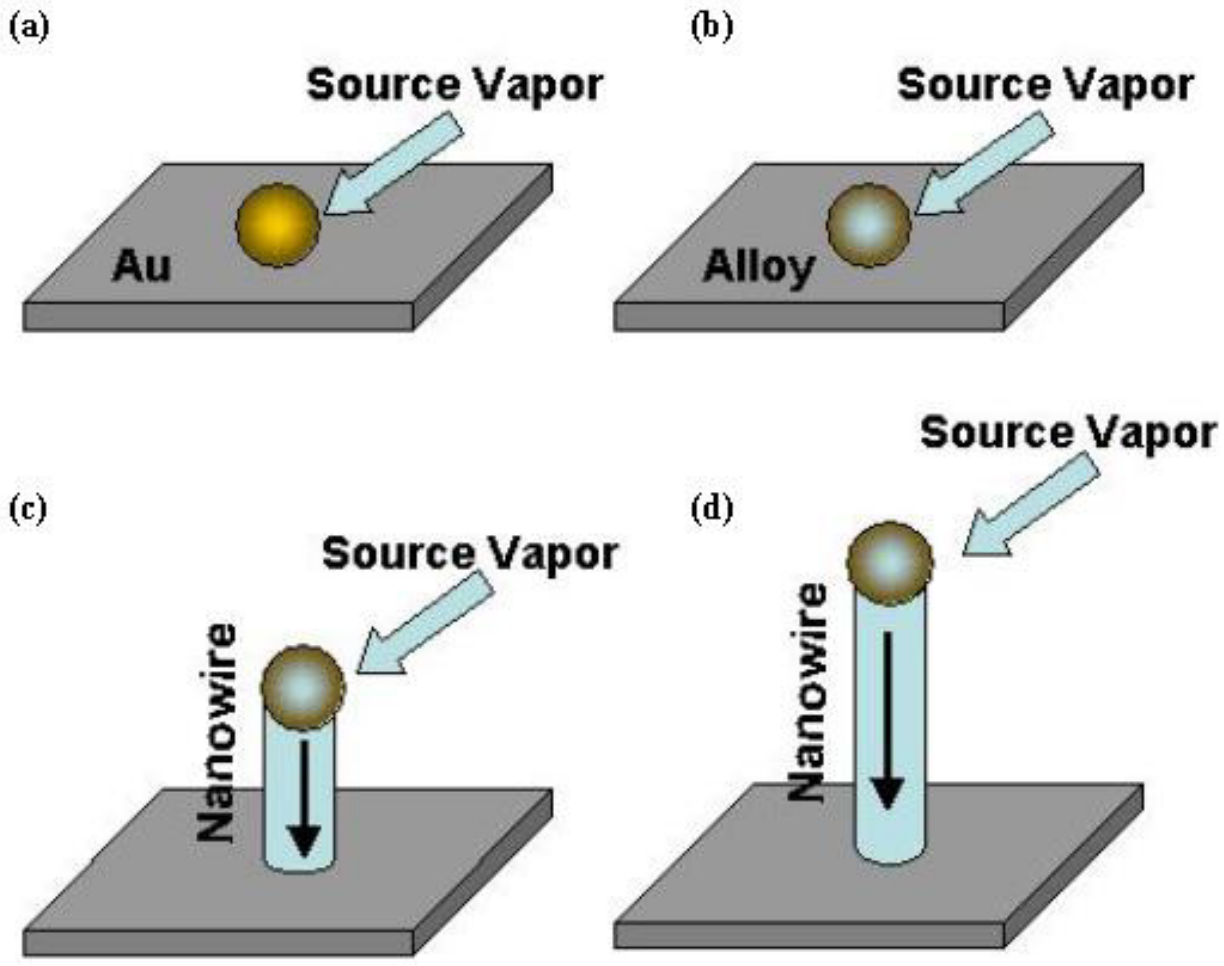

Figure 3.5: Schematic illustrating the various stages of the vapor-liquid-solid growth.

reactant vapor is no longer available (see Figure 3.5d). Metal particles are frequently observed at the growth tip of the nanostructure as a consequence of this process.

There are several benefits in using the VLS mechanism over the VS mechanism. The first is dimensionality control. It has been asserted that the diameter of the catalyst directly affects the cross-section dimensionality of the nanostructure[69]. This is somewhat intuitive since the volume of the solid being precipitated out of the catalyst is limited to cross-sectional area of the catalyst. In addition to size control, the VLS affords the

capability of site-specific growth. The catalysts act as preferential nucleation sites, allowing for patterned or arrays of nanostructures to be synthesized. If techniques like e-beam lithography are further explored and understood, then those techniques would allow researchers to more precisely position or pattern nano-sized catalytic particles on substrates. Lastly, the VLS process provides the ability to synthesize aligned nanostructures. If a single crystal substrate is carefully chosen based on the lattice parameters, then the substrate at the liquid-solid interface can act as a template for growth. This has already been demonstrated for ZnO nanowires and a sapphire substrate[109].

3.3 Experimental Procedure

3.3.1: General Nanobelt Synthesis

There are several processing parameters such as temperature, pressure, carrier gas (including gas species and its flow rate), evaporation time period and substrate, which can be controlled and need to be selected properly before and/or during the thermal vaporization. The source temperature selection mainly depends on volatility of the source material. Usually, it is slightly lower than the melting point of the source. The pressure can be determined according to the evaporation rate or vapor pressure of the source material(s). However, this thermodynamic data is not always available for certain materials. As stated previously, all of the synthesis conducted in this dissertation used a PVD technique and as such the carrier gasses used were either nitrogen (N_2) or argon (Ar) due to their non-reactivity. A flow rate of 50 sccm was consistently used for all experiments as was a evaporation time of 60 minutes. The substrates used to carry out synthesis could be

classified into two categories: polycrystalline substrate and single-crystalline substrates. The use of a particular type of substrate over another was determined by the experiment design of the individual synthesis runs.

The first step in the synthesis process was preparing the alumina tube. The tube was routinely cleaned with ethanol prior to the run. After cleaning, the tube was placed inside the furnace so that the source material and collection substrates could be loaded inside. A designated amount of source material was weighed on a Denver Instrument XE-3100D mass balance. The source was then transferred to an alumina boat and inserted into the center of the tube. Deposition substrates, either single-crystal or polycrystalline, were cut and placed onto long high temperature substrate, referred to as the collection substrate. The purpose of the collection substrate was to easily position the deposition substrates inside the furnace. The collection substrate is 14.6cm long rectangular piece of alumina cut from an unused synthesis tube. The collection substrate, lined with deposition substrates, was positioned 13cm away from the end of the tube and downstream from the source. This corresponded to a distance of 10.5cm from the closest edge of the collection substrate to center of the furnace. Once the substrates and source material were in position, the synthesis chamber was sealed in order to begin the evacuation process.

The thermal evaporation process is very sensitive to the concentration of oxygen in the growth system. Oxygen influences not only the volatility of the source material, the stoichiometry of the vapor phase, but also the formation of the products. As such, the second step of the synthesis process involved conducting a simple evacuation process to reduce the initial oxygen content in the system prior to synthesis. The mechanical pump is tuned on and the diaphragm isolation valve, closed at this point, is slowly opened so that

the purging rate of the chamber is ~100 mbar/s. This relatively slow evacuation rate was employed to ensure that the powder source material would not be pulled from center of the tube and redeposited on the substrates during the evacuation process. The ultimate vacuum for the system was ~3×10^{-3} mbar. The system was held at this pressure for a minimum of 30 minutes, after which the synthesis process could begin.

A designated pressure and temperature set point were chosen prior to the synthesis process. The furnace was heated at a ramp rate of 20 ºC/min, giving a minimum of 30 minutes before the furnace reached a temperature where evaporation would occur. During this time, the carrier gas was introduced into the chamber. By adjusting the course and fine valves on the vacuum system, the rate of evacuation for the chamber could be manipulated. This capability allowed us to use the carrier gas to increase the system pressure to a specific set point before evaporation of the source material began. The pressure set point was always achieved before the lowest possible sublimation temperature was reached. This ensured that no deposition would occur before the pressure set point was attained in the chamber.

The system was held at constant pressure and temperature for a designated 60 minutes. After which the furnace was turned off. In order to quench the system as quickly as possible, a fan was used to circulate cool air on the exposed alumina tube. This was critical for temperatures that were much higher than the minimum sublimation temperature of the source material. If the system was permitted to cool slowly, then deposition could occur for several minutes after the furnace was turned off. In addition, as the system cools the temperature gradient changes which could possibly affect the morphology of the as-deposited material. The large air gap between the alumina tube and

insulation collars permitted cool air to flow inside the furnace and aid in the quenching process. The pressure was also maintained throughout the duration of the cooling process, to ensure that this parameter would not influence morphology during the cool down. Quenching the system from the designated synthesis temperature to below the minimum sublimation temperature took anywhere from 5-30 minutes depending on the disparity between those two temperatures. Once the cooling process was complete, the flow of the carrier gas into the system was stopped, and the diaphram valve fully opened so that any potentially harmful vapor still left in the chamber would be purged from the system.

3.3.2: Temperature Gradient

Knowing the local substrate temperature was critical to my investigations. As such, the temperature gradient for several different source temperatures were measured. A S-type thermocouple element (Platinum 10% Rhodium) sheathed in an alumina sleeve, was inserted into the furnace while under a 300mbar vacuum. A series of data points were taken at various positions within the furnace, so that the temperature gradient across the entire furnace could be extrapolated. Although all of the data for the measured temperature gradients were taken using a 300 mbar chamber pressure, previous unpublished studies demonstrated no change in the temperature gradient with varied chamber pressure, which is to be expected. Below are the data for four distinct source temperatures and their corresponding temperature gradients (see Figure 3.6). A best-fit curve was calculated for each. The equation for this curve was then used to extrapolate the local substrate temperatures for synthesis runs with the corresponding source

temperatures. The substrate positions were documented and then correlated to their local temperature by way of the best-fit curve.

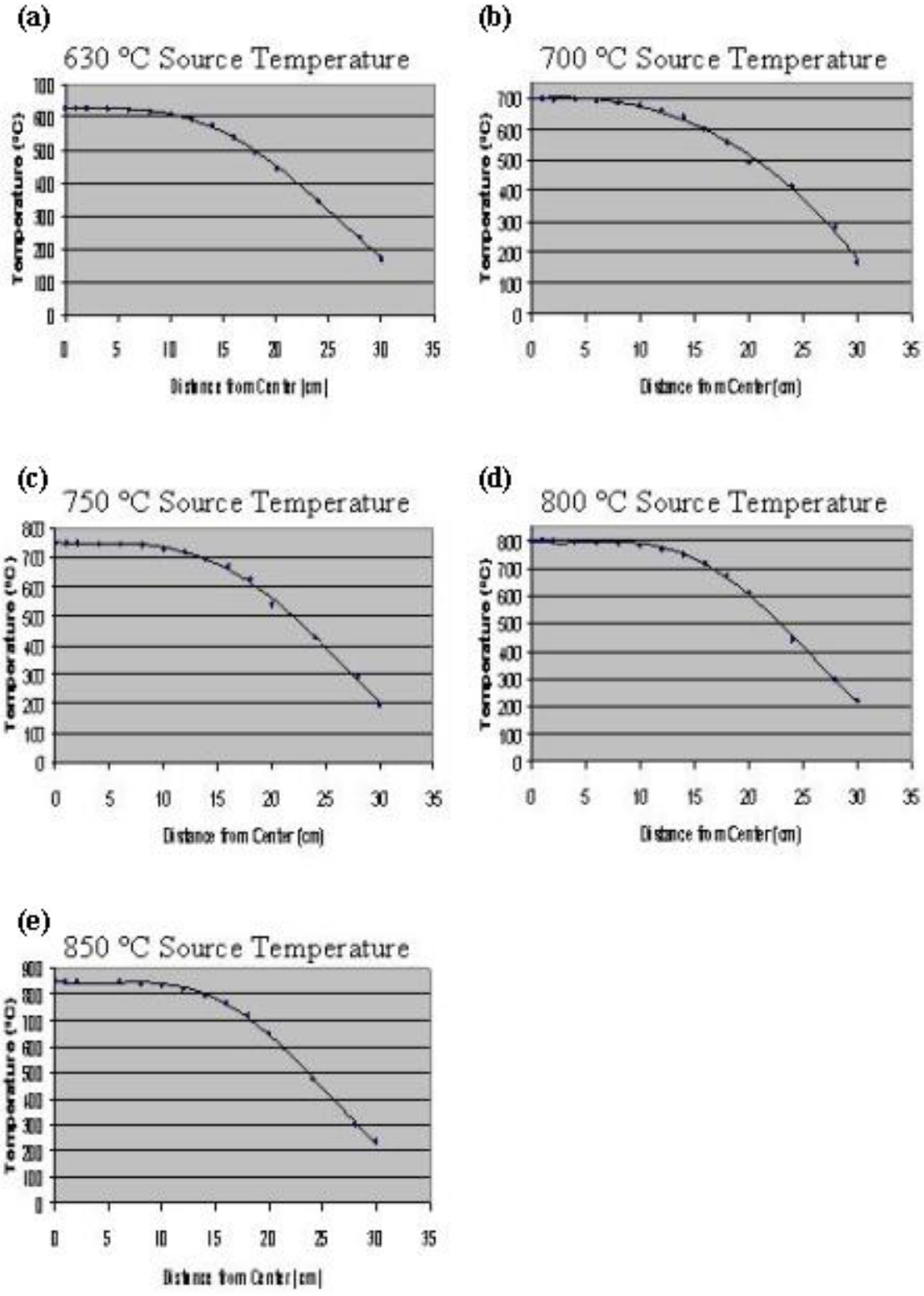

Figure 3.5: Temperature gradients for source temperatures of a) 630ºC, b) 700ºC, c) 750ºC, d) 800ºC, and e) 850ºC.

CHAPTER IV

ZINC SULFIDE

For decades, the II-VI compounds have been extensively researched due to their potential in optoelectronic applications. In particular, zinc sulfide is a direct wide bandgap semiconductor[119] (3.68 eV), has a high refractive index[89] and a high transmittance[90] in the visible range. It is this high refractive index and transmittance that first prompted my investigation into synthesizing nanobelts from ZnS. Because of the geometry and faceted nature of the nanobelt structure, they seemed prime candidates for use as optical waveguides. Earlier research conducted by Yang *et al*.[109] demonstrates that the cleaved (0001) planes of ZnO nanowires acted as mirrors trapping in light. Applying this same principle to nanobelts which are comprised entirely of flat crystallographic planes, the light could be trapped in not just one, but all three directions. This phenomenon would only be enhanced by the high refractive index of ZnS. It should be noted that in Chapter II of this dissertation, information about SnO_2 nanobelt being used as waveguides was given. However the idea for synthesizing ZnS nanobelts came well before that research was conducted.

4.1 Zinc Sulfide Phase Transformation

The zinc blend crystal structure derives its name from the material, zinc sulfide. It is then no surprise that ZnS exhibits this crystallographic configuration at room temperature. The zinc blend structure can be described as a set of cubes repeating throughout the crystal with the sulfur anions located at the corners and at the center of

each face. Within the volume of the cube, there is also an additional four zinc cations positioned in half of the tetrahedral sites or the ¼, ¼ , ¼-type positions (see Figure 4.1).

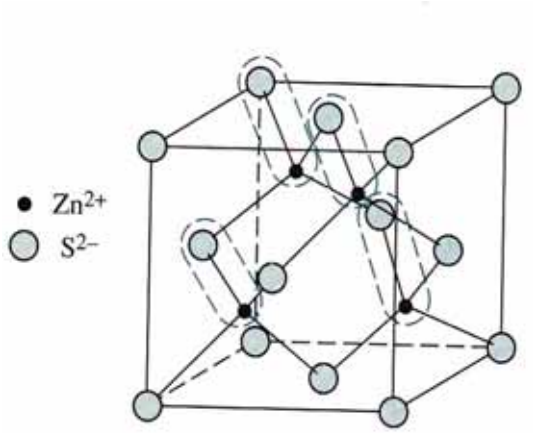

Figure 4. 1: Schematic of zinc blend ZnS.

However, ZnS can undergo phase transformation from the cubic zinc blend crystal structure to a hexagonal crystal structure at elevated temperatures. The cubic and hexagonal crystal structures of ZnS are quite similar. The stacking sequence of the (111) cubic plane within a crystal can be represented by an ABCABCABC pattern, where each letter represents a (111) plane. If, however, the stacking sequence of the (111) cubic plane is altered from ABCABCABC to ABABABAB, the crystal structure being described is the hexagonal form of ZnS. Although not stable in the bulk at room temperature, this hexagonal crystal structure or wurtzite ZnS crystal structure can be formed at elevated temperatures[120]. The transformation from zinc blend to wurtzite occurs at 1020 ºC. There have been reports of stable wurtzite ZnS but all involved nano-sized materials[121,122], demonstrating a possible nanoscale effect on the crystal structure of ZnS.

4.2 Zinc Sulfide Nanostructures

The procedures for synthesizing nanostructures from zinc sulfide are described in detail in Section 3.3.1 of this dissertation. Commercial grade zinc sulfide was used as the source material for all of the experiments. There were two forms of ZnS that were used as the source material, a powder consisting of small ZnS particulates and a sintered or pressed powder forming pellets of ZnS. Chemically the two forms were identical and even the purity (99.9%) was equivalent. In the investigation of the as-deposited material, no appreciable difference in the morphology could be detected.

The chamber pressure and source temperature for synthesis were 300 mbar and 1050 ºC, respectively. Although primarily all of the experiments were run at a source temperature of 1050 ºC, a brief investigation demonstrated the possibility of successfully synthesizing ZnS nanostructures using a source temperature as low as 950 ºC.

Argon was chosen as the carrier gas for this synthesis setup due to its nobility. The substrates used to grow these ZnS nanostructures were polycrystalline alumina (99.7% purity) cut into 1-3 cm long rectangular substrates which lined the inside of the chamber. Unless specified, no catalysts were dispersed onto the substrates, thereby employing the VS growth mechanism during synthesis.

Although the original intent in studying ZnS was to synthesize this material into the nanobelt morphology, an unexpected result was observed when four types of morphologies were collected in the as-deposited material: nanobelts, nanocombs/nanosaws, nanowindmills and nanowires. The length and width of each of these morphologies could be several microns in length, however the thickness of the structures is consistently in the nanometer range. For this reason, all of these structures

are classified as one-dimensional ZnS nanostructures. This research was a significant for two reasons. The first being that up to that point in time the only one-dimensional ZnS nanostructure that had been synthesized was ZnS nanowires. The article[82] reporting these discoveries was the first to publish the synthesis of ZnS nanobelts, nanocombs, or nano-windmills. The second was that all of the nanostructures had the hexagonal wurtzite crystal structure. The samples were left out in open air and exposed to light for several months, and no spontaneous transformation into the more stable zinc blend crystal structure was observed. Within a year, several papers from various groups throughout the world reported similar findings of synthesizing ZnS nanobelts, further validating the significance of these findings.

4.2.1: Zinc Sulfide Nanowindmills and Nanowires

One of the more fascinating aspects of the ZnS nanostructures is how all four different types of morphologies can be present within a single experimental run. As the distance from the source material increases, corresponding in a decrease in the local substrate temperature, a particular morphologies population may decrease as another morphology population increases. This can continue over the entire deposition range of the material. However, in general two morphologies will exist simultaneously seemingly without one growing at the expense of the other, such as the nanowindmill and nanowire structures. Both the nanowindmills and nanowires are high temperature morphologies. It is however worth note that the nanowindmills are in far less abundance in the deposited material than the nanowire structures.

The ZnS nanowires are the most abundant morphology received in the deposition zones closest to the source material. They are all single crystal and grow along the [0001], corresponding to the c-axis of the wurtzite crystal structure. Because the growth mechanism employed in this synthesis was the VS mechanism, many individual nanostructures can be seen growing from a single "seed" site (see Figure 4.2). The diameter of the individual nanowires range from 30nm to 600nm, while their lengths reaching up to tens of microns.

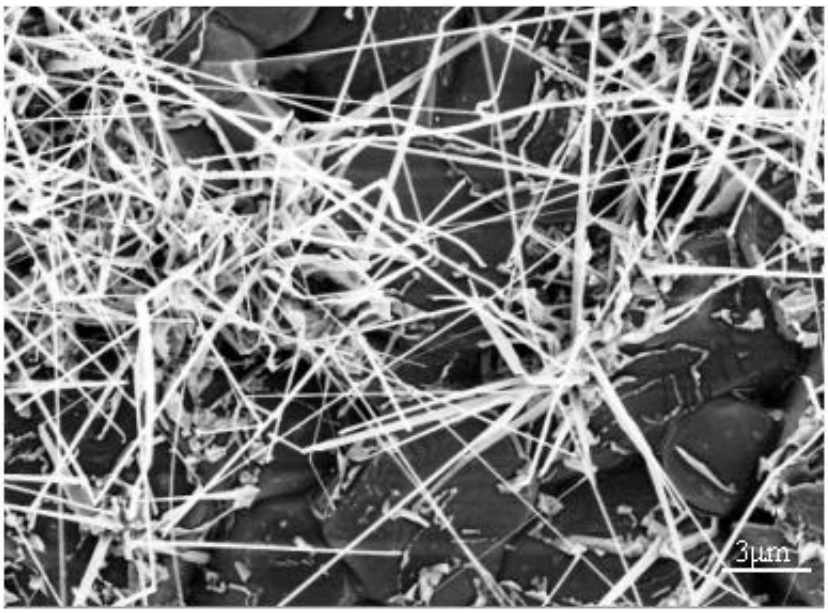

Figure 4. 2: Low magnification SEM image of VS-grown ZnS nanostructures.

Interspersed among the nanowires are a nanostructure with six-fold symmetry that closely resemble a windmill (see Figure 4.3a). Like the nanowires, the nanowindmills

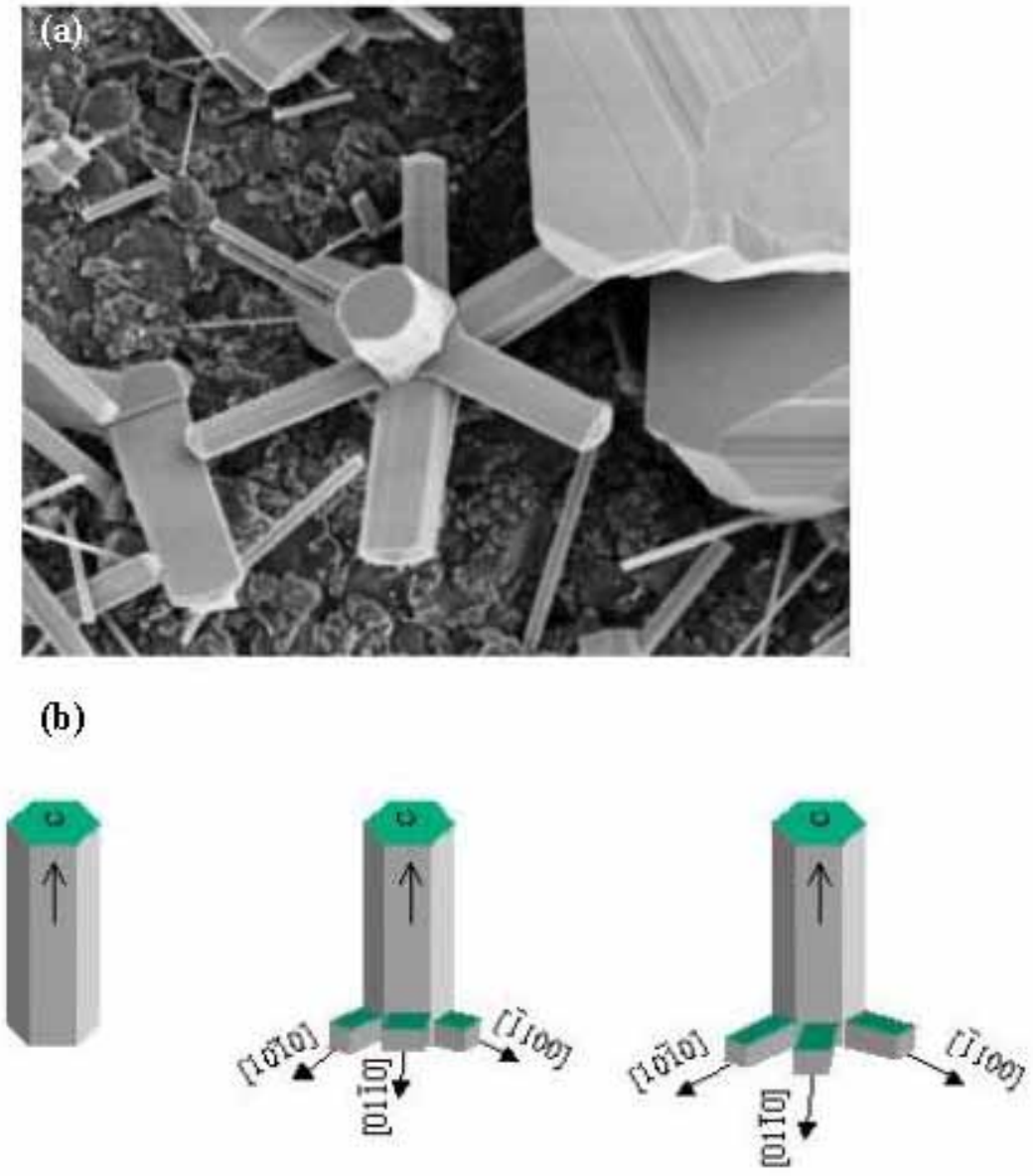

Figure 4. 3: (a) SEM image of a ZnS nanowindmill and (b) schematic of proposed windmill growth process.

have the wurtzite crystal structure and a primary growth direction of [0001]. The six blades of the windmill grow along $\pm[10\bar{1}0]$, $\pm[0\bar{1}10]$ and $\pm[\bar{1}100]$, as shown schematically in Figure 4.3b. This type of structure has been previously observed for hexagonal ZnO[123,124]. The six wings can grow laterally and interconnect to form a faceted structure as the one shown in Figure 4.3b, where the side facets are likely to be $(10\bar{1}1)$, $(\bar{1}011)$, $(01\bar{1}1)$, $(0\bar{1}11)$, $(\bar{1}101)$ and $(1\bar{1}01)$.

The growth of such a structure is believed to be due to a secondary growth which is likely also a vapor-solid mechanism. Figure 4.3b illustrates how the proposed mechanism works. First an individual nanowire grows along the c-axis. Due to the nature of the wurtzite crystal structure, the wire is not cylindrical in cross-section but hexagonal. At some point either during the synthesis or during the cooling down process, a secondary growth is triggered at the surface of the side walls of the nanowire. Growth continues laterally forming the blades of the windmill. At this time, it is unclear why the blades grow from the surface of the wires of the wire growing laterally and increasing in thicker. However results from work conducted with cadmium selenide, to be discussed at great lengths later on in this thesis, indicate that the secondary mechanism that forms the blades is due to a VS mechanism which requires additional energy to overcome a possible energy barrier associated with growing on the $(10\bar{1}1)$, $(\bar{1}011)$, $(01\bar{1}1)$, $(0\bar{1}11)$, $(\bar{1}101)$ and $(1\bar{1}01)$ side facets. Therefore this secondary growth process likely occurs at elevated temperatures and not during the cooling process. The data collected from the ZnS nanostructure study supports this since all nanowindmills were observed at the highest temperature zones of the as-deposited material.

4.2.2: Zinc Sulfide Nanobelts

Both the nanobelt and nanosaw/nanocomb morphology are intimately intermingled in the mid and lower temperature zones of the as-synthesized material. There were no obvious regions where only nanobelts or only the nanosaws/nanocombs grown. This is likely a consequence of the VS mechanism.

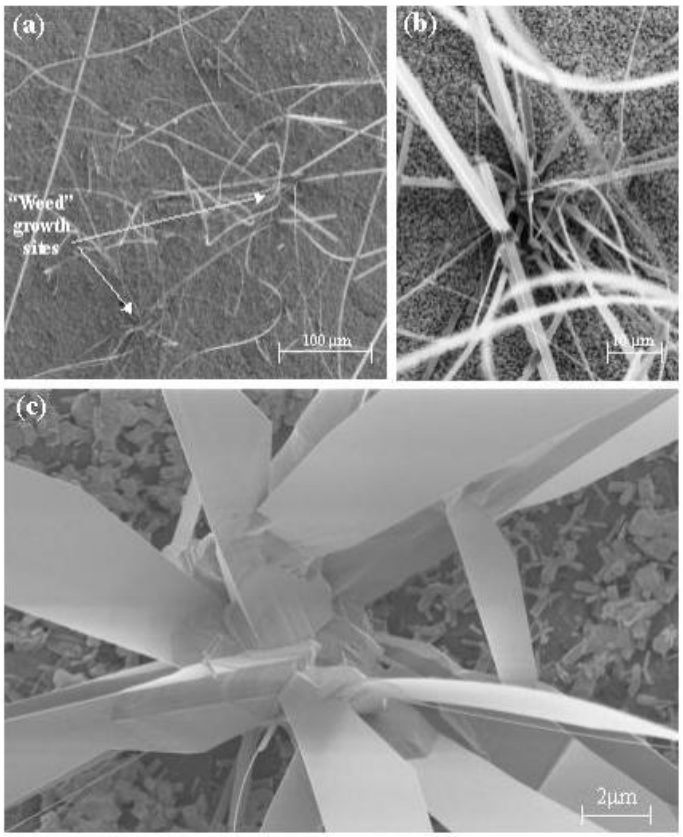

Figure 4. 4: a) Low magnification SEM image demonstrating the "weed" growth caused by the VS mechanism, b and c) SEM images of the "seed" crystal of two different ZnS weeds.

The growth of the nanobelts does not show any specific pattern, rather they are nucleated and grown in concentrated bunches randomly distributed on the substrate covered by a thin film layer of polycrystalline ZnS. This is common observation for one-dimensional nanostructures of II-VI compounds grown at high temperatures. A single

crystal in the ZnS thin film layer acts as a "seed" to nucleate the growth of one-dimensional ZnS nanostructures (see Figure 4.4). A closer examination of a "seed" reveals that multiple structures, nanobelts, nanosaws, and nanocombs grow from an individual nucleation site. Because the size or positioning of the "seed" crystal cannot be predetermined, the VS mechanism offers little in the way of controlling the dimensionality, concentration, or location of the ZnS nanostructures.

The nanobelts studied in this investigation demonstrate uniform rectangular cross-sections, are single crystals, have a low-defect concentration and high flexibility without

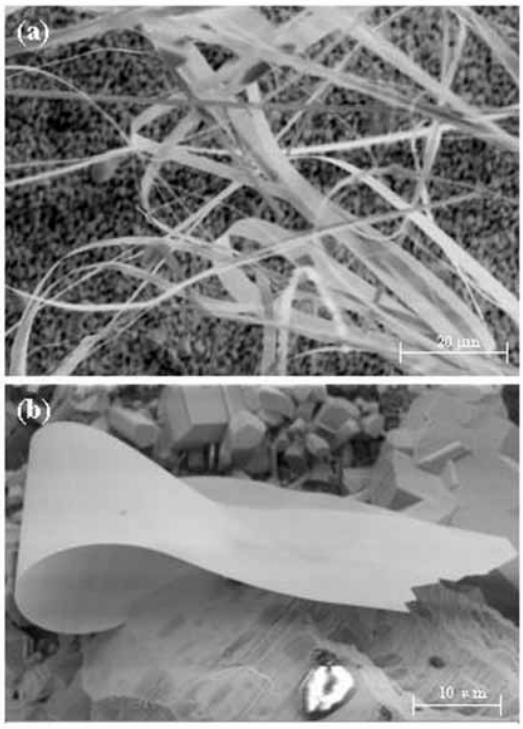

Figure 4. 5: SEM images of ZnS nanobelts.

fracture, and can be grown to lengths that extend to over 100 μm (see Figure 4.5), all similar characteristics to the previously synthesized transparent conducting oxide nanobelts. However there is one disparity that immediately stands out from the

previously synthesized nanobelts, that being the extremely large aspect ratio of the ZnS nanobelts. The width of the nanobelts ranged from 2-20 μm and thickness from 50-600nm. This gives an aspect ratio approximately four times greater than that of zinc sulfide. Figure 4.5b demonstrates an extreme case for the large aspect ratio of ZnS nanostructures, where the morphology is more like a sheet than a belt. A TEM study reveals that the nanobelts also have the wurtzite crystal structure and are stable at room temperature. The zinc sulfide nanobelts, like the ZnO nanobelts, grow along the [0001] with side facets of $(01\bar{1}0)$ and top and bottom surfaces of $(2\bar{1}\bar{1}0)$.

4.2.3: Zinc Sulfide Nanosaws and Nanocombs

Although synthesizing nanobelts was a significant accomplishment, the most intriguing aspect of the ZnS nanostructures was the saw- and comb-like structures. These types of structures had only been observed twice before in two different materials. With ZnS nanosaws and nanocombs now entering the arena of nanoscience, perhaps this material could further the understanding on the mechanism controlling the shape of these two morphologies.

The names nanosaw and nanocomb are derived from the similarity these morphologies have with the shapes of saws and combs (see Figure 4.6). Like a saw or a comb, these nanostructures are thin, long, and have an asymmetric nature about their shape. The distinguishing characteristic separating the saws and combs are the shape of their respective teeth. The prefix "nano" is attached to saw and comb for these nanostructures because the thickness of each structure is in the nano-regime, classifying these two morphologies as one-dimensional nanostructures. In examining the nanosaws

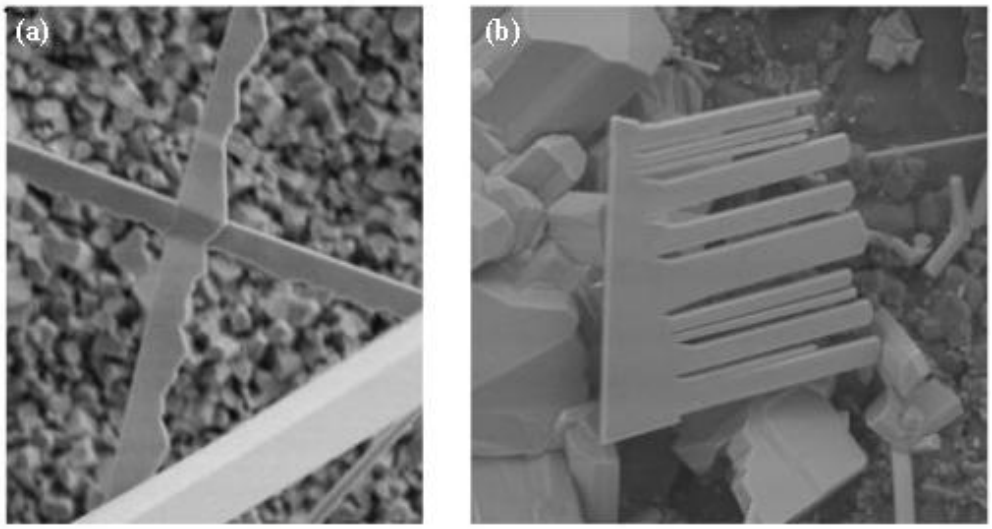

Figure 4. 6: SEM images of a ZnS (a) nanosaw and (b) nanocomb.

and nanocombs, they bear a striking similarity to nanobelts that have either comb or saw teeth growing on one particular side of the belt. A TEM investigation reveals that the saw- and comb-like structures are both wurtzite, single-crystals, and have the (0001) planes as their side facets (see Figure 4.7). The nanosaws and nanocombs grow along the $[01\bar{1}0]$, which is different from the [0001] growth direction of the ZnS nanobelts. By altering the growth direction, the surface facets will correspondingly change such that the polar (0001) surfaces will shift from the end facets of the belt to the side facets.

In every nanosaw and nanocombs structure examined in the TEM, the teeth always grew along the polar (0001). The teeth of the nanosaw lie along the $[01\bar{1}0]$ with their top facets being the same as the nanobelt top and bottom surfaces, the $(2\bar{1}\,\bar{1}0)$ planes. The saw teeth themselves are defined by crystallographic planes close to $(0\bar{1}13)$ and $(01\bar{1}3)$. This differs from the comb teeth of the nanocombs in that teeth are defined by the lower-energy facets of (0001) and $(01\bar{1}0)$. The comb teeth still lie along the $[01\bar{1}0]$ and have top and bottom surfaces of $(2\bar{1}\,\bar{1}0)$.

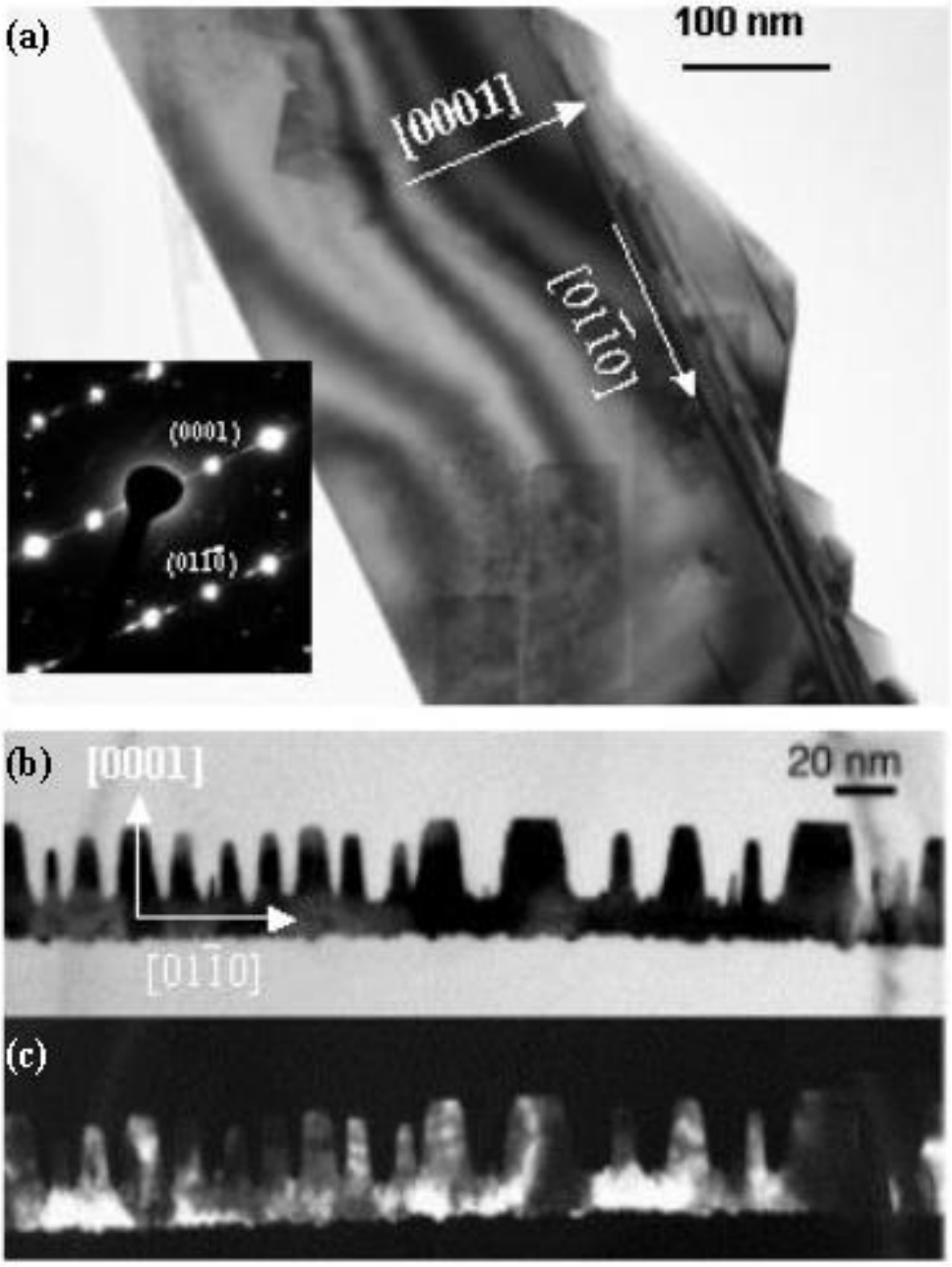

Figure 4. 7: (a) TEM image of a ZnS nanosaw and (b) bright field and (c) dark field TEM images of a ZnS nanocomb.

4.3: Spontaneous Polarization-induced Asymmetric Growth

It was imperative that an understanding of the mechanism controlling the growth of the ZnS nanosaws and nanocombs be achieved. The first step in understanding this growth phenomenon was to examine what characteristics the ZnO nanosaw, GaN nanosaw, and ZnS nanosaws shared.

Immediately it is evident that all three materials have the wurtzite crystal structure. In fact, all materials demonstrating the nanosaw and nanocomb morphologies shared the same growth direction, $[01\bar{1}0]$, and the same surface facets where the teeth would grown from, the (0001) planes. Therefore there must be something about the wurtzite crystal structure, possibly independent of the cations and anions, which promote the growth of these structures.

4.3.1: Self-catalyzed Growth of Polar Surfaces

When we examined the wurtzite crystal structure earlier, one of the significant findings was the polar surface of the basal planes. To illustrate this we schematically represent the wurtzite crystal structure (space group $P6_3mc$) with non-specific cations and anions positioned in their respective location within the unit cell. The (0001) plane, which corresponds to the top basal plane of the structure, is comprised entirely of cations. Conversely, the $(000\bar{1})$ plane, which corresponds to the bottom basal plane, is comprised entirely of anions. Because these two crystallographic planes consist of either all cations or all anions, the oppositely charged ions produce positively charged Zn-(0001) and negatively charged S-$(000\bar{1})$ polar surfaces. The consequence of this is a resulting

normal dipole moment and spontaneous polarization along the *c*-axis as well as a divergence in surface energy.

It is these polar surfaces and the differing chemical reactivities of the species at these surfaces that may gives rise to the growth of the asymmetric saw/comb teeth on one side of the nanobelt, while the other side is straight and smooth. If a nanobelt grows such that the side surfaces are the polar ±(0001), then a secondary growth may occur. If the chemical reactivities of the two polar surfaces are different, then a preferential growth will spontaneously and simultaneously occur at the more chemically active surface, yielding an asymmetric morphology. After examining hundreds of nanosaws and nanocombs, the length of the teeth for the combs and saws are generally equal. This indicates that the growth of the teeth *is* spontaneous and occurs simultaneously. The Zn-terminated polar surface is chemically active, while the S-terminated polar surface is relatively inactive, resulting in a spontaneous polarization-induced asymmetric (SPA) growth of the ZnS nanostructure.

4.3.2: Phase Transformation

A detailed study of ZnS has led to some interesting discoveries relating to the growth of the saw and teeth structures. As stated previously, many of the bulk or thin films of II-VI semiconductors can exist in the typically more stable zinc blend structure, but the nanobelts and nanosaws presented here are dominated by the wurtzite structure. High-resolution TEM image recorded near the root of the nanoteeth of ZnS indicates the existence of a different phase, which is several atomic layers in thickness and corresponds to the zinc blend structured ZnS (see Figure 4.8). The zinc blend is a result

of changing the stacking sequence from ABAB for the hexagonally structured wurtzite to ABCABC. The energies for the two phases are quite close [125] and it is relatively easy to stimulate phase transformation. It is possible that a secondary growth process occurs whereby small islands nucleate on the flat (0001) surface forming a few atomic layers of zinc blend ZnS. From the structural information provided by Figure 4.8b and 4.8c, the top and bottom surfaces of the wurtzite phase are the $\pm(2\bar{1}\bar{1}0)$ low energy facets, but the corresponding planes for zinc blend phase are ± (011), which are the high energy facets for cubic system and are thus energetically unfavorable. Therefore, the width of the zinc blend strip is limited for reducing the surface energy, but a continuous growth as driven by the catalytic active Zn-terminated (0001) surface tends to re-nucleate the wurtzite phase. This nucleation is epitaxial but a multiple nuclei case along the length of the nanobelt is most likely, possibly resulting in the growth of the nanoteeth on one side.

This investigation of the ZnS nanosaws and nanocombs using high-resolution TEM is not without its caveats. Although the wurtzite ZnS nanostructures have demonstrated stability over time without a spontaneous transformation into the more stable zinc blend structure, the wurtzite phase is a metastable phase at room temperature. However, we have observed experimentally the sensitivity of this metastable phase under the electron beam.

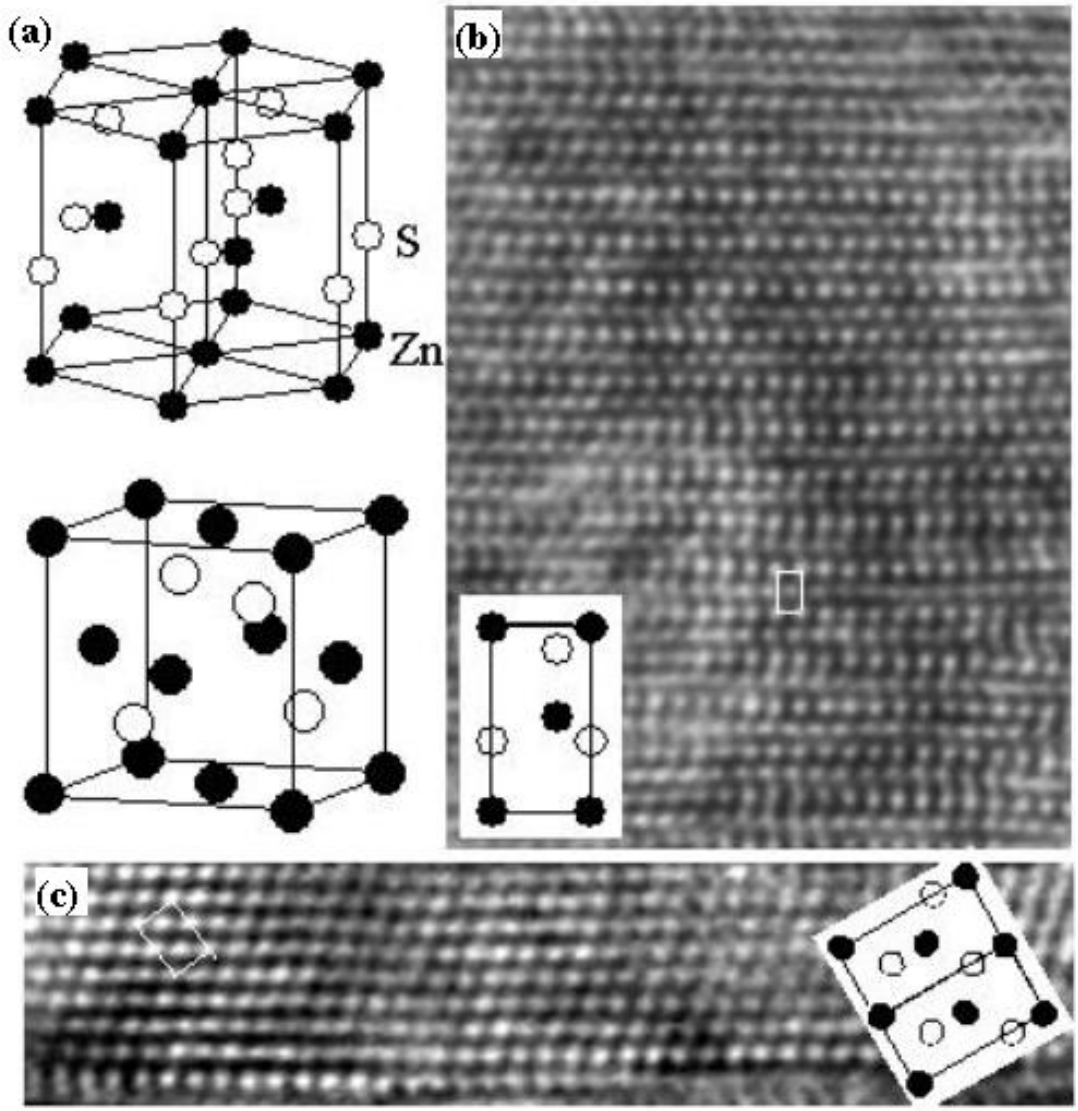

Figure 4. 8: a) Unit-cell models for the hexagonal and cubic phases. b) [$2\bar{1}\bar{1}0$] High-resolution TEM image of the wurtzite ZnS. c) [$01\bar{1}$] High-resolution TEM image of the zinc blend ZnS. The inserts are the projections of the corresponding unit cells

4.4: Sensitivity of Wurtzite ZnS Nanostructures to the Electron Beam

One has to be cautious in identifying phase transformation because the electron beam can induce phase transformation as well. Taking ZnS as an example, the wurtzite structured ZnS is unstable under the electron beam illumination in TEM and it may transform to zinc blend structure. Shown in Figures 4.9a and 4.9b are two images recorded from the same area before and after the sample was illuminated for about 10 min under 200 kV electrons, showing an increase in density of planar defects. Electron diffraction pattern recorded from the area shows the co-existence of the hexagonal wurtzite structure and the cubic zinc blend structure (Figure 4.9c). The orientation relationship between the two phases are: $[2\bar{1}\,\bar{1}\,0] \parallel [01\bar{1}]$, and $(0001) \parallel (111)$. The two phases co-exist by sharing the same (0001) or (111) plane. It is also known that the cubic phase ZnS typically has the {111} twins. The existence of the twins is indicated by the electron diffraction pattern, and the diffraction spots and the corresponding indexes from the hexagonal phase, the cubic phase and its twin are illustrated in Figure 4.9d.

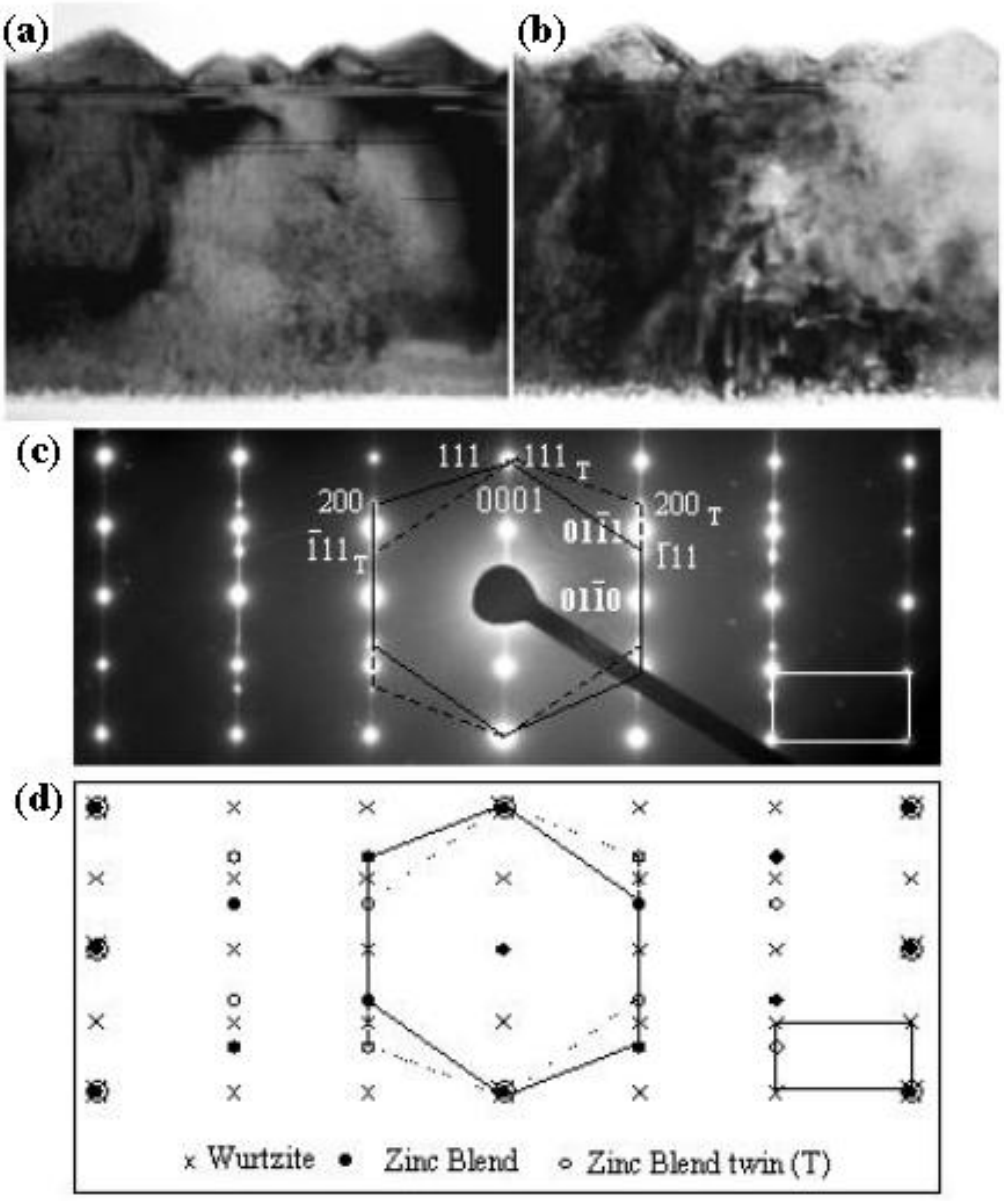

Figure 4. 9: (a,b) TEM images of a ZnS nanosaw prior and after illumination by the electron beam for 10 min., showing the formation of planar defects. c) Electron diffraction pattern recorded from the area which can be indexed as the coexistence of the hexagonal and cubic phases with the presence of twins in the cubic phase. d) A schematic showing the systematic reflections corresponding with the experimental pattern shown in (c).

4.5: VLS-grown ZnS Nanostructures

The main thrust of the research in this dissertation was to gain and understanding of mechanisms controlling growth so that a reasonable amount of control could be exerted over these nanostructures. It was in this vain that the implementation of the VLS growth mechanism for ZnS nanostructures was introduced. From the results given above, it is clear that manipulating the position, concentration density, or dimensionality would not be possible using the VS growth mechanisms.

To experimentally identify if the VLS mechanism would indeed allow more control over various aspect of the nanostructures, a substrate was partially coated with a metal catalyst, while another section of the substrate was left void of any catalyst. This experimental setup would directly allow the comparison of VS-grown ZnS nanostructures with VLS-grown ZnS nanostructures under the exact same kinetic and thermodynamic conditions.

To distribute catalysts onto the substrate a solution of 3nm gold particles were suspended in a water solution and dispersed on to a polycrystalline alumina silicon substrate. The experimental parameters for this synthesis were exactly same as the previously synthesized VS growth. These parameters were used in order to ensure that both the VLS and VS mechanisms would occur for this synthesis.

Figure 4.10 is a low magnification image of the alumina substrate. The line demarcates the areas where gold catalysts were present and where they were not. Immediately in examining this image three characteristics become apparent. The first is the density of the nanostructures. In the VLS growth, the catalysts act as site-specific nucleation sites. The density of the VLS-grown nanostructures is expected to be higher

since the VS-grown sites must either randomly walk the surface until a large enough "seed" is deposited and nucleation occurs or the grain boundaries on the Al_2O_3 have sufficient surface energy to promote nucleation of a seed crystal at the surface. These two types of nucleation events for VS growth are still small in comparison to the number of gold particles dispersed onto the substrate.

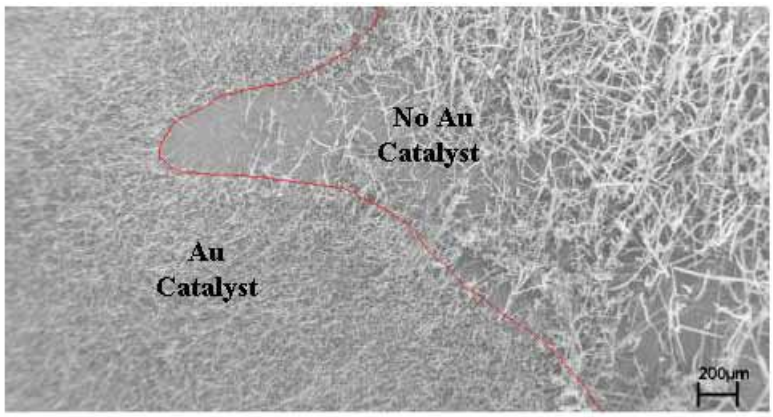

Figure 4. 10: Low magnification SEM of substrate partially coated with a catalyst to promote VLS growth and partially left void of catalysts for VS growth.

The second characteristic observable in this image is the dimensionality of the structures. The VS-grown nanostructures are considerably larger than the catalytically grown nanostructures. The reduced dimensionality of the VLS-grown nanostructures is indicative of the size confinement induced by the catalyst. As the supersaturated catalysts precipitate the solid in order to maintain a eutectic composition, the solid being produced is limited to the diameter of the catalyst. It is this property that allows some control over dimensionality of the nanostructures to be achieved. However, in examining the VLS-grown structures more closely, it is evident that the width of the nanobelts are larger than the catalysts (see Figure 4.11). This is may be due to the particular growth conditions of this experiment. Since VS growth is also being simultaneously employed,

as the solid is being ejected from the gold, a secondary growth may occur laterally on the nanostructures. The nanobelts grows in width, but maintain their uniform thickness.

The third characteristic of these structures is the catalyst to nanostructure ratio. As seen from Figure 4.11, only one nanostructure grows from the catalyst. This is in stark contrast from the VS-grown nanostructures were not only did multiple types of nanostructures, i.e. belt, saws, wires, but it was common to observe 10-20 ZnS nanostructures growing from a single "seed" crystal. By controlling the size of the catalysts, it is possible to have a single nanostructure grow from one catalyst.

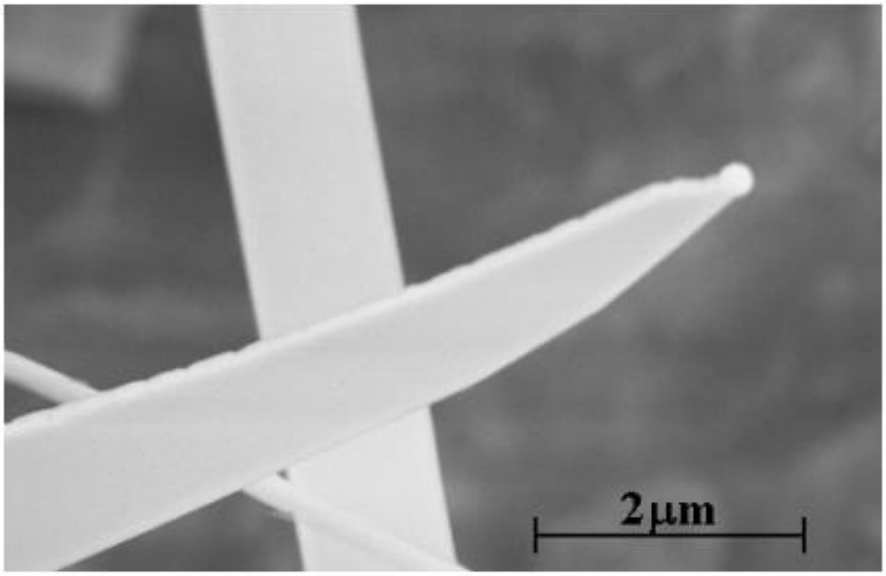

Figure 4. 11: SEM image of a single nanobelt growing from a gold catalyst.

The results from the VLS-grown ZnS nanostructures indicate that in order to attain more control over the synthesis process that the vapor-liquid-solid mechanism must be employed. The use of a catalyst enables manipulation of key parameters like dimensionality, positioning, and concentration density of the nanostructures.

CHAPTER V

CADMIUM SELENIDE

Wurtzite structured cadmium selenide (CdSe) is an important II-VI semiconducting compound. CdSe quantum dots are the most extensively studied quantum nanostructure due the size tunable properties, and they have been used as a model system for investigating a wide range of nano-scales electronic, optical, optoelectronic and chemical processes[4]. CdSe was also the first example for demonstrating self-assembled semiconductor nanocrystal superlattices[126]. With a direct bandgap of 1.8 eV, CdSe quantum dots have been used for laser diodes[127], nanosensing[18], and biomedical imaging[19].

Although CdSe quantum dots have been the dominant material for studying quantum confined effect, there are only a few reports on the synthesis of quasi-one-dimensional CdSe nanostructures. Shape controlled synthesis of CdSe nanorods[128], template assisted synthesis of CdSe nanowires[129] and nanotubes[130] have been demonstrated through electrochemical and chemical approaches. Two-dimensional arrays of CdSe pillars have been fabricated using e-beam lithography[131]. These nanowire and nanotubes are composed of nano-size grains and they are polycrystalline in nature, thus, the grain boundary scattering could greatly affect the optoelectronic performance.

It was this void in the literature that first inspired my research into the cadmium selenide system. The successful synthesis of cadmium selenide nanobelts could open an entirely new arena of investigation into one-dimensional quantum confinement. Nanobelts are not only single crystals, avoiding the grain boundary scattering of the

previously synthesized CdSe nanowires and nanotubes, but due to the nature of the nanobelt geometry it is possible to grow a nanobelt in such a way that only the thickness would reside in the nano-regime. This would enable researchers to study the effects of true one-dimensional confinement, unlike nanowires where the entire cross-section is in the nanoscale.

5.1: Cadmium Selenide Nanostructures

The procedure for synthesizing CdSe nanostructures is detailed in Section 3.3.1. Commercial grade cadmium selenide (99.995% purity) was used as the source material for all of the experiments. During the preliminary study of this system, the chamber pressure for synthesis was 300 mbar and the source temperature was 750 ºC. Nitrogen was chosen as the carrier gas for this synthesis setup and the substrates used to grow these CdSe nanostructures were polycrystalline alumina (99.7% purity) and single crystal silicon substrates (boron, p-type, (100)) cut into 1-3 cm long rectangular substrates which lined the inside of the chamber. After the success of the ZnS VLS experiments, the substrate for the CdSe investigation were coated with gold catalysts to promote VLS growth.

Three types of morphologies were collected in the as-deposited material: nanobelts, nanocombs/nanosaws, and nanowires. The CdSe nanostructures are almost completely identical to their ZnS counterparts, and would require a chemical or TEM analysis to discern the two systems. Both sets of nanostructures exhibit the wurtzite crystal structure, although it is of note that the most stable form of CdSe is the wurtzite crystal structure. This preliminary research into CdSe was a significant in that it was the

first report[83] of the successfully synthesize of CdSe nanobelts and nanosaws/nanocomb. The article was even highlighted in Nature[132] a few months after it was published.

5.1.1: Cadmium Selenide Nanowires

Like ZnS, the CdSe nanowires are most abundantly found in the high temperature zones of the as-deposited material. The CdSe nanowires are all single crystal and grow along the [0001], corresponding to the c-axis of the wurtzite crystal structure. Because the growth mechanism employed in this synthesis was the VLS mechanism, it common for a gold particle to be present at the end of a nanowire.

The CdSe nanowires were the only one-dimensional nanostructures to grow on both the alumina and silicon substrates. Figure 5.1 is a collection of SEM images from

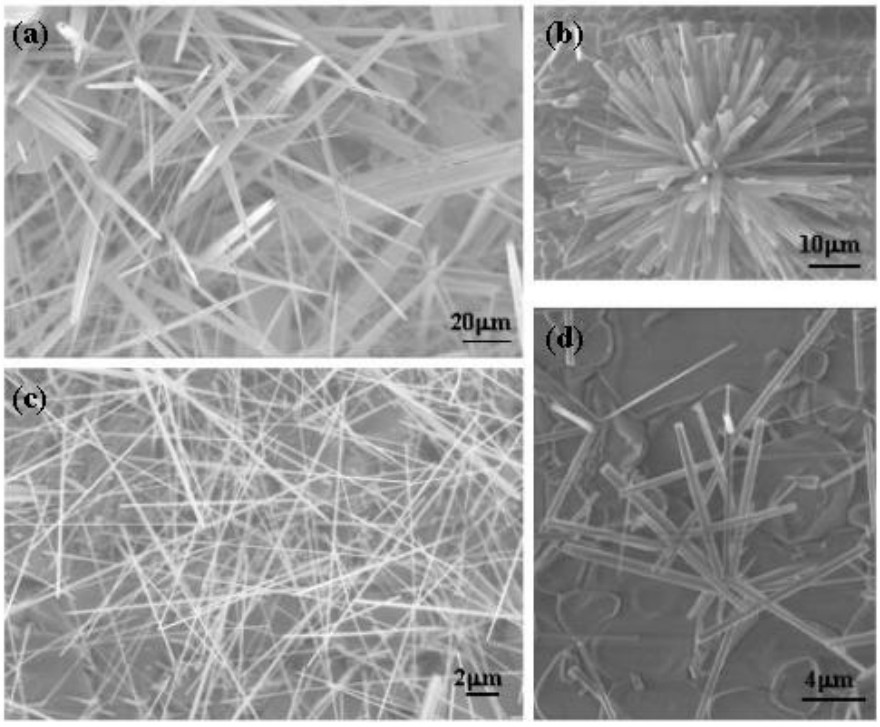

Figure 5. 1: SEM images of CdSe nanowires on (a) a single-crystal silicon substrate and (b-d) alumina substrates.

both the single-crystal substrates and the polycrystalline substrates. In the background of Figures 5.1 (b-d), there are large rounded features. Those are the individual grains of the polycrystalline alumina substrate. The nanowires grown on the alumina substrate also form weed-like growth, where this was not evident in the single-crystal substrates. This is likely due to a VS growth process.

Although the aim of the experimental setup was to only promote VLS growth, if the local temperature is high enough, VS growth can simultaneously occur. The local grain boundaries for the alumina substrates can provide energetically favorable sites for growth of a seed crystal. As has been observed in other materials systems, the seed crystal can stimulate multiple one-dimensional nanostructures to grow, yielding the structures in Figure 5.1b. This VS weed growth is not observed in the silicon deposition due to the surface energy of the substrate. The grain boundaries and defects in the alumina substrates act as sites for heterogeneous nucleation of the seed crystals. This type of growth, thermodynamically, is much easier to promote, and thus requires less energy from the system. Since the silicon substrates are single crystal and theoretically have no dislocation or line defects, than in order to nucleate a seed crystal on the surface, the growth must be through a homogeneous process. From a thermodynamic prospective, this is much harder than heterogeneous nucleation of a crystal.

5.1.2: Cadmium Selenide Nanobelts

It is unclear why the CdSe nanobelts grow only on the silicon substrate and not the alumina substrate. The nanobelts studied in this investigation demonstrate a rectangular cross-sections, are single-crystals, have a low-defect concentration, high

flexibility without fracture, and can be grown to lengths that extend to over 100 μm (see Figure 5.2), all similar characteristics to the nanobelts synthesized from other types materials. Like the ZnS system, all of the nanostructures have the wurtzite crystal structure. A TEM study reveals that the nanobelts consistently grow along the $[01\bar{1}0]$ with side facets of (0001) and top and bottom surfaces of $(2\bar{1}\bar{1}0)$. This growth direction for the CdSe nanobelts is the same growth direction as the ZnS nanosaws and nanocombs.

Figure 5.2a illustrates a commonly observed characteristic of the VLS-grown nanobelts. The nanobelts, although having uniform thickness, can grow in width as we move along the longitudinal axis and away from the catalyst. This is believed to be due to a secondary VS growth, as demonstrated in the previous section. At higher deposition temperatures, it is possible to have VLS and VS growth simultaneously. As is for the

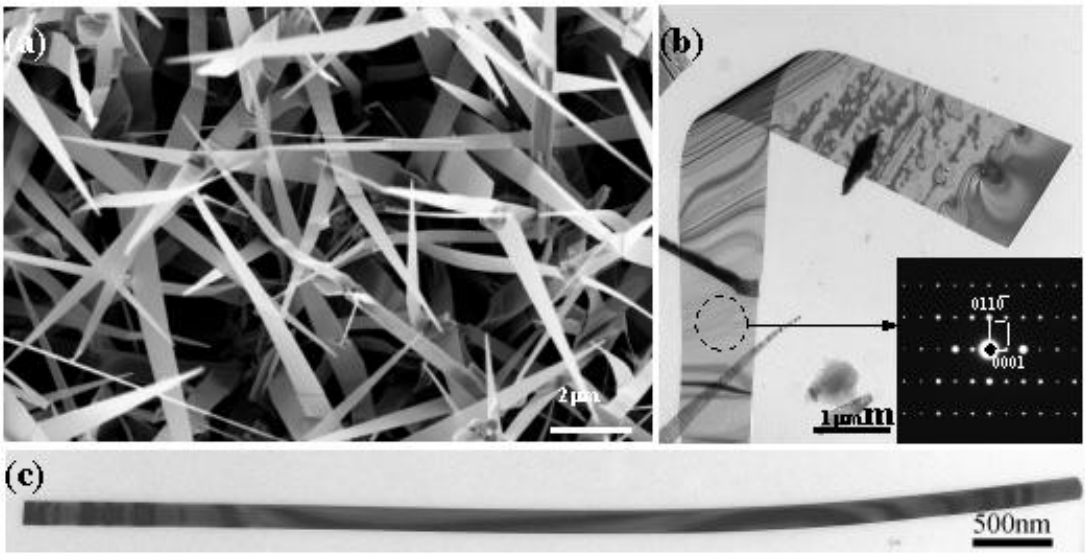

Figure 5. 2: (a) SEM and (b and c) TEM images of CdSe nanobelts.

case of the nanobelts, growth initially occurs through the VLS mechanism, whereby the nanobelt grows in length all the while being confined by the catalyst in its lateral direction. If the conditions are right, a secondary VS growth process occurs, where material is deposited on the sides of the nanobelt, making the belt wider. Growth in the longitudinal direction continues, as does the secondary VS growth. This is what leads to the triangular shape of the nanobelts in Figure 5.2a.

This triangular shape for the nanobelts can be eliminated by reducing the deposition temperature and thereby not permitting VS growth. Vapor-liquid-solid growth on single crystal substrates can occur at lower temperatures than the vapor-solid growth mechanism. As such, lowering the temperature for deposition can allow for uniform cross-section nanobelts to grow (see Figure 5.2c). For those nanobelts that do have a uniform cross-section, the aspect ratio for the CdSe nanobelts has been measured on average to be ~13.

5.1.3: Cadmium Selenide Nanosaws and Nanocombs

Unlike with the ZnS system, cadmium selenide was approached in the hopes of not only synthesizing nanobelts but also the nanosaw and nanocomb morphology. Since cadmium selenide has the wurtzite crystal structure and should therefore have positively and negatively charged polar planes, this material could help verify if the proposed SPA growth model is valid.

A TEM investigation reveals that the saw- and comb-like structures are both single-crystals, and have the (0001) polar planes as their side facets (see Figure 5.3). Just was the case with ZnS, the asymmetry of the nanostructures side surfaces, one jagged and

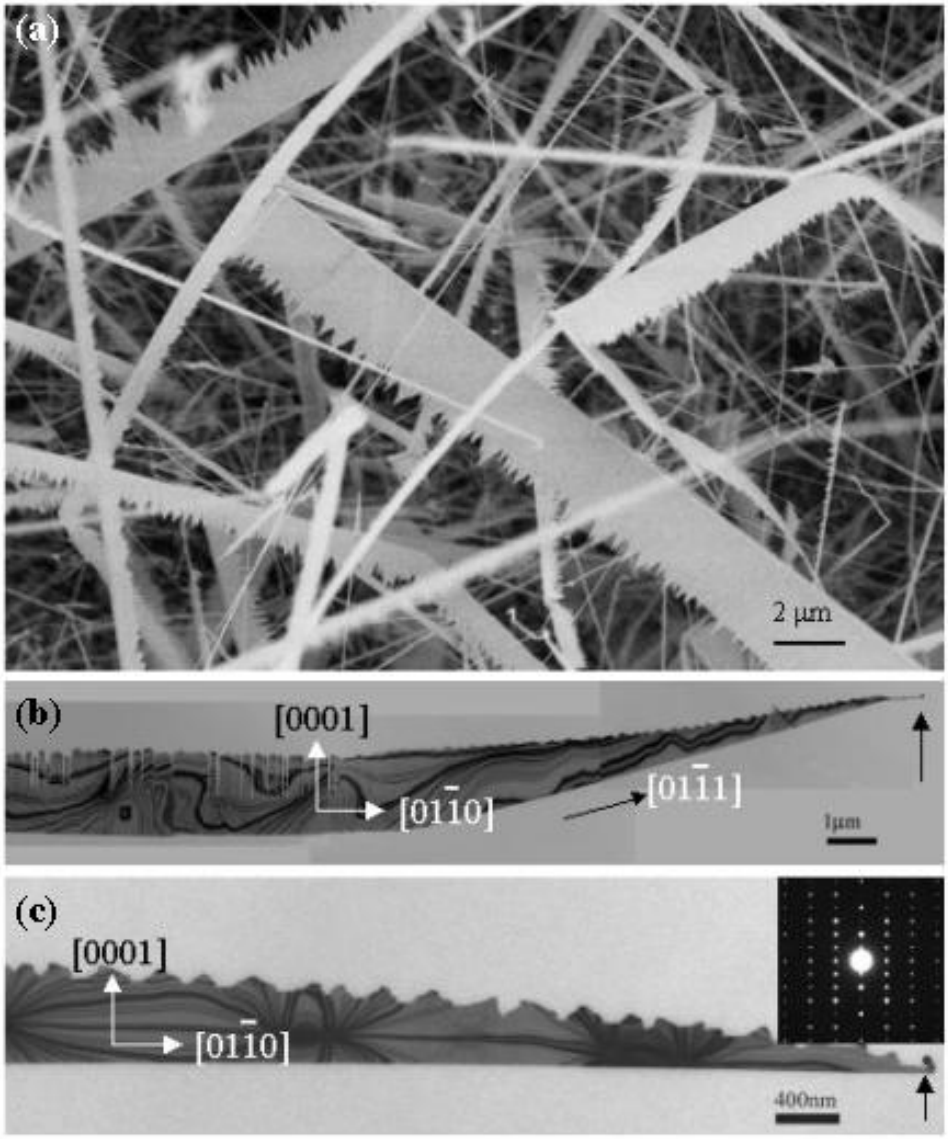

Figure 5. 3: (a) SEM image of as-deposited CdSe nanosaws and nanocombs. TEM images of (b) nanocomb and (c) nanosaw structures. Arrows point to gold catalysts at the end of the structures.

the other smooth, is due to their differing chemical compositions. The orientation of the crystal planes in the nanobelt results in the side surfaces terminating in either all cadmium cations or selenium anions. The teeth of the nanosaws and nanocombs lie along the $[01\bar{1}0]$ with their top facets being the same as the nanobelt top and bottom surfaces, the $(2\bar{1}\bar{1}0)$ planes. When we examined the wurtzite ZnS crystal structure earlier, the basal planes were the positively charged Zn-terminated (0001) and the negatively charged S-terminated $(000\bar{1})$. Analogously for CdSe, the basal planes are the positively charged Cd-terminated (0001) and the negatively charged Se-terminated $(000\bar{1})$. Again, it is believed that the more chemically active Cd-terminated polar surface results in a spontaneous polarization-induced asymmetric (SPA) growth.

5.2: Cadmium Selenide SPA Growth

As stated previously, many of the bulk or thin films of II-VI semiconductors can exist in both the zinc blend and wurtzite structure. High-resolution TEM image recorded near the root of the nanoteeth of the CdSe nanosaws indicates a change from wurtzite CdSe to zinc blend CdSe that is several atomic layers in thickness (see Figure 5.4b). This same phenomenon was observed in the ZnS nanosaws and nanocombs. Just as with ZnS, the energies for the two CdSe phases are quite close[125] and it is relatively easy to stimulate a phase transformation. As small islands of zinc blend CdSe corresponding to the ±(011) zinc blend phase, are nucleated on the flat (0001) Cd-terminated surface, the growth of the zinc blend islands is impinged due to the high surface energy associated with the ±(011). Therefore, the width of the zinc blend strip is limited in order to reduce the surface energy. However, a continuous growth is driven by the catalytic active Cd-

terminated (0001) surface and tends to re-nucleate the wurtzite phase, giving a series of teeth along the (0001).

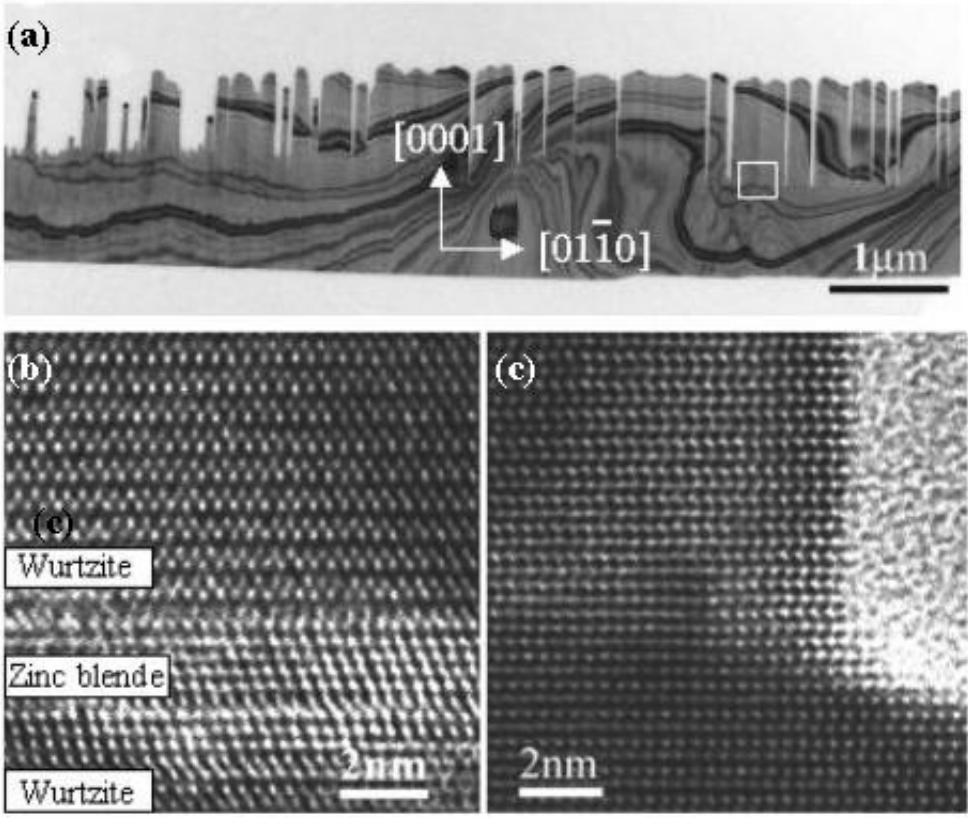

Figure 5. 4: (a) TEM image of CdSe nanocombs. (b) High-resolution TEM image of boxed area in (a) at root of nanotooth showing the zinc blend layers. (c) High-resolution TEM image of nanotooth.

5.2.1: Convergent Beam Electron Diffraction

When using conventional TEM diffraction techniques, there is always an 180˚ ambiguity associated with the data. This being the case, it is impossible to know with certainty from the diffraction patterns whether it truly is the Cd-terminated (0001) nucleating the teeth, or if it is the other Se-terminated polar plane which is inducing the asymmetric growth.

To verify the hypothesis of the cation-induced growth, a powerful TEM technique called convergent beam electron diffraction (CBED) is employed. This technique differs from conventional electron diffraction in the shape of the incident beam. In normal TEM, the e-beam is a point source that strikes a sample for one direction and is then diffracted, giving diffractions dots. With the CBED technique, the e-beam is changed from a point source to having a conical shape (see Figure 5.5). Now as the cone-shaped

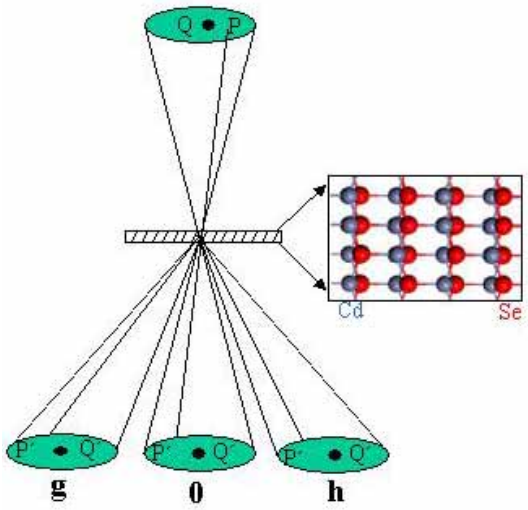

Figure 5. 5: Ray diagram of CBED technique.

e-beam strikes the sample, instead of "seeing" the crystal from only one direction, the e-beam "sees" the crystal from many different directions simultaneously. This results in a change from what were once diffraction dots in conventional TEM to diffraction discs in the convergent beam technique. CBED is a powerful technique because it can yield information such as crystal structure factor, strain, charge density distribution, and most importantly for this investigation, symmetry.

Due to wurtzite's inherent non-central symmetry, the CBED technique may be applied to determine the polarity along the [0001]. One requirement of this technique is that the sample is of a minimum thickness that will allow for strong dynamic diffraction. In order to differentiate the Cd-terminated (0001) surface from the Se-terminated $(000\bar{1})$ surface in the wurtzite structure, the $[2\bar{1}\,\bar{1}\,0]$ zone-axis CBED patterns were taken experimentally (see Figure 5.6b). The different polarity associated with the Cd cations surface and the Se anion surface results in different diffraction contrast in the ±(0001) diffraction discs (see Figure 5.6b). The quantitative interpretation of the experimental CBED pattern relies on a dynamic simulation conducted by a Bloch wave program[133]. CBED patterns with a $[2\bar{1}\,\bar{1}\,0]$ zone-axis were simulated and compared to the experimental data. A comparison of the best-matched simulated image (see Figure 5.6c) suggests that the nanoteeth are indeed located along the Cd-terminated [0001]. A similar study was conducted for ZnO134 and ZnS[135]. For ZnO, the CBED technique also revealed that the Zn-terminated (0001) surface catalyzed the asymmetric growth and not the more chemically inert O-terminated $(000\bar{1})$ surface. The study conducted with ZnS nanosaws and nanocombs was unable to determine which surface the teeth were catalyzed from due to samples being too thin to allow for dynamic diffraction. The CBED study of CdSe nanosaws and nanocombs help validate the SPA growth mechanism by demonstrating that indeed the polar cation surface consistently promotes the asymmetric growth of nanobelts.

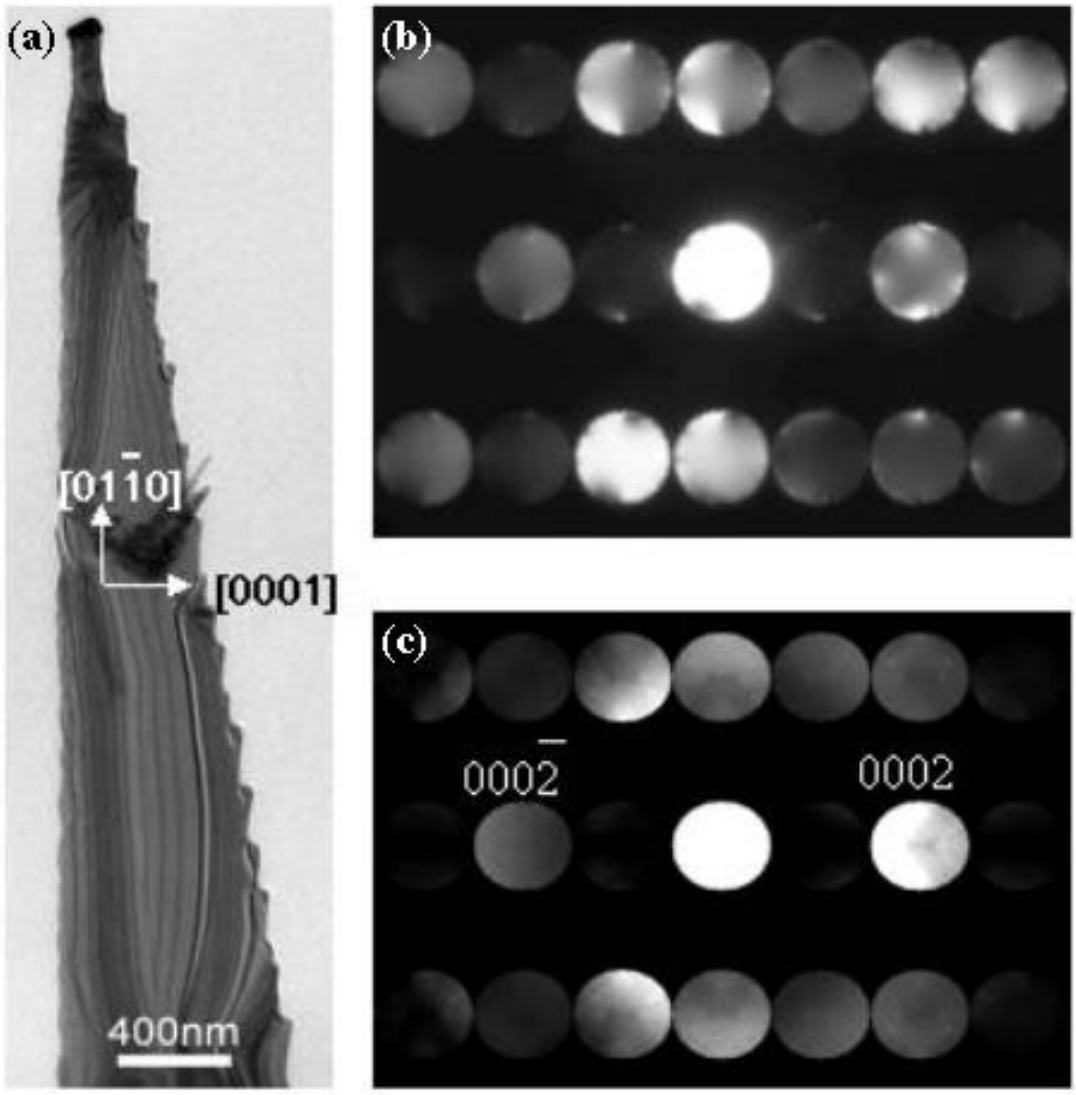

Figure 5. 6: (a) TEM image of CdSe nanosaws. (b) Experimental CBED pattern taken from (a). (c) Calculated CBED pattern from the Bloch wave program Error! Bookmark not defined.**.**

5.3: Temperature and Pressure Effects on Morphology

A control on the size and shape of CdSe nanocrystals is one of the most important parameters for CdSe quantum dots. Small changes in dimensionality or geometry can have significant impacts on the physical properties of the nanocrystal[1361]. This holds true for 1D nanostructures as well. To meet the large scale, controlled and designed synthesis of nanostructures, it is desperate to systematically find experimental conditions under which the desired nanostructures are synthesized reproducibly, at large quantity, and with controlled morphology. To accomplish this, it is necessary to systematically investigate the experimental parameters and/or the underlying mechanisms that determine the morphology and dimensionality of 1D CdSe nanostructures.

The following sections detail the first systematic study on growth of 1D CdSe nanostructures by varying two fundamental experimental conditions. Over 150 experiments were conducted in order to investigate the morphology dependence of three different types of nanostructures: nanowires, nanobelts, and nanosaws, over various substrate temperatures and pressures. The result of this work yields a "roadmap" for the controlled growth of 1D CdSe nanostructures. This research serves as a guidance and "menu" for the scale up synthesis of CdSe nanostructures.

5.3.1: Temperature and Pressure Experiments

To investigate the relationships between morphology, temperature, and pressure of this material, the source temperature of the system was held constant, while the pressure was systematically varied to one of nine possible set points: 800, 700, 600, 500,

400, 300, 200, 100, and 4 mbar. This was repeated for five different source temperatures: 850, 800, 750, 700, and 630 ºC, yielding a total of forty-five distinct experimental sets.

In order for this investigation to have any real meaning, a full understanding of the reproducibility of the results and robustness of the experimental setup must be quantified. Synthesizing 100% nanobelts with uniform dimensionality is of little significance if it can't be reliably replicated. Therefore, to quantify the reproducibility of our results, each of the experimental setup was run a minimum of three times, with each replication run a minimum of three weeks apart from each other.

The procedure for synthesis remained the same as what was detailed in section 3.3.1. Nitrogen was selected as the carrier gas and a 2nm non-continuous layer of gold was thermally evaporated onto (100) p-type silicon wafers, which were cut and used as a deposition substrates.

To narrow the scope of this study, only one-dimensional nanostructures grown via the vapor-liquid-solid mechanism were identified. This excluded all of the data from the experiments with a source temperature of 850 ºC and most of the data from the 800ºC source temperature experiments owing to an epitaxial growth of a CdSe polycrystalline film. The film acted as a buffer layer for the silicon substrates, whereby nucleation of 1D CdSe nanostructures was able to occur at the grain edges of polycrystalline layer via a vapor-solid mechanism. This introduces an entirely new set of growth conditions for the system. As such, VS growth was eliminated from this study owing to the additional complexity and its lack of control during growth as compared to VLS growth.

Due to the temperature gradient inherent in the synthesis setup being used, not only was the source temperature and chamber pressure considered in this investigation,

but local substrate temperature was also examined. The temperature gradient for each of the source temperatures (850, 800, 750, 700, and 630 ºC) was measured and the temperature profiles of each plotted (see Figure 3.6). From the collected data, curves were fit to each of the source temperatures (see Table 5.1). These curves describe the temperature gradient along the length of the tube furnace, and can be used to calculate the local temperature at any given distance within the furnace.

Table 5. 1: Temperature gradient equations

Source Temperature	Equation Describing Temperature Gradient
850ºC	$y = 0.0027x^4 - 0.1682x^3 + 2.1847x^2 - 8.5804x + 850$
800ºC	$y = 0.0023x^4 - 0.1428x^3 + 1.7757x^2 - 6.6904x + 800$
750ºC	$y = 0.0014x^4 - 0.0892x^3 + 0.9013x^2 - 3.1155x + 751.39$
700ºC	$y = -0.00001x^4 - 0.0074x^3 - 0.4221x^2 - 2.344x + 700$
630ºC	$y = 0.0012x^4 - 0.0714x^3 + 0.5955x^2 - 2.1095x + 629.86$

5.3.2: Correlating Substrate Position to Local Temperature

The first step in correlating substrate position with local temperature is tabulating the lengths of the silicon substrates for each experiment (see Tables B.1-B.5 in Appendix B). Tables B.3, given as an example on the following page, has the measured lengths of all substrates in the columns marked, "Length." The columns marked "Distance," represent the position of the deposition substrate on the collection substrate. Therefore in Run 2 of the 750ºC and 600mbar experiment (see Table B.3), the third substrate in that run is 1.9cm long and is positioned 6.4cm away from the end of the collection substrate (closest to the source). In order to have as little variability as possible between each

Table B.3: Table of positions and lengths for deposition substrate with a source temperature of 750˚C

	Run 1		Run 2		Run 3	
750°C & 800mbar	**Distance**	Length	Distance	Length	**Distance**	Length
	0-3.7	3.7cm	0-3.6	3.6cm	0-4.3	4.3cm
	3.7-7.7	4.0cm	3.6-7.6	4.0cm	4.3-8.6	4.3cm
	7.7-12.2	4.5cm	7.6-10.2	2.6cm	8.6-11.4	2.8cm
750°C & 700mbar	**Distance**	Length	Distance	Length	**Distance**	Length
	0-2.5	2.5cm	0-3.1	3.1cm	0-3.0	3.0cm
	2.5-4.2	1.7cm	3.1-5.0	1.9cm	3.0-5.0	2.0cm
	4.2-7.0	2.8cm	5.0-7.8	2.8cm	5.0-7.8	2.8cm
	7.0-9.4	2.4cm	7.8-10.8	3.0cm	7.8-10.9	3.1cm
	9.4-11.4	2.0cm			10.9-12.4	1.5cm
750°C & 600mbar	**Distance**	Length	Distance	Length	**Distance**	Length
	0-3.3	3.3cm	0-3.2	3.2cm	0-3.1	3.1cm
	3.3-6.6	3.3cm	3.2-6.4	3.2cm	3.1-6.1	3.0cm
	6.6-8.7	2.1cm	6.4-8.3	1.9cm	6.1-8.1	2.0cm
	8.7-9.7	1.0cm	8.3-8.8	0.5cm	8.1-9.2	1.1cm
	9.7-11.1	1.4cm			9.2-10.3	1.1cm
750°C & 500mbar	**Distance**	Length	Distance	Length	**Distance**	Length
	0-3.1	3.1cm	0-3.1	3.1cm	0-3.1	3.1cm
	3.1-5.8	2.7cm	3.1-5.9	2.8cm	3.1-5.9	2.8cm
	5.8-7.2	1.5cm	5.9-6.9	1.0cm	5.9-8.0	2.1cm
	7.2-8.8	1.6cm	6.9-8.6	1.7cm	8.0-10.6	2.6cm
	8.8-10.8	2.0cm	8.6-10.3	1.7cm	10.6-12.8	2.2cm
750°C & 400mbar	**Distance**	Length	Distance	Length	**Distance**	Length
	0-2.1	2.1cm	0-1.8	1.8cm	0-1.8	1.8cm
	2.1-5.2	3.1cm	1.8-5.0	3.2cm	1.8-4.9	3.1cm
	5.2-8.4	3.2cm	5.0-8.3	3.3cm	4.9-8.1	3.2cm
	8.4-10.3	1.9cm	8.3-8.8	0.5cm	8.1-9.9	1.8cm
			8.8-9.2	0.4cm	9.9-11.2	1.3cm
750°C & 300mbar	**Distance**	Length	Distance	Length	**Distance**	Length
	0-3.0	3.0cm	0-2.9	2.9cm	0-2.8	2.8cm
	3-6.2	3.2cm	2.9-6.0	3.1cm	2.8-5.3	2.5cm
	6.2-8.0	1.8cm	6.0-7.6	1.6cm	5.3-8.0	2.7cm
	8.0-11.5	2.5cm	7.6-9.4	1.8cm	8.0-10.2	2.2cm
			9.4-10.7	1.3cm	10.2-11.3	1.1cm
750°C & 200mbar	**Distance**	Length	Distance	Length	**Distance**	Length
		4.0cm	0-2.3	2.3	0-4.1	4.1cm
		3.7cm	2.3-3.5	1.2	4.1-8.0	3.9cm
		3.2cm	3.5-5.1	1.6	8.0-9.8	1.8cm
		1.0cm	5.1-6.6	1.5	9.8-11.2	1.4cm
750°C & 100mbar	**Distance**	Length	Distance	Length	**Distance**	Length
	0-3.0	3.0cm	0-2.9	2.9cm	0-3.2	3.2cm
	3-5.5	2.5cm	2.9-5.4	2.5cm	3.2-6.4	3.2cm
	5.5-8.2	2.7cm	5.4-7.7	2.3cm	6.4-8.6	2.2cm
	8.2-10.4	2.2cm	7.7-9.9	2.2cm	8.6-10.8	2.2cm
	10.4-11.5	1.1cm	9.9-11.0	1.1cm	10.8-12.0	1.2cm
750°C & 4mbar	**Distance**	Length	Distance	Length	**Distance**	Length
	0-2.4	2.4cm	0-2.4	2.4cm	0-2.4	2.4cm
	2.4-6.2	3.8cm	2.4-6.1	3.7cm	2.4-6.1	3.7cm
	6.2-9.4	3.2cm	6.1-9.6	3.5cm	6.1-9.3	3.2cm

replication of a given experimental setup, the substrates for a particular experimental setup (i.e. Runs 1-3 for 750˚C and 600mbar) were cut to similar lengths.

The next step in the process is to use the fitted curves from the measured temperature gradients to calculate the temperature ranges each substrate lies between. As described in section 3.3.1, the collection substrate is 10.5cm away from the center of the tube. The values for the deposition substrates listed in the "Distance" column of Tables B.1-B.5 are measured with respect to their position on the collection substrate. To convert these to distances relative to the center of the furnace, a value of 10.5cm is added to each quantity, i.e. a value from Tables B.1-B.5 that equals 3.4cm corresponds to a distance of 13.9cm away from the center of the tube. All of the values of distance in the columns marked "cm" for Tables B.6-B.10 in Appendix B are the converted values from Tables B.1-B.5 giving the position of the deposition substrate in relation to the center of the tube. As an example, Table B.8 is given on the next page. The columns marked "°C" are the calculated local temperatures for corresponding "cm" values.

5.3.3: Correlating Morphology to Local Temperature

Scanning electron microscopy was used to determine the morphology of the as-deposited materials on each individual substrate. Tables B.11-B.15 (see Appendix B) give the observations for each experimental setup and their respective replications. The temperature zones given in Tables B.11-B.15 are taken from the values calculated from Tables B.6-B.10. Using this information, the morphologies are correlated to the local temperature zones that they were grown in.

Table B.8:Correlating substrate position with local temperature using equations from Table 5.1 for a source temperature of 750°C.

	800mbar		700mbar		600mbar		500mbar		400mbar		300mbar		200mbar		100mbar		4mbar	
	cm	°C	cm	°C	cm	°C	cm	°C	cm	°C	cm	°C	cm	°C	cm	°C	cm	°C
Run 1	10.5	731.8	10.5	731.8	10.5	731.8	10.5	731.8	10.5	731.8	10.5	731.8	10.5	731.8	10.5	731.8	10.5	731.8
	14.2	690.4	13	707.2	13.8	696.39	13.6	699.24	12.6	712.1	16.7	644.2	12.8	709.7	13.5	700.6	12.9	708.5
	18.2	609.1	14.7	682.4	17.1	635.35	16.3	652.6	15.7	664.5	18.5	601.4	15.6	666.4	16	658.7	16.7	644.2
	22.7	473.5	17.5	626.1	19.2	582.73	17.7	621.39	18.9	590.9	20.4	548.1	17.1	635.35	18.7	596.2	19.9	562.9
			19.9	562.9	20.2	554.1	19.3	579.97	20.8	535.9	22	497.2			20.9	532.8	23.2	456
			21.9	500.6	21.6	510.42	20.3	551.11							21.9	500.6	25.4	374.7

	800mbar		700mbar		600mbar		500mbar		400mbar		300mbar		200mbar		100mbar		4mbar	
	cm	°C	cm	°C	cm	°C	cm	°C	cm	°C	cm	°C	cm	°C	cm	°C	cm	°C
Run 2	10.5	731.8	10.5	731.8	10.5	731.8	10.5	731.8	10.5	731.8	10.5	731.8	10.5	731.8	10.5	731.8	10.5	731.8
	14.1	691.9	13.6	699.2	13.7	697.83	13.6	699.24	12.3	715.5	13.4	702	14	693.45	13.4	702	12.9	708.5
	18.1	611.6	15.5	668.3	16.9	639.81	16.4	650.53	15.5	668.3	16.5	648.4	15.6	666.4	15.9	660.6	14.1	691.9
	20.7	539	18.3	606.6	18.8	593.56	17.4	628.48	18.8	593.6	18.1	611.6	17.1	635.35	18.2	609.1	16.6	646.3
			21.3	520.1	19.3	579.97	19.1	585.47	19.3	580	19.9	562.9			20.4	548.1	20.1	557.1
							20.8	535.87	19.7	568.7	21.2	523.3			20.8	535.9	21.7	507.2
															22.5	480.3	25.8	359.4

	800mbar		700mbar		600mbar		500mbar		400mbar		300mbar		200mbar		100mbar		4mbar	
	cm	°C	cm	°C	cm	°C	cm	°C	cm	°C	cm	°C	cm	°C	cm	°C	cm	°C
Run 3	10.5	731.8	10.5	731.8	10.5	731.8	10.5	731.8	10.5	731.8	10.5	731.8	10.5	731.8	10.5	731.8	10.5	731.8
	14.8	680.7	13.5	700.6	13.6	699.24	18.6	598.83	12.3	715.5	13.3	703.3	14.6	684.03	13.7	697.8	12.9	708.5
	19.1	585.5	15.5	668.3	16.6	646.31	16.4	650.53	15.4	670.1	15.8	662.6	18.5	601.43	16.9	639.8	16.6	646.3
	21.9	500.6	18.3	606.6	18.6	598.83	20.4	548.11	18.6	598.8	18.5	601.4	20.3	551.11	19.1	585.5	19.8	565.8
			21.4	516.9	19.7	568.69	21.7	507.16	20.4	548.1	20.7	539	21.7	507.16	21.3	520.1	23	463
			22.9	466.5	20.8	535.87			21.7	507.2	21.8	503.9			21.6	510.4	25	389.9
															23.5	445.3		

Although information relating the morphology to local deposition temperature is useful, most of the substrates have at least two, if not all three, morphologies growing in a single temperature zone. In order to more fully investigate the dependency of morphology on temperature and pressure, the population density of each nanostructure must be determined. This was achieved by taking a statistical sampling of the different structures for each temperature zone. Using SEM images, one hundred eighty nanostructures from each temperature zone were randomly counted and grouped into one of three categories: nanosaws, nanobelts, or nanowires. The total for each morphology population was divided by the total number of nanostructures counted, 180, to yield a population density percentage. As an example, Table B.13 is given on the next page. The letters S, B, and W represent the nanosaw, nanobelt, and nanowire morphologies, respectively. Therefore, in Run 3 of the 750˚C and 300mbar experiment (see Table B.13), the temperature zone of 663˚C-601˚C has 72% of the as-deposited morphology consisting of nanosaws, while the remaining 28% are nanobelts.

5.4: Graphical Analysis of Temperature and Pressure Effects

In presenting the experimental data graphically, three colors: red, blue, and green were used to signify the nanosaws, nanobelt, and nanowire morphologies, respectively. To make the information as rich as possible, varying shades or darkness of each color were used to represent the population density percentage of the corresponding nanostructure.

Figures A.1-A.4 (see Appendix A) plot the population percentages of nanosaws/nanocombs under four different source temperatures. The nanocomb structures

Table B.13: Relating the observed morphologies and their respective population density to local temperature ranges for experimental setup with a source temperature of 750˚C.

Run 1			Run 2			Run 3		
750ºC & 800mbar	Type of Deposit		**750ºC & 800mbar**	Type of Deposit		**750ºC & 800mbar**	Type of Deposit	
732C-473C	No Deposit		732C-539C	No Deposit		732C-501C	No Deposit	
750ºC & 700mbar	Type of Deposit		**750ºC & 700mbar**	Type of Deposit		**750ºC & 700mbar**	Type of Deposit	
732C-501C	No Deposit		732C-520C	No Deposit		732C-467C	No Deposit	
750ºC & 600mbar	Type of Deposit		**750ºC & 600mbar**	Type of Deposit		**750ºC & 600mbar**	Type of Deposit	
732C-583C	No Deposit		732C-580C	No Deposit		732C-536C	No Deposit	
583C-554C	Wires							
554C-510C	No Deposit							
750ºC & 500mbar	Type of Deposit		**750ºC & 500mbar**	Type of Deposit		**750ºC & 500mbar**	Type of Deposit	
732C-669C	No Deposit		732C-628C	No Deposit		732C-599C	No Deposit	
669C-580C	Wires		628C-585C	Wires		599C-548C	SPA	
580C-551C	No Deposit		585C-536C	SPA & Belts	**B-32%, S-68%**	548C-507C	No Deposit	
750ºC & 400mbar	Type of Deposit		**750ºC & 400mbar**	Type of Deposit		**750ºC & 400mbar**	Type of Deposit	
732C-665C	No Deposit		732C-715C	No Deposit		732C-715C	No Deposit	
625C-591C	Belts & Wires	**B-44%, W-56%**	715C-594C	Wires		715C-599C	Wires	
591C-536C	No Deposit		594C-580C	SPA & Belts	**B-40%, S-60%**	599C-548C	SPA & Belts	**B-54%, S-46%**
			580C-569C	SPA & Belts	**B-51%, S-49%**	548C-507C	No Deposit	
750ºC & 300mbar	Type of Deposit		**750ºC & 300mbar**	Type of Deposit		**750ºC & 300mbar**	Type of Deposit	
732C-644C	No Deposit		732C-648C	No Deposit		732C-663C	No Deposit	
644C-601C	SPA/Belts/Wires	**B-25%, W-52%, S-23%**	648C-612C	SPA & Belts	**B-31%, S-69%**	663C-601C	SPA & Belts	**B-28%, S-72%**
601C-548C	SPA/Belts/Wires	**B-27%, W-51%, S-21%**	612C-563C	SPA & Belts	**B-66%, S-34%**	601C-539C	SPA & Belts	**B-44%, S-56%**
548C-497C	Wires		563C-523C	No Deposit		539C-504C	SPA & Belts	**B-44%, S-56%**
750ºC & 200mbar	Type of Deposit		**750ºC & 200mbar**	Type of Deposit		**750ºC & 200mbar**	Type of Deposit	
732C-710C	No Deposit		732C-693C	No Deposit		732C-684C	Wires	
693C-666C	SPA & Wires	**S-36% & W-64%**	693C-666	SPA & Wires	**S-45% W-55%**	684C-601C	SPA/Belts/Wires	**B-29%, W-52%, S-19%**
666C-635C	SPA/Belts/Wires	**S-27%, B-19%, W-55%**	666C-635C	SPA/Belts/Wires	**B-31%, W-18%, S-51%**	601C-551C	SPA/Belts/Wires	**B-32%, W-32%, S-36%**
						551C-507C	No Deposit	
750ºC & 100mbar	Type of Deposit		**750ºC & 100mbar**	Type of Deposit		**750ºC & 100mbar**	Type of Deposit	
732C-701C	No Deposit		732C-702C	No Deposit		732C-698C	No Deposit	
701C-596C	Wires		702C-661C	Wires		698C-640C	Wires	
596C-533C	SPA/Belts/Wires	**B-17%, W-49%, S-34%**	661C-609C	SPA & Wires	**W-49%, S-51%**	640C-585C	SPA/Belts/Wires	**B-20%, W-24%, S-56%**
533C-501C	SPA/Belts/Wires	**B-21%, W-53%, S-26%**	609C-548C	SPA/Belts/Wires	**B-19%, W-40%, S-41%**	585C-520C	SPA/Belts/Wires	**B-34%, W-49%, S-16%**
			548C-523C	Wires		520C-497C	Wires	
			523C-514C	No Deposit		497C-445C	No Deposit	
750ºC & 4mbar	Type of Deposit		**750ºC & 4mbar**	Type of Deposit		**750ºC & 4mbar**	Type of Deposit	
732C-708C	No Deposit		732C-704C	No Deposit		732C-708C	No Deposit	
708C-644C	SPA		704C-646C	SPA & Belts	**B-28%, S-72%**	708C-646C	SPA/Belts/Wires	**B-24%, W-49%, S-27%**
644C-562C	SPA & Belts	**B-7%, S-93%**	646C-557C	SPA & Belts	**B-49%, S-51%**	646C-566C	SPA & Belts	**B-12%, S-88%**
562C-456C	SPA/Belts/Wires	**B-11%, W-78%, S-10%**	557C-507C	SPA/Belts/Wires	**B-35%, W-52%, S-13%**	566C-463C	Belts	
456C-375C	No Deposit		507C-360C	No Deposit		463C-390C	SPA/Belts/Wires	**B-13%, W-63%, S-24%**

are grouped with the nanosaws morphology throughout the rest of this thesis for simplicity. Both structures are a product of SPA growth and therefore are likely influenced similarly by the experimental parameters. To illustrate the different components of the graphs, Figure A.1 is given on the following page. The horizontal axis of the graph is the pressure in the growth chamber, and the vertical axis is the local temperature of the substrate. The graphs provide the local temperature ranges (vertical bar) at which nanosaw growth can be found. The different colors of the vertical bars represent the population percentage of that morphology observed at a given substrate temperature and pressure. The darker the color, in this case darker the red, the higher percentage of nanosaws observed in the as-deposited material. For a given chamber pressure, there are multiple vertical bars. This signifies the replications of each experiment., i.e. Run 1, Run 2, and Run 3., and despite the bars being shifted from one another along the horizontal axis, they were all run at the same chamber pressure. (The bars were shifted intentionally in order to visually differentiate them.)

The nanobelt (see Figure A.5-A.8) and nanowire (see Figure A.9-A.12) morphologies are graphed in an identical manner and can be found in Appendix A. What is important about these graphs is that they demonstrate that the experimental results are reproducible. Each group of data from Runs 1-3 exist over similar temperature ranges and the values for population percentages are comparable. There is, of course, some variance between runs, both in the deposition temperatures and population percentages of the morphologies. This will be discussed later in this dissertation.

In order to more easily observe trends in the morphologies, the three replications of each experimental setup are consolidated into one data set. This was achieved by

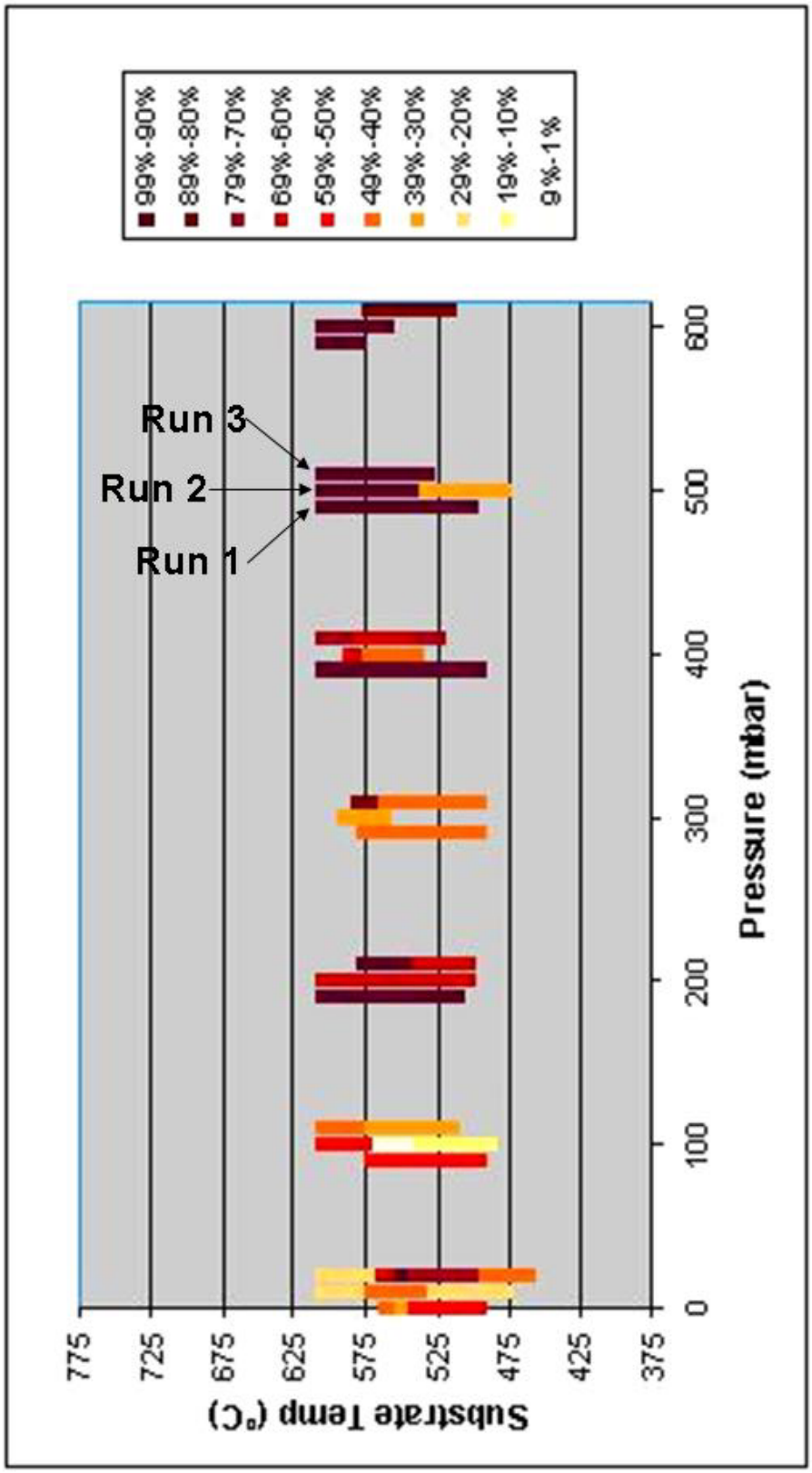

Figure A.1: Graph of nanosaw population for pressure experiments with a source temperature of 630°C.

taking data from Tables B.11-B.15 and averaging the population percentages of the respective morphologies together. Table B.16, found in Appendix B, gives the averaged population density and corresponding deposition temperature zones for all experimental setups. The data is now replotted where the individual bars on each graph represent multiple experimental runs that have been averaged together in order to adequately clarify the large amount of information collected. Figures A.13-A.24 (see Appendix A) are the plots of the averaged runs for the four different source temperatures and the three different morphologies.

Upon inspection of Figures A.13-A.16 two trends relating to population percentage become apparent. The first is pressure dependence. The highest population percentage of the nanosaw morphology can consistently be found at pressures of 300 mbar or larger. There appears to be a direct relationship between the observed population percentage of nanosaw structures and the overall system pressure; as the system pressure decreases, the population percentage of the nanosaw morphology also decreases, with the lowest population percentage of nanocombs and nanosaws being found when the system pressure is at its lowest, 4 mbar. This pressure-population percentage relationship is independent of source temperature.

Also independent of source temperature is the relationship between the population percentage and substrate temperature. At a constant pressure, the population percentage of the nanosaw growth decreases with decreasing local temperature. Typically the highest population percentages of saw- and comb-like structures within any given run will be near the hottest zone of the deposition area.

In general, the population percentage of nanobelts increases as the local temperature decreases in the system (see Figure A.17-A.20). The highest population percentage of nanobelts can be found at or near the coldest region in the deposition area. This is in contrast to the trend observed in the nanosaws. TEM analysis has already revealed that both the nanosaws and nanobelt morphologies grow along the $[01\bar{1}0]$ and have the same side and top surfaces. Since these two structures can be considered identical in every other way, the nanobelts may be considered nanosaws without SPA growth and vice versa. Therefore, it may be that the lower synthesis temperatures, where the nanobelts grow, is unable to overcome an energy barrier required for stimulating the SPA growth on the Cd-terminated (0001) surface, leaving behind the nanobelt morphology. Like the nanosaws, the nanobelts also demonstrate a dependence on chamber pressure. The population percentage of nanobelts decreases as the pressure increases. The population percentage of nanobelts is significantly larger at 4 mbar than that at 500 mbar, regardless of source temperature.

For nanowires, however, there is no distinct dependence on pressure (see Figures A.21-A.24). The only discernable tendency is a consistently high population percentage of nanowire growth at higher temperatures and higher pressures. In the region of high temperature and high pressures, the morphology was almost completely dominated by nanowires.

The opposite trends in the population percentages of nanobelts and nanosaws versus pressure or temperature could be interpreted as the follows. At lower growth temperature, the nanobelts are formed. As the growth temperature increases, some of the nanobelts could be transformed into the saw shape due to the self-catalyzed SPA growth.

As presented in section 5.3, the "teeth" of the nanosaws and the nanocombs are due to the secondary growth on the Cd-terminated (0001) surface. There may be an energy barrier associated with self-catalysis of the Cd^{2+} ions that must be overcome in order to grow the teeth of the SPA structures. If there is insufficient thermal energy provided locally, the secondary growth process may be very slow. This could be the basis for the decrease in population percentage of nanosaws at lower temperature.

One general trend that runs throughout the entire experiment is that the deposition occurs at approximately the same temperature range regardless the temperature at the source materials. This may indicate that the temperature at the source is to stimulate the vaporization of the source materials, and the subsequent growth is controlled by the local temperature and pressure at the substrate. There is an increase in the growth temperature range where deposition occurs with a decrease in the system pressure. In comparing the temperature ranges for deposition at 500 mbar to that at 4 mbar, the ranges for growth can increase anywhere from a factor of two to as large as a factor of 5.8. The possible mechanism controlling this phenomenon will be discussed later in greater detail. It should be noted that this trend was not applied to synthesis runs with a source temperature of 800ºC or higher due to the formation of thin films.

5.5: Statistical Analysis of Temperature and Pressure Effects

The graphic representation of the temperature versus pressure data provided the ability to observe macroscopic trends in the morphologies as certain experimental parameters were changed. However, there are two caveats in using this method of analysis. The first is that the observations were based on an averaging of the

experimental outputs, which could suppress more subtle trends in the raw data. The second is that the conclusions drawn from the observations gave little insight into the specific conditions necessary to isolate a morphology or exert control over the growth. To attain a more quantitative and accurate analysis of CdSe nanostructure growth, a series of statistical techniques were employed.

5.5.1: Binomial Generalized Linear Model

Here, the outcome of each trial (a specific combination of source temperature, pressure, and distance from the center) is considered binary depending on whether growth of a specific nanostructure is observed or not. Experiments that consist of repeated trials, each with two possible outcomes, are known as binomial experiments and can therefore be modeled using a binomial generalized linear model. To do this, each nanostructure is treated separately in order to satisfy the binomial criteria of having only two outcomes, growth or no growth.

First to be examined are the nanosaw structures. Let p_s be the probability of getting a nanosaw/nanocomb. The model we are trying to fit has the form:

$$y = b_0 + b_1 X_1 + b_2 X_2 + ...$$

where X_1, X_2, etc. are the causal variables or predictors. For this study they are temperature, pressure, and distance. Considering the expression on the right hand side of the equation, the value of y can lie anywhere between positive and negative infinity. However, p_s lies between 0 and 1 and therefore it is improper to simply substitute p_s

directly in place of y. It is then necessary for a transformation to be made on p_s that will give the correct upper and lower boundaries. An appropriate transformation would be the logic link function, which is expressed as:

$$y = \log \frac{p_s}{1 - p_s}$$

The quantity $p_s/1\text{-}p_s$ is the odds ratio of getting a certain structure. This transformation is preferable to other link functions in that it is theoretically simpler and easy to interpret. With this logic link transformation, the statistical model will give the probability of getting a nanosaw structure anywhere between positive and negative infinity. A model must then be fit to this logic link expression in terms of the experimental variables: source temperature (T), chamber pressure (P), and distance away from the center of the furnace (D).

The next step in this process is determining what terms should be included in the model. Should quadratic or cubic terms for T, P, and D be included? Are the interaction terms significant (e.g. TP, PD, etc.)? A graphic representation of the observed proportions against T, P, and D help in determining the type of function that will best model the observed data. This is achieved by taking the total number of an observed morphology and dividing it by the total number of observations for a given set of experimental parameters. For instance, to calculate the observed proportion of nanosaws against temperature, the total number of nanosaws observed with a source temperature of 630˚C is divided by the total number of observations at that source temperature. This is repeated for all source temperatures, then again for each morphology. The result is a plot

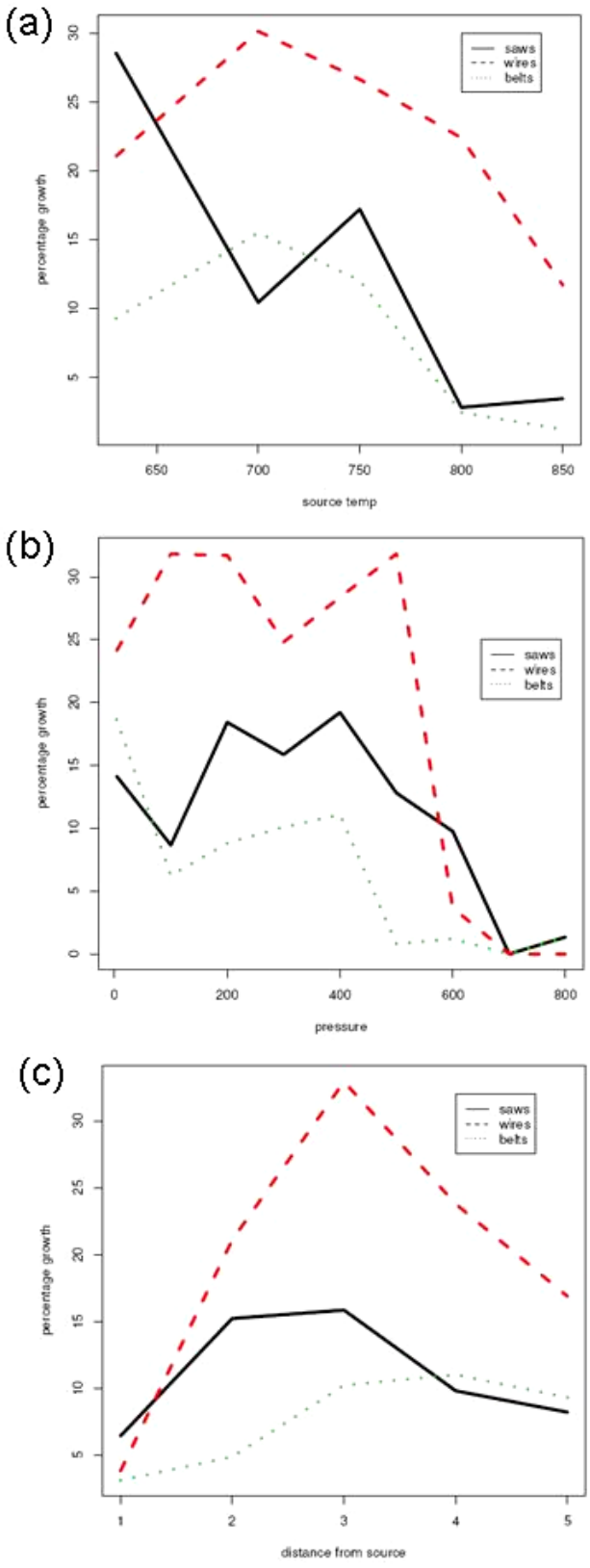

Figure A.25: Observed proportions plotted against (a) T, (b) P, and (c) D

of the observed average percentage growth versus temperature (see Figure A.25a) irrespective of the other causal variables. A similar process can be done for the other experimental variables, chamber pressure and distance (see Figures A.25b and A.25c). What these plots suggest is that a second-order model can represent the T, P, and D relationships. Examining Figures A.25, the overall trend can be represented by a quadratic equation. There is some deviation in the trend, however, this fluctuation is attributed to noise in the system which will be investigated later. In addition to plotting The observed proportion against the individual experimental parameters, the data can be plotted versus the interaction of two variables. Figure A.28 is a plot of the

Table B.17: Binomial gerneralized linear model for nanosaws

	Estimate	Std. Error	z value	Pr(> |z|)
(Intercept)	-62.029089	2.885522	-21.49666	0
temp	0.138759	0.006984	19.86762	0
pres	0.197253	0.006352	31.05308	0
avgdist	1.829829	0.126699	14.44235	0
tempsq	-0.000152	0.000005	-29.44989	0
pressq	-0.000008	0.000000	-26.58828	0
avgdistsq	-0.142052	0.002603	-54.57758	0
temp:pres	-0.000274	0.000009	-29.54354	0
pres:avgdist	-0.011406	0.000376	-30.37497	0
temp:avgdist	0.004120	0.000192	21.43290	0
temp:pres:avgdist	0.000016	0.000001	29.50666	0

pressure/temperature interaction of the observed proportions for CdSe nanowires. Because the curves for each individual source temperature are not parallel to each other, there is good reason to believe that there is some effect between the interaction of source temperature and chamber pressure on the morphology. Plots of the interactions of the three variables have can be seen in Figures A.26-A.28 in Appendix A for each morphology. The importance of these plots is that they reveal the significance of the interaction terms for the model.

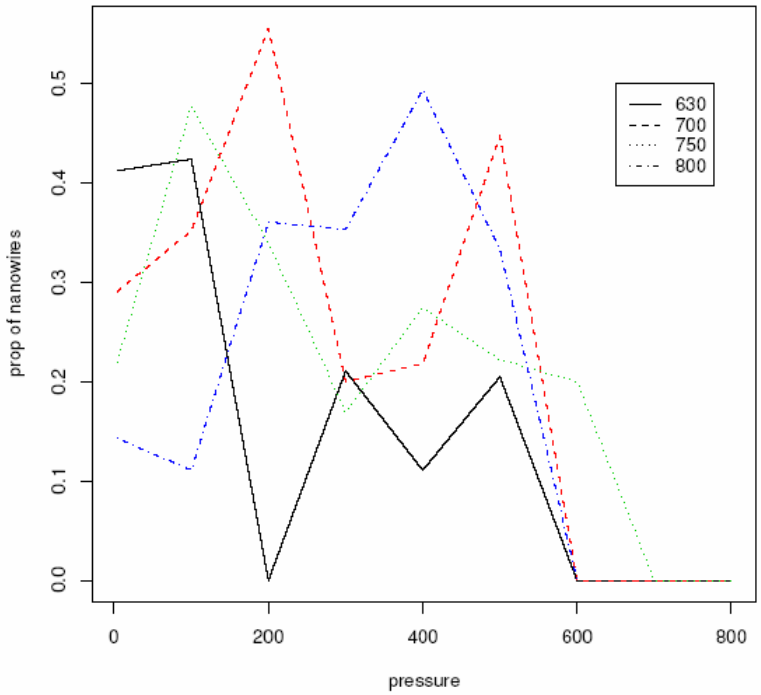

Figure A.28: Interaction plots of (a) temperature-distance, (b) pressure-distance and (c) temperature-pressure for the CdSe nanowires.

Fitting the generalized linear model with a binomial link to the data requires the aid of computer software. The R program, which is a powerful statistics program, will

allow the estimation of the coefficients for the experimental variables and their interactions. By employing R to use the method of maximum likelihood, the program takes the given experimental data and calculates constants for the $\log\frac{p_s}{1-p_s}$ expression. Table B.17 gives the calculated constants (column marked, "Estimate") as well as the associated error in those estimates. Since the data set is a sample, there will be some error, however the standard deviation are low enough to give significance to the study. The z values, which are the ratios of the estimated constants and their respective standard error values, can be used as a measure of statistical significance. If the z value is large, then the estimated constant is considered significant for use in the model.

Using the values calculated from the R program, the fitted model for the nanosaw morphology is:

$$\begin{aligned}\log\frac{p_s}{1-p_s} = &-62.029089 + 0.138759T + 0.197253P + 1.829829D \\ &-0.000152T^2 - 0.000008P^2 - 0.142052D^2 \\ &-0.000274TP - 0.011406PD + 0.004120DT + 0.000016TDP\end{aligned}$$

To test the validity of the model, the residuals of the data are plotted against the three experimental variables. The residuals are the difference between the observed percentage of nanosaws for a given set of T, P, and D and the calculated percentage from the model. For a model to be considered good, the values should be symmetric around zero. This is somewhat intuitive since there is an equal likelihood that the model will predict values greater and smaller than the actual observed data.

This entire procedure was carried out for the nanobelts and nanowires as well. Tables B.17-B.19 contain the generated coefficients for the two nanostructures. In examining Table B.19, the variable corresponding to the temperature-pressure-distance

Table B.20: Equations of the fitted statistical model for each CdSe morphology.

Nanostructure	Binomial Generalized Linear Fitted Model
Nanosaw/ Nanocombs	$\log \frac{p_s}{1-p_s} = -62.029089 + 0.138759T + 0.197253P + 1.829829D - 0.000152T^2 - 0.000008P^2 - 0.142052D^2 - 0.000274TP - 0.011406PD + 0.004120DT + 0.000016TPD$
Nanobelts	$\log \frac{p_b}{1-p_b} = -119.53352 + 0.31894T + 0.14682P + 1.02154D - 0.00026T^2 + 0.000002P^2 - 0.07927D^2 - 0.00020TP - 0.01020PD + 0.00257TD + 0.00001TPD$
Nanowires	$\log \frac{p_w}{1-p_w} = -37.00079 + 0.08163T - 0.01083P + 1.05962D - 0.00008T^2 - 0.00001P^2 - 0.06208D^2 + 0.00003TP - 0.00056PD + 0.00158TD$

interaction for the nanowires is not present. This is due to a low z value for this interaction variable. The value suggested that it was not significant, and therefore rather than include a variable that cannot assist in the prediction of growth it was taken out. Figures A.29-A.31 in Appendix A are the residual plots against T, P, and D for the nanobelts and nanowires. Since all residual plots demonstrate an even spread about zero, then the model has included all necessary variables sufficiently describes the observed

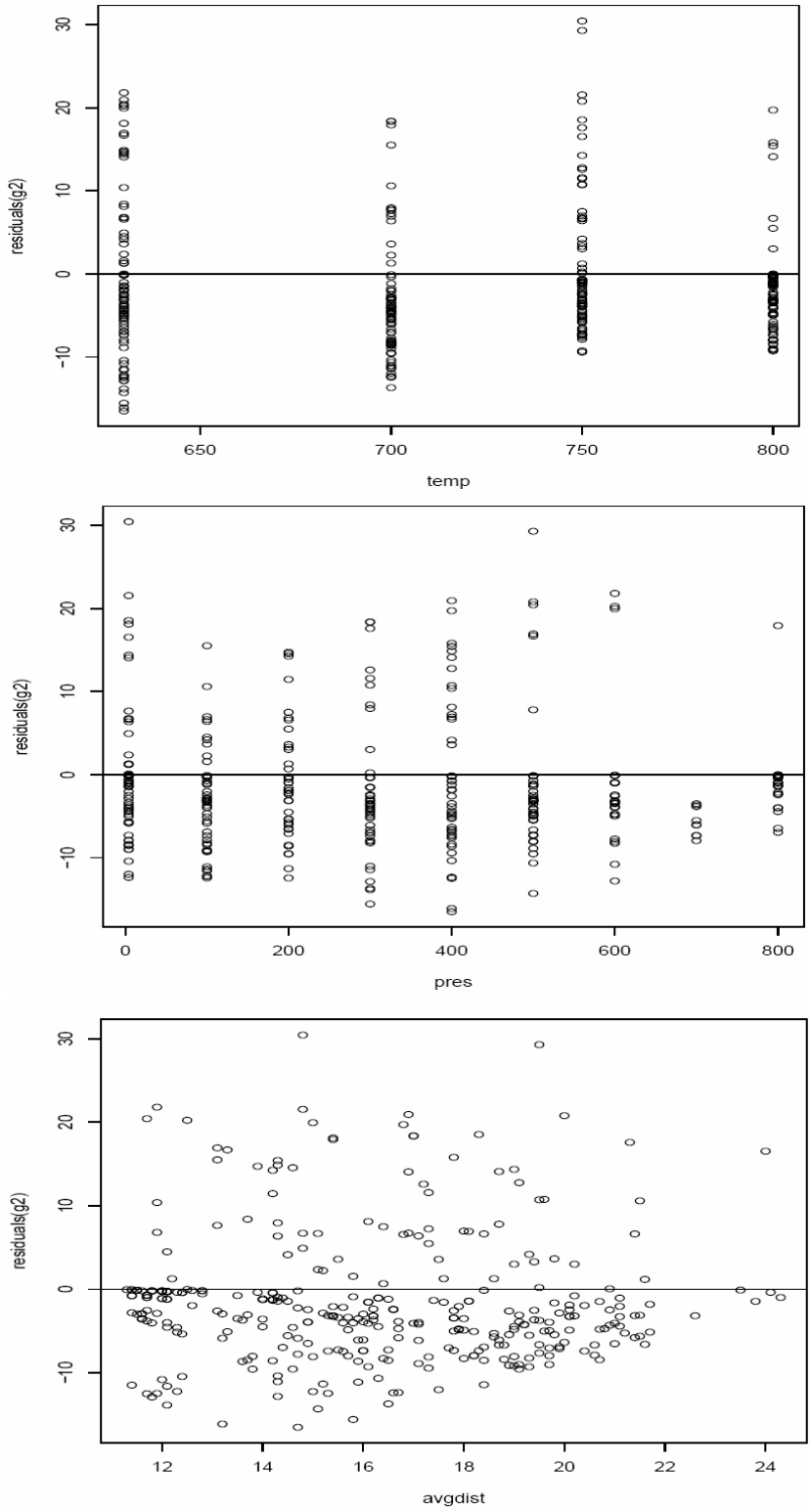

Figure A.29: Residual plots against (a) temperature, (b) pressure, and (c) distance for nanosaws/nanocombs.

data set. The equations for the fitted models for all of the nanostructures are given in Table B.20.

5.5.2: Growth Optimization

The models in Table B.20 describe the growth of each individual nanostructure. There are areas of high and low yield among all the various combinations of the three process parameters. To calculate the region of highest yield, the global maxima must be attained. This is achieved by maximizing p_n. So that the models do not extrapolate from the experimental data set, the maxima is bound between: $630^{\circ}C \leq T \leq 800^{\circ}C$, $4mbar \leq P \leq 800mbar$, $11cm \leq D \leq 22cm$. Numerically, the global maxima, which in this case corresponds to the largest percentage of nanosaw/nanocomb growth, is calculated to be

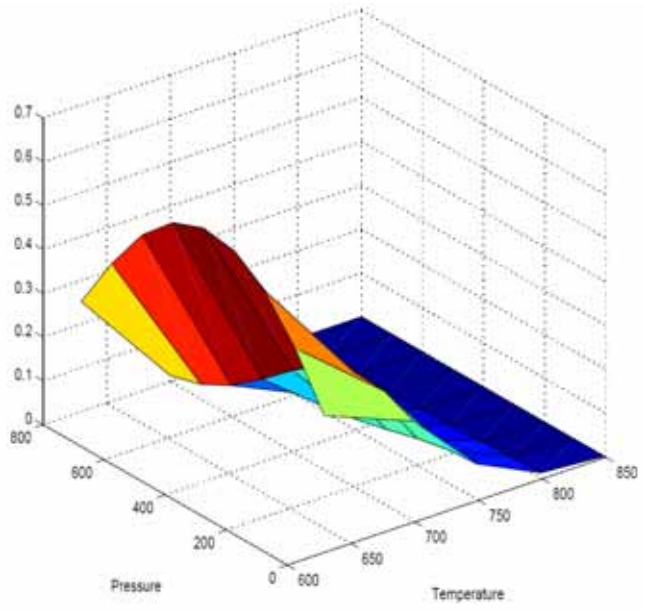

Figure A.32: Predicted proportion of nanosaws/nanocombs at a given distance 17.7cm away from the source.

T*= 630.0000˚C, P*=399.9989, and D*=13.7099, with a p^*_s=0.5826. Figure A.32 is a graph of the global maxima and the surrounding area. This procedure was used to find the optimum growth parameters for nanobelts and nanowires. Table B.20lists the experimental parameters for optimum growth, as well as the probability, p_n, of each nanostructure. Lastly the surface of the nanobelt and nanowire morphologies and their

Table B.20: List of optimized parameters for each of the nanostructures using two analytical methods.

	Statistcal Analysis				*Graphical Analysis*	
	T* (ºC)	**P* (mbar)**	**D* (cm)**	**p_n**	**Local Temperature (ºC)**	**P* (mbar)**
Nanosaws	630.0000	399.9989	13.7099	0.5826	Moderate	Above 300
Nanobelts	699.9744	4.0000	17.7094	0.7711	Low	4
Nanowires	699.9728	59.9998	17.1713	0.4550	High	N/A

respective global maxima are shown in Figures A.33 and A.36.The maximized parameters for T, P, and D that were calculated from the model closely resemble the assertions made in the previous section about the growth trends of the individual CdSe nanostructures (see Table B.21). When investigating the growth trends graphically, the nanobelts were found in the largest concentrations at low pressures and lower local substrate temperatures. The nanosaws contrastingly were observed in the most abundance at higher local substrate temperature and pressures of over 300mbar. The statistical model gives the optimum parameters in terms of source temperature and distance of the substrate from center of the tube. Converting these two parameters to local temperature, the optimum values for nanosaws and nanobelts are T= 571˚C and P= 400 mbar, and T =567˚C and P= 4 mbar, respectively.

The statistical analysis has helped give a more quantitative examination of the temperature versus pressure investigation. Optimum experimental parameters for each

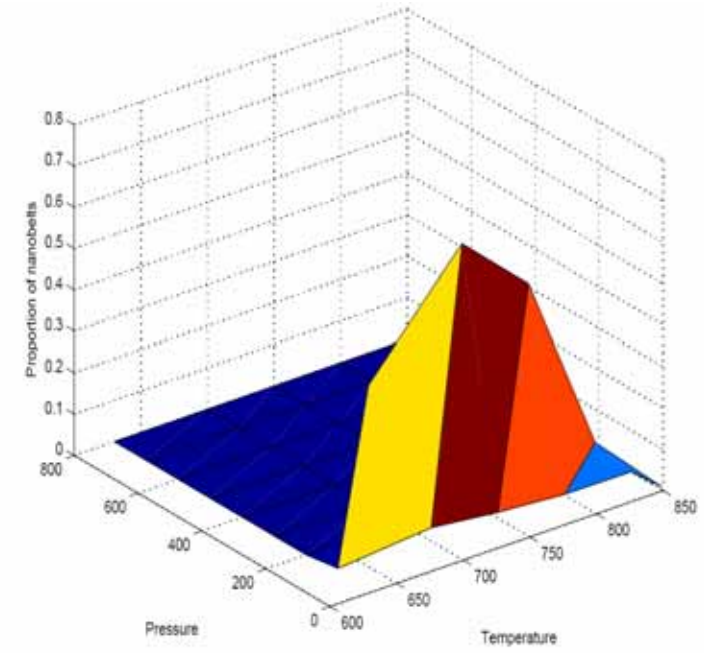

Figure A.33: Predicted proportion of nanobelts at a given distance 13.7cm away from the source.

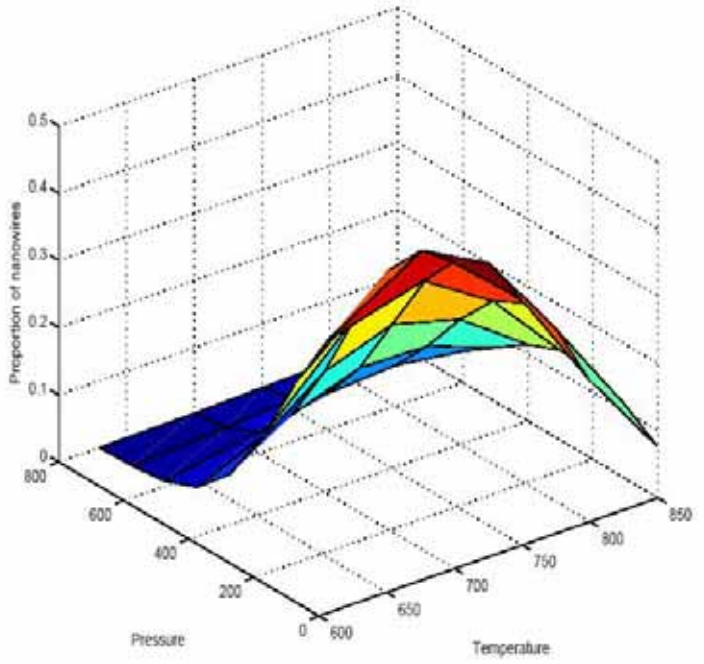

Figure A.34: Predicted proportion of nanowires at a given distance 17.1cm away from the source.

morphology have been calculated as well as a statistical model that can be used to predict growth outside of the experimental boundaries of this study. It has also yielded experimental evidence as to a critical energy barrier necessary to promote SPA growth in one-dimensional CdSe nanostructures. Because the statistical model is not based on an average of the data, it gives a more definitive understanding into the growth of one-dimensional CdSe nanostructures.

5.6: Variance Analysis

In examining Tables B.11-B.15, there is some variance between the three experimental runs. Despite a great deal of care going into the replication of each experimental setup, there are some uncontrollable internal and external influences that cause a deviation in the overall outputs of the experiment. A variance analysis can help gain a better understanding of the experimental parameters and their effects on the synthesis process. This information can then be used to make the setup more robust and give a higher likelihood for reproducibility.

5.6.1: Growth Optimization

When the temperature, pressure, and distance are specified at certain levels, the actual values vary around that set point, which is due internal noise in the system. This deviation in the set values can induces variation into the growth of the nanostructures. In the prior study, the experimental parameters (T, P, and D) were assumed to be constant. However for the variance analysis, these parameters are treated as values with some confidence interval indicative of the observed variance in the synthesis process. By

utilizing the knowledge of the variations in the process parameters T, P, and D around their set values μ_T, μ_P, μ_D, a study can be conducted whereby the effect of this inner noise on the yield of nanostructures is more fully understood.

To do this, T, P, and D are assumed to be normally distributed variables around their respective set values. Specifically:

$$T \sim N\left(\mu_T, \sigma_T^2\right)$$
$$P \sim N\left(\mu_P, \sigma_P^2\right)$$
$$D \sim N\left(\mu_D, \sigma_D^2\right)$$

where σ^2_T, σ^2_P, σ^2_D can be estimated from data on the variation of T, P, and D.

The variation in source temperature is observed to be ±7˚C corresponding to μ_T = 630˚C and 700˚C; and ±6˚C corresponding to μ_T = 750, 800, and 850˚C. These values for the variance are observed and recorded from the internal thermal couple in the tube furnace. The average variance is thus ±6.4˚C or 12.8˚C. Equating this to $6\sigma_T$, which is considered to be the natural spread of a normal distribution variable, σ_T is estimated to be 2.13.

The variation in D is ±0.2cm for all levels of μ_D. Thus, $\sigma_D = \frac{2 \times 0.2}{6} = 0.067$.

The case of pressure is different. For the process parameters T and D, the variance was fairly if not completely constant for all set values. The variation in P, however, changes with the set value as shown in Table B.22. A plot of σ_P against μ_P is shown in Figure A.35. A regression line (through the origin) is obtained to express the relationship between σ_P and μ_P:

$$\sigma_P = 0.025006\mu_P$$

Now that σ_T, σ_P, σ_D have been estimated, robust parameters for optimizing each morphology can again be calculated using the growth model from the previous section. These values for optimum growth may deviate from the previous set because not only is a large population of growth a prerequisite but also small amount of variance around those set values. These two factors may be in competition with each other and thus yield different optimization parameters. This type of growth optimization is of particular importance for industrial scale up where robust conditions are necessary to ensure the quality of a product.

First to be examined is the nanosaw growth. Let $\eta_s = \log\frac{p_s}{1-p_s}$ for simplicity. By simply plugging in η_s into the model for nanosaw growth, it now takes the form:

$$\begin{aligned}\eta_s = & - 62.029089 + 0.138759T + 0.197253P + 1.829829D \\ & - 0.000152T^2 - 0.000008P^2 - 0.142052D^2 \\ & - 0.000274TP - 0.011406PD + 0.004120DT + 0.000016TPD\end{aligned}$$

Since T, P, D are now random variables, assuming them to be independent, the above expression can be written as:

$$
\begin{aligned}
E(\eta_s) = \; & - \; 62.029089 + 0.138759\mu_T + 0.197253\mu_P + 1.829829\mu_D \\
& - \; 0.000152(\sigma_T^2 + \mu_T^2) - 0.000008(\sigma_P^2 + \mu_P^2) - 0.142052(\sigma_D^2 + \mu_D^2) \\
& - \; 0.000274\mu_T\mu_P - 0.011406\mu_P\mu_D + 0.004120\mu_D\mu_T + 0.000016\mu_T\mu_P\mu_D
\end{aligned}
$$

$E(\eta_s)$ denotes the mean or average value of η_s for set values μ_T, μ_P, μ_D. Substituting σ^2_T = 2.13, σ^2_P = 0.0025006, σ^2_D = 0.0067 in the rigt hand side of the above equation, $E(\eta_s)$ can be expressed soley in terms of μ_T, μ_P, μ_D.

However, expressing the variance of η_s, $Var(\eta_s)$, in terms of μ_T, μ_P, μ_D is not so straightforward, and a Monte Carlo simulation is necessary. For each combinations of μ_T, μ_P, μ_D (μ_T = 630, 700, 750, 800C; μ_P = 4, 100, 200, ….800mbar; μ_D = 12, 14, 16, 18, 20cm) the following are done:

1. 5000 observations on T, P, D are generated from the respective normal distributions and η_s is obtained using the original fitted model for nanosaw growth.
2. The variance of those 5000 η_s values is computed.
3. Using a linear regression, a model is fitted to express $Var(\eta_s)$ in terms of μ_T, μ_P, μ_D.

Like in the previous section, the R program was used to estimate the coefficients for model. Table B.23 gives the regression results for the variance of nanosaws. Because a regression model and not a generalized linear model, is being used, what was before z values, are now t values. Analogously, these values are used as a measure of the

statistical significance of the model parameters. This yields an expression for the variance in the nanosaw growth, which is given below:

$$\begin{aligned} Var(\eta_s) &= 0.95496535 - 0.00189549\mu_T + 0.00000134\mu_T^2 - 0.00286610\mu_P + 0.00000016\mu_P^2 \\ &- 0.03514362\mu_D + 0.00107943\mu_D^2 + 0.00000407\mu_T\mu_P + 0.00016365\mu_P\mu_D \\ &- 0.00000024\mu_T\mu_P\mu_D \end{aligned}$$

For the best growth conditions for nanosaws, $E(\eta_s)$ must be maximized and $Var(\eta_s)$ must be minimized. This will lead to a combination of μ_T, μ_P, μ_D that maximize the growth and decreases excessive variation. In maximizing $E(\eta_s)$ the optimum settings are $\mu_T = 630^{\circ}C$, $\mu_P = 405mbar$ and $\mu_D = 13.7cm$. Serendipitously, these values are almost exactly the optimized values calculated in the above section. It can therefore be concluded that this set of values corresponds to regions of T, P, and D where small perturbations in the experimental parameters has little effect on the overall growth.

Table B.23: Regression results for variance of nanosaws.

	Estimate	Std. Error	t value	$\Pr(>\|t\|)$
Intercept	0.93853948	0.08278561	11.336988	0
T	-0.00185031	0.00022540	-8.208843	0
T^2	0.00000131	0.00000016	8.283869	0
P	-0.00281948	0.00007490	-37.644143	0
P^2	0.00000016	0.00000001	18.100024	0
D	-0.03526263	0.00248239	-14.205092	0
D^2	0.00108425	0.00007686	14.106898	0
TP	0.00000401	0.00000010	39.205854	0
PD	0.00016130	0.00000443	36.385254	0
TPD	-0.00000023	0.00000001	-38.565603	0

Table B.27: Optimized growth values for statistical and variance analysis.

	Statistcal Analysis			*Variance Analysis*		
	T^* (°C)	**P^* (mbar)**	**D^* (cm)**	**μ_T^* (°C)**	**μ_P^* (mbar)**	**μ_D^* (cm)**
Nanosaws	630	400	13.7	630	405	13.7
Nanobelts	700	4	17.7	701	4	17.7
Nanowires	700	60	17.2	681	4	17.2

To further understand the impact of temperature, pressure, and distance on the mean and variance of nanosaw growth, a plot of $E(\eta_s)$ and $Var(\eta_s)$ versus the experimental set values, μ_T, μ_P, μ_D is necessary. Figures A.36-A.381 (see Appendix A) plot the average values of η_s and the variance of each value as a function of the experimental parameters. In each case, the largest value for $E(\eta_s)$ is taken from a region where the corresponding variance in those experimental parameters is at a minimum.

This variance analysis was carried out for the nanobelts and nanowires as well. Tables B.23-B.27 (see Appendix B) contain the estimated coefficients, $Var(\eta_s)$ equations for all three morphologies, and the optimum growth conditions for each CdSe nanostructure, respectively. The optimum values calculated in the variance analysis are close to those calculated from the previous statistical analysis. The only large disparity between the two is the pressure value for the optimization of nanowire growth. This is due to the nature of the surface depicted in Figure A.34. Although the global maxima occurs at a pressure of 60mbar, the slope of the surface about that specific value is large enough to significantly alter the morphology with the slightest deviation. Values about 4mbar for nanowires are much less affected by perturbations. Although the percentage of

nanowires grown at this pressure may be less than at the statistical optimum, this value calculated from the variance analysis is much more robust.

5.6.2: Variance in Morphology

From the outset, control over the growth of one-dimensional nanostructures was the main goal of this investigation. A systematic study of the growth varying the different process parameters has yielded the set values for T, P, and D for maximizing the growth of a particular structure as well as general trends in the growth which has helped to understand the underlying mechanisms that promote the growth of one nanostructure over the other. In addition to the insight gained about CdSe nanostructures, a better understanding about the process and synthesis setup has been achieved. This information can help uncover more subtle trends or mechanisms that govern this material system.

Experimental evidence indicated that the local temperature determined the morphology of the nanostructures. Higher temperatures induced nanosaws or nanowire growth, while lower temperatures promoted the growth of nanobelts. Yet even at high temperatures, where SPA growth should be dominate, nanobelts can still be observed in the as-deposited material. One explanation of this is an internal variance in the source temperature of the system.

Polycrystalline alumina tubes are used in the experimental setup due to their stability at high temperature. However, the thermal conductivity of alumina is extremely low. This becomes of importance during the ramping up process as the furnace is raised from room temperature to some set point. The C1 controller being used to regulate the heating of the chamber measures the temperature outside of the alumina tube. Since the

thermal conductivity of alumina is so poor, the temperature being measured outside of the tube is on the order of 100˚C lower than inside the tube. This is significant because once the thermocouple controlling the heating of the furnace reaches the set point, the controller stop ramping up the furnace. This in turn slows down the actual ramping up process as the temperature inside the tube must now reach the set point through a "thermal momentum" of the system.

Table B.30: Time and temperature delays between inner and outer thermocouples for ramping up and cooling down a source temperature of 750˚C.

Ramp Up		Cool Down	
Minutes	Temperature (ºC)	Minutes	Temperature (ºC)
-2	624	0	750
-1	**644**	1	724
0	664	2	717
1	682	3	701
2	700	4	693
3	718	5	676
4	728	6	652
5	733	**7**	**631**
6	741	8	605
7	744	9	575
8	746		
9	748		
10	749		
11	750		

By inserting a thermocouple inside of the tube, temperature measurements inside and outside of the tube could be made simultaneously. Table B.28-B.31 (see Appendix B) gives the measured disparity of the temperature inside the alumina. The columns marked "Minutes" in Tables B.28-B.31 give measurements of time in relationship to when the thermocouple outside the alumina tube reaches the set point.

Therefore, at a time equal to 3 signifies 3 minutes after the outside thermocouple reached the set point for a source temperature. This lag in the ramp is significant in the initial growth and final growth products. The minimum source temperature necessary to promote growth is 630˚C. For a source temperature of 750˚C, the source temperature reaches the minimum temperature for deposition, 630˚C, twelve minutes before it reaches the actual set point value. During these twelve minutes, deposition is occurring at conditions unspecified by the experimental setup. Analogously during the cooling down process, the thermal conduction of the alumina tube prevents instant quenching of the system. For several minutes after the furnace is turned off, the source temperature inside the furnace slowly lowers, allowing for growth again to occur at unspecified conditions.

This internal variance is unavoidable in the current synthesis setup, and may be the source of nanobelt deposition in the high temperature regions of the furnace. As the

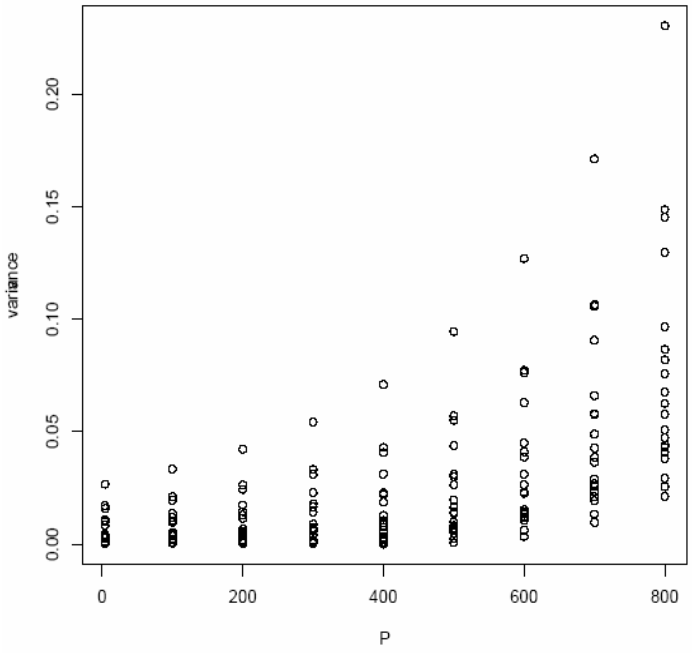

Figure A.45: Var(η_s) against pressure.

temperature lowers during the cooling process, the energy of the system can no longer initiate the SPA growth mechanism, leaving behind nanobelts. This may also be the cause of variations in morphology in relationship to the different temperature zones.

To alleviate this problem, a transfer system must be added to the synthesis setup. Having a retractable arm, which can insert substrates in and out of the tube, would give more control over the growth of these nanostructures. As the tube ramps up, substrates would be outside of the deposition zones until the furnace reached the designated process parameters. Once these conditions are met, substrates could be inserted and grow under exact conditions. After which, the substrates could be removed before the cooling process began to avoid growth during the cool down period. Implementing this new apparatus would assist in increasing the confidence interval of a predictive model by decreasing any variance or artifacts due to internal noise of the synthesis system

5.6.3: Variance in Reproducibility

Earlier in the section 5.4.3, a figure plotting the local temperature versus pressure for nanosaws grown with a source temperature of 630˚C (see Figure A.1) was shown to demonstrate the reliability of the experiments. Three different experimental runs were made under the same conditions with growth outputs that closely resembled one another. Although in general the replications of each experiment do have similar products, deviation does exist. It is important to understand where this divergence in results is initiated from so that more precise control over these nanostructures can be attained.

The variance models of the individual nanostructures reveals that pressure is the largest contributor to the inconsistency between experimental runs. In studying Tables

B.23-B.25 (see Appendix B), it is clear that the variance by far has the largest t values. For the nanobelt and nanowire structures, the variance model does not even consider all of the processing parameters. The T^2 and D^2 terms are omitted because they offer no significance to the variance model and the interaction parameters that are included are all associated with pressure. Using a step-wise regression technique, roughly 80% of the variance in growth can be accounted for by the pressure alone. This quantity indactes how important this parameters is in the reporoducibility of one-dimensional CdSe nanostructures.

A consequence of this pressure variance may be the observed trend where deposition appears to increase with decreasing pressure, independent of the source temperature. Figures A.45-A.47 is a plot of the variance versus pressure. The figures demonstrate the strong effect of pressure on the variance, particularly at higher values of pressure where variance drastically increases. Since the model is based on a binomial outcome (growth or no growth), the observed trend in the data may be an artifact of the pressure variance. Perhaps there is no increase in the deposition region with respect to lower pressures, but instead at higher pressures the variance is so high that growth in not allowed to occur. At this point no definitive conclusions can be made about this trend until the pressure variance is eliminated or at the very least greatly reduced.

To minimize this effect, a more precise pressure control system must be fitted onto the experimental setup. As the equipment exists now, the pressure is controlled manually through a system of valves and analog gauges that can only control measure temperature within 10mbar increments. Using a MKS 626 baritron capacitance manometer, the pressure is measured with a digital gauge sensitive enough to detect

changes in pressure of 0.2mbar. This gauge will be feed to a computer controlled switch that will that will monitor and adjust a valve to maintain the pressure set point to within a few tenths of a millibar. This addition to the experimental setup should drastically reduce the variance in the synthesis process and increase the reproducibility.

CHAPTER VI

CONCLUSION

Since the turn of the century, one-dimensional nanostructures have slowly gained momentum as a dominate field of research within the nanoscience community. With the emergence of this new class of materials, a tremendous amount of research and funding has been poured into investigating these structures. Yet there is still a wealth of discoveries in this field, just waiting to be tapped.

The focus of this work has been to gain an understanding of the underlying mechanisms controlling the one-dimensional nanostructure growth. This thesis gives a systematic investigation into the growth of one-dimensional nanostructures of select II-VI compounds with the wurtzite crystal structure, with the largest emphasis being on cadmium selenide. By systematically altering two process parameters a further understanding into the formation of one nanostructure over another was achieved. The study revealed that the local temperature plays an intricate and dominate role in the formation of nanosaws and nanobelts. Other process parameters like pressure and source temperature do play some role in determining morphology, but appear to be less significant.

For the first time, a statistical approaches was used to gain insight into the fabrication of one-dimensional nanomaterials. Taking all of the raw data from the systematic pressure versus temperature experiments, statistical models describing and predicting the growth of each one-dimensional structures were attained. These models

allow for the optimization of growth for any particular one-dimensional CdSe nanostructure.

A second statistical analysis was conducted on the experimental data to measure the variance in the synthesis process and determine if how the different aspect of the experimental setup effected the experimental output. This type of analysis allows for quantitatively determination of the variability and robustness of the experimental setup and process. Armed with this knowledge, suggested alterations and modifications are suggested for the setup in order to reduce variability, increase yield, and gain insight into the more subtle mechanisms controlling growth of these nanomaterials.

The goal of gaining more control and understanding over the growth of these one-dimensional nanostructures within this experimental setup has be achieved. Yet there is still a great amount of opportunity for more discovery and investigation, particularly in the modification of the synthesis setup and the statistical analysis, but that is left to someone else.

APPENDIX A

FIGURES

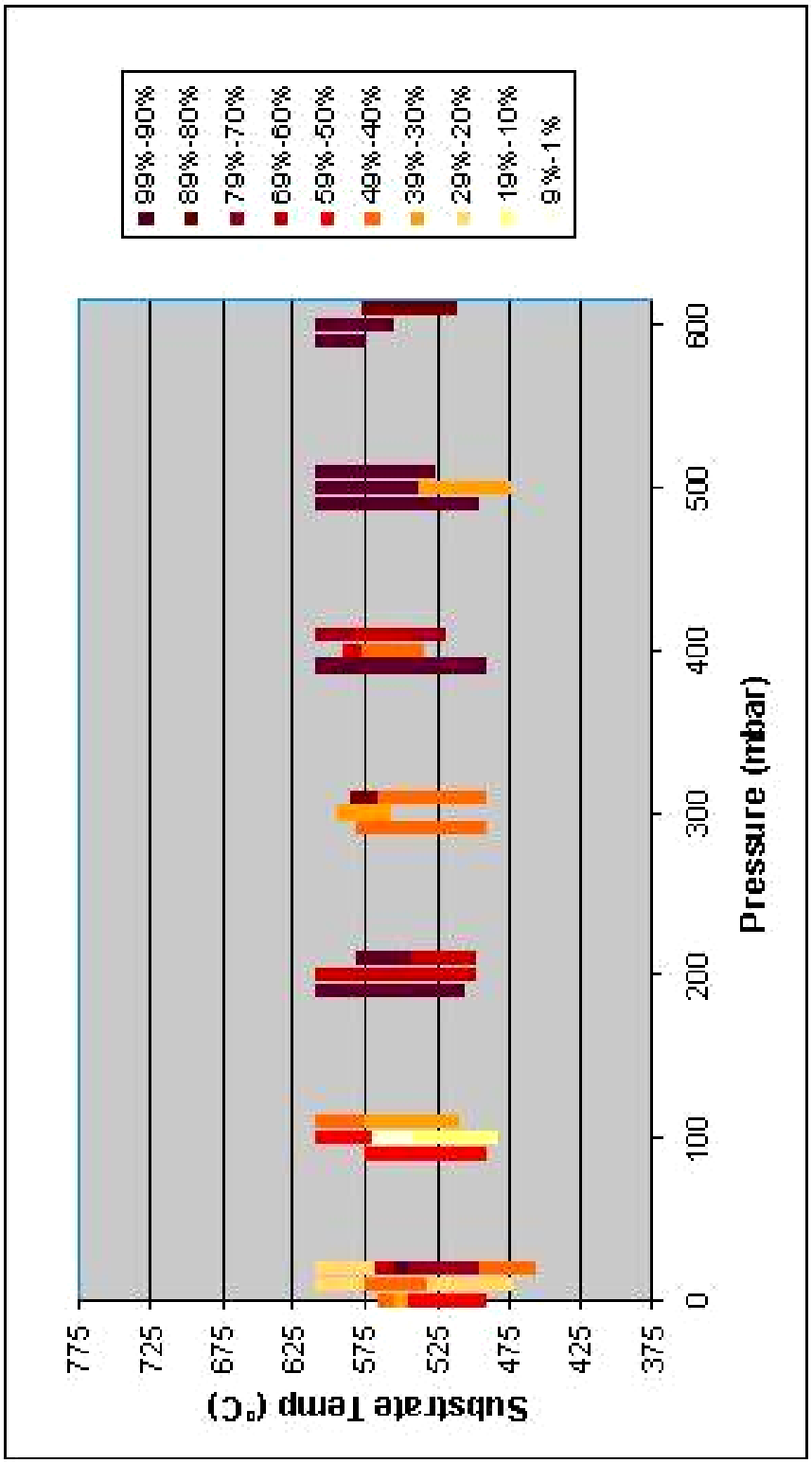

Figure A.1: Graph of nanosaw population for pressure experiments with a source temperature of 630°C

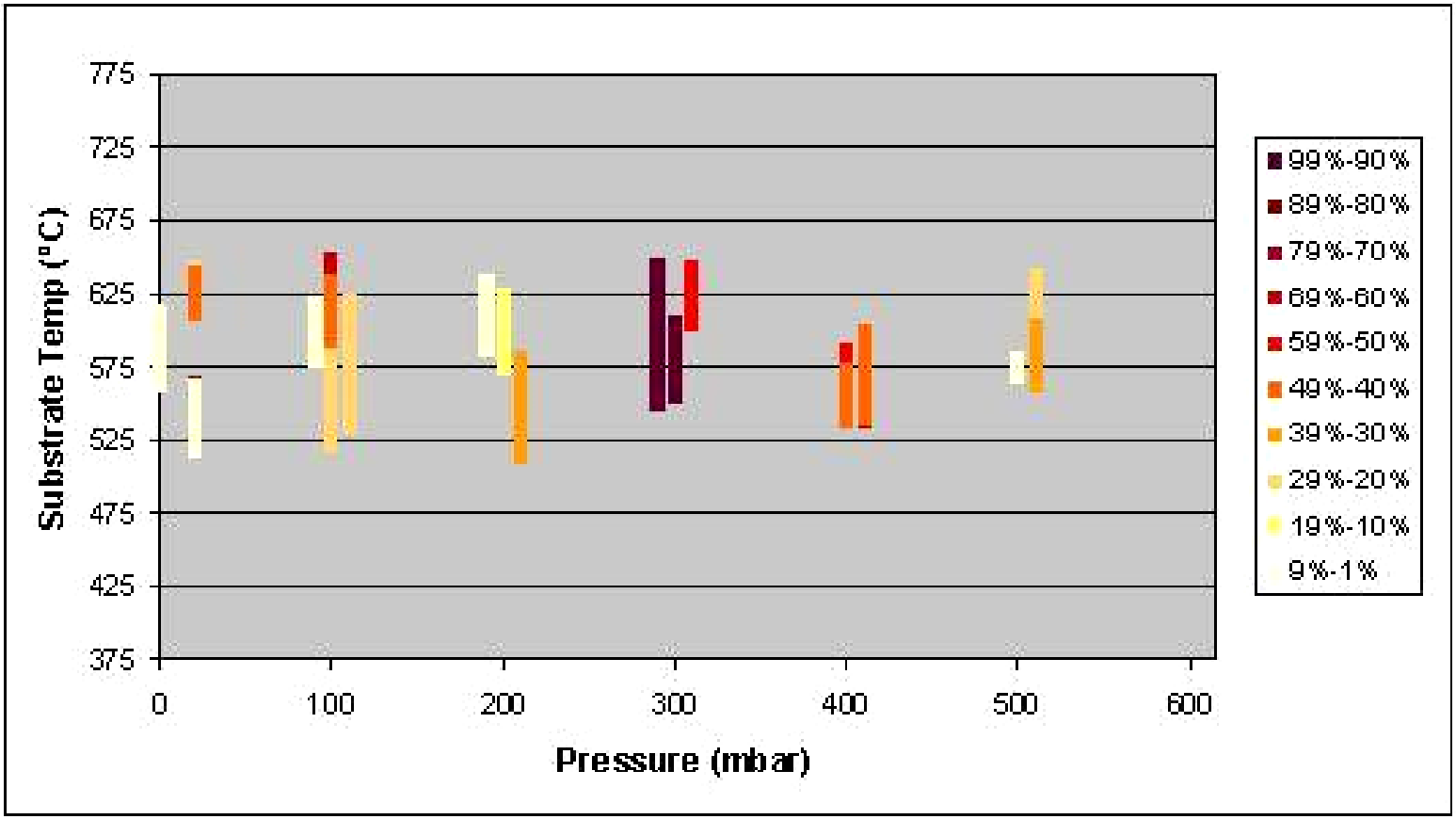

Figure A.2: Graph of nanosaw population for pressure experiments with a source temperature of 700°C

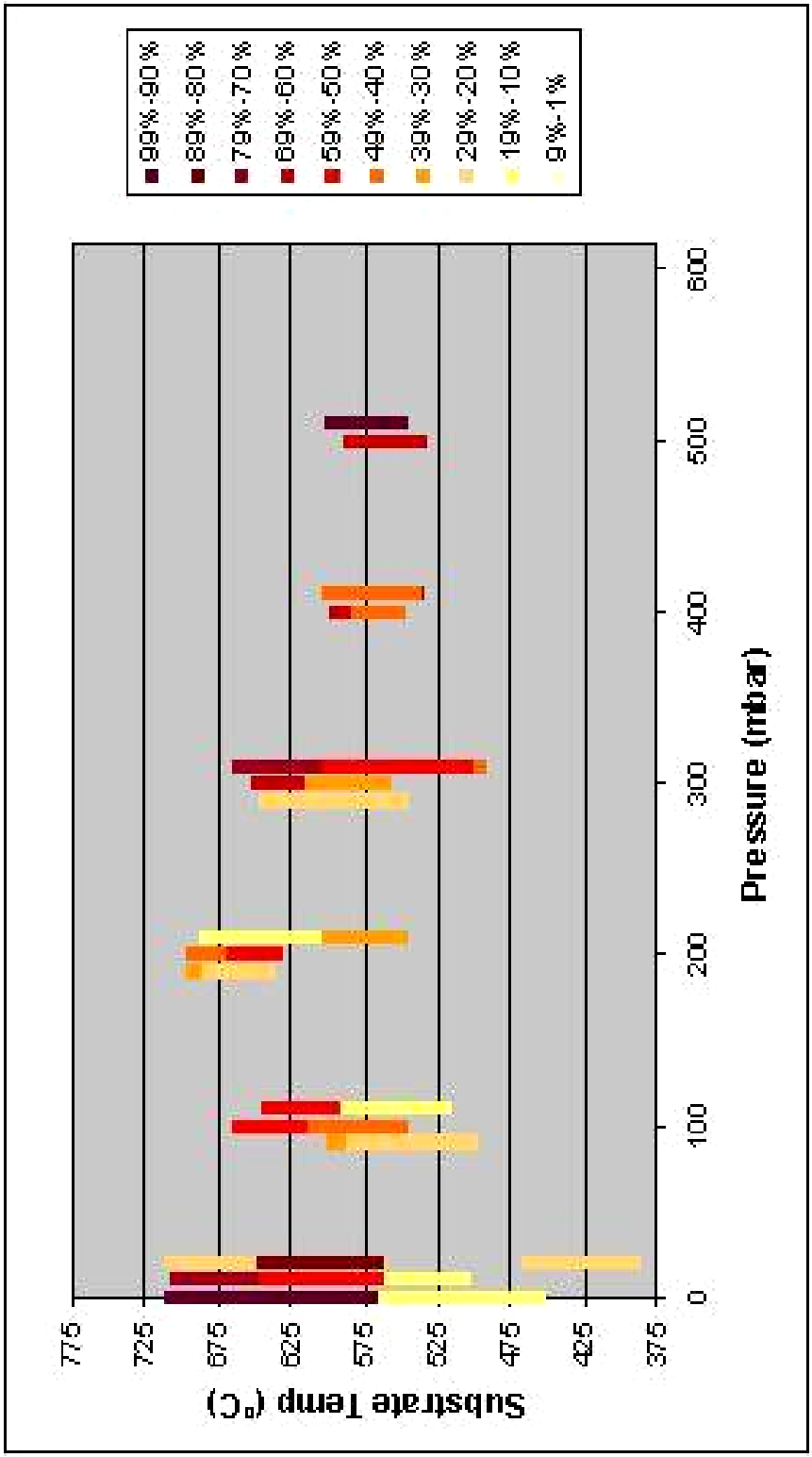

Figure A.3: Graph of nanosaw population for pressure experiments with a source temperature of 750°C

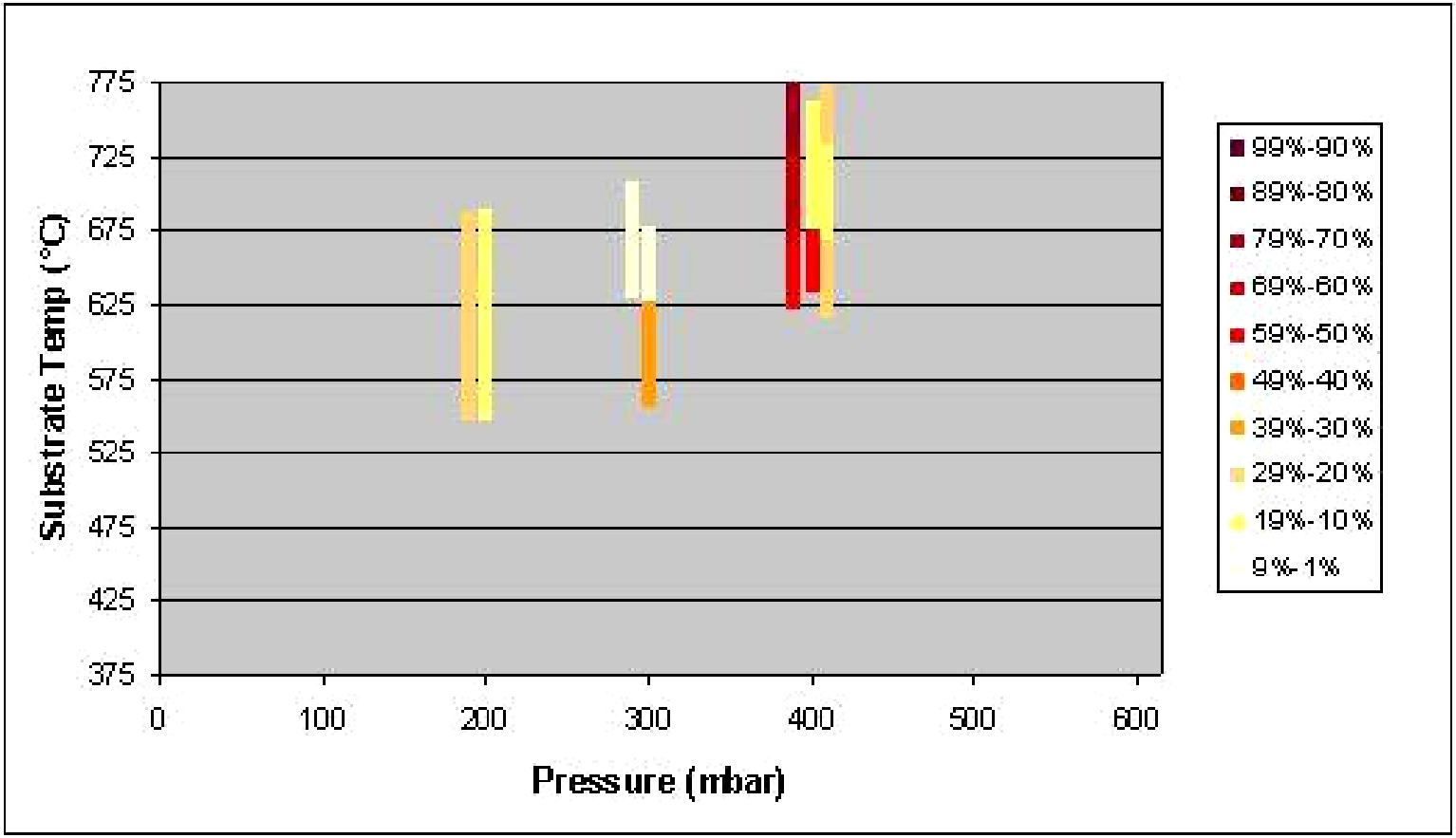

Figure A.4: Graph of nanosaw population for pressure experiments with a source temperature of 800°C

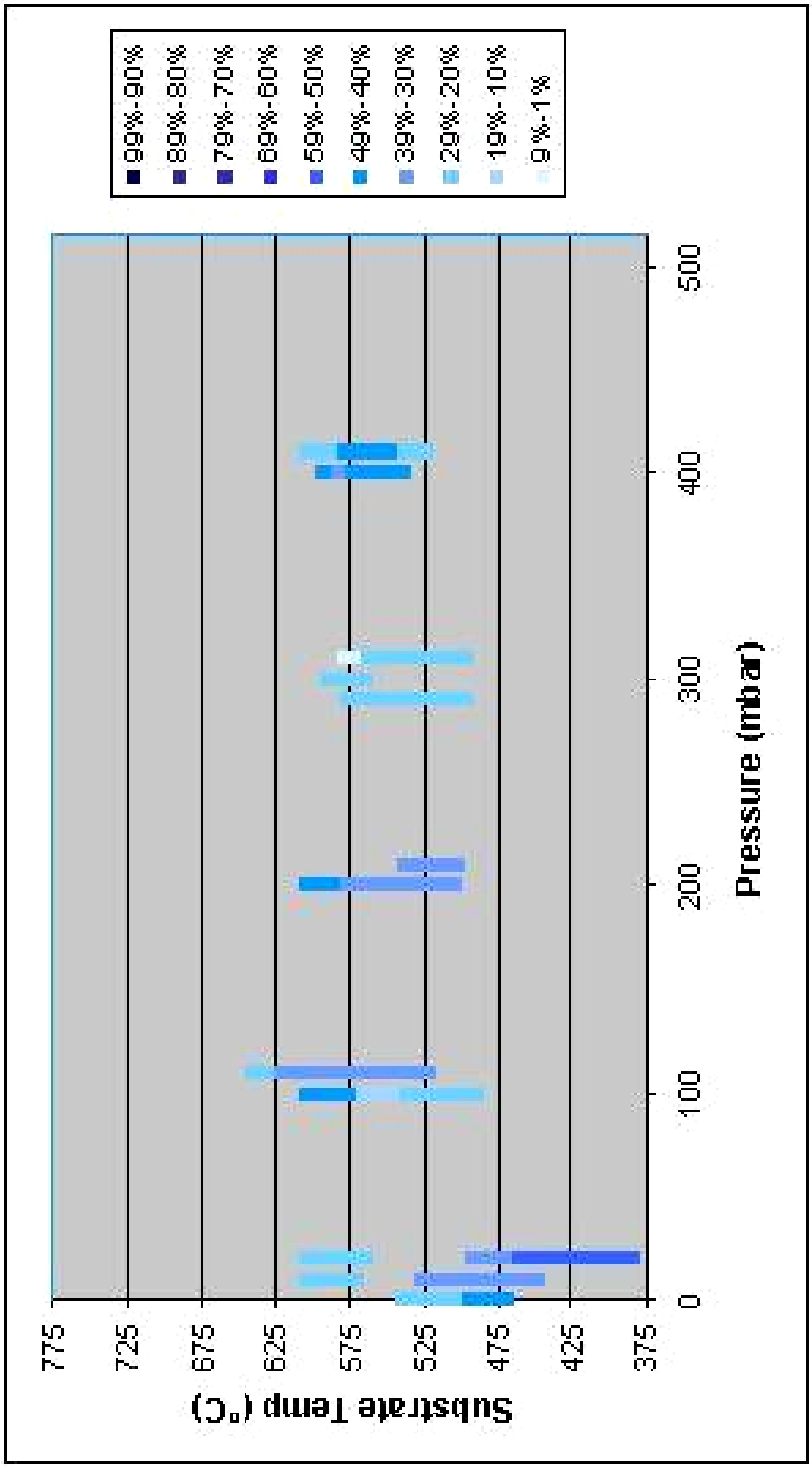

Figure A.5: Graph of nanobelt population for pressure experiments with a source temperature of 630°C

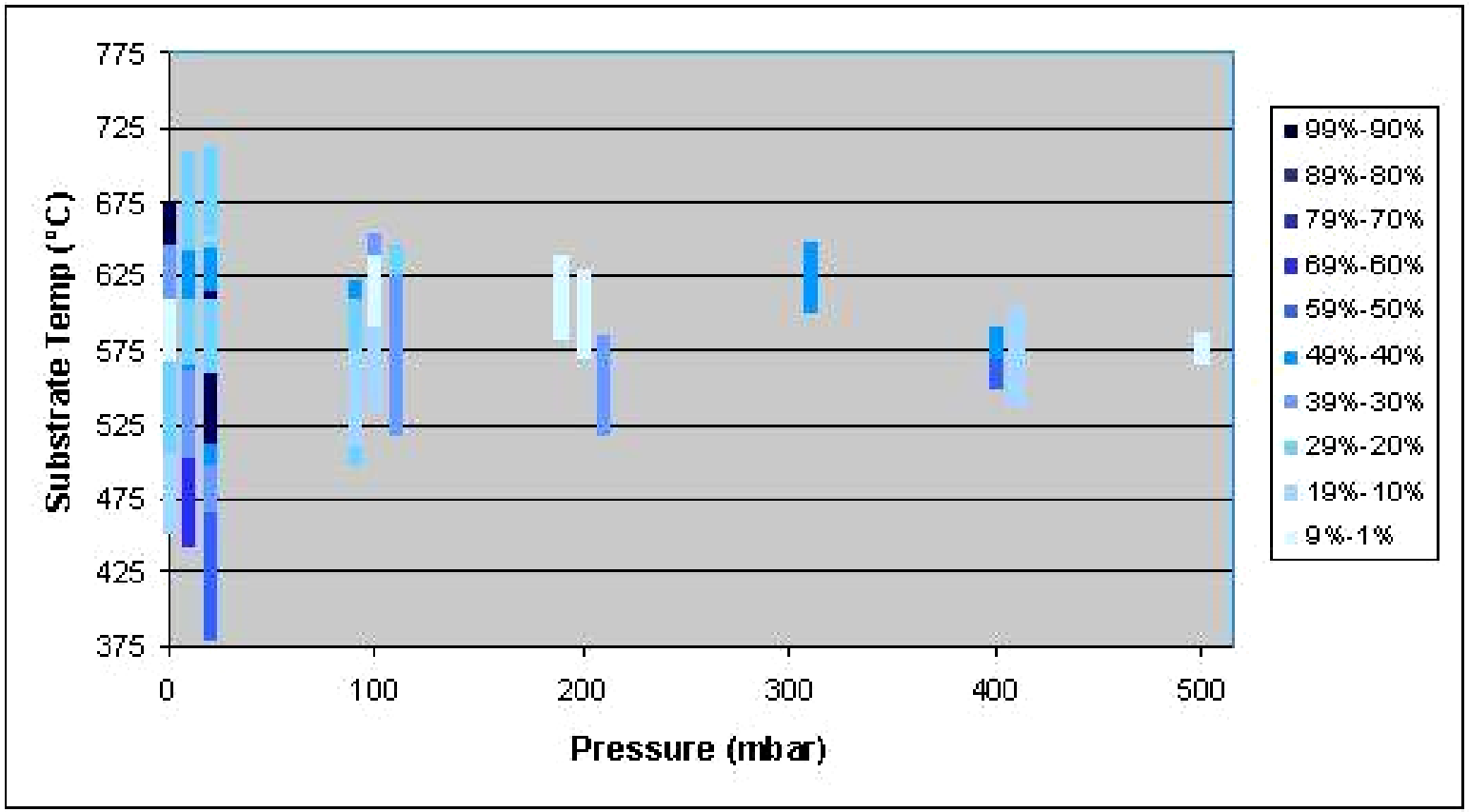

Figure A.6: Graph of nanobelt population for pressure experiments with a source temperature of 700˚C

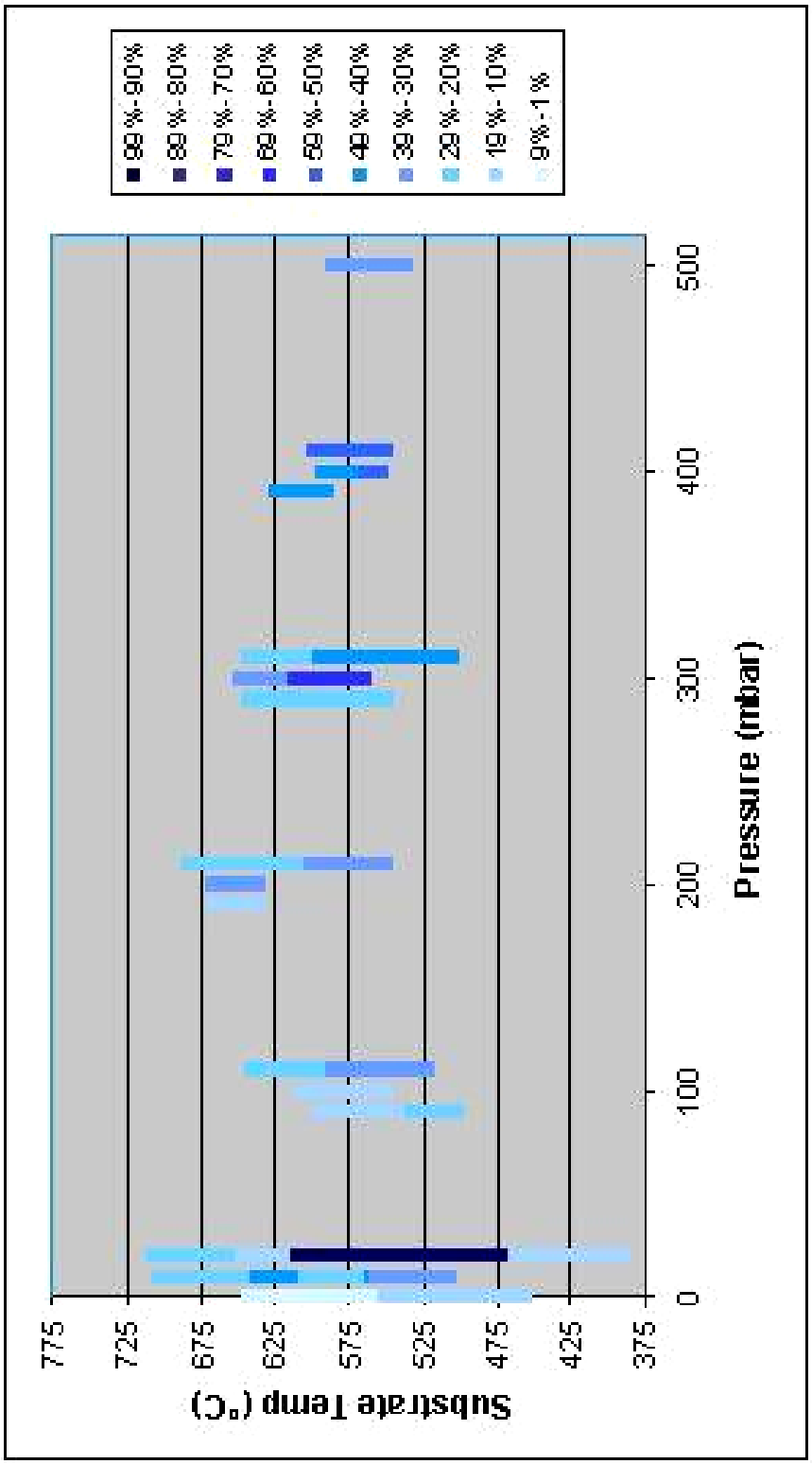

Figure A.7: Graph of nanobelt population for pressure experiments with a source temperature of 750°C

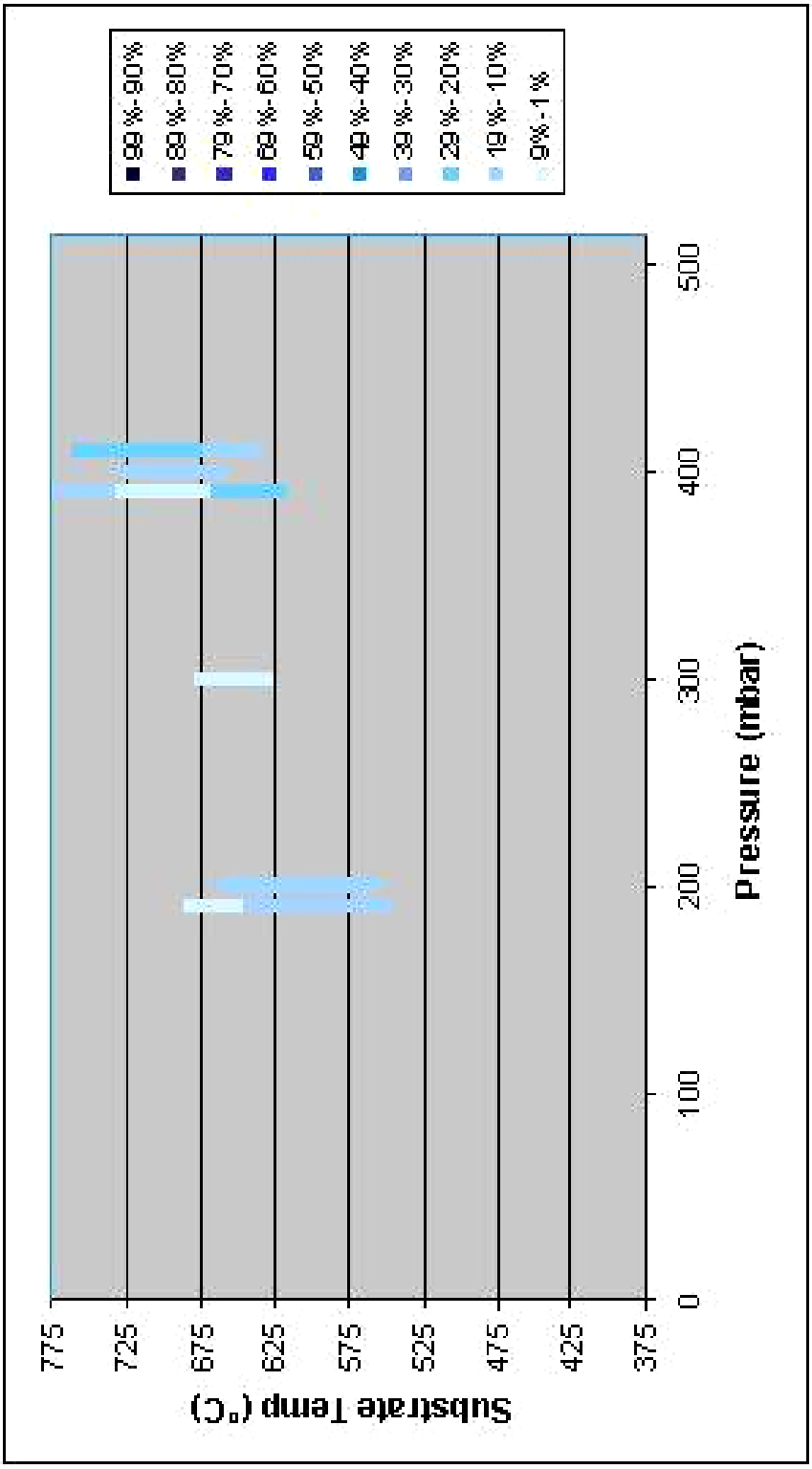

Figure A.8: Graph of nanobelt population for pressure experiments with a source temperature of 800°C

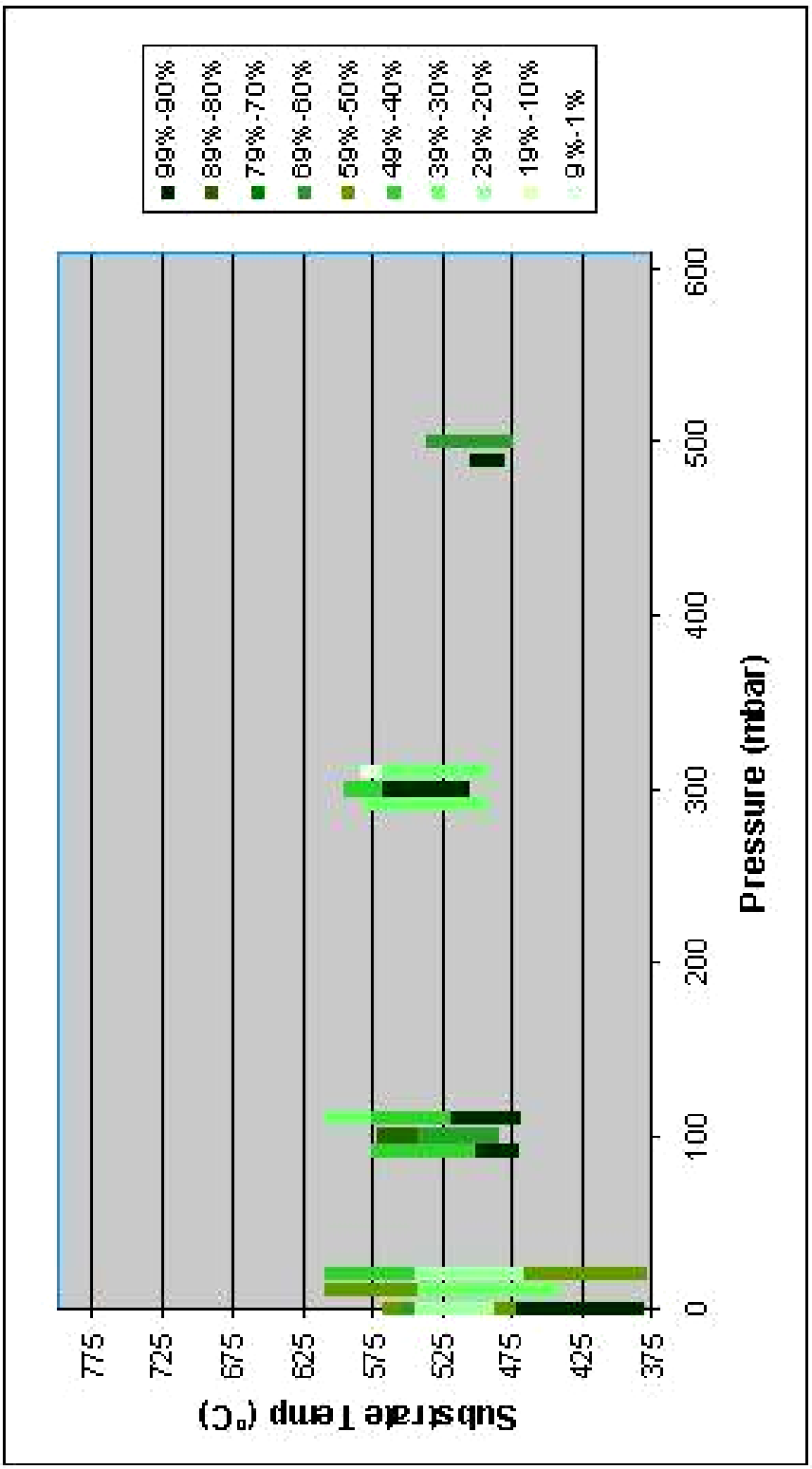

Figure A.9 Graph of nanowire population for pressure experiments with a source temperature of 630°C

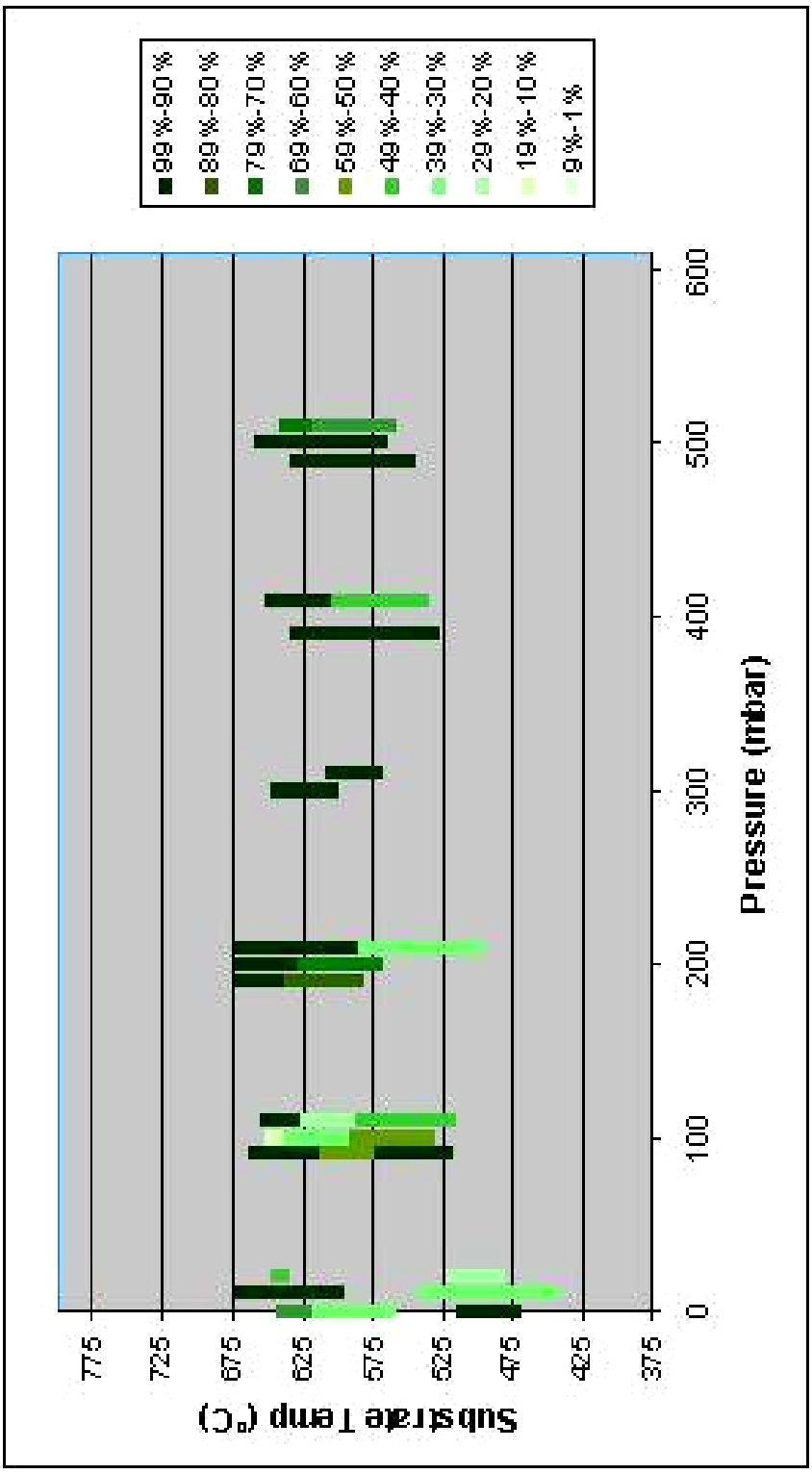

Figure A.10: Graph of nanowire population for pressure experiments with a source temperature of 700°C

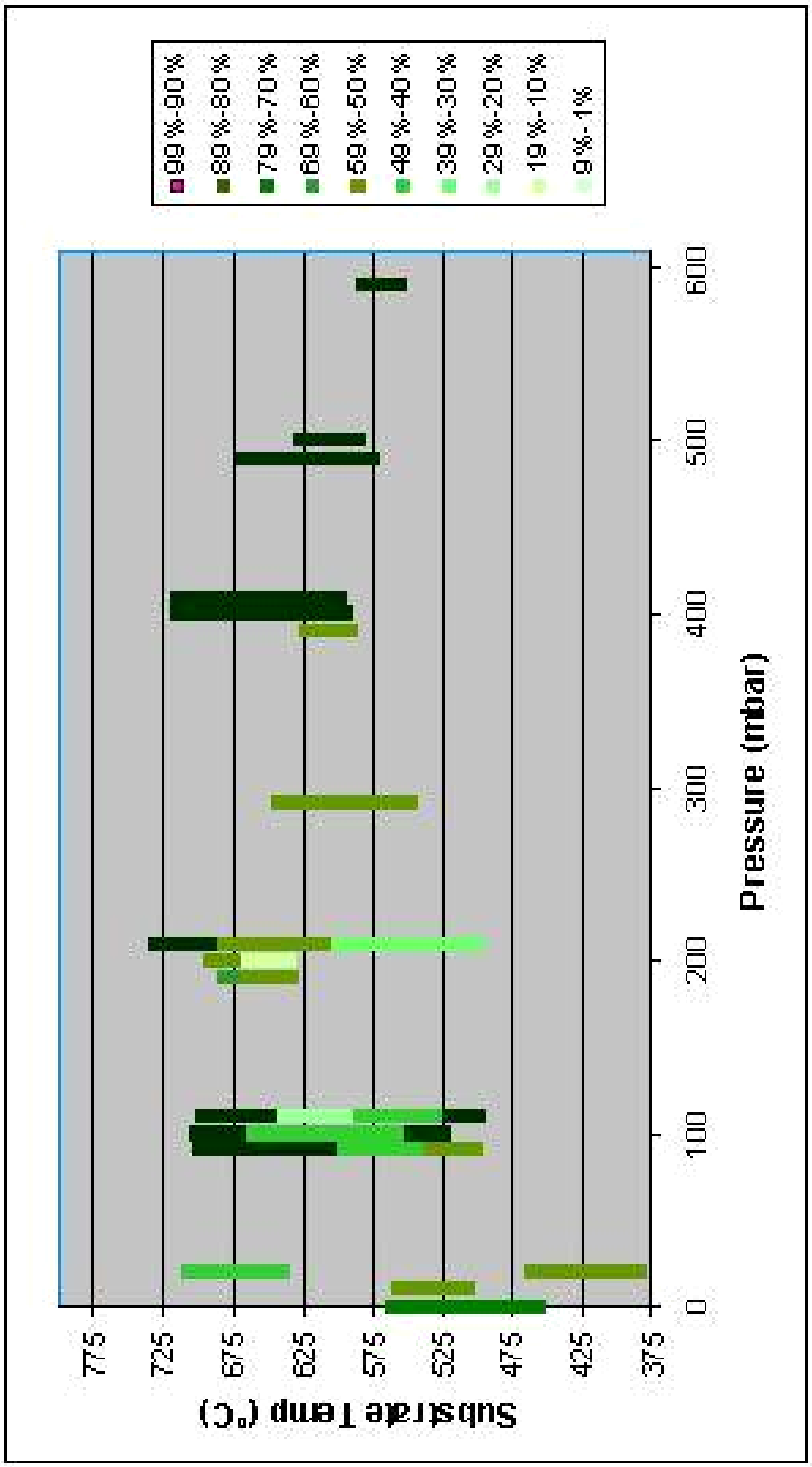

Figure A.11: Graph of nanowire population for pressure experiments with a source temperature of 750°C

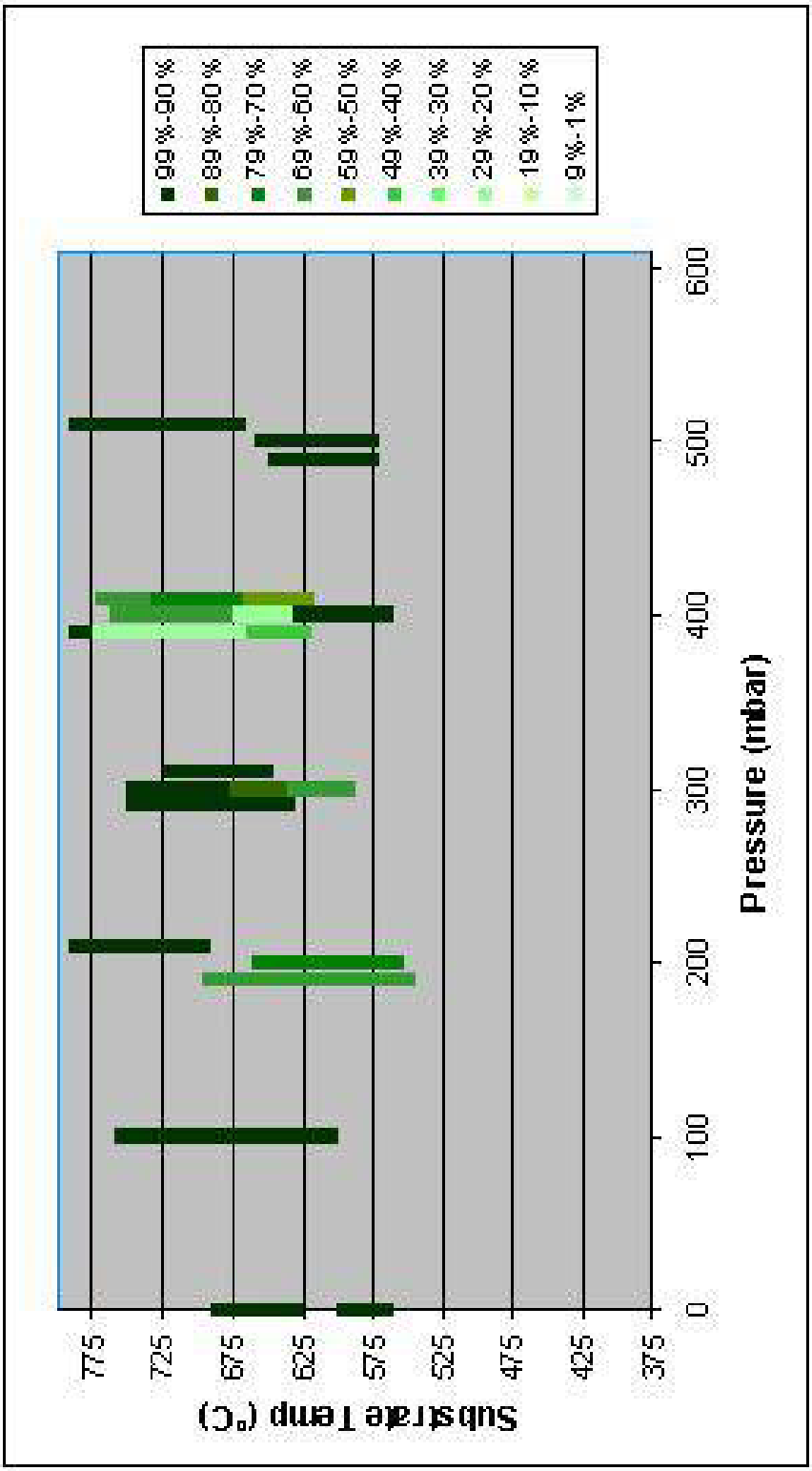

Figure A.12: Graph of nanowire population for pressure experiments with a source temperature of 800°C

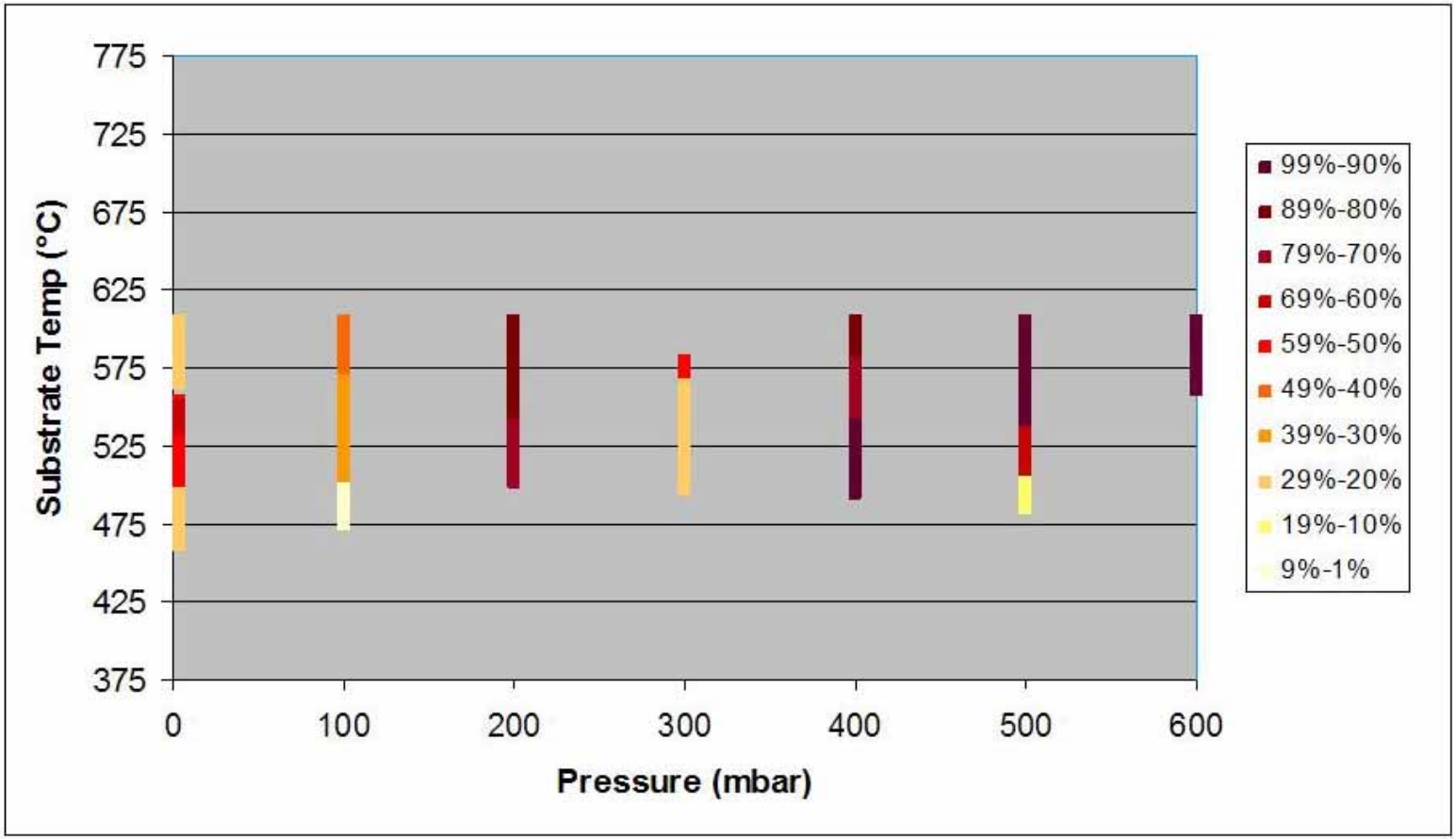

Figure A.13: Graph of average nanosaw population for pressure experiments with a source temperature of 630°C.

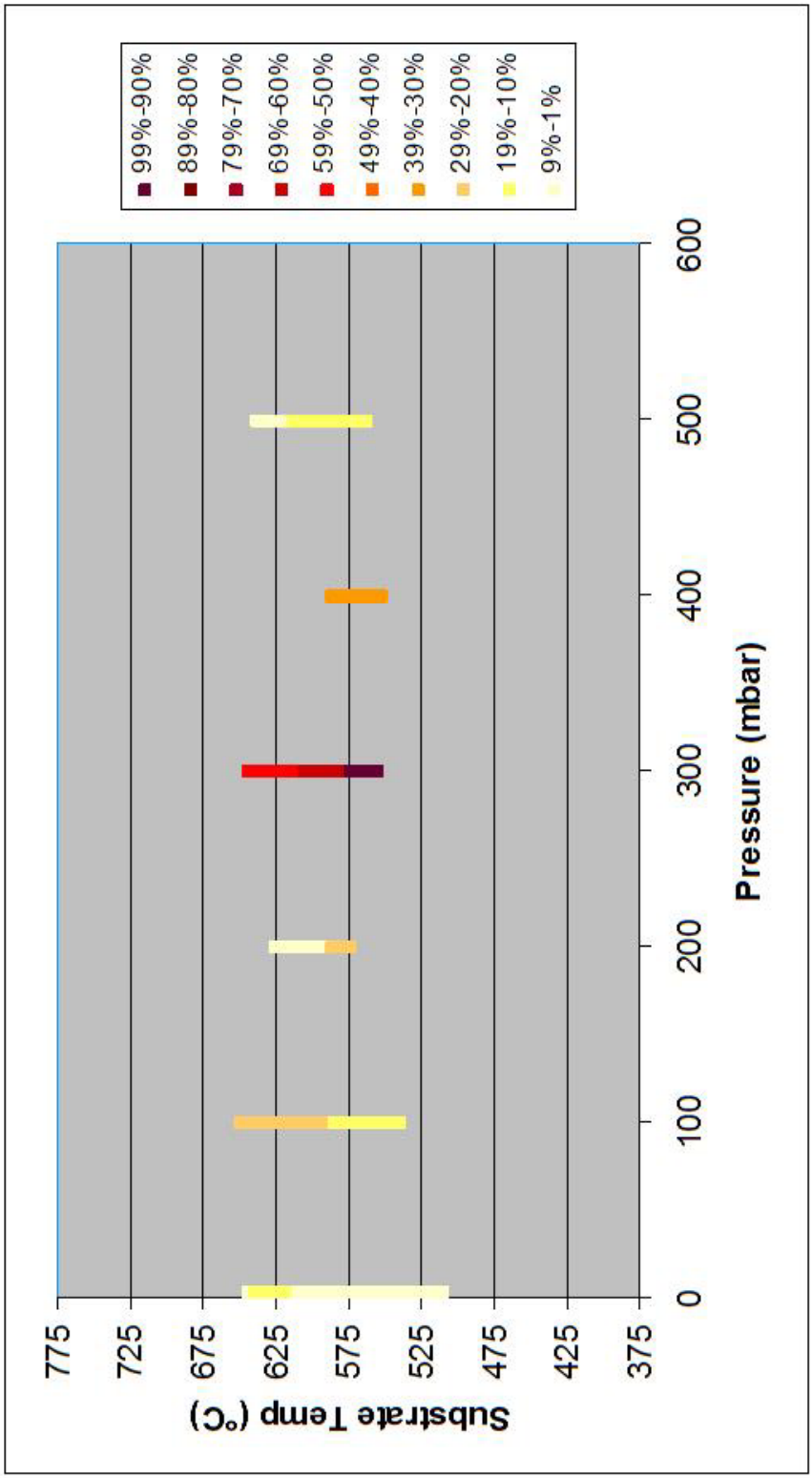

Figure A.14: Graph of average nanosaw population for pressure experiments with a source temperature of 700°C.

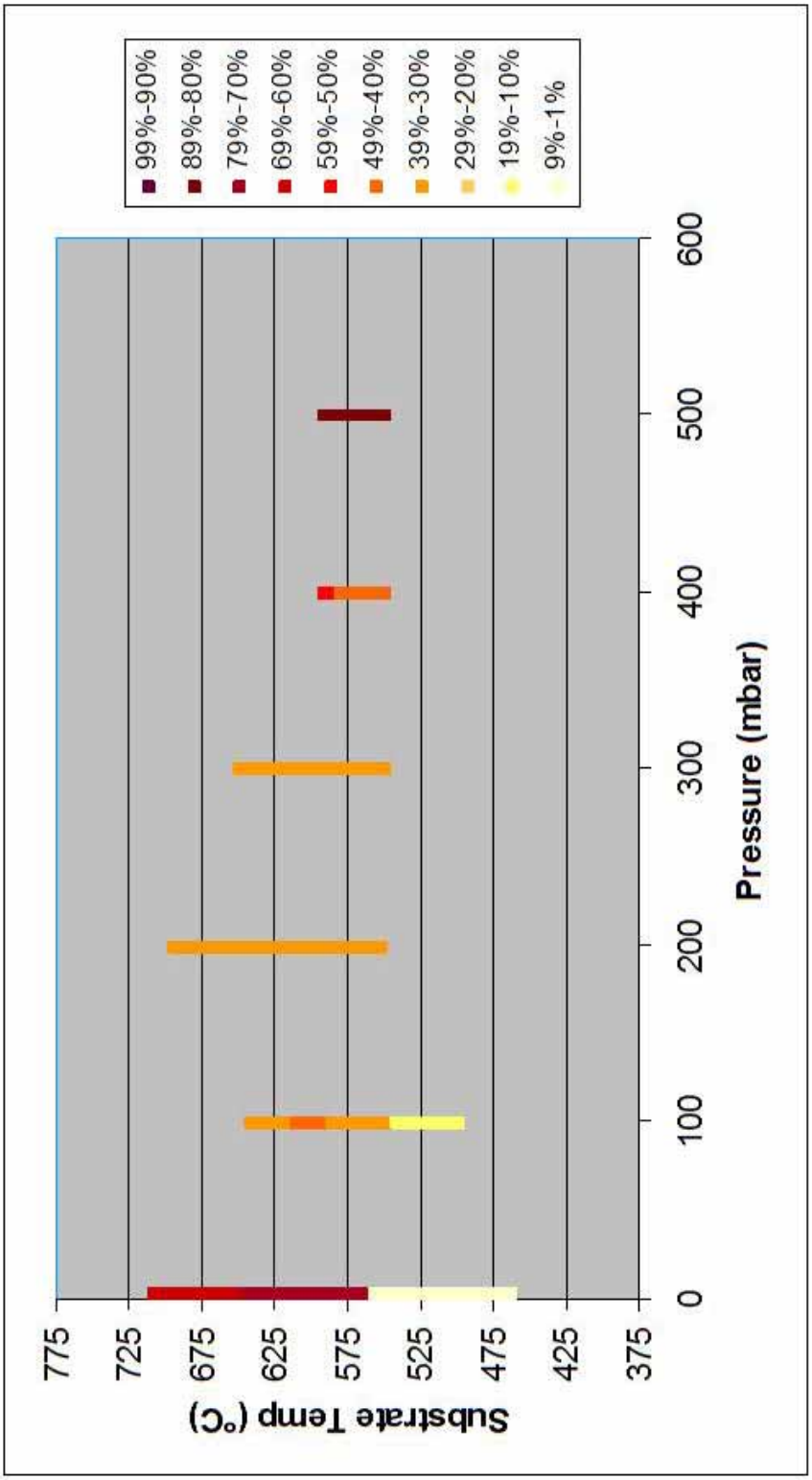

Figure A.15: Graph of average nanosaw population for pressure experiments with a source temperature of 750°C.

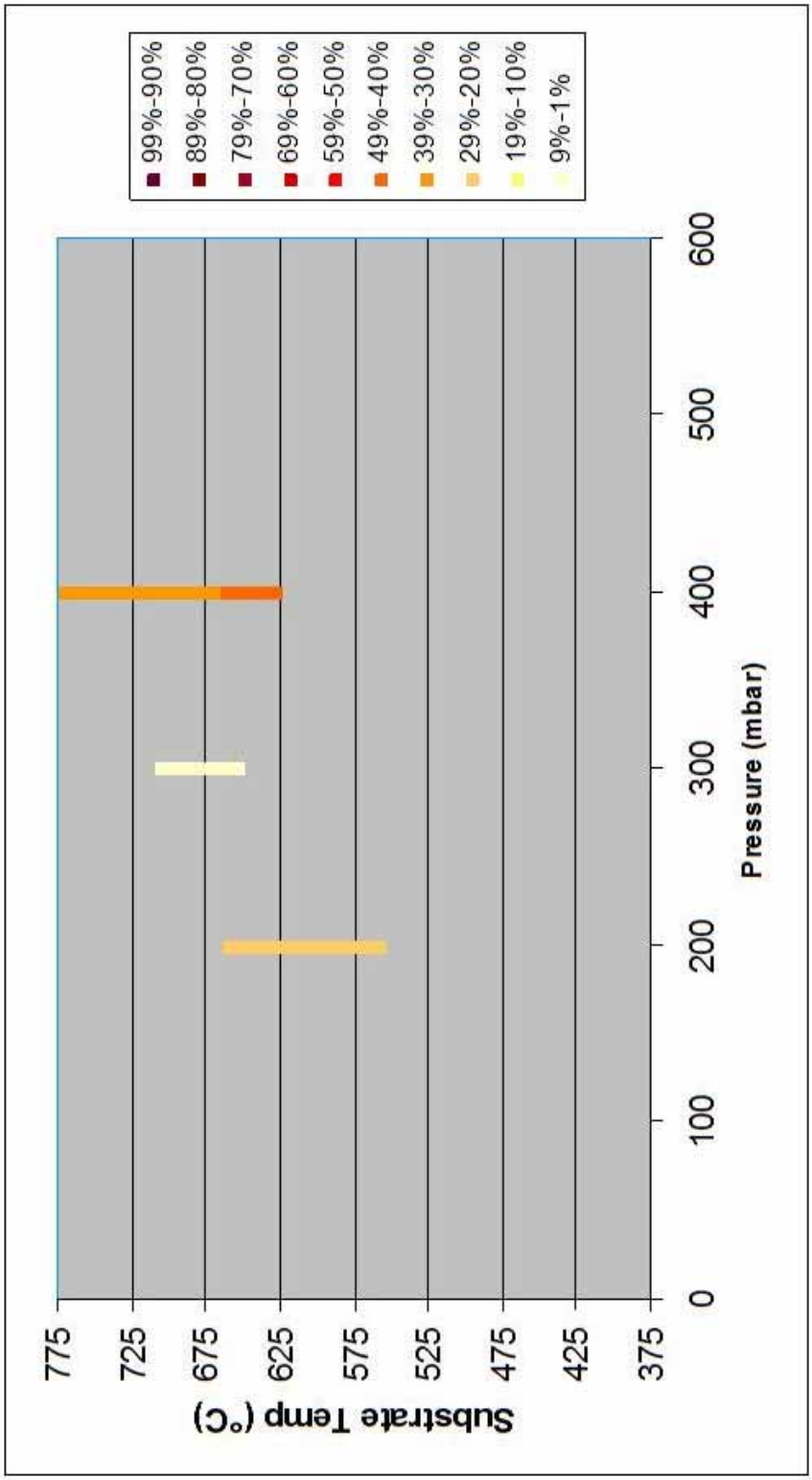

Figure A.16: Graph of average nanosaw population for pressure experiments with a source temperature of 800°C.

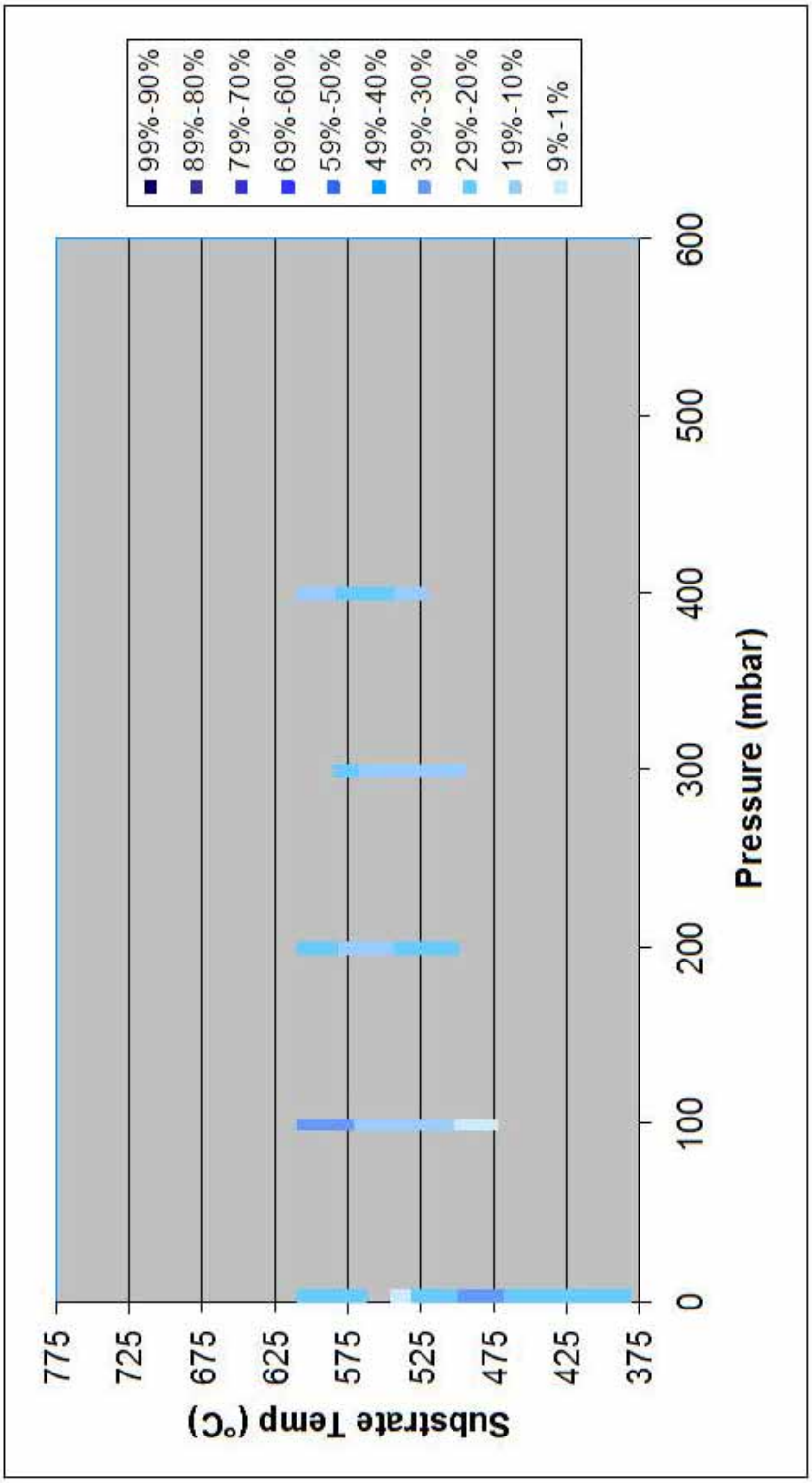

Figure A.17: Graph of average nanobelt population for pressure experiments with a source temperature of 630°C.

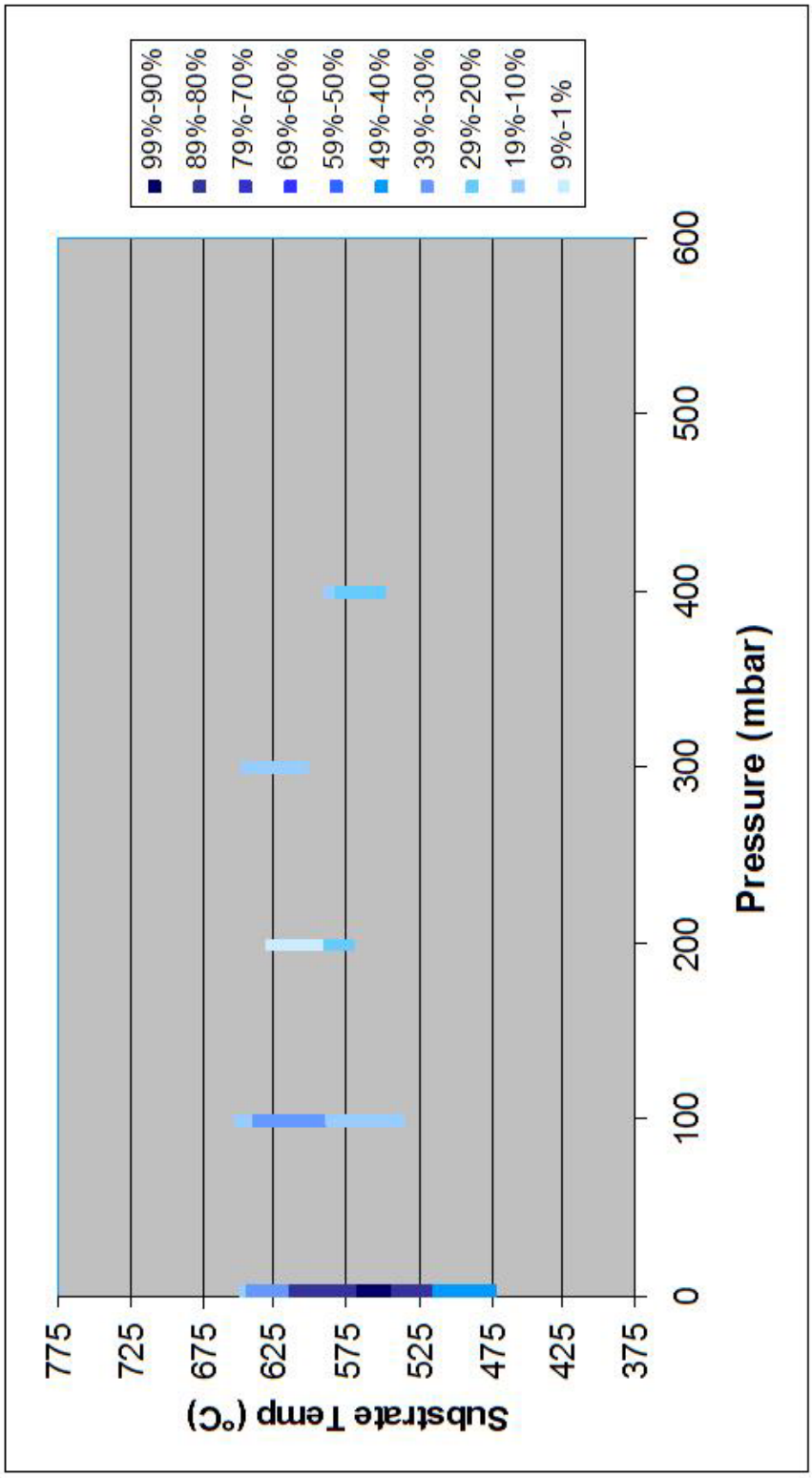

Figure A.18: Graph of average nanobelt population for pressure experiments with a source temperature of 700°C.

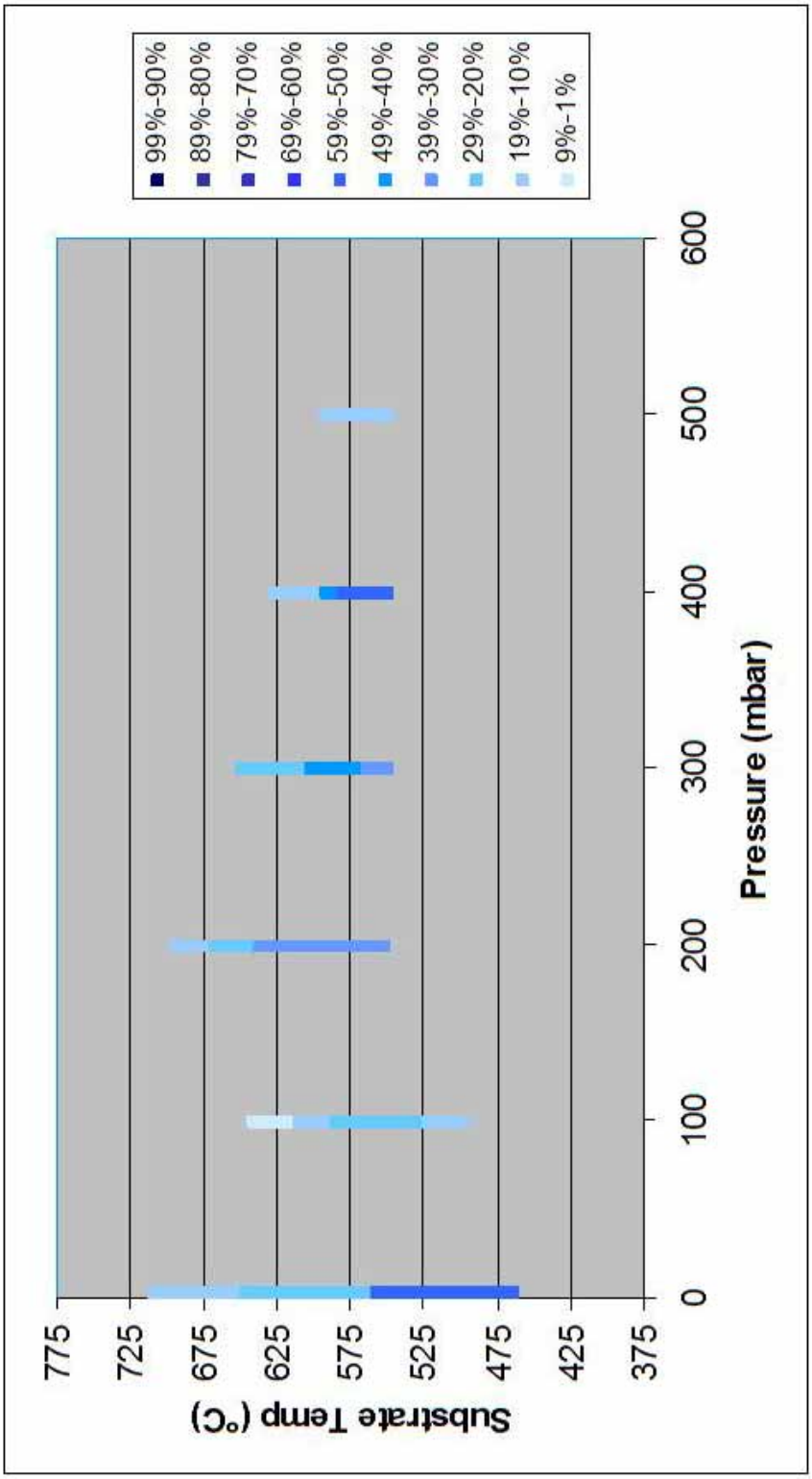

Figure A.19: Graph of average nanobelt population for pressure experiments with a source temperature of 750°C

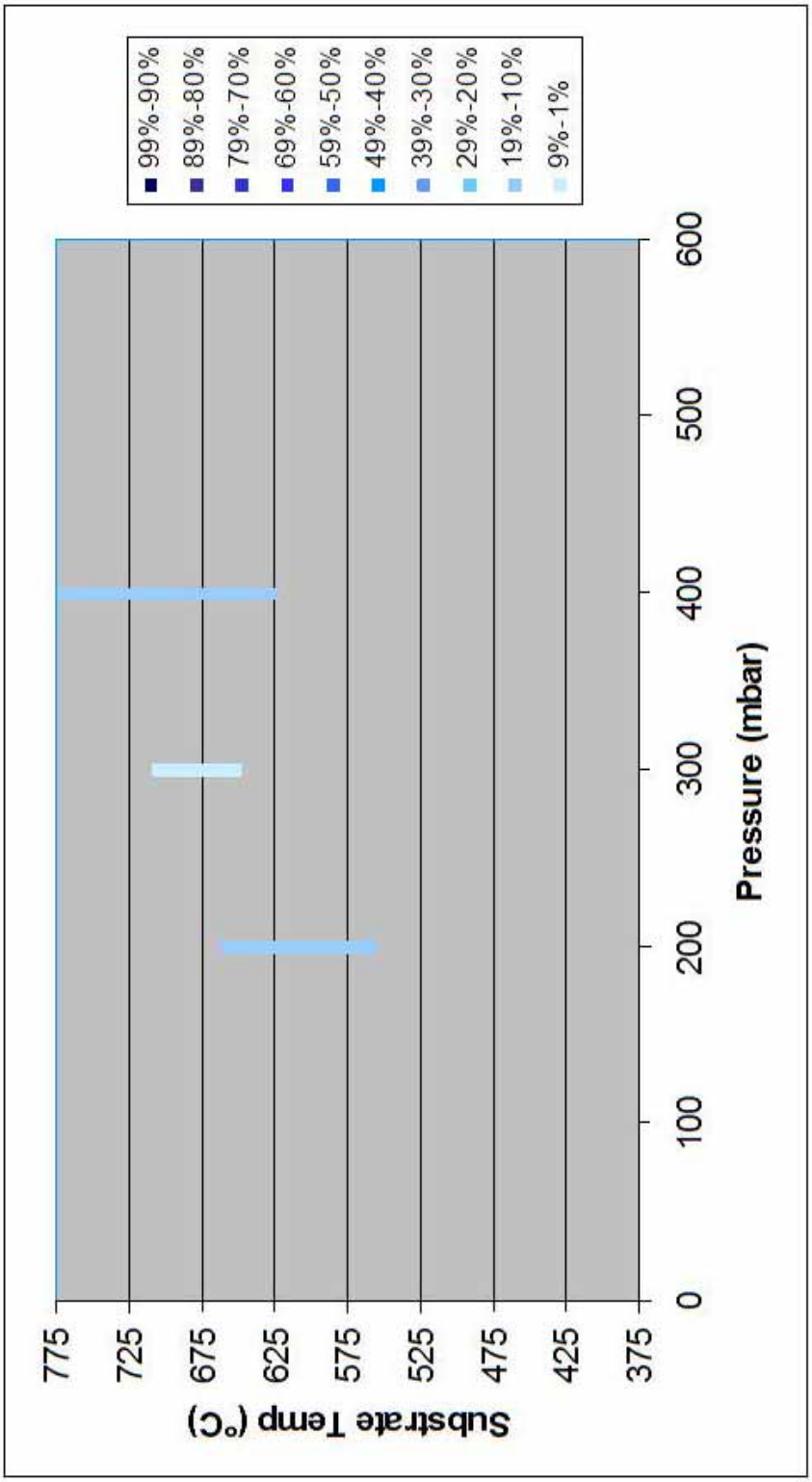

Figure A.20: Graph of average nanobelt population for pressure experiments with a source temperature of 800°C

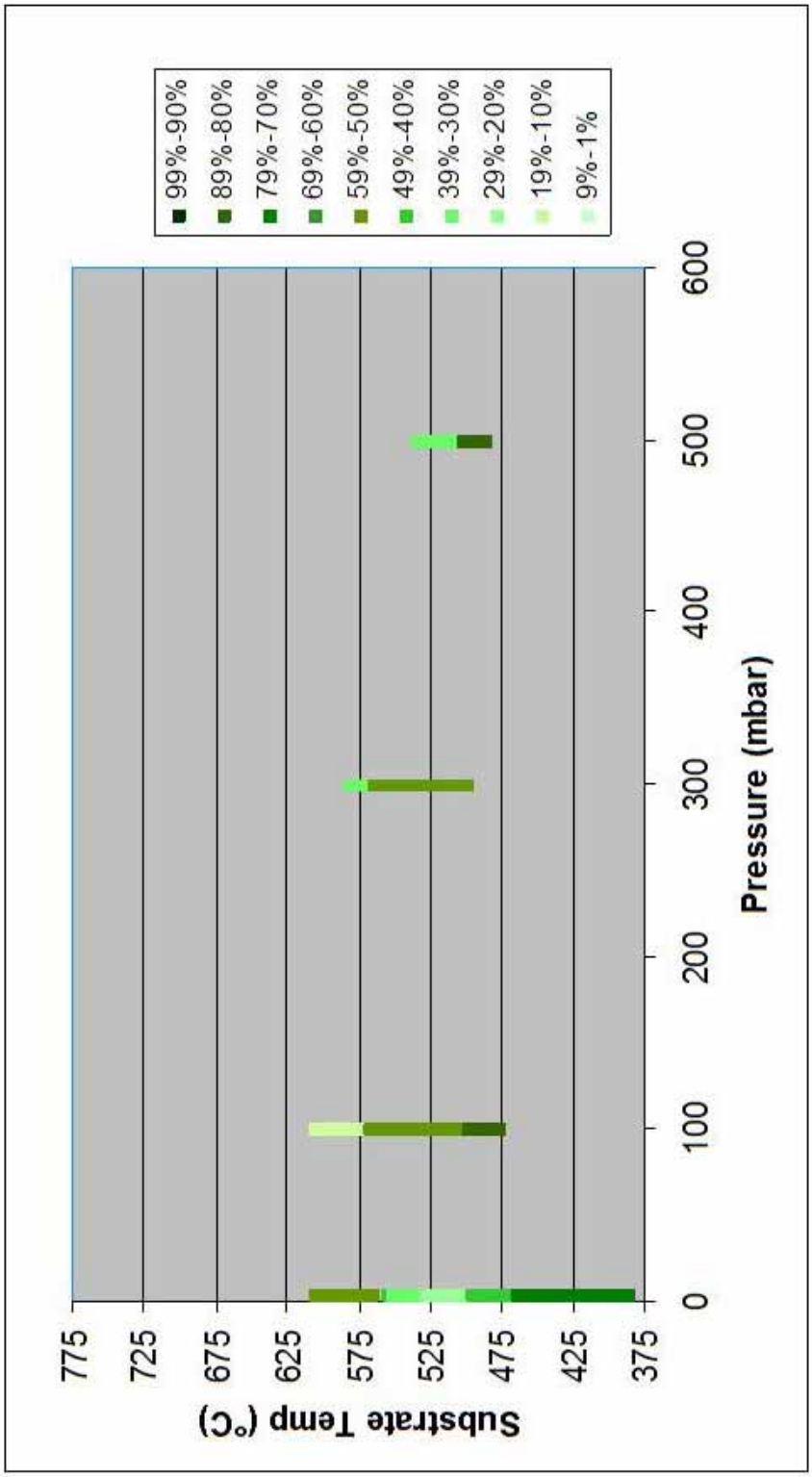

Figure A.21: Graph of average nanowire population for pressure experiments with a source temperature of 630°C

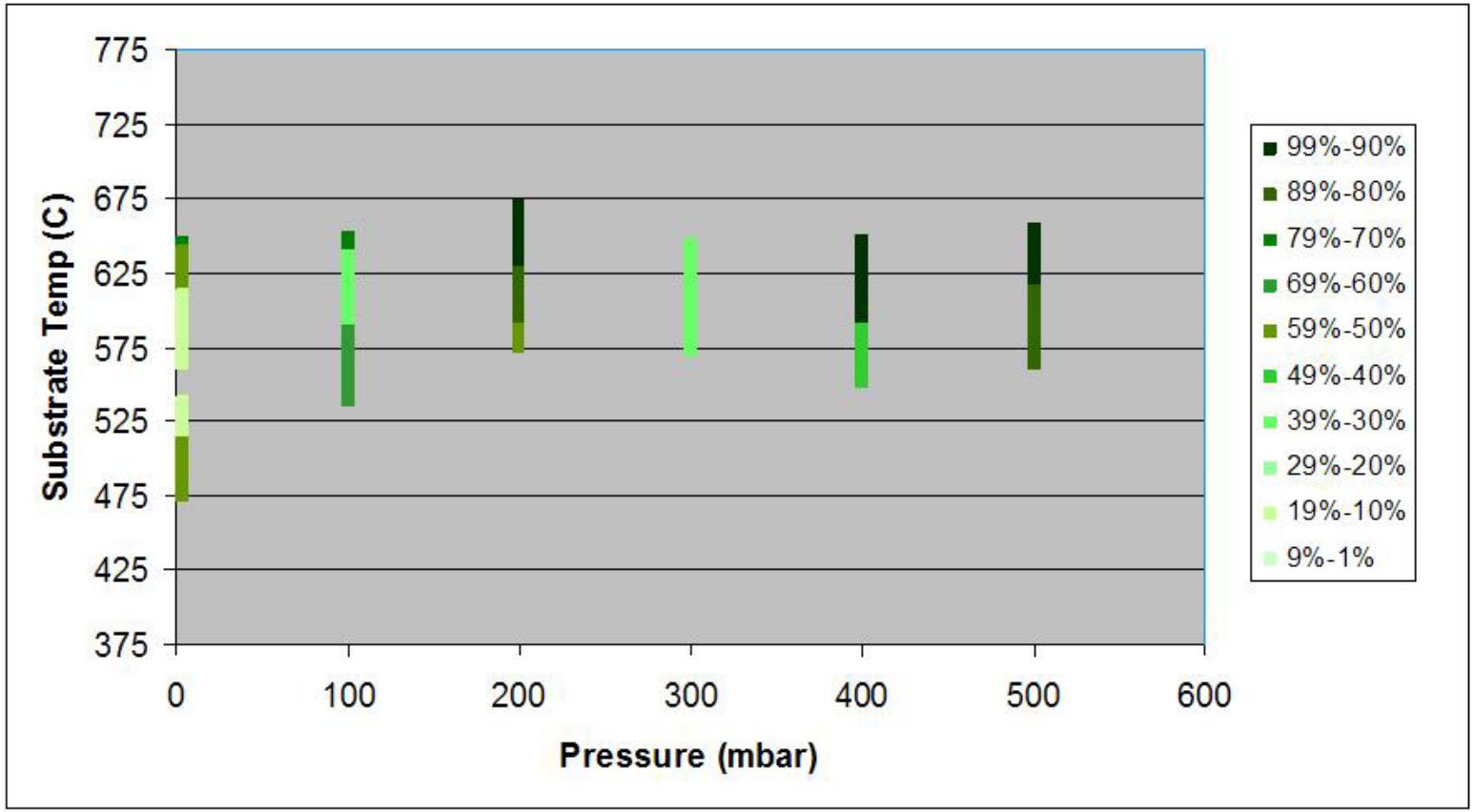

Figure A.22: Graph of average nanowire population for pressure experiments with a source temperature of 700˚C

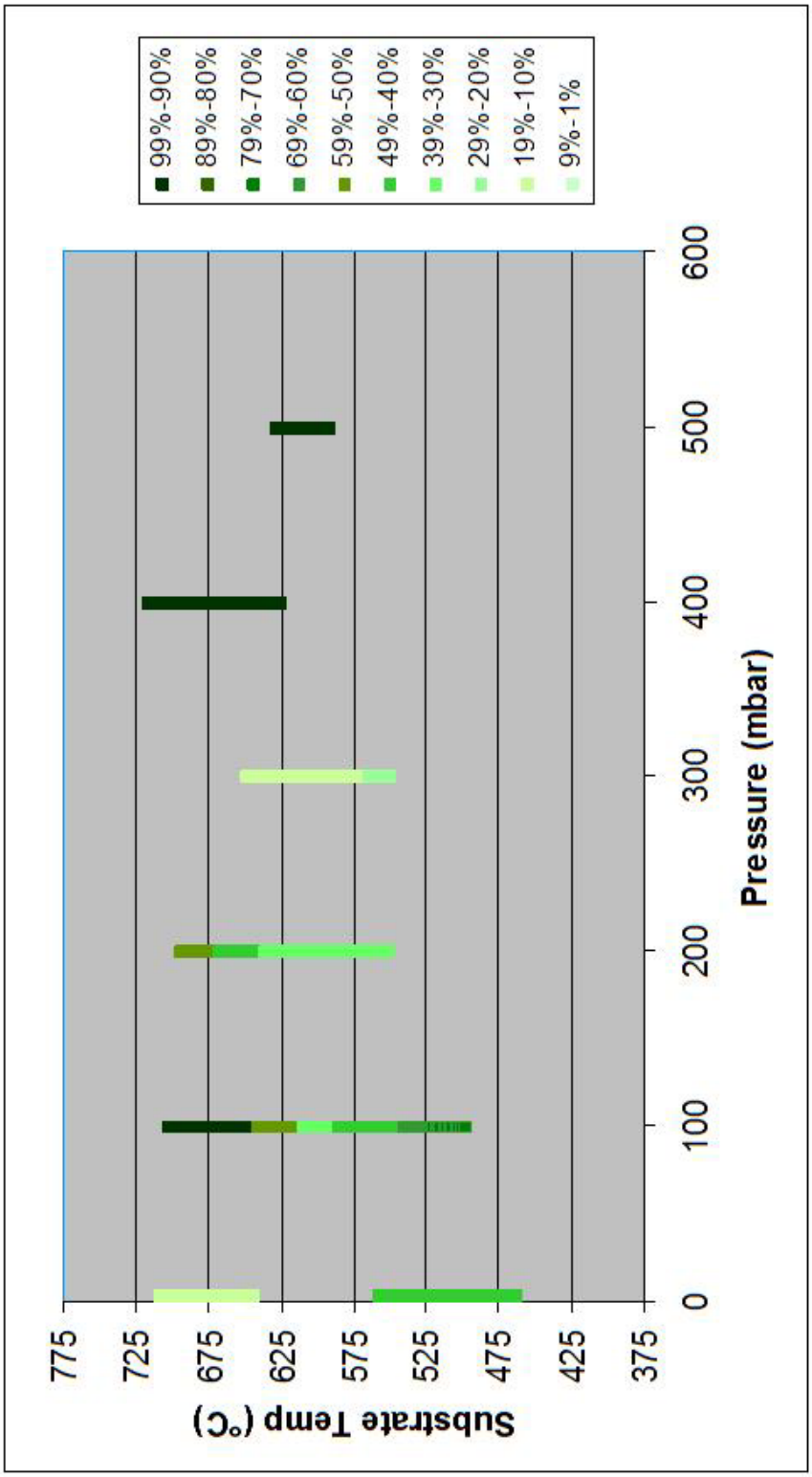

Figure A.23: Graph of average nanowire population for pressure experiments with a source temperature of 750°C

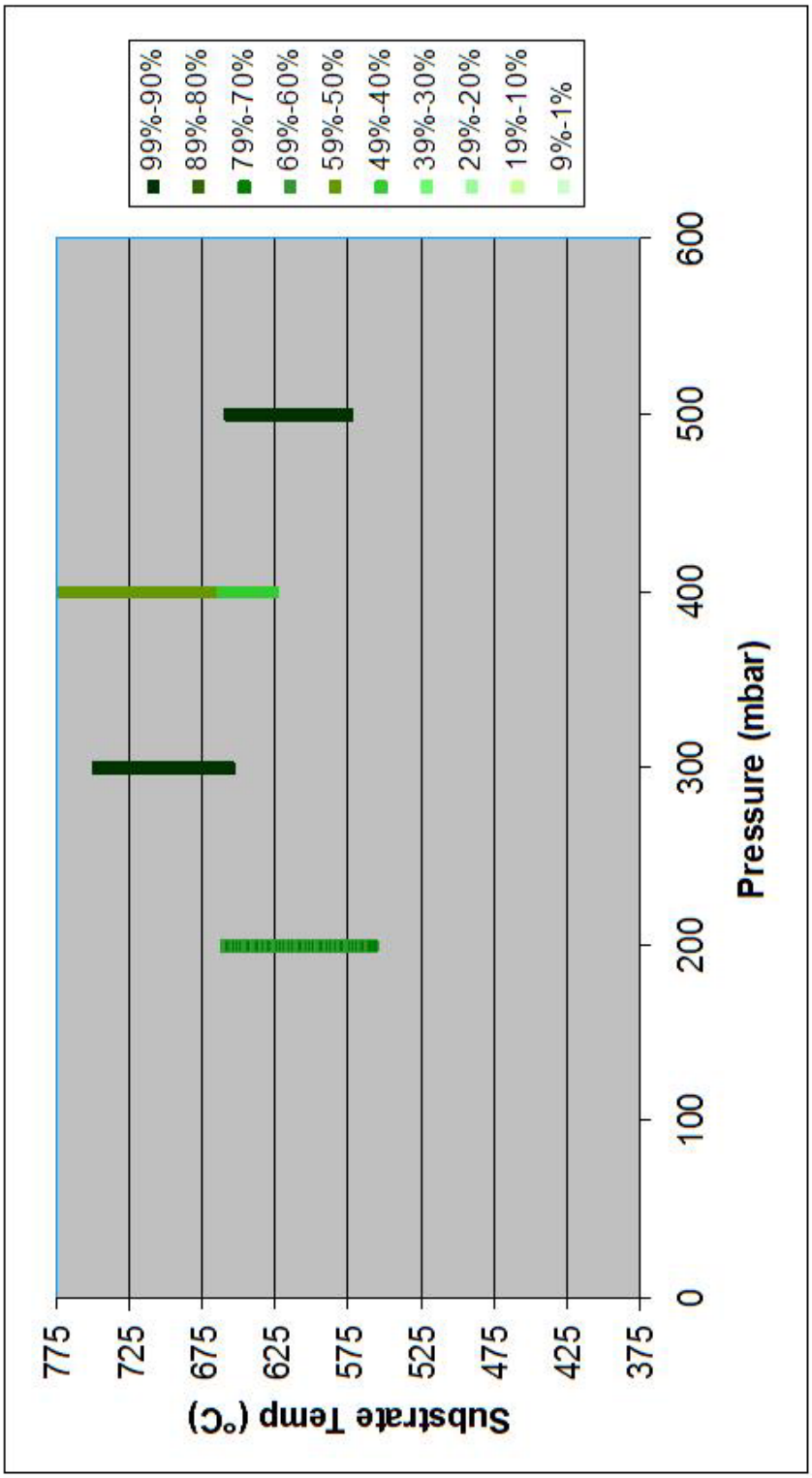

Figure A.24: Graph of average nanowire population for pressure experiments with a source temperature of 800°C

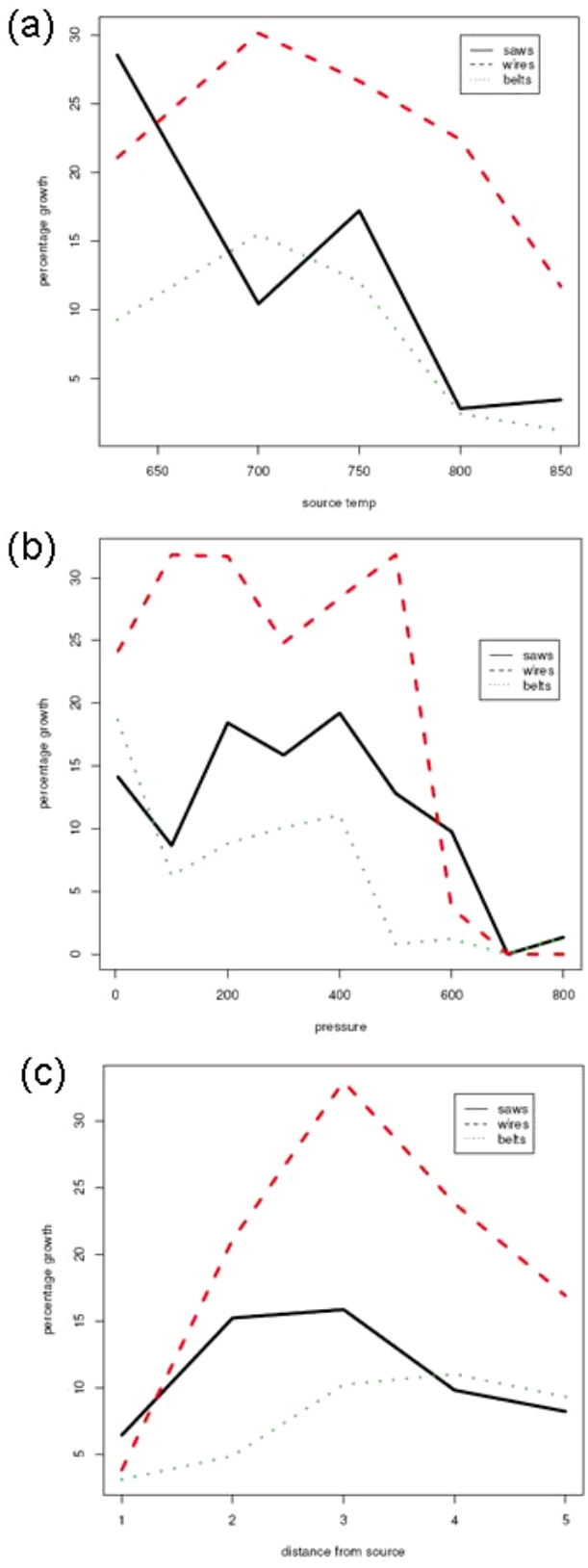

Figure A.25: Observed proportions plotted against (a) T, (b) P, and (c) D.

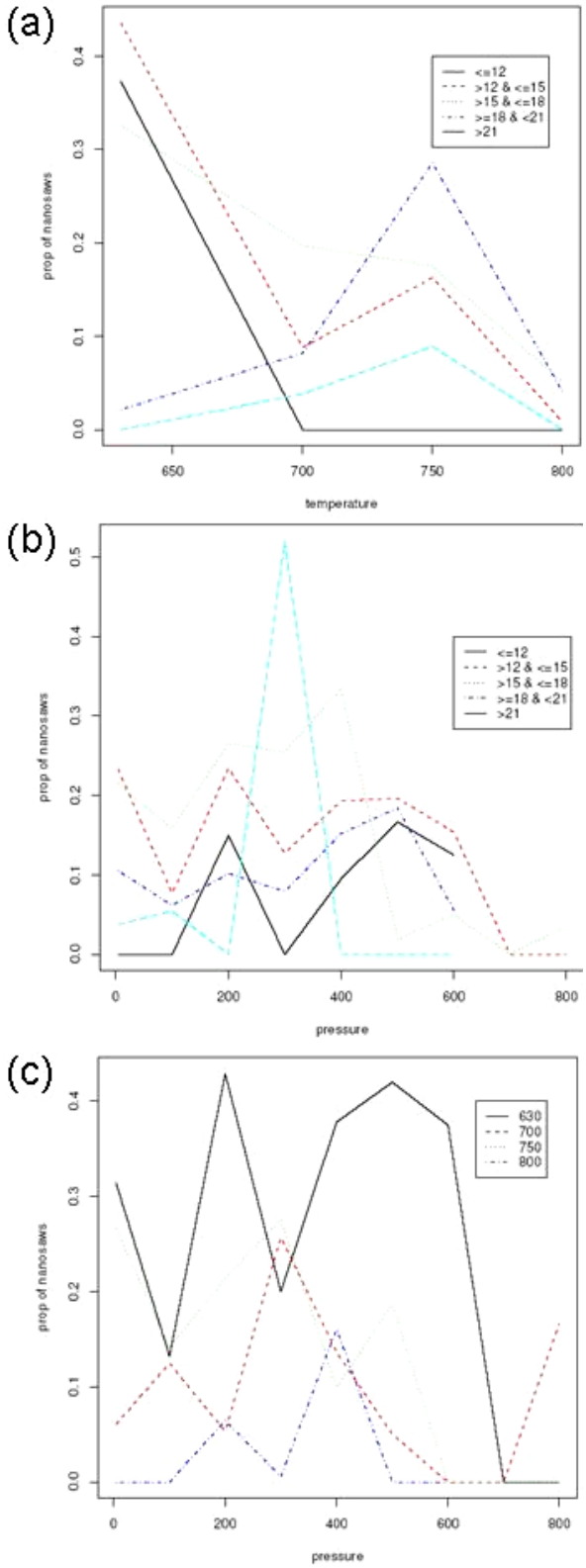

Figure A.26: Interaction plots of (a) temperature-distance, (b) pressure-distance and (c) temperature-pressure for the CdSe nanosaws.

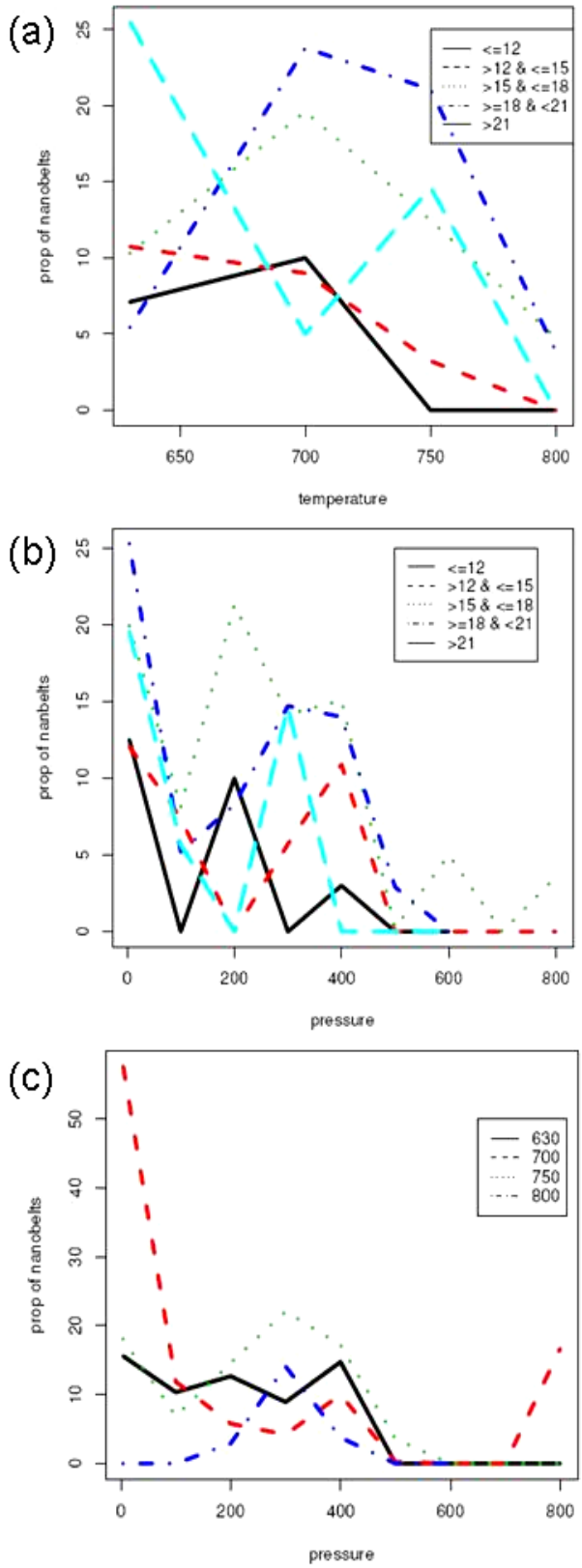

Figure A.27: Interaction plots of (a) temperature-distance, (b) pressure-distance and (c) temperature-pressure for the CdSe nanobelts.

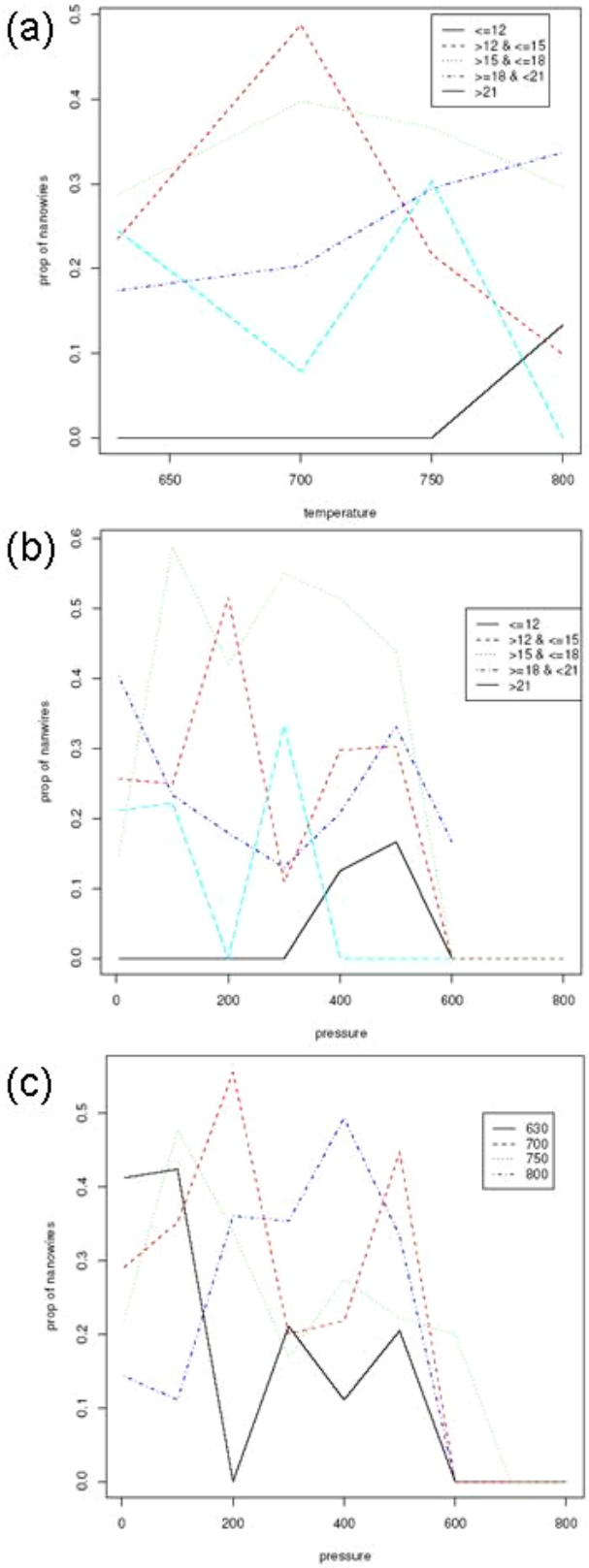

Figure A.28: Interaction plots of (a) temperature-distance, (b) pressure-distance and (c) temperature-pressure for the CdSe nanowires.

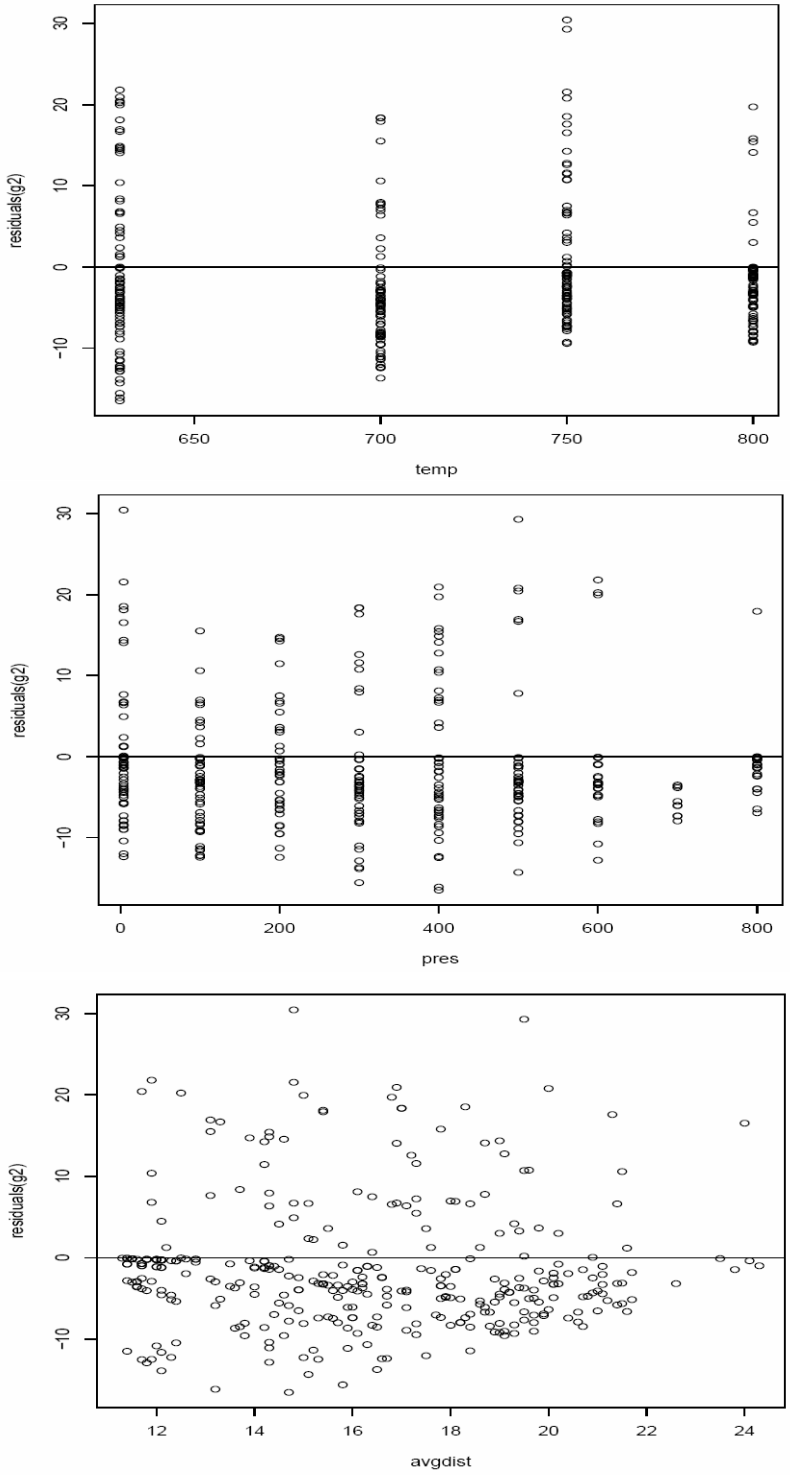

Figure A.29: Residual plots against (a) temperature, (b) pressure, and (c) distance for nanosaws/nanocombs.

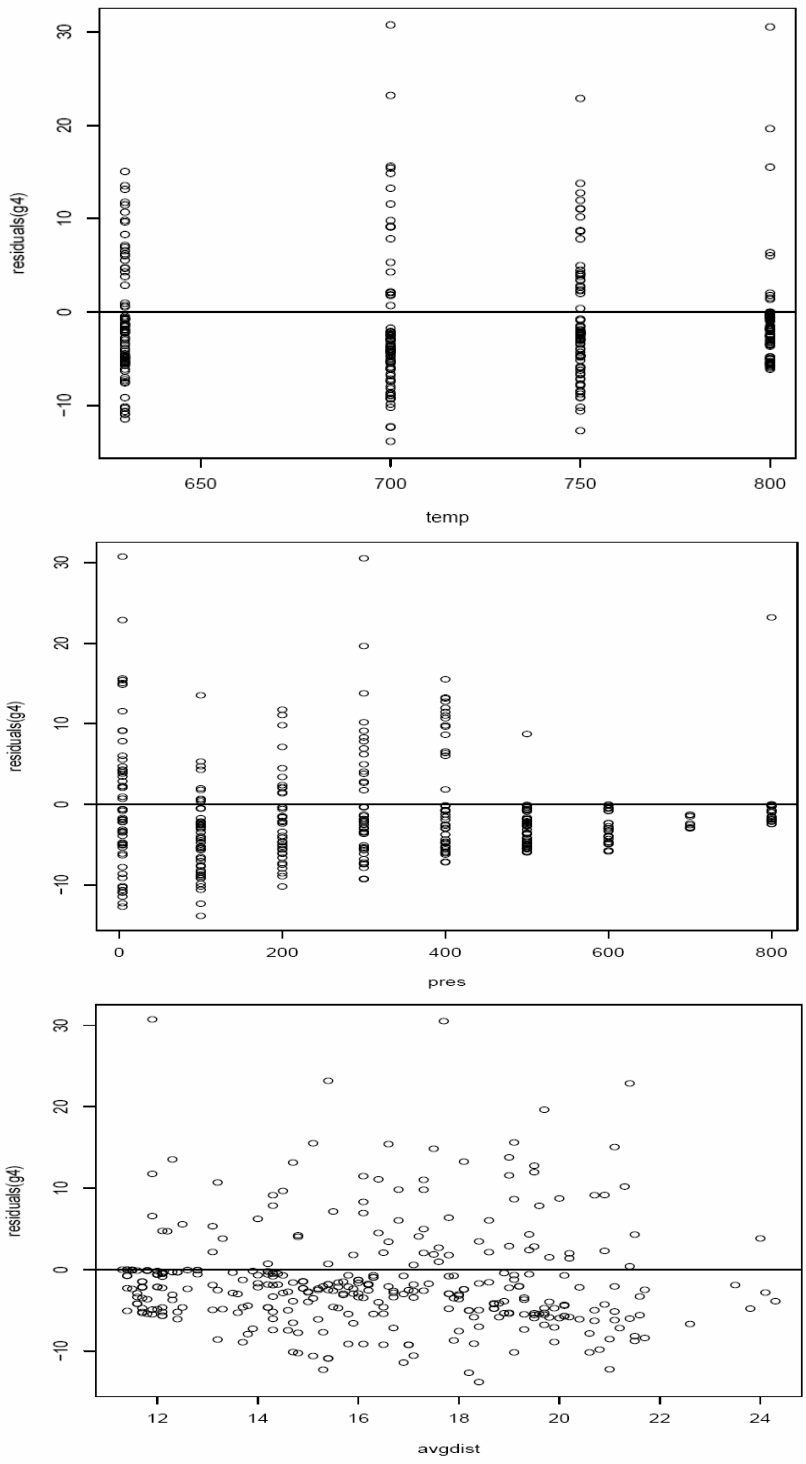

Figure A.30: Residual plots against (a) temperature, (b) pressure, and (c) distance for nanobelts.

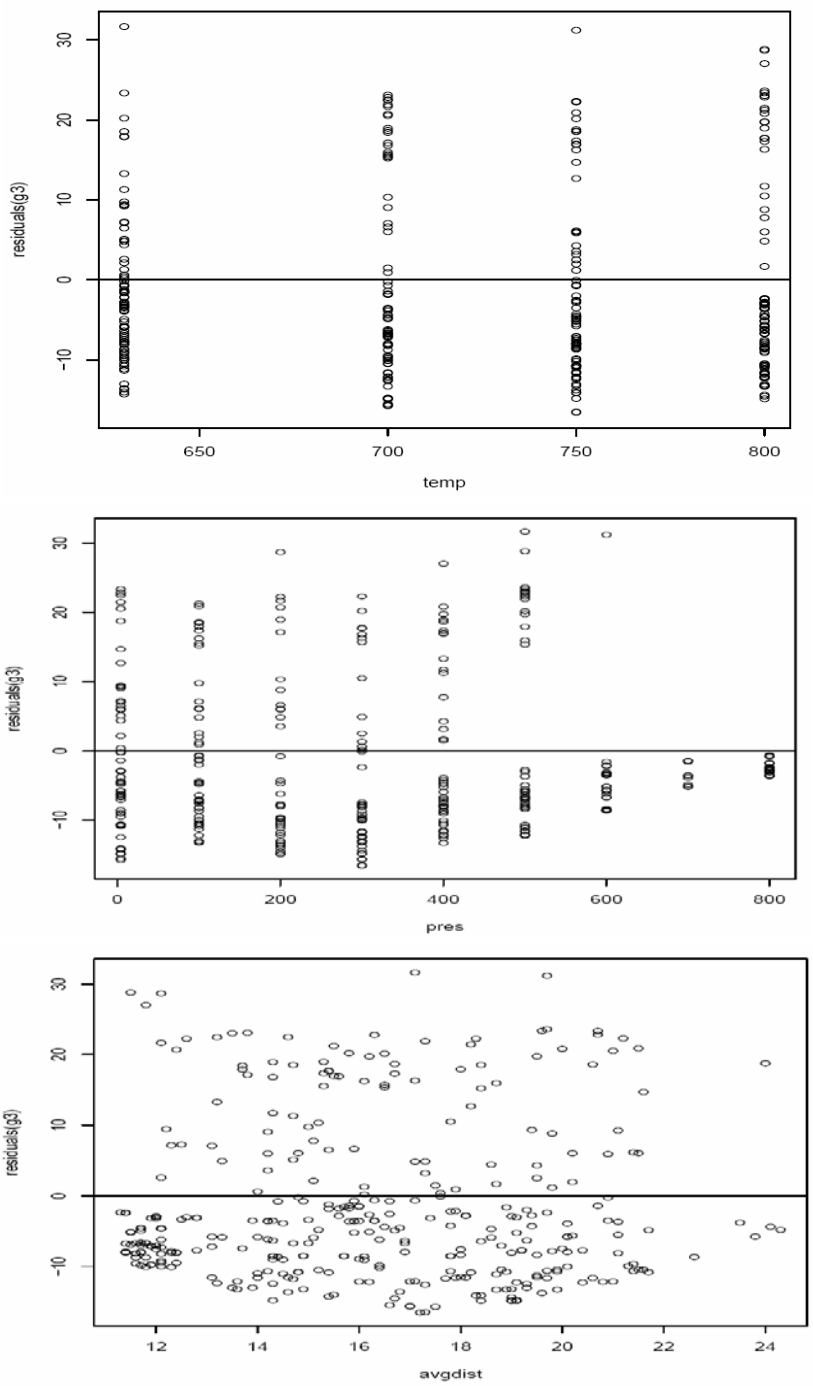

Figure A.31: Residual plots against (a) temperature, (b) pressure, and (c) distance for nanowires.

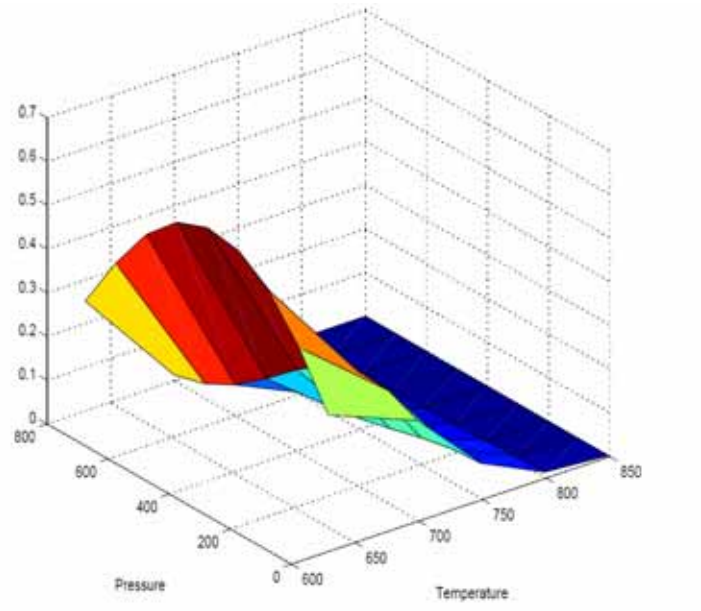

Figure A.32: Predicted proportion of nanosaws/nanocombs at a given distance 17.7cm away from the source.

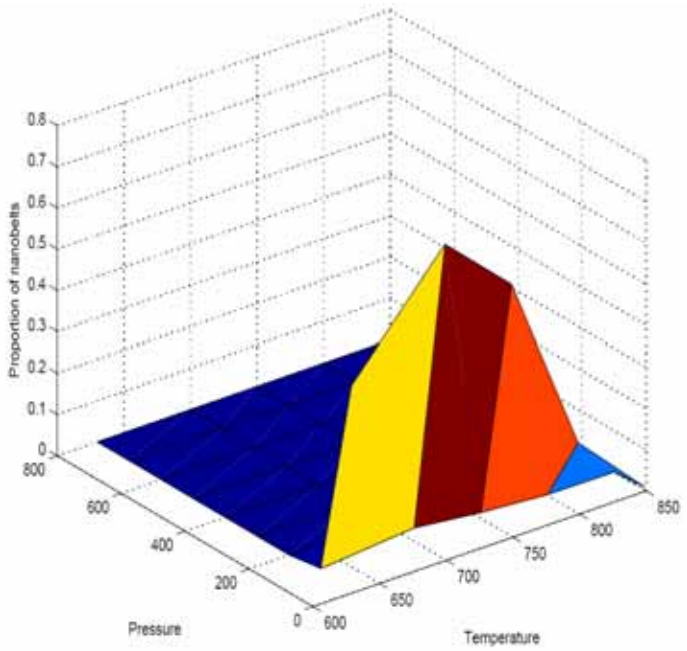

Figure A.33: Predicted proportion of nanobelts at a given distance 13.7cm away from the source.

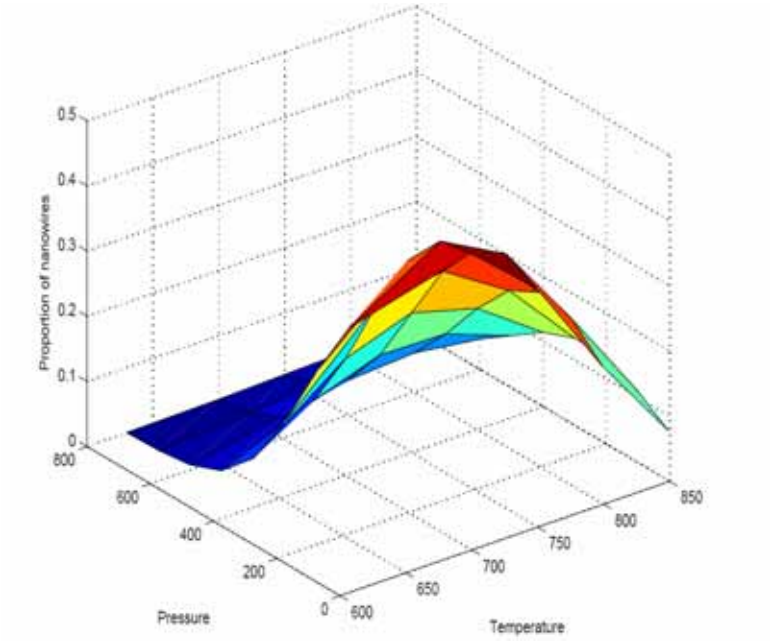

Figure A.34: Predicted proportion of nanowires at a given distance 17.1cm away from the source.

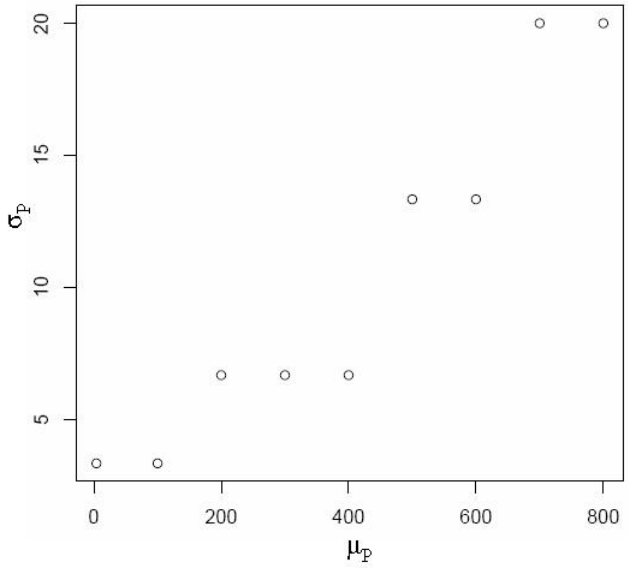

Figure A.35: Plot of μ_P against σ_P.

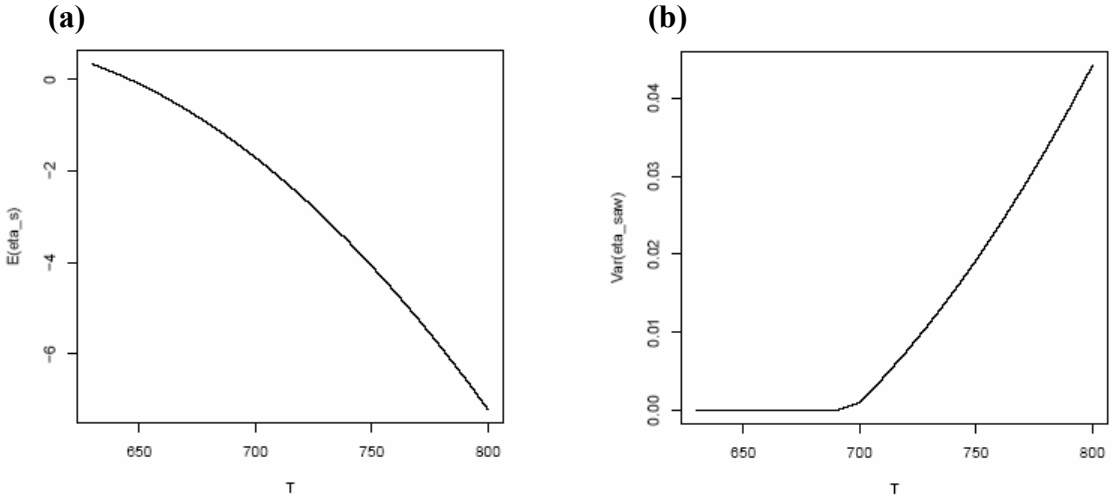

Figure A.36: (a) E(η_s) against temperature at 405mbar and 13.7cm and (b)Var(η_s) against temperature at 405mbar and 13.7cm.

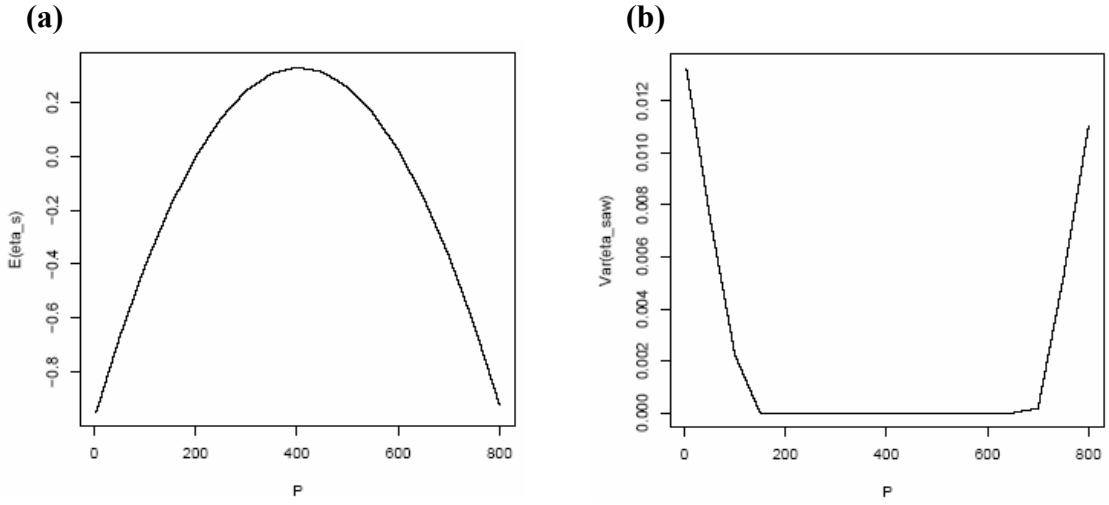

Figure A.37: (a) E(η_s) against pressure at 630˚C and 13.7cm and (b) Var(η_s) against pressure at 630˚C and 13.7cm.

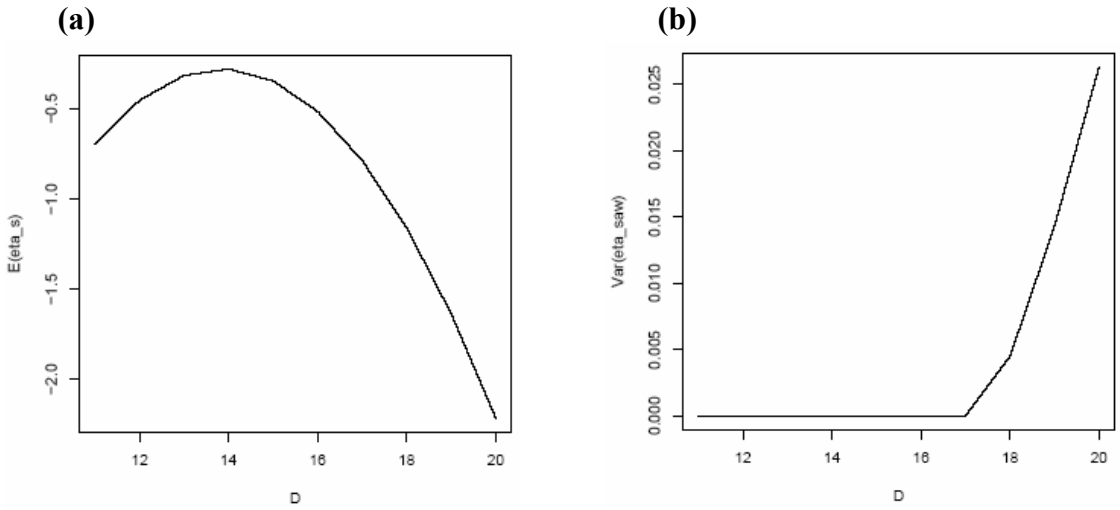

Figure A.38: (a) E(η_s) against distance at 630˚C and 405mbar and (b)Var(η_s) against distance at 630˚C and 405mbar.

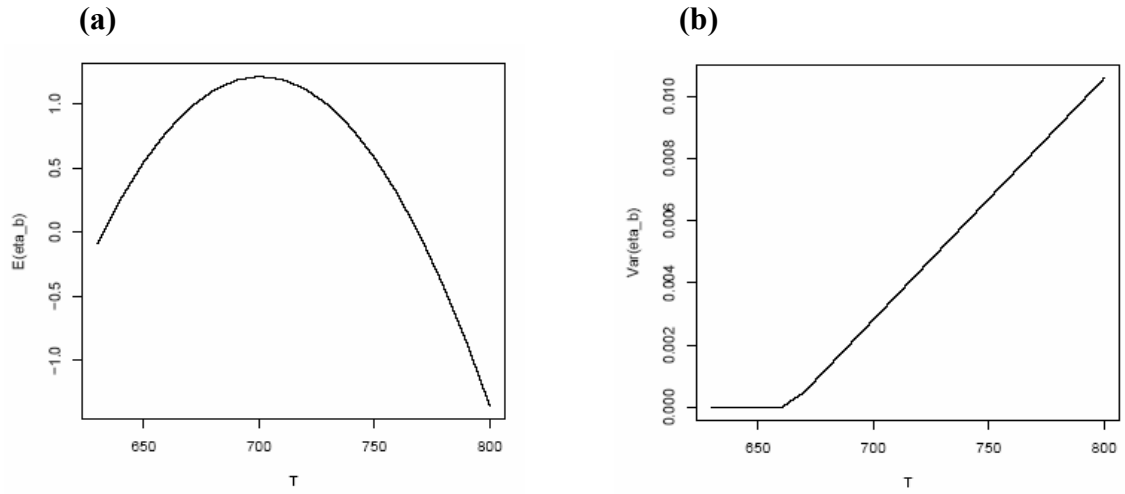

Figure A.39: (a) E(η_b) against temperature at 4mbar and 17.7cm and (b) Var(η_b) against temperature at 4mbar and 17.7cm.

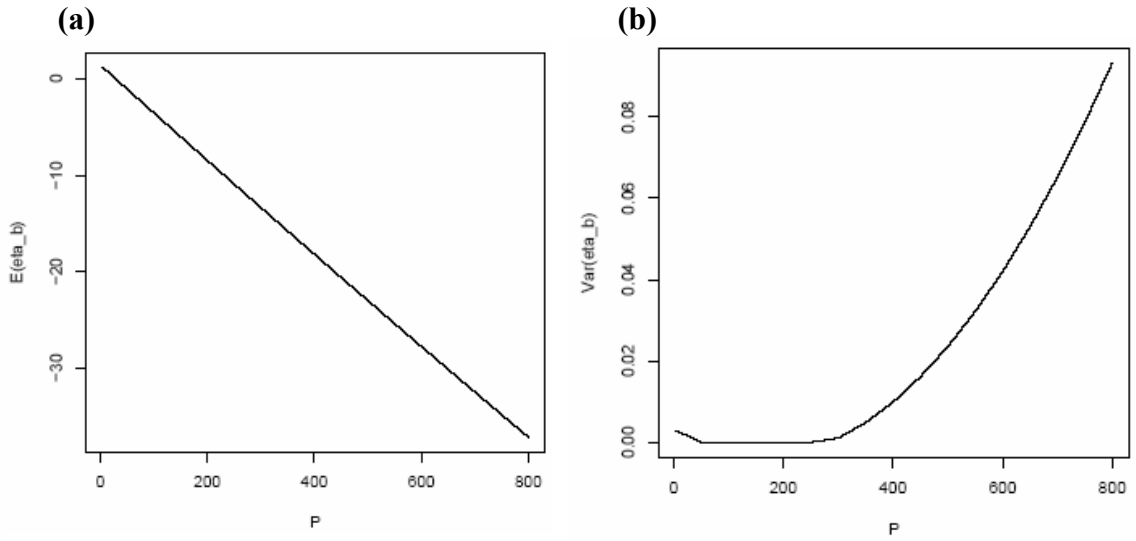

Figure A.40: (a) $E(\eta_s)$ against pressure at 701˚C and 17.7cm and (b) $Var(\eta_s)$ against pressure at 701˚C and 17.7cm

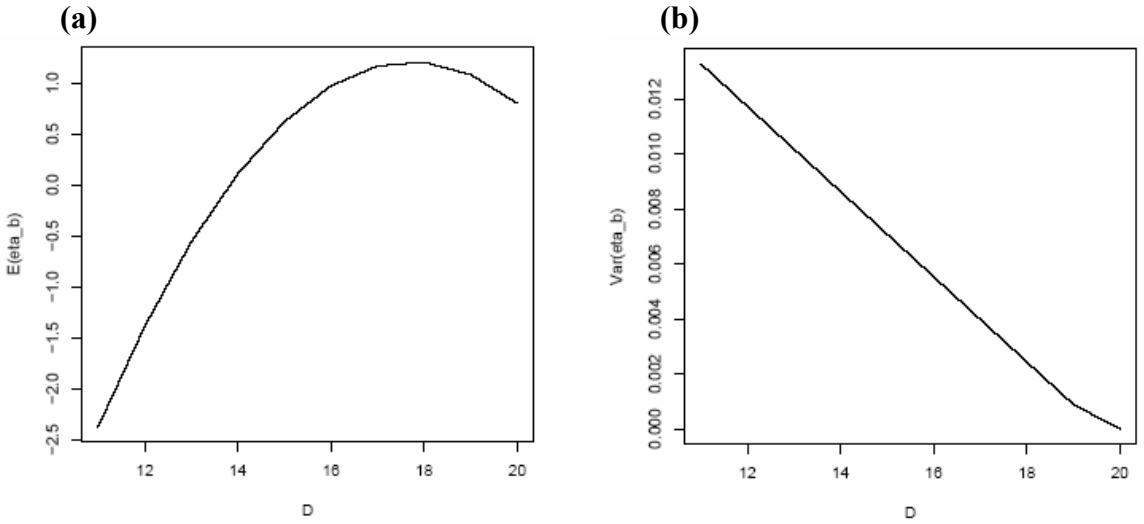

Figure A.41: (a) $E(\eta_b)$ against distance at 701˚C and 4mbar and (b) $Var(\eta_b)$ against distance at 701˚C and 4mbar.

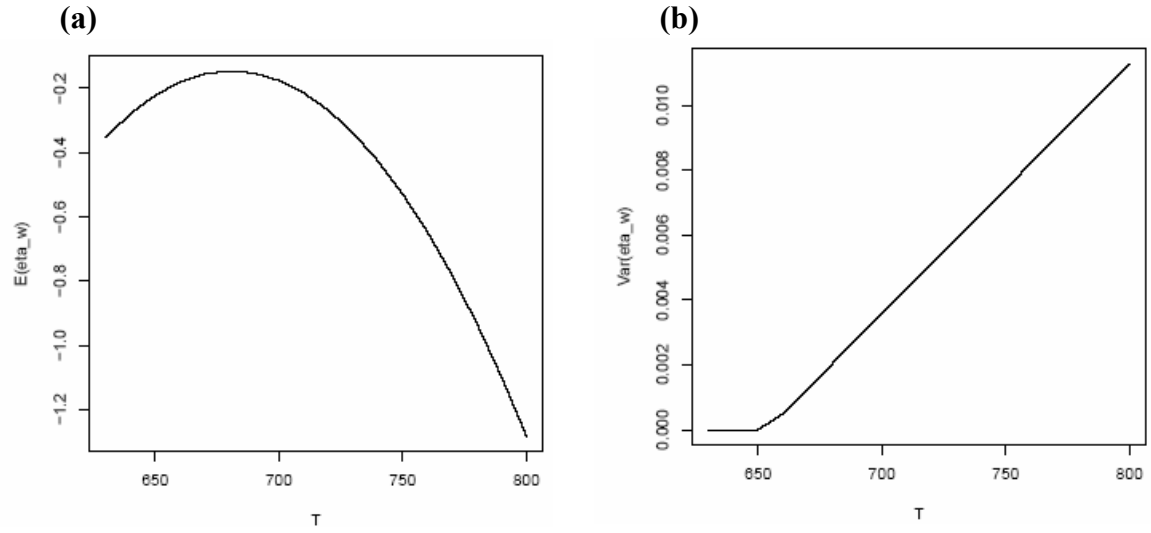

Figure A.42: (a) $E(\eta_w)$ against temperature at 4mbar and 17.2cm and (b) $Var(\eta_w)$ against temperature at 4mbar and 17.2cm

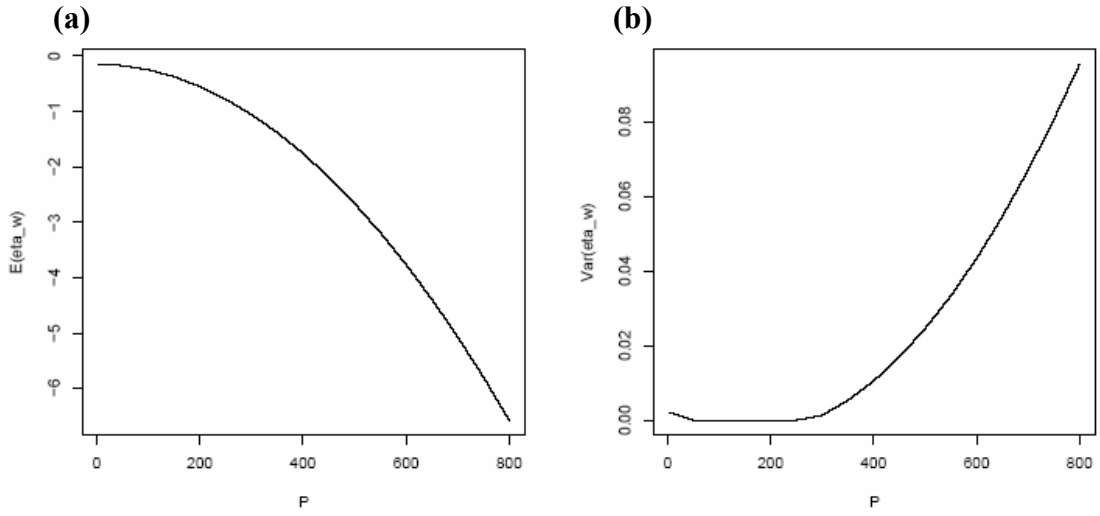

Figure A.43: (a) $E(\eta_w)$ against pressure at 681˚C and 17.2cm and (b) $Var(\eta_w)$ against pressure at 681˚C and 17.2cm.

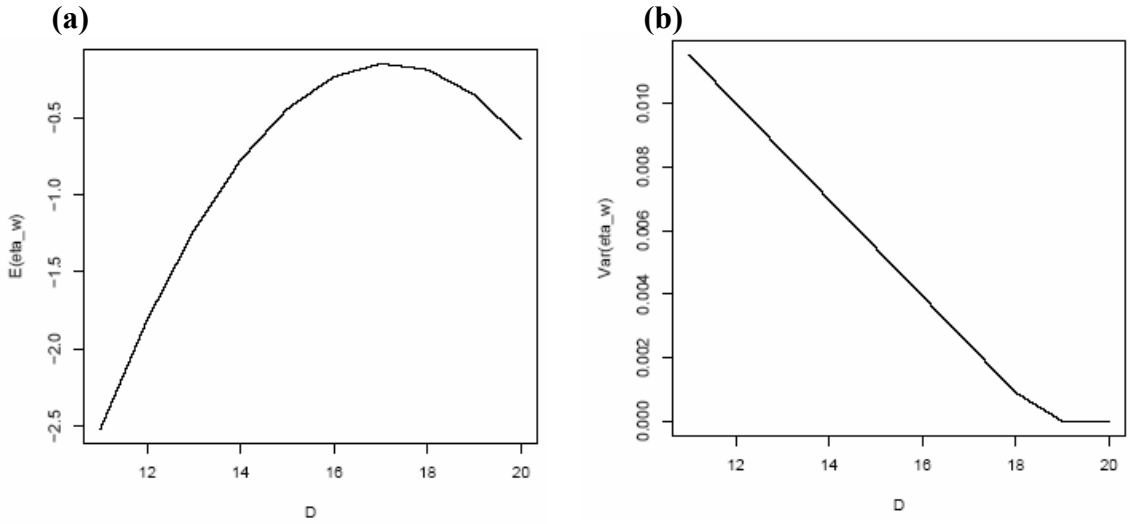

Figure A.44: (a) $E(\eta_w)$ against distance at 681˚C and 4mbar and (b) $Var(\eta_w)$ against distance at 681˚C and 4mbar.

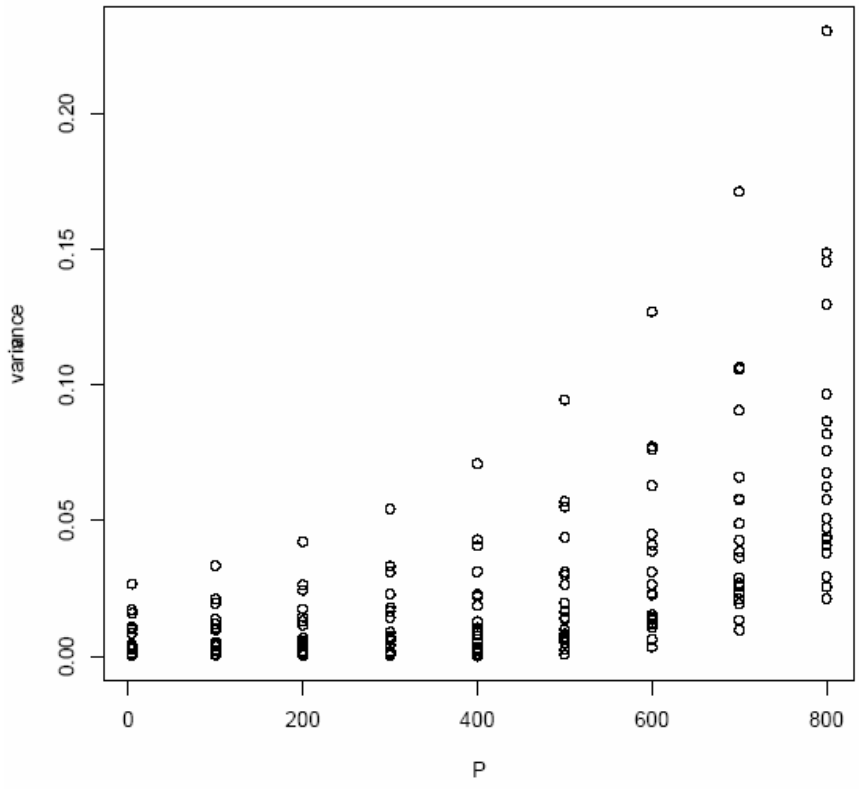

Figure A.45: $Var(\eta_s)$ against pressure.

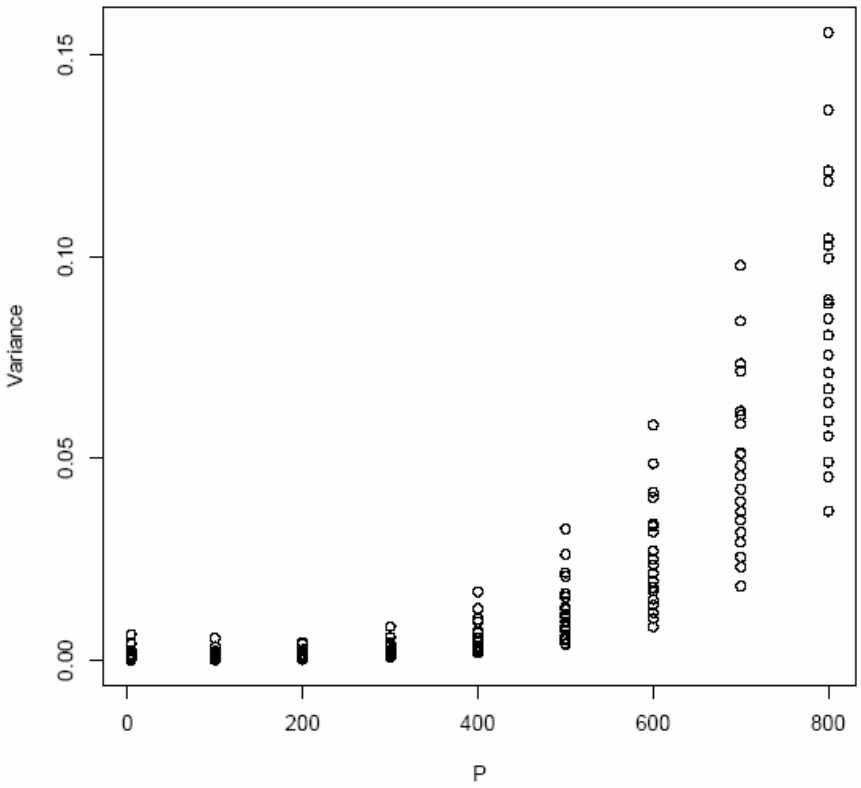

Figure A.46: Var(η_b) against pressure.

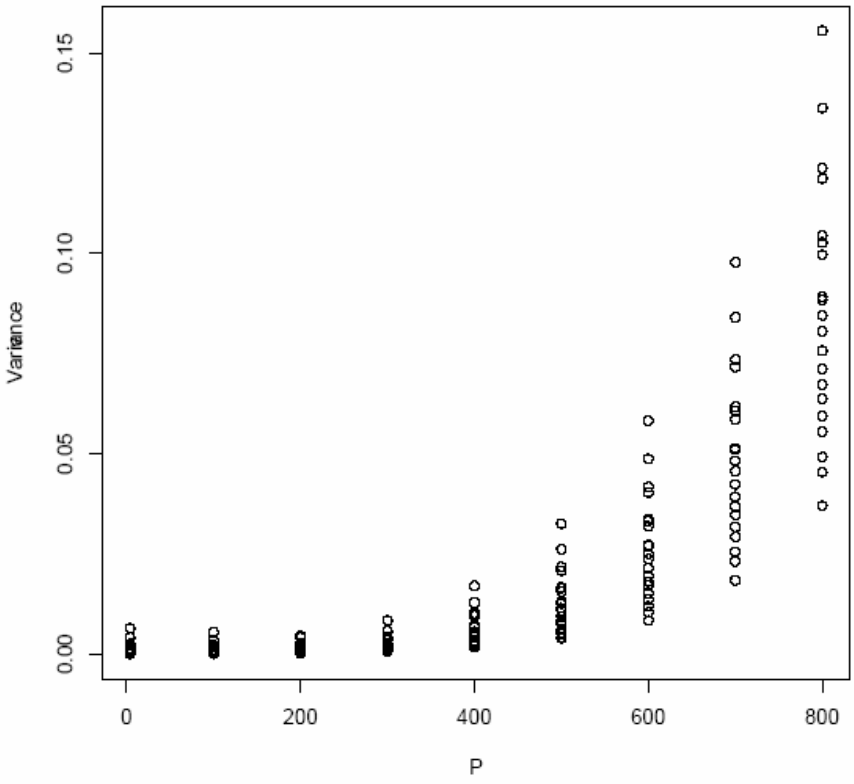

Figure A.47: Var(η_w) against pressure.

APPENDIX B

TABLES

Table B.1: Table of positions and lengths for deposition substrate with a source temperature of 630˚C.

	Run 1		Run 2		Run 3	
630°C & 800mbar	Distance	Length	Distance	Length	Distance	Length
	0-2.5	2.5cm	0-2.3	2.3cm	0-2.5	2.5cm
	2.5-4.3	1.8cm	2.3-4.6	2.3cm	2.5-4.2	1.7cm
	4.3-5.8	1.3cm	4.6-7.6	3.0cm	4.2-5.5	1.3cm
	5.8-6.7	1.1cm	7.6-9.7	2.1cm	5.5-6.7	1.2cm
	6.7-7.7	1.0cm	9.7-11.6	1.9cm	6.7-7.7	1.0cm
	7.7-8.8	1.1cm				
630°C & 700mbar	Distance	Length	Distance	Length	Distance	Length
	0-3.5	3.5cm	0-3.0	3.0cm	0-3.0	3.0cm
	3.5-5.7	2.2cm	3.0-5.0	2.0cm	3.0-4.7	1.7cm
	5.7-6.9	1.2cm	5.0-8.2	3.2cm	4.7-7.1	2.4cm
	6.9-8.3	1.4cm	8.2-10.9	2.7cm	7.1-10.4	3.3cm
	8.3-10.8	2.5cm				
630°C & 600mbar	Distance	Length	Distance	Length	Distance	Length
	0-2.7	2.7cm	0-2.3	2.3cm	0-3.0	3.0cm
	2.7-4.8	2.1cm	2.3-3.9	1.6cm	3.0-6.0	3.0cm
	4.8-6.9	2.1cm	3.9-5.6	1.7cm	6.0-9.0	3.0cm
			5.6-9.9	4.3cm	9.0-10.7	1.7cm
			9.9-10.9	1.0cm		
630°C & 500mbar	Distance	Length	Distance	Length	Distance	Length
	0-2.6	2.6cm	0-2.3	2.3cm	0-2.9	2.9cm
	2.6-5.2	2.6cm	2.3-4.0	1.7cm	2.9-5.6	2.7cm
	5.2-7.9	2.7cm	4.0-5.1	1.1cm	5.6-9.2	3.6cm
	7.9-9.8	1.9cm			9.2-11.5	2.3cm
630°C & 400mbar	Distance	Length	Distance	Length	Distance	Length
	0-2.5	2.5cm	0-3.0	3.0cm	0-2.7	2.7cm
	2.5-3.4	0.9cm	3.0-5.3	2.3cm	2.7-5.3	2.6cm
	3.4-5.0	1.6cm	5.3-7.5	2.2cm	5.3-7.8	2.5cm
	5.0-7.5	2.5cm	7.5-9.6	2.1cm	7.8-10.4	2.6cm
	7.5-9.1	1.6cm				
	9.1-10.4	1.3cm				
	10.4-11.6	1.2cm				
630°C & 300mbar	Distance	Length	Distance	Length	Distance	Length
	0-2.4	2.4cm	0-1.7	1.7cm	0-2.5	2.5cm
	2.4-3.8	1.4cm	1.7-3.8	2.1cm	2.5-3.8	1.3cm
	3.8-7.4	3.6cm	3.8-6.7	2.9cm	3.8-7.4	3.6cm
	7.4-8.9	1.5cm	6.7-10.2	3.5cm	7.4-8.9	1.5cm
	8.9-9.9	1.0cm			8.9-10.0	1.1cm
630°C & 200mbar	Distance	Length	Distance	Length	Distance	Length
	0-4.0	4.0cm	0-2.8	2.8cm	0-2.8	2.8cm
	4.0-6.7	2.7cm	2.8-5.2	2.4cm	2.8-5.3	2.5cm
	6.7-11.1	4.4cm	5.2-7.1	1.9cm	5.3-7.2	1.9cm
	11.1-12.1	1.0cm	7.1-9.2	2.1cm	7.2-9.6	2.4cm
	12.1-13.0	0.9cm				
630°C & 100mbar	Distance	Length	Distance	Length	Distance	Length
	0-3.2	3.2cm	0-3.6	3.6cm	0-3.2	3.2cm
	3.2-5.7	2.5cm	3.6-5.4	1.8cm	3.2-6.6	2.4cm
	5.7-7.4	1.7cm	5.4-7.8	2.4cm	6.6-8.4	1.8cm
	7.4-8.4	1.0cm	7.8-9.1	1.3cm	8.4-9.2	0.8cm
	8.4-9.5	1.1cm	9.1-10.1	1.0cm	9.2-10.4	1.2cm
	9.5-10.3	0.8cm				
	10.3-10.8	0.5cm				
630°C & 4mbar	Distance	Length	Distance	Length	Distance	Length
	0-3.8	3.8cm	0-3.3	3.3	0-3.7	3.7cm
	3.8-4.6	0.8cm	3.3-5.9	2.6	3.7-4.6	0.9cm
	4.6-5.2	0.6cm	5.9-8.3	2.4	4.6-5.2	0.6cm
	5.2-7.5	2.3cm	8.3-9.8	1.5	5.2-7.6	2.4cm
	7.5-8.7	1.2cm			7.6-8.9	1.3cm
	8.7-11.7	3.0cm			8.9-11.8	2.9cm
					11.8-13.1	1.3cm

Table B.2: Table of positions and lengths for deposition substrate with a source temperature of 700°C.

	Run 1		Run 2		Run 3	
700°C & 800mbar	**Distance**	Length	Distance	Length	**Distance**	Length
	0-2.9	2.9cm	0-1.7	1.7cm	0-2.7	2.7cm
	2.9-5.4	2.5cm	1.7-4.1	2.4cm	2.7-5.1	2.4cm
	5.4-8.7	3.3cm	4.1-7.2	3.1cm	5.1-8.3	3.2cm
	8.7-10.6	1.9cm	7.2-9.8	2.6cm	8.3-10.1	1.8cm
700°C & 700mbar	**Distance**	Length	Distance	Length	**Distance**	Length
	0-4.2	4.2cm	0-2.6	2.6cm	0-2.4	2.4cm
	4.2-8.1	3.9cm	2.6-5.4	2.9cm	2.4-5.1	2.7cm
	8.1-9.7	1.6cm	5.4-7.9	2.5cm	5.1-7.6	2.5cm
	9.7-10.7	1.0cm			7.6-9.0	2.4cm
					9.0-10.8	1.8cm
700°C & 600mbar	**Distance**	Length	Distance	Length	**Distance**	Length
	0-1.4	1.4cm	2.0-3.7	1.7cm	0-1.3	1.3cm
	1.4-2.9	1.5cm	3.7-5.5	1.8cm	1.3-2.8	1.5cm
	2.9-4.4	1.5cm	5.5-8.6	3.1cm	2.8-4.2	1.4cm
	4.4-5.9	1.4cm	8.6-11.8	3.2cm	4.2-5.5	1.3cm
	5.9-9.0	3.1cm			5.5-8.3	2.8cm
700°C & 500mbar	**Distance**	Length	Distance	Length	**Distance**	Length
	0-2.7	2.7cm	1.7-4.4	2.7cm	0-1.9	1.9cm
	2.7-5.3	2.6cm	4.4-7.1	2.7cm	1.9-4.6	2.7cm
	5.3-8.0	2.8cm	7.1-8.7	1.6cm	4.6-7.4	2.8cm
	8.0-9.6	1.6cm	8.7-9.4	0.7cm	7.4-9.0	1.6cm
					9.0-12.2	3.2cm
700°C & 400mbar	**Distance**	Length	Distance	Length	**Distance**	Length
	0-3.5cm	3.5cm	3.3-4.8	1.5cm	0-1.0	1.0cm
	3.5-8.8	3.3cm	4.8-6.2	1.4cm	1.0-2.1	1.1cm
	8.8-11.6	2.8cm	6.2-7.3	1.1cm	2.1-5.4	3.3cm
	11.6-12.5	0.9cm	7.3-8.6	1.3cm	5.4-8.5	3.1cm
	12.5-13.5	1.0cm			8.5-10.6	2.1cm
700°C & 300mbar	**Distance**	Length	Distance	Length	**Distance**	Length
	0-2.3	2.3cm	0-2.1	2.1cm	0-2.5	2.5cm
	2.3-4.6	2.6cm	2.1-5.4	3.3cm	2.5-5.1	2.6cm
	4.6-6.3	1.7cm	5.4-7.2	2.8cm	5.1-7.8	2.7cm
	6.3-8.1	1.8cm	7.2-10.5	3.3cm	7.8-10.6	2.8cm
700°C & 200mbar	**Distance**	Length	Distance	Length	**Distance**	Length
	0-3.1	3.1cm	0-3.8	3.8cm	0-3.2	3.2cm
	3.1-6.2	3.1cm	3.8-6.9	3.1cm	3.2-6.5	3.3cm
	6.2-10.7	4.5cm	6.9-10.2	3.3cm	6.5-9.7	3.2cm
	10.7-11.8	1.1cm			9.7-12.0	2.3cm
	11.8-12.5	0.7cm				
700°C & 100mbar	**Distance**	Length	Distance	Length	**Distance**	Length
	0-4.3cm	4.3cm	0-3.1	3.1cm	0-4.1	4.1cm
	4.3-6.5	2.2cm	3.1-6.2	3.1cm	4.1-6.4	2.3cm
	6.5-9.3	2.8cm	6.2-8.6	2.4cm	6.4-9.4	3.0cm
	9.3-12.6	3.3cm	8.6-11.9	3.3cm	9.4-12.6	3.2cm
					12.6-14.5	1.9cm
4mbar	**Distance**	Length	Distance	Length	**Distance**	Length
	0-2.7	2.7cm	0-5.3	5.3cm	0-2.8	2.8cm
	2.7-4.6	1.9cm	5.3-8.6	3.3cm	2.8-4.8	2.0cm

Table B.3: Table of positions and lengths for deposition substrate with a source temperature of 750˚C.

	Run 1		Run 2		Run 3	
750°C & 800mbar	**Distance**	Length	Distance	Length	**Distance**	Length
	0-3.7	3.7cm	0-3.6	3.6cm	0-4.3	4.3cm
	3.7-7.7	4.0cm	3.6-7.6	4.0cm	4.3-8.6	4.3cm
	7.7-12.2	4.5cm	7.6-10.2	2.6cm	8.6-11.4	2.8cm
750°C & 700mbar	**Distance**	Length	Distance	Length	**Distance**	Length
	0-2.5	2.5cm	0-3.1	3.1cm	0-3.0	3.0cm
	2.5-4.2	1.7cm	3.1-5.0	1.9cm	3.0-5.0	2.0cm
	4.2-7.0	2.8cm	5.0-7.8	2.8cm	5.0-7.8	2.8cm
	7.0-9.4	2.4cm	7.8-10.8	3.0cm	7.8-10.9	3.1cm
	9.4-11.4	2.0cm			10.9-12.4	1.5cm
750°C & 600mbar	**Distance**	Length	Distance	Length	**Distance**	Length
	0-3.3	3.3cm	0-3.2	3.2cm	0-3.1	3.1cm
	3.3-6.6	3.3cm	3.2-6.4	3.2cm	3.1-6.1	3.0cm
	6.6-8.7	2.1cm	6.4-8.3	1.9cm	6.1-8.1	2.0cm
	8.7-9.7	1.0cm	8.3-8.8	0.5cm	8.1-9.2	1.1cm
	9.7-11.1	1.4cm			9.2-10.3	1.1cm
750°C & 500mbar	**Distance**	Length	Distance	Length	**Distance**	Length
	0-3.1	3.1cm	0-3.1	3.1cm	0-3.1	3.1cm
	3.1-5.8	2.7cm	3.1-5.9	2.8cm	3.1-5.9	2.8cm
	5.8-7.2	1.5cm	5.9-6.9	1.0cm	5.9-8.0	2.1cm
	7.2-8.8	1.6cm	6.9-8.6	1.7cm	8.0-10.6	2.6cm
	8.8-10.8	2.0cm	8.6-10.3	1.7cm	10.6-12.8	2.2cm
750°C & 400mbar	**Distance**	Length	Distance	Length	**Distance**	Length
	0-2.1	2.1cm	0-1.8	1.8cm	0-1.8	1.8cm
	2.1-5.2	3.1cm	1.8-5.0	3.2cm	1.8-4.9	3.1cm
	5.2-8.4	3.2cm	5.0-8.3	3.3cm	4.9-8.1	3.2cm
	8.4-10.3	1.9cm	8.3-8.8	0.5cm	8.1-9.9	1.8cm
			8.8-9.2	0.4cm	9.9-11.2	1.3cm
750°C & 300mbar	**Distance**	Length	Distance	Length	**Distance**	Length
	0-3.0	3.0cm	0-2.9	2.9cm	0-2.8	2.8cm
	3-6.2	3.2cm	2.9-6.0	3.1cm	2.8-5.3	2.5cm
	6.2-8.0	1.8cm	6.0-7.6	1.6cm	5.3-8.0	2.7cm
	8.0-11.5	2.5cm	7.6-9.4	1.8cm	8.0-10.2	2.2cm
			9.4-10.7	1.3cm	10.2-11.3	1.1cm
750°C & 200mbar	**Distance**	Length	Distance	Length	**Distance**	Length
		4.0cm	0-2.3	2.3	0-4.1	4.1cm
		3.7cm	2.3-3.5	1.2	4.1-8.0	3.9cm
		3.2cm	3.5-5.1	1.6	8.0-9.8	1.8cm
		1.0cm	5.1-6.6	1.5	9.8-11.2	1.4cm
750°C & 100mbar	**Distance**	Length	Distance	Length	**Distance**	Length
	0-3.0	3.0cm	0-2.9	2.9cm	0-3.2	3.2cm
	3-5.5	2.5cm	2.9-5.4	2.5cm	3.2-6.4	3.2cm
	5.5-8.2	2.7cm	5.4-7.7	2.3cm	6.4-8.6	2.2cm
	8.2-10.4	2.2cm	7.7-9.9	2.2cm	8.6-10.8	2.2cm
	10.4-11.5	1.1cm	9.9-11.0	1.1cm	10.8-12.0	1.2cm
750°C & 4mbar	**Distance**	Length	Distance	Length	**Distance**	Length
	0-2.4	2.4cm	0-2.4	2.4cm	0-2.4	2.4cm
	2.4-6.2	3.8cm	2.4-6.1	3.7cm	2.4-6.1	3.7cm
	6.2-9.4	3.2cm	6.1-9.6	3.5cm	6.1-9.3	3.2cm

Table B.4: Table of positions and lengths for deposition substrate with a source temperature of 800˚C.

	Run 1		Run 2		Run 3	
800°C & 800mbar	**Distance**	Length	Distance	Length	**Distance**	Length
	0-1.7	1.7cm	0-1.7	1.7cm	0-1.6	1.6cm
	1.7-2.8	1.1cm	1.7-2.8	1.1cm	1.6-2.6	1.0cm
	2.8-4.6	1.8cm	2.8-4.3	1.5cm	2.6-4.2	1.7cm
	4.6-6.9	2.3cm	4.3-6.6	2.3cm	4.2-6.3	2.1cm
	6.9-8.3	1.4cm	6.6-7.5	0.9cm	6.3-7.4	1.4cm
800°C & 600mbar	**Distance**	Length	Distance	Length	**Distance**	Length
	0-1.9	1.9cm	0-1.9	1.9cm	0-1.9	1.9cm
	1.9-5.7	3.8cm	1.9-5.8	3.9cm	1.9-5.7	3.8cm
	5.7-8.8	3.1cm	5.8-9.0	3.2cm	5.7-8.9	3.2cm
	8.8-10.4	1.6cm	9.0-10.2	1.2cm	8.9-10.5	1.6cm
800°C & 500mbar	**Distance**	Length	Distance	Length	**Distance**	Length
	0-2.5	2.5cm	0-2.6	2.6cm	0-2.0	2.0cm
	2.5-5.4	2.9cm	2.6-4.7	2.1cm	2.0-4.0	2.0cm
	5.4-6.3	0.9cm	4.7-6.2	1.5cm	4.0-7.3	3.3cm
	6.3-6.9	0.6cm	6.2-7.0	0.8cm		
	6.9-8.1	1.2cm	7.0-7.8	0.8cm		
	8.1-10.3	2.2cm	7.8-10.3	2.5cm		
800°C & 400mbar	**Distance**	Length	Distance	Length	**Distance**	Length
	0-2.6	2.6cm	0-3.0	3.0cm	0-2.2	2.2cm
	2.6-5.0	2.4cm	3.0-6.1	3.1cm	2.2-4.8	2.6cm
	5.0-7.6	2.6cm	6.1-8.4	2.3cm	4.8-7.5	2.7cm
	7.6-8.8	1.1cm	8.4-10.5	2.1cm	7.5-8.9	1.4cm
	8.8-9.2	0.4cm				
800°C & 300mbar	**Distance**	Length	Distance	Length	**Distance**	Length
	0-3.8	3.8cm	0-3.8	3.8cm	0-3.6	3.6cm
	3.8-5.9	2.1cm	3.8-5.9	1.6cm	3.6-5.2	1.6cm
	5.9-8.5	2.6cm	5.9-8.6	2.7cm	5.2-7.9	2.7cm
	8.5-11.3	2.8cm	8.6-9.8	1.2cm	7.9-9.1	1.2cm
800°C & 200mbar	**Distance**	Length	Distance	Length	**Distance**	Length
	0-3.1	3.1cm	0-4.6	4.6cm	0-3.2	3.2cm
	3.1-5.3	2.2cm	4.6-7.7	3.1cm	3.2-6.3	3.1cm
	5.3-8.3	3.0cm	7.7-10.8	3.1cm	6.3-9.4	3.1cm
	8.3-11.0	2.7cm			9.4-12.7	3.3cm
800°C & 100mbar	**Distance**	Length	Distance	Length	**Distance**	Length
	0-3.1	3.1cm	0-3.2	3.2cm	0-3.1	3.1cm
	3.1-6.3	3.2cm	3.2-6.7	3.5cm	3.1-6.6	3.5cm
	6.3-10.5	4.2cm	6.7-10.2	3.5cm	6.6-10.9	4.3cm
800°C & 4mbar	**Distance**	Length	Distance	Length	**Distance**	Length
	0-3.0	3.0cm	0-2.9	2.9cm	0-3.0	3.0cm
	3-4.3	1.3cm	2.9-4.1	1.2cm	3.0-4.5	1.5cm
	4.3-6.6	2.3cm	4.1-6.3	2.2cm	4.5-6.7	2.2cm
	6.6-8.7	2.1cm	6.3-8.3	2.0cm	6.7-8.6	1.9cm
	8.7-9.7	1.0cm				

Table B.5: Table of positions and lengths for deposition substrate with a source temperature of 850˚C.

	Run 1		Run 2		Run 3	
850°C & 800mbar	**Distance**	Length	Distance	Length	**Distance**	Length
	0-2.3	2.3cm	0-2.3	2.3cm	0-2.3	2.3cm
	2.3-5.1	2.8cm	2.3-4.9	2.6cm	2.3-4.8	2.5cm
	5.1-8.2	3.1cm	4.9-8.1	3.2cm	4.8-8.0	3.2cm
	8.2-10	1.8cm	8.1-9.9	1.8cm	8.0-9.8	1.8cm
	10-11.2	1.2cm				
850°C & 600mbar	**Distance**	Length	Distance	Length	**Distance**	Length
	0-2.4	2.4cm	0-2.6	2.6cm	0.-2.4	2.4cm
	2.4-5.0	2.6cm	2.6-5.2	2.6cm	2.4-5.0	2.6cm
	5.0-7.5	2.5cm	5.2-7.8	2.6cm	5.0-7.5	2.5cm
	7.5-10.3	2.8cm	7.8-10.6	2.8cm	7.5-10.4	2.9cm
					10.4-12.4	2.0cm
850°C & 300mbar	**Distance**	Length	Distance	Length	**Distance**	Length
	0-2.3	2.3cm	0-1.8	1.8cm	0-1.8	1.8cm
	2.3-5.0	2.7cm	1.8-3.2	2.5cm	1.8-4.1	2.3cm
	5.0-7.4	2.4cm	3.2-5.4	2.2cm	4.1-6.2	2.1cm
	7.4-9.2	1.8cm	5.4-7.1	1.7cm	6.2-8.1	1.9cm
	9.1-12.3	3.2cm	7.1-8.6	1.5cm	8.1-9.9	1.8cm
850°C & 100mbar	**Distance**	Length	Distance	Length	**Distance**	Length
	0-4.1	4.1cm	0-3.6	3.6cm	0-3.7	3.7cm
	4.1-7.5	3.4cm	3.6-6.9	3.3cm	3.7-7.1	3.4cm
	7.5-8.8	1.3cm	6.9-9.3	2.4cm	7.1-9.3	2.2cm
	8.8-11.5	2.7cm	9.3-10.9	1.6cm	9.3-10.8	1.5cm
					10.8-12.8	2.0cm
					12.8-14.2	1.4cm
850°C & 4mbar	**Distance**	Length	Distance	Length	**Distance**	Length
	0-3.8	3.8cm	0-3.3	3.3cm	0-3.4	3.4cm
	3.8-8.5	4.7cm	3.3-6.4	3.1cm	3.4-6.5	3.1cm
	8.5-11	2.5cm	6.4-9.3	2.9cm	6.5-9.5	3.0cm
	11-14.1	3.1cm	9.3-12.3	3.0cm	9.5-11.3	2.8cm

Table B.6: Correlating substrate position with local temperature using equations from Table 5.1 for a source temperature of 630˚C.

	800mbar		700mbar		600mbar		500mbar		400mbar		300mbar		200mbar		100mbar		4mbar	
	cm	°C	cm	°C	cm	°C	cm	°C	cm	°C	cm	°C	cm	°C	cm	°C	cm	°C
Run 1	10.5	605.3	10.5	605.3	10.5	605.3	10.5	605.3			10.5	605.296	10.5	605.3	10.5	605.3	10.5	605.3
	13	580.48	14	567.22	13.2	578	13.1	579.25	10.5	605.3	12.9	581.702	14.5	559.9	13.7	571.41	14.3	562.86
	14.8	555.19	16.2	531.06	15.3	547	15.7	540.12	13	580.48	13.6	572.763	17.2	511.5	16.2	531.06	15.1	550.35
	16.3	529.19	17.4	507.31	17.4	507.3	18.4	485.42	13.9	568.64	14.3	562.859	21.6	403.8	17.9	496.6	15.7	540.12
	17.2	511.46	18.8	476.15			20.3	438.93	15.5	543.61	17.9	496.596	22.6	375.2	18.9	473.79	18	494.4
	18.2	489.94	21.3	412.12					18	494.4	19.4	461.715	23.5	348.5	20	446.67	19.2	466.6
	19.3	464.16							19.6	456.77	20.4	436.314			20.8	425.71	22.2	386.79
									20.9	423.02					21.3	412.12		
									22.1	389.66								

	800mbar		700mbar		600mbar		500mbar		400mbar		300mbar		200mbar		100mbar		4mbar	
	cm	°C	cm	°C	cm	°C	cm	°C	cm	°C	cm	°C	cm	°C	cm	°C	cm	°C
Run 2	10.5	605.3	10.5	605.3	10.5	605.3	10.5	605.3	10.5	605.3	10.5	605.296	10.5	605.3	10.5	605.3	10.5	605.3
	12.8	582.9	13.5	574.1	12.8	582.9	12.8	582.9	12.8	582.9	12.2	589.691	13.3	576.7	14.1	565.79	13.8	570.03
	15.1	550.35	15.5	543.61	14.4	561.4	14.5	559.85	13.5	574.1	14.3	562.859	15.7	540.1	15.9	536.56	16.4	527.3
	18.1	492.18	18.7	478.49	16.1	532.9	15.6	541.88	15.8	538.35	17.2	511.46	17.6	503.1	18.3	487.69	18.8	476.15
	20.2	441.52	21.4	409.36	20.4	436.3			18	494.4	20.7	428.384	19.7	454.3	19.6	456.77	20	446.67
	22.1	389.66			21.4	409.4			20.1	444.1					20.6	431.04		

	800mbar		700mbar		600mbar		500mbar		400mbar		300mbar		200mbar		100mbar		4mbar	
	cm	°C	cm	°C	cm	°C	cm	°C	cm	°C	cm	°C	cm	°C	cm	°C	cm	°C
Run 3	10.5	605.3	10.5	605.3	10.5	605.3	10.5	605.3	10.5	605.3	10.5	605.296	10.5	605.3	10.5	605.3	10.5	605.3
	13	580.48	13.5	574.1	13.5	574.1	13.4	575.42	13.2	577.99	13	580.483	13.3	576.7	13.7	571.41	14.4	561.36
	14.7	556.76	15.2	548.69	16.5	525.4	16.1	532.91	15.8	538.35	14.3	562.859	15.8	538.4	17.1	513.51	15.1	550.35
	16	534.74	17.6	503.08	19.5	459.2	19.7	454.27	16.6	523.45	17.9	496.596	17.7	500.9	18.9	473.79	15.7	540.12
	17.2	511.46	20.9	423.02	21.2	414.9	22	392.51	18.3	487.69	19.4	461.715	20.1	444.1	19.7	454.27	18.1	492.18
	18.2	489.94							20.9	423.02	20.5	433.686			20.9	423.02	19.8	451.75
																	22.3	383.92
																	24.6	314.87

Table B.7: Correlating substrate position with local temperature using equations from Table 5.1 for a source temperature of 700˚C.

Run 1

800mbar		700mbar		600mbar		500mbar		400mbar		300mbar		200mbar		100mbar		4mbar	
cm	ºC	cm	ºC	cm	ºC	cm	ºC	cm	ºC	cm	ºC	cm	ºC	cm	ºC	cm	ºC
10.5	669.39	10.5	669.39	10.5	669.39	10.5	669.39	10.5	669.39	10.5	669.387	10.5	669.39	10.5	669.39	10.5	669.39
13.4	637.49	14.7	619.27	12.6	647.47	13.2	640.07	14	629.39	12.7	646.27	13.6	634.85	12.6	647.47	13.2	640.07
15.9	600.17	18.6	548.75	13.4	637.49	14	629.39	19.3	533.42	15.2	611.586	16.7	586.18	14.8	617.77	15.1	613.15
19.2	535.67	20.2	512.46	14.9	616.24	18.5	550.87	22.1	463.38	16.9	582.524	21.2	487.46	17	580.67	17.9	563.24
21.1	490.04	21.2	487.46	16.4	591.55	20.1	514.86	23	437.79	21.2	487.456	22.3	457.83	19.8	521.95	20.3	510.04
				19.5	528.89			24	407.51			23	437.79	23.1	434.85	21.7	474.27

Run 2

800mbar		700mbar		600mbar		500mbar		400mbar		300mbar		200mbar		100mbar		4mbar	
cm	ºC	cm	ºC	cm	ºC	cm	ºC	cm	ºC	cm	ºC	cm	ºC	cm	ºC	cm	ºC
10.5	669.39	10.5	669.39	10.5	669.39	10.5	669.39	10.5	669.39	10.5	669.387	10.5	669.39	10.5	669.39	10.5	669.39
12.2	652.11	13.1	641.34	12.5	648.65	12.2	652.11	13.8	632.15	12.9	643.834	14.3	625.15	12.6	647.47	15.8	601.85
14.6	620.76	15.9	600.17	14.2	626.58	14.9	616.24	15.3	610	15.6	605.158	17.4	573.09	13.6	634.85	19.1	537.89
17.7	567.23	18.4	552.98	16	598.48	16.9	582.52	16.7	586.18	18.3	555.066	20.7	500.18	16.7	586.18	22.7	446.49
20.3	510.04			19.1	537.89	17.6	569.2	17.8	565.25	21.1	490.038			17.9	563.24		
				22.3	457.83	19.2	535.67	18.4	552.98					18.1	559.19		
						19.9	519.61	19.1	537.89					19.1	537.89		
														22.4	455.02		

Run 3

800mbar		700mbar		600mbar		500mbar		400mbar		300mbar		200mbar		100mbar		4mbar	
cm	ºC	cm	ºC	cm	ºC	cm	ºC	cm	ºC	cm	ºC	cm	ºC	cm	ºC	cm	ºC
10.5	669.39	10.5	669.39	10.5	669.39	10.5	669.39	10.5	669.39	10.5	669.387	10.5	669.39	10.5	669.39	10.5	669.39
13.2	640.07	12.9	643.83	11.8	656.53	12.4	649.82	11.5	659.7	13	642.594	13.7	633.51	13.6	634.85	12.9	643.83
15.6	605.16	15.6	605.16	13.3	638.79	15.1	613.15	12.6	647.47	15.6	605.158	17	580.67	16.9	582.52	13.3	638.79
18.8	544.46	18.1	559.19	14.7	619.27	17.9	563.24	15.9	600.17	17.4	573.091	20.2	512.46	19.9	519.61	15.3	610
20.6	502.67	19.5	528.89	16	598.48	19.5	528.89	19	540.1	18.3	555.066	22.5	452.2	23.1	434.85	17.9	563.24
		21.3	484.86	18.8	544.46	22.7	446.49	21.1	490.04	21.1	490.038			25	375.26	20	517.24
																21.3	484.86

Table B.8: Correlating substrate position with local temperature using equations from Table 5.1 for a source temperature of 750˚C.

Run 1

800mbar		700mbar		600mbar		500mbar		400mbar		300mbar		200mbar		100mbar		4mbar	
cm	°C	cm	°C	cm	°C	cm	°C	cm	°C	cm	°C	cm	°C	cm	°C	cm	°C
10.5	731.8	10.5	731.8	10.5	731.8	10.5	731.8	10.5	731.8	10.5	731.8	10.5	731.8	10.5	731.8	10.5	731.8
14.2	690.4	13	707.2	13.8	696.39	13.6	699.24	12.6	712.1	16.7	644.2	12.8	709.7	13.5	700.6	12.9	708.5
18.2	609.1	14.7	682.4	17.1	635.35	16.3	652.6	15.7	664.5	18.5	601.4	15.6	666.4	16	658.7	16.7	644.2
22.7	473.5	17.5	626.1	19.2	582.73	17.7	621.39	18.9	590.9	20.4	548.1	17.1	635.35	18.7	596.2	19.9	562.9
		19.9	562.9	20.2	554.1	19.3	579.97	20.8	535.9	22	497.2			20.9	532.8	23.2	456
		21.9	500.6	21.6	510.42	20.3	551.11							21.9	500.6	25.4	374.7

Run 2

800mbar		700mbar		600mbar		500mbar		400mbar		300mbar		200mbar		100mbar		4mbar	
cm	°C	cm	°C	cm	°C	cm	°C	cm	°C	cm	°C	cm	°C	cm	°C	cm	°C
10.5	731.8	10.5	731.8	10.5	731.8	10.5	731.8	10.5	731.8	10.5	731.8	10.5	731.8	10.5	731.8	10.5	731.8
14.1	691.9	13.6	699.2	13.7	697.83	13.6	699.24	12.3	715.5	13.4	702	14	693.45	13.4	702	12.9	708.5
18.1	611.6	15.5	668.3	16.9	639.81	16.4	650.53	15.5	668.3	16.5	648.4	15.6	666.4	15.9	660.6	14.1	691.9
20.7	539	18.3	606.6	18.8	593.56	17.4	628.48	18.8	593.6	18.1	611.6	17.1	635.35	18.2	609.1	16.6	646.3
		21.3	520.1	19.3	579.97	19.1	585.47	19.3	580	19.9	562.9			20.4	548.1	20.1	557.1
						20.8	535.87	19.7	568.7	21.2	523.3			20.8	535.9	21.7	507.2
														22.5	480.3	25.8	359.4

Run 3

800mbar		700mbar		600mbar		500mbar		400mbar		300mbar		200mbar		100mbar		4mbar	
cm	°C	cm	°C	cm	°C	cm	°C	cm	°C	cm	°C	cm	°C	cm	°C	cm	°C
10.5	731.8	10.5	731.8	10.5	731.8	10.5	731.8	10.5	731.8	10.5	731.8	10.5	731.8	10.5	731.8	10.5	731.8
14.8	680.7	13.5	700.6	13.6	699.24	18.6	598.83	12.3	715.5	13.3	703.3	14.6	684.03	13.7	697.8	12.9	708.5
19.1	585.5	15.5	668.3	16.6	646.31	16.4	650.53	15.4	670.1	15.8	662.6	18.5	601.43	16.9	639.8	16.6	646.3
21.9	500.6	18.3	606.6	18.6	598.83	20.4	548.11	18.6	598.8	18.5	601.4	20.3	551.11	19.1	585.5	19.8	565.8
		21.4	516.9	19.7	568.69	21.7	507.16	20.4	548.1	20.7	539	21.7	507.16	21.3	520.1	23	463
		22.9	466.5	20.8	535.87			21.7	507.2	21.8	503.9			21.6	510.4	25	389.9
														23.5	445.3		

Table B.9: Correlating substrate position with local temperature using equations from Table 5.1 for a source temperature of 800˚C.

	800mbar		600mbar		500mbar		400mbar		300mbar		200mbar		100mbar		4mbar	
	cm	ºC	cm	ºC	cm	ºC	cm	ºC	cm	ºC	cm	ºC	cm	ºC	cm	ºC
Run 1	10.5	788.17	10.5	788.17	10.5	788.17	10.5	788.17	10.5	788.17	10.5	788.17	10.5	788.17	10.5	788.17
	12.2	774.32	12.4	772.18	13	765.08	13.1	763.79	14.3	746.041	13.6	756.92	13.6	756.92	13.5	758.35
	13.3	761.13	16.2	708.92	15.9	715.53	15.5	723.9	16.4	704.368	15.8	717.67	16.8	694.89	14.8	737.35
	15.1	731.77	19.3	624.83	16.5	702.04	18.1	660.73	19	634.183	18.8	640.28	21	567.42	17.1	687.45
	17.4	679.75	20.1	598.72	17.4	679.75	19.3	624.83	21.8	538.054	21.5	549.23			19.2	627.98
	18.8	640.28	20.9	570.99	18.6	646.27	19.7	611.98							20.2	595.34
					20.8	574.54									21.1	563.83

	800mbar		600mbar		500mbar		400mbar		300mbar		200mbar		100mbar		4mbar	
	cm	ºC	cm	ºC	cm	ºC	cm	ºC	cm	ºC	cm	ºC	cm	ºC	cm	ºC
Run 2	10.5	788.17	10.5	788.17	10.5	788.17	10.5	788.17	10.5	788.17	10.5	788.17	10.5	788.17	10.5	788.17
	12.2	774.32	12.4	772.18	13.1	763.79	13.5	758.35	14.3	746.041	15.1	731.77	13.7	755.46	13.4	759.76
	13.3	761.13	16.4	704.37	15.2	729.85	16.6	699.69	16.4	704.368	18.2	657.89	17.2	684.92	14.6	740.92
	15.1	731.77	19.5	618.46	16.7	697.3	18.9	637.25	18.2	657.894	21.3	556.57	19.6	615.23	16.8	694.89
	17.4	679.75	20.7	578.07	17.5	677.12	21	567.42	19.1	631.093			20.7	578.07	18.8	640.28
	18.8	640.28			18.3	655.03			20.3	591.932						
					20.8	574.54										

	800mbar		600mbar		500mbar		400mbar		300mbar		200mbar		100mbar		4mbar	
	cm	ºC	cm	ºC	cm	ºC	cm	ºC	cm	ºC	cm	ºC	cm	ºC	cm	ºC
Run 3	10.5	788.17	10.5	788.17	10.5	788.17	10.5	788.17	10.5	788.17	10.5	788.17	10.5	788.17	10.5	788.17
	12.1	775.35	12.4	772.18	12.5	771.07	12.7	768.76	14.1	749.301	13.7	755.46	13.6	756.92	13.5	758.35
	13.1	763.79	16.2	708.92	14.5	742.66	15.3	727.9	15.7	719.774	16.8	694.89	17.1	687.45	15	733.66
	14.7	739.15	19.4	621.66	17.8	669.06	18	663.53	18.4	652.137	19.9	605.4	21.4	552.91	17.2	684.92
	16.8	694.89	21	567.42			19.4	621.66	19.6	615.235	23.2	483.68			18.4	652.14
	17.9	666.31													19.1	631.09

Table B.10: Correlating substrate position with local temperature using equations from for a source temperature of 850°C.

	800mbar		600mbar		300mbar		100mbar		4mbar	
	cm	°C	cm	°C	cm	°C	cm	°C	cm	°C
Run 1	10.5	844.97	10.5	844.97	10.5	844.97	10.5	844.97	10.5	844.97
	12.8	825.28	12.9	824.05	12.8	825.28	14.6	798.11	14.3	803.4
	15.6	778.22	15.5	780.36	15.5	780.36	18	716.34	19	684.86
	18.7	694.64	18	716.34	16.7	752.31	19.3	674.8	21.5	593.17
	20.5	631.9	19.4	671.39	17.9	719.3	22	572.89	24.6	460.1
	21.7	585.12	20.1	646.66	18.8	691.41				
			20.8	620.55	19.7	660.97				
					22.8	539.36				
Run 2	cm	°C	cm	°C	cm	°C	cm	°C	cm	°C
	10.5	844.97	10.5	844.97	10.5	844.97	10.5	844.97	10.5	844.97
	12.8	825.28	13.1	821.5	12.3	830.92	14.1	806.76	13.8	811.53
	15.4	782.47	15.7	776.04	13.7	813.06	17.4	733.65	16.9	747.15
	18.6	697.83	18.3	707.23	15.9	771.57	19.8	657.43	19.8	657.43
	20.4	635.63	21.1	608.96	16.9	747.15	21.4	597.15	22.8	539.36
					19.1	681.54				
Run 3	cm	°C	cm	°C	cm	°C	cm	°C	cm	°C
	10.5	844.97	10.5	844.97	10.5	844.97	10.5	844.97	10.5	844.97
	12.8	825.28	12.9	824.05	12.3	830.92	14.2	805.1	13.9	809.98
	15.3	784.55	15.5	780.36	14.6	798.11	17.6	728.01	17	744.52
	18.5	701	18	716.34	16.7	752.31	19.8	657.43	20	650.28
	20.3	639.34	20.9	616.71	18.6	697.83	21.3	601.11	21.8	581.07
			22.9	535.08	20.4	635.63	23.3	517.8		
							24.7	455.59		

Table B.11 Relating the observed morphologies and their respective population density to local temperature ranges for experimental setup with a source temperature of 630°C.

Run 1			Run 2			Run 3		
630°C & 800mbar	Type of Deposit		**630°C & 800mbar**	Type of Deposit		**630°C & 800mbar**	Type of Deposit	
605C-464C	No Deposit		605C-390C	No Deposit		605C-490C	No Deposit	
630°C & 700mbar	Type of Deposit		**630°C & 700mbar**	Type of Deposit		**630°C & 700mbar**	Type of Deposit	
605C-412C	No Deposit		605C-409C	No Deposit		605C-423C	No Deposit	
630°C & 600mbar	Type of Deposit		**630C & 600mbar**	Type of Deposit		**630C & 600mbar**	Type of Deposit	
605C-578C	SPA		605C-561C	SPA		605C-574C	No Deposit	
578C-547C	No Deposit		561C-409C	No Deposit		574C-516C	SPA	
547C-507C	No Deposit					516C-387C	No Deposit	
630°C & 500mbar	Type of Deposit		**630°C & 500mbar**	Type of Deposit		**630°C & 500mbar**	Type of Deposit	
605C-501C	SPA		605C-533C	SPA		605C-533C	SPA	
501C-485C	Wires		533C-478C	SPA & Wires	**S-36% W-64%**	533C-393C	No Deposit	
485C-439C	No Deposit		478C-409C	No Deposit				
630°C & 400mbar	Type of Deposit		**630°C & 400mbar**	Type of Deposit		**630°C & 400mbar**	Type of Deposit	
605C-494C	SPA		605C-583C	No Deposit		605C-578C	SPA & Belts	**B-24%, S-76%**
494C-390C	No Deposit		583C-574C	SPA & Belts	**B-37%, S- 63%**	578C-538C	SPA & Belts	**B-41%, S-69%**
			574C-538C	SPA & Belts	**B-41% S-59%**	538C-523C	SPA & Belts	**B-29%, S-71%**
			538C-494C	SPA		523C-423C	No Deposit	
			494C-444C	No Deposit				
630°C & 300mbar	Type of Deposit		**630°C & 300mbar**	Type of Deposit		**630°C & 300mbar**	Type of Deposit	
605C-576C	No Deposit		605C-590C	No Deposit		605C-580C	No Deposit	
576C-563C	SPA/Belts/Wires	**B-27%, W-33%, S-40%**	590C-563C	SPA/Belts/Wires	**B-20%, W-45%, S-35%**	580C-563C	SPA/Belts/Wires	**B-8%, W-7%, S-85%**
563C-497C	SPA/Belts/Wires	**B-24%, W-36%, S-40%**	563C-511C	Wires		563C-497C	SPA/Belts/Wires	**B-28%, W-32%, S-40%**
497C-436C	No Deposit		511C-428C	No Deposit		497C-434C	No Deposit	
630°C & 200mbar	Type of Deposit		**630°C & 200mbar**	Type of Deposit		**630°C & 200mbar**	Type of Deposit	
605C-511C	SPA		605C-577C	SPA & Belts	**B-40%, S-60%**	605C-577C	No Deposit	
511C-349C	No Deposit		577C-503C	SPA & Belts	**B-35% S-65%**	577C-538C	SPA	
			503C-454C	No Deposit		538C-501C	SPA & Belts	**B-39%, S-61%**
						501C-444C	No Deposit	
630°C & 100mbar	Type of Deposit		**630°C & 100mbar**	Type of Deposit		**630°C & 100mbar**	Type of Deposit	
605C-571C	No Deposit		605C-566C	SPA & Belts	**B-49%, S-51%**	605C-571C	SPA/Belts/Wires	**B-20%, W-33%, S-47%**
571C-497C	SPA & Wires	**W-49%, S-51%**	566C-537C	SPA/Belts/Wires	**B-12%, W-80%,S-08%**	571C-514C	SPA/Belts/Wires	**B-23%, W-41%, S-36%**
497C-474C	Wires		537C-488C	SPA/Belts/Wires	**B-20%, W-63%, S-17%**	514C-474C	Wires	
474C-412C	No Deposit		488C-431C	No Deposit		474C-423C	No Deposit	
630°C & 4mbar	Type of Deposit		**630°C & 4mbar**	Type of Deposit		**630°C & 4mbar**	Type of Deposit	
650C-563C	No Deposit		605C-570C	SPA/Belts/Wires	**S-28%, B-20%, W-52%**	605C-564C	SPA/Belts/Wires	**B-25%, W-48%, S-27%**
563C-550C	SPA & Wires	**W-59%, S-41%**	570C-527C	SPA & Wires	**S-50% & W-50%**	564C-550C	SPA/Wires	**W-40%, S-60%**
550C-540C	SPA & Wires	**W-67%, S-33%**	527C-476C	SPA/Belts/Wires	**S-23%, B-32%, W-45%**	550C-540C	SPA	
540C-494C	SPA/Belts/Wires	**B-28%,W-21%, S-51%**	476C-447C	Belts & Wires	**B-33% & W-67%**	540C-492C	SPA & Wires	**W-22%, S-78%**
494C-467C	Belts & Wires	**B-45%,W-55%**				492C-462C	SPA/Belts/Wires	**B-31%, W-26%, S-43%**
467C-387C	Wires					462C-384C	Belts & Wires	**B-51%, W-49%**
						384C-315C	No Deposit	

Table B.12: Relating the observed morphologies and their respective population density to local temperature ranges for experimental setup with a source temperature of 700°C.

Run 1			Run 2			Run 3		
700ºC & 800mbar	Type of Deposit		**700ºC & 800mbar**	Type of Deposit		**700ºC & 800mbar**	Type of Deposit	
669C-490C	No Deposit		669C-553C	SPA & Belts		669C-503C	No Deposit	
700ºC & 700mbar	Type of Deposit		**700ºC & 700mbar**	Type of Deposit		**700ºC & 700mbar**	Type of Deposit	
669C-487C	No Deposit		669C-553C	No Deposit		669C-485C	No Deposit	
700ºC & 600mbar	Type of Deposit		**700ºC & 600mbar**	Type of Deposit		**700ºC & 600mbar**	Type of Deposit	
669C-529C	No Deposit		669C-458C	No Deposit		669C-544C	No Deposit	
700ºC & 500mbar	Type of Deposit		**700ºC & 500mbar**	Type of Deposit		**700ºC & 500mbar**	Type of Deposit	
669C-629C	No Deposit		669C-652C	No Deposit		669C-650C	No Deposit	
629-551C	Wires		652C-582C	Wires		650C-613C	Wires	
551C-515C	No Deposit		582C-569C	SPA/Belts/Wires	**W-95%, B-3%, S-2%**	613C-563C	SPA & Wires	**S-23% W-77&**
			569C-520C	No Deposit		563C-529C	SPA & Wires	**S-35% W-65%**
						529C-446C	No Deposit	
700ºC & 400mbar	Type of Deposit		**700ºC & 400mbar**	Type of Deposit		**700ºC & 400mbar**	Type of Deposit	
669C-629C	No Deposit		669C-586C	No Deposit		669C-647C	No Deposit	
629C-533C	Wires		586C-565C	SPA & Belts	**B-42%, S-58%**	647C-600C	Wires	
533C-408C	No Deposit		565C-552C	SPA & Belts	**B-51% S-49%**	600C-540C	SPA /Belts/Wires	**B-17%, W-40%, S-43%**
			552C-538C	No Deposit		540C-490C	No Deposit	
700ºC & 300mbar	Type of Deposit		**700ºC & 300mbar**	Type of Deposit		**700ºC & 300mbar**	Type of Deposit	
669ºC-646C	No Deposit		669C-643C	No Deposit		669C-643C	No Deposit	
646C-547C	SPA		643C-605C	Wires		643C-605C	Spa & Belts	**B-42%, S-57%**
			605C-555C	SPA		605C-573C	Wires	
			555C-490C	No Deposit		573C-490C	No Deposit	
700ºC & 200mbar	Type of Deposit		**700ºC & 200mbar**	Type of Deposit		**700ºC & 200mbar**	Type of Deposit	
669C-635C	Wires		669C-625C	Wires		669C-581C	Wires	
635C-586C	SPA/Belts/Wires	**B-8%, W-89%, S-3%**	625C-573C	Wires/SPA/Belts	**B-9%, W-79%, S-12%**	581C-512C	SPA/Belts/Wires	**B-35%, W-32%, S-33%**
586C-438C	No Deposit		573C-500C	No Deposit		512C-452C	No Deposit	
700ºC & 100mbar	Type of Deposit		**700ºC & 100mbar**	Type of Deposit		**700ºC & 100mbar**	Type of Deposit	
669C-659C	No Deposit		669C-648C	No Deposit		669C-650C	No Deposit	
659C-618C	Wires		648C-635C	SPA/Belts/Wires	**B-30%, W-10%, S-60%**	650C-621C	Wires	
618C-581C	SPA/Belts/Wires	**B-45%, W-51%, S-4%**	635C-586C	SPA/Belts/Wires	**B-25%, W-33%, S-42%**	621C-583C	SPA/Belts/Wires	**B-35%, W-29% S-30%**
581C-522C	Wires		586C-538C	SPA/Belts/Wires	**B-13%, W-58%, S-28%**	583C-520C	SPA/Belts/Wires	**B-30%,W-47% S-23%**
522C-435C	No Deposit		538C-455C	No Deposit		520C-375C	No Deposit	
700ºC & 4mbar	Type of Deposit		**700ºC & 4mbar**	Type of Deposit		**700ºC & 4mbar**	Type of Deposit	
669C-640C	Belts		669C-602C	Wires		669C-644C	No Deposit	
640C-613C	Belts & Wires	**B-33%, W-67%**	602C-538C	Belts		644C-639C	SPA/Belts/Wires	**B-24%, W-48%, S-28%**
613C-563C	SPA/Belts/Wires	**B-59%, W-32%, S-8%**	538C-446C	Belts & Wires	**B-69%, W-31%**	639C-610C	SPA & Belts	**B-60% S-40%**
563C-510C	Belts					610C-563	Belts	
510C-474C	Wires					563C-517C	SPA & Be;ts	**B-91% S-9%**
						517C-485C	Belts & Wires	**B-71%, W-29%**

Table B.13: Relating the observed morphologies and their respective population density to local temperature ranges for experimental setup with a source temperature of 750˚C.

Run 1			Run 2			Run 3		
750°C & 800mbar	Type of Deposit		**750°C & 800mbar**	Type of Deposit		**750°C & 800mbar**	Type of Deposit	
732C-473C	No Deposit		732C-539C	No Deposit		732C-501C	No Deposit	
750°C & 700mbar	Type of Deposit		**750°C & 700mbar**	Type of Deposit		**750°C & 700mbar**	Type of Deposit	
732C-501C	No Deposit		732C-529C	No Deposit		732C-467C	No Deposit	
750°C & 600mbar	Type of Deposit		**750°C & 600mbar**	Type of Deposit		**750°C & 600mbar**	Type of Deposit	
732C-583C	No Deposit		732C-589C	No Deposit		732C-536C	No Deposit	
583C-554C	Wires							
554C-510C	No Deposit							
750°C & 500mbar	Type of Deposit		**750°C & 500mbar**	Type of Deposit		**750°C & 500mbar**	Type of Deposit	
732C-669C	No Deposit		732C-628C	No Deposit		732C-599C	No Deposit	
669C-580C	Wires		628C-585C	Wires		599C-548C	SPA	
580C-551C	No Deposit		585C-536C	SPA & Belts	**B-32%, S-68%**	548C-507C	No Deposit	
750°C & 400mbar	Type of Deposit		**750°C & 400mbar**	Type of Deposit		**750°C & 400mbar**	Type of Deposit	
732C-665C	No Deposit		732C-715C	No Deposit		732C-715C	No Deposit	
625C-591C	Belts & Wires	**B-44%, W-56%**	715C-594C	Wires		715C-599C	Wires	
591C-536C	No Deposit		594C-589C	SPA & Belts	**B-49%, S-51%**	599C-548C	SPA & Belts	**B-54%, S-46%**
			589C-569C	SPA & Belts	**B-51%, S-49%**	548C-507C	No Deposit	
750°C & 300mbar	Type of Deposit		**750°C & 300mbar**	Type of Deposit		**750°C & 300mbar**	Type of Deposit	
732C-644C	No Deposit		732C-648C	No Deposit		732C-663C	No Deposit	
644C-601C	SPA/Belts/Wires	**B-25%, W-52%, S-23%**	648C-612C	SPA & Belts	**B-31%, S-69%**	663C-601C	SPA & Belts	**B-28%, S-72%**
601C-548C	SPA/Belts/Wires	**B-27%, W-51%, S-21%**	612C-563C	SPA & Belts	**B-66%, S-34%**	601C-539C	SPA & Belts	**B-44%, S-56%**
548C-497C	Wires		563C-523C	No Deposit		539C-584C	SPA & Belts	**B-44%, S-56%**
750°C & 200mbar	Type of Deposit		**750°C & 200mbar**	Type of Deposit		**750°C & 200mbar**	Type of Deposit	
732C-710C	No Deposit		732C-693C	No Deposit		732C-684C	Wires	
693C-666C	SPA & Wires	**S-36% & W-64%**	593C-666	SPA & Wires	**S-45% W-55%**	684C-601C	SPA/Belts/Wires	**B-29%, W-52%, S-19%**
666C-635C	SPA/Belts/Wires	**S-27%, B-19%, W-55%**	666C-635C	SPA/Belts/Wires	**B-31% W-18%, S-51%**	601C-551C	SPA/Belts/Wires	**B-32%, W-32%, S-36%**
						551C-507C	No Deposit	
750°C & 100mbar	Type of Deposit		**750°C & 100mbar**	Type of Deposit		**750°C & 100mbar**	Type of Deposit	
732C-701C	No Deposit		732C-702C	No Deposit		732C-698C	No Deposit	
701C-596C	Wires		702C-661C	Wires		698C-640C	Wires	
596C-533C	SPA/Belts/Wires	**B-17%, W-49%, S-34%**	661C-609C	SPA & Wires	**W-49%, S-51%**	640C-585C	SPA/Belts/Wires	**B-20%, W-24%, S-56%**
533C-501C	SPA/Belts/Wires	**B-21%, W-53%, S-26%**	609C-548C	SPA/Belts/Wires	**B-19% W-40%, S-41%**	585C-520C	SPA/Belts/Wires	**B-34%, W-49%, S-16%**
			548C-523C	Wires		520C-497C	Wires	
			523C-514C	No Deposit		497C-445C	No Deposit	
750°C & 4mbar	Type of Deposit		**750°C & 4mbar**	Type of Deposit		**750°C & 4mbar**	Type of Deposit	
732C-708C	No Deposit		732C-704C	No Deposit		732C-708C	No Deposit	
708C-644C	SPA		704C-646C	SPA & Belts	**B-28%, S-72%**	708C-646C	SPA/Belts/Wires	**B-24%, W-49%, S-27%**
644C-562C	SPA & Belts	**B-7%, S-93%**	646C-557C	SPA & Belts	**B-49%, S-51%**	646C-566C	SPA & Belts	**B-12%, S-88%**
562C-456C	SPA/Belts/Wires	**B-11%, W-78%, S-10%**	557C-507C	SPA/Belts/Wires	**B-35% W-52%, S-13%**	566C-463C	Belts	
456C-375C	No Deposit		507C-369C	No Deposit		463C-390C	SPA/Belts/Wires	**B-13%, W-63%, S-24%**

Table B.14: Relating the observed morphologies and their respective population density to local temperature ranges for experimental setup with a source temperature of 800˚C.

Run 1			Run 2			Run 3		
800ºC & 800mbar	Type of Deposit		**800ºC & 800mbar**	Type of Deposit		**800ºC & 800mbar**	Type of Deposit	
788C-640C	No Deposit		788C-640C	No Deposit		788C-666C	No Deposit	
800ºC & 600mbar	Type of Deposit		**800ºC & 600mbar**	Type of Deposit		**800ºC & 600mbar**	Type of Deposit	
788C-571C	No Deposit		788C-578C	No Deposit		788C-567C	No Deposit	
800ºC & 500mbar	Type of Deposit		**800C & 500mbar**	Type of Deposit		**800C & 500mbar**	Type of Deposit	
788C-646C	No Deposit		788C-655C	No Deposit		788C-669C	Wires	
646C-574C	Wires		655C-575C	Wires				
800ºC & 400mbar	Type of Deposit		**800ºC & 400mbar**	Type of Deposit		**800ºC & 400mbar**	Type of Deposit	
788C-770C	Wires		788C-758C	No Deposit		788C-769C	No Deposit	
770C-724C	SPA & Wires	**W-24%, S-76%**	758C-670C	SPA/Belts/Wires	**B-22%, W-67%, S-11%**	769C-728C	SPA/Belts/Wires	**B-15%, W-60%, S-25%**
724C-661C	SPA/Belts/Wires	**B-11%, W-27%, S-62%**	670C-637C	SPA/Belts/Wires	**B-16%, W-27%,S-57%**	728C-664C	SPA/Belts/Wires	**B-5%, W-76%, S-19%**
661C-625C	SPA & Wires	**W-45%, S-55%**	637C-567C	Wires		664C-622C	SPA/Belts/Wires	**B-25%, W-53%, S-22%**
625C-612C	Wires							
800ºC & 300mbar	Type of Deposit		**800ºC & 300mbar**	Type of Deposit		**800ºC & 300mbar**	Type of Deposit	
788C-746C	No Deposit		788C-746C	No Deposit		788C-720C	No Deposit	
746C-704C	Wires		746C-674C	Wires		720C-652C	Wires	
704C-634C	SPA & Wires	**W-92%, S-8%**	674C-631C	SPA/Belts/Wires	**B-8%, W-85%, S-7%**	652C-615C	No Deposit	
634C-538C	No Deposit		631C-592C	SPA & Wires	**W-69%, S-31%**			
800ºC & 200mbar	Type of Deposit		**800ºC & 200mbar**	Type of Deposit		**800ºC & 200mbar**		
788C-757C	No Deposit		788C-658C	Epitaxy		788C-695C	Wires	
757C-682C	Epitaxy		658C-557C	SPA/Belts/Wires	**B-12%, W-73%, S-15%**	695C-605C	Epitaxy	
682C-640C	SPA/Belts/Wires	**B-8%, W-64%, S-27%**				605C-484C	No Deposit	
640C-549C	SPA/Belts/Wires	**B-12%, W-60%, S-28%**						
800ºC & 100mbar	Type of Deposit		**800ºC & 100mbar**	Type of Deposit		**800ºC & 100mbar**	Type of Deposit	
788C-695C	No Deposit		788C-755C	No Deposit		788C-757C	No Deposit	
695C-567C	No Deposit		755C-602C	Wires		757C-553C	Epitaxy	
			602C-578C	No Deposit				
800ºC & 4mbar	Type of Deposit		**800ºC & 4mbar**	Type of Deposit		**800ºC & 4mbar**	Type of Deposit	
788C-737C	No Deposit		788C-741C	No Deposit		788C-734C	No Deposit	
737C-687C	No Deposit		741C-695C	Epitaxy		734C-685C	Epitaxy	
687C-628C	Wires		695C-640C	Epitaxy		685C-672C	Epitaxy	
628C-595C	Epitaxy					672C-631C		
595C-564C	Wires							

Table B.15: Relating the observed morphologies and their respective population density to local temperature ranges for experimental setup with a source temperature of 850°C.

Run 1		Run 2		Run 3	
850°C & 800mbar	Type of Deposit	**850°C & 800mbar**	Type of Deposit	**850°C & 800mbar**	Type of Deposit
845C-825C	No Deposit	845C-825C	No Deposit	845C-825C	No Deposit
825C-778C	No Deposit	825C-782C	No Deposit	825C-785C	No Deposit
778C-695C	No Deposit	782C-698C	No Deposit	785C-701C	No Deposit
695C-632C	No Deposit	698C-636C	No Deposit	701C-639C	No Deposit
632C-585C	No Deposit				
850°C & 600mbar	Type of Deposit	**850°C & 600mbar**	Type of Deposit	**850°C & 600mbar**	Type of Deposit
845C-824C	No Deposit	845C-822C	No Deposit	845C-824C	No Deposit
824C-780C	No Deposit	822C-776C	No Deposit	824C-780C	No Deposit
780C-716C	SPA & Belts	776C-707C	No Deposit	780C-716C	No Deposit
716C-621C	SPA & Wires	707C-609C	No Deposit	716C-617C	No Deposit
				617C-535C	No Deposit
850°C & 300mbar	Type of Deposit	**850°C & 300mbar**	Type of Deposit	**850°C & 300mbar**	Type of Deposit
845C-825C	No Deposit	845C-831C	No Deposit	845C-831C	No Deposit
825C-780C	No Deposit	831C-813C	No Deposit	831C-798C	No Deposit
780C-719C	No Deposit	813C-772C	No Deposit	798C-752C	No Deposit
719C-661C	No Deposit	772C-728C	No Deposit	752C-698C	No Deposit
661C-539C	No Deposit	728C-682C	No Deposit	698C-635C	No Deposit
850°C & 100mbar	Type of Deposit	**850°C & 100mbar**	Type of Deposit	**850°C & 100mbar**	Type of Deposit
845C-807C	No Deposit	845C-807C	No Deposit	845C-805C	No Deposit
807C-734C	No Deposit	807C-734C	No Deposit	805C-728C	No Deposit
734C-657C	No Deposit	734C-657C	No Deposit	728C-657C	No Deposit
657C-597C	No Deposit	657C-597C	No Deposit	657C-601C	No Deposit
			No Deposit	601C-518C	No Deposit
				518C-456C	No Deposit
850°C & 4mbar	Type of Deposit	**850°C & 4mbar**	Type of Deposit	**850°C & 4mbar**	Type of Deposit
845C-803C	No Deposit	845C-812C	No Deposit	845C-810C	No Deposit
803C-685C	No Deposit	812C-747C	No Deposit	810C-745C	No Deposit
685C-593C	No Deposit	747C-657C	No Deposit	745C-650C	No Deposit
593C-460C	No Deposit	657C-539C	No Deposit	650C-581C	No Deposit

Table B.16: Average of the three experimental runs for each temperature versus pressure experimental setup.

630°C & 800mbar	Type of Deposit		700°C & 800mbar	Type of Deposit		750°C & 800mbar	Type of Deposit		800°C & 800mbar	Type of Deposit		850°C & 800mbar	Type of Deposit
605C-490C	No Deposit		669C-503C	No Deposit		732C-501C	No Deposit		788C-666C	No Deposit		845C-585C	No Deposit
630°C & 700mbar	Type of Deposit		700°C & 700mbar	Type of Deposit		750°C & 700mbar	Type of Deposit		800°C & 600mbar	Type of Deposit		850°C & 600mbar	Type of Deposit
605C-423C	No Deposit		669C-485C	No Deposit		732C-467C	No Deposit		788C-567C	No Deposit		845C-535C	No Deposit
630°C & 600mbar	Type of Deposit		700°C & 600mbar	Type of Deposit		750°C & 600mbar	Type of Deposit						
605C-561C	SPA		669C-544C	No Deposit		732C-536C	No Deposit						
561C-387C	No Deposit												
630°C & 500mbar	Type of Deposit		700°C & 500mbar	Type of Deposit		750°C & 500mbar	Type of Deposit		800C & 500mbar	Type of Deposit			
605C-533C	SPA		669C-654C	No Deposit		732C-628C	No Deposit		788C-655C	No Deposit			
533C-531C	SPA & Wires	S-68% W-32%	654C-637C	Wires		628C-590C	Wires		655C-575C	Wires			
531C-485C	SPA & Wires	S-18% W-82%	637C-613C	SPA & Wires	S-8% W-92%	590C-548C	SPA & Belts	B-16% S-84%					
			613C-563C	SPA & Wires	S-12% W-88%	548C-507C	No Deposit						
			563C-449C	No Deposit									
630°C & 400mbar	Type of Deposit		700°C & 400mbar	Type of Deposit		750°C & 400mbar	Type of Deposit		800°C & 400mbar	Type of Deposit			
605C-578C	SPA & Belts	B-11%, S-89%	669C-647C	No Deposit		732C-715C	No Deposit		788C-769C	No Deposit			
578C-538C	SPA & Belts	B-24%, S-76%	647C-586C	Wires		715C-625C	Wires		769C-724C	SPA/Belts/Wires	B-12%, S-37%, W-51%		
538C-523C	SPA & Belts	B-10% S-90%	586C-565C	SPA /Belts/Wires	B-19%, S-34%, W-47%	625C-591C	Belts & Wires	B-15% W-85%	724C-660C	SPA/Belts/Wires	B-13%, S-31%, W-56%		
523C-494C	SPA		565C-552C	SPA /Belts/Wires	B-23%, S-31%, W-46%	591C-580C	Belts & SPA	B-47%, S-53%	660C-625C	SPA/Belts/Wires	B-14%, S-45%, W-41%		
494C-444C	No Deposit		552C-490C	No Deposit		580C-548C	Belts & SPA	B-53% S-47%	625C-612C	Wires			
						548C-507C	No Deposit		612C-580C	No Deposit			
630°C & 300mbar	Type of Deposit		700°C & 300mbar	Type of Deposit		750°C & 300mbar	Type of Deposit		800°C & 300mbar	Type of Deposit		850°C & 300mbar	Type of Deposit
605C-580C	No Deposit		669C-643C	No Deposit		732C-648C	No Deposit		788C-746C	No Deposit		845C-539C	No Deposit
580C-563C	SPA/Belts/Wires	B-20%, W-31%, S-69%	643C-605C	SPA/Belts/Wires	B-14%, S-52%, W-34%	648C-601C	SPA/Belts/Wires	B-28%, S-55%, W-17%	746C-704C	Wires			
563C-497C	SPA/Belts/Wires	B-17%, W-56%, S-27%	605C-573C	SPA & Wires	S-67%, W-33%	601C-563C	SPA/Belts/Wires	B-46%, S-37%, W-17%	704C-652C	SPA/Belts/Wires	B-3%, S-7%, W-90%		
497C-434C	No Deposit		573C-555C	SPA		563C-549C	SPA/Belts/Wires	B-35%, S-39%, W-26%	652C-538C	No Deposit			
			550C-490C	No Deposit		548C-523C	No Deposit						
630°C & 200mbar	Type of Deposit		700°C & 200mbar	Type of Deposit		750°C & 200mbar	Type of Deposit		800°C & 200mbar				
605C-577C	SPA & Belts	B-20% S-80%	669C-625C	Wires		732C-693C	No Deposit		788C-658C	No Deposit			
577C-538C	SPA & Belts	B-12% S-88%	625C-586C	SPA/Belts/Wires	B-6%, S-5%, W-89%	693C-666C	SPA/Belts/Wires	B-10%, S-33%, W-57%	658C-557C	SPA/Belts/Wires	B-12%, S-22%, W-66%		
538C-501C	SPA & Belts	B-29%, S-71%	586C-573C	SPA/Belts/Wires	B-23%, S-23%, W-54%	666C-635C	SPA/Belts/Wires	B-26%, S-32%, W-42%	557C-484C	No Deposit			
501C-444C	No Deposit		573C-438C	No Deposit		635C-551C	SPA/Belts/Wires	B-32%, S-32%, W-36%					
						551C-507C	No Deposit						
630°C & 100mbar	Type of Deposit		700°C & 100mbar	Type of Deposit		750°C & 100mbar	Type of Deposit		800°C & 100mbar	Type of Deposit		850°C & 100mbar	Type of Deposit
605C-566C	SPA/Belts/Wires	B-35%, W-17%, S-47%	669C-648C	No Deposit		732C-701C	No Deposit		788C-553C	No Deposit		845C-456C	No Deposit
571C-537C	SPA/Belts/Wires	B-12%, W-67%, S-31%	648C-635C	SPA/Belts/Wires	B-10%, S-20%, W-70%	701C-640C	Wires						
537C-497C	SPA/Belts/Wires	B-14%, W-51%, S-35%	635C-586C	SPA/Belts/Wires	B-37%-, S-25%, W-38%	640C-609C	SPA/Belts/Wires	B-7%, S-36%, W-57%					
497C-474C	SPA/Belts/Wires	B-7%, W-87%, S-6%	586C-538C	SPA/Belts/Wires	B-14%, S-17%, W-69%	609C-585C	SPA/Belts/Wires	B-18%, S-44%, W-38%					
474C-423C	No Deposit		538C-455C	No Deposit		585C-540C	SPA/Belts/Wires	B-23%, S-34%, W-46%					
						540C-520C	SPA/Belts/Wires	B-20%, S-13%, W-67%					
						520C-497C	SPA/Belts/Wires	B-11%, S-13%, W-76%					
						497C-445C	No Deposit						
630°C & 4mbar	Type of Deposit		700°C & 4mbar	Type of Deposit		750°C & 4mbar	Type of Deposit		800°C & 4mbar	Type of Deposit		850°C & 4mbar	Type of Deposit
605C-564C	SPA/Belts/Wires	B-23%, W-50%, S-27%	669C-644C	No Deposit		732C-708C	No Deposit		788C-631C	No Deposit		845C-460C	No Deposit
564C-550C	SPA/Wires	S-54% W-46%	644C-639C	SPA/Belts/Wires	B-19%, S-9%, W-72%	708C-644C	SPA/Belts/Wires	B-17%, S-66%, W-17%					
550C-540C	SPA/Wires	S-61% W-39%	639C-610C	SPA/Belts/Wires	B-33%, S-13%, W-54%	644C-557C	SPA & Belts	B-23%, S-77%					
540C-527C	SPA/Belts/Wires	B-9%, W-31%, S-60%	610C-563C	SPA/Belts/Wires	B-86%, S-3%, W-11%	557C-463C	SPA/Belts/Wires	B-50%, S-8%, W-42%					
527C-494C	SPA/Belts/Wires	B-20%, W-29%, S-51%	563C-538C	SPA & Belts	B-97%, S-3%	463C-390C	No Deposit						
494C-462C	SPA/Belts/Wires	B-36%, W-42%, S-22%	538C-510C	SPA/Belts/Wires	B-87%, S-3%, W-10%								
462C-384C	Belts/Wires	B-28% W-72%	510C-474C	Belts & Wires	B-47%, W-53%								
384C-315C	No Deposit												

Table B.17: Binomial generalized linear model for nanosaws/nanocombs.

	Estimate	Std. Error	z value	Pr(> |z|)
(Intercept)	-62.029089	2.885522	-21.49666	0
temp	0.138759	0.006984	19.86762	0
pres	0.197253	0.006352	31.05308	0
avgdist	1.829829	0.126699	14.44235	0
tempsq	-0.000152	0.000005	-29.44989	0
pressq	-0.000008	0.000000	-26.58828	0
avgdistsq	-0.142052	0.002603	-54.57758	0
temp:pres	-0.000274	0.000009	-29.54354	0
pres:avgdist	-0.011406	0.000376	-30.37497	0
temp:avgdist	0.004120	0.000192	21.43290	0
temp:pres:avgdist	0.000016	0.000001	29.50666	0

Table B.18: Binomial generalized linear model for nanobelts.

	Estimate	Std. Error	z value	Pr(> |z|)
(Intercept)	-119.53352	3.36618	-35.51017	0
temp	0.31894	0.00856	37.26053	0
pres	0.14682	0.00755	19.45637	0
avgdist	1.02154	0.12071	8.46241	0
tempsq	-0.00026	0.00001	-41.85251	0
pressq	0.00000	0.00000	-5.08686	0
avgdistsq	-0.07927	0.00213	-37.17361	0
temp:pres	-0.00020	0.00001	-18.91180	0
temp:avgdist	0.00257	0.00018	14.46455	0
pres:avgdist	-0.01020	0.00046	-22.37778	0
temp:pres:avgdist	0.00001	0.00000	21.63272	0

Table B.19: Binomial generalized linear model for nanowires.

	Estimate	Std. Error	z value	Pr(> |z|)
(Intercept)	-37.00079	1.73326	-21.34745	0
temp	0.08163	0.00453	18.02887	0
pres	-0.01083	0.00073	-14.72920	0
avgdist	1.05962	0.05609	18.88989	0
tempsq	-0.00008	0.00000	-24.69610	0
pressq	-0.00001	0.00000	-45.75654	0
avgdistsq	-0.06208	0.00123	-50.27455	0
temp:pres	0.00003	0.00000	33.87103	0
pres:avgdist	-0.00056	0.00002	-25.17008	0
temp:avgdist	0.00158	0.00007	23.93682	0

Table B.20: Equations of the fitted statistical model for each CdSe morphology.

Nanostructure	Binomial Generalized Linear Fitted Model
Nanosaw/ Nanocombs	$\log\frac{p_s}{1-p_s} = -62.029089 + 0.138759T + 0.197253P + 1.829829D - 0.000152T^2 - 0.000008P^2 - 0.142052D^2 - 0.000274TP - 0.011406PD + 0.004120DT + 0.000016TPD$
Nanobelts	$\log\frac{p_b}{1-p_b} = -119.53352 + 0.31894T + 0.14682P + 1.02154D - 0.00026T^2 + 0.000002P^2 - 0.07927D^2 - 0.00020TP - 0.01020PD + 0.00257TD + 0.00001TPD$
Nanowires	$\log\frac{p_w}{1-p_w} = -(-37.00079 + 0.08163T - 0.01083P + 1.05962D - 0.00008T^2 - 0.00001P^2 - 0.06208D^2) + 0.00003TP - 0.00056PD + 0.00158TD$

Table B.21: List of optimized parameters for each of the nanostructures using two analytical methods.

	Statistcal Analysis				*Graphical Analysis*	
	T* (ºC)	**P* (mbar)**	**D* (cm)**	**p_n**	**Local Temperature (ºC)**	**P* (mbar)**
Nanosaws	630.0000	399.9989	13.7099	0.5826	Moderate	Above 300
Nanobelts	699.9744	4.0000	17.7094	0.7711	Low	4
Nanowires	699.9728	59.9998	17.1713	0.4550	High	N/A

Table B.22: σ_P corresponding to different set values of μ_P.

μ_P	Total variation	$6\sigma_P$	σ_P
4	± 10	20	3.33
100	± 10	20	3.33
200	± 20	40	6.67
300	± 20	40	6.67
400	± 20	40	6.67
500	± 40	80	13.33
600	± 40	80	13.33
700	± 60	120	20.00
800	± 60	120	20.00

Table B.23: Regression results for variance of nanosaws.

	Estimate	Std. Error	t value	$\Pr(>\|t\|)$
Intercept	0.93853948	0.08278561	11.336988	0
T	-0.00185031	0.00022540	-8.208843	0
T^2	0.00000131	0.00000016	8.283869	0
P	-0.00281948	0.00007490	-37.644143	0
P^2	0.00000016	0.00000001	18.100024	0
D	-0.03526263	0.00248239	-14.205092	0
D^2	0.00108425	0.00007686	14.106898	0
TP	0.00000401	0.00000010	39.205854	0
PD	0.00016130	0.00000443	36.385254	0
TPD	-0.00000023	0.00000001	-38.565603	0

Table B.24: Regression results for variance of nanobelts.

	Estimate	Std. Error	t value	$\Pr(>\|t\|)$
Intercept	-0.02514759	0.01155462	-2.176409	0.03088015
T	0.00007998	0.00001431	5.588434	0.00000009
P	0.00008992	0.00002513	3.577754	0.00044970
P^2	0.00000024	0.00000001	28.489675	0.00000000
D	-0.00157033	0.00031801	-4.938014	0.00000185
TP	-0.00000045	0.00000003	-15.085820	0.00000000
PD	0.00000841	0.00000067	12.594898	0.00000000

Table B.25: Regression results for variance of nanowires.

	Estimate	Std. Error	t value	Pr(> |t|)
Intercept	-0.02514759	0.01155462	-2.176409	0.03088015
T	0.00007998	0.00001431	5.588434	0.00000009
P	0.00008992	0.00002513	3.577754	0.00044970
P^2	0.00000024	0.00000001	28.489675	0.00000000
D	-0.00157033	0.00031801	-4.938014	0.00000185
TP	-0.00000045	0.00000003	-15.085820	0.00000000
PD	0.00000841	0.00000067	12.594898	0.00000000

Table B.26: Equations for variance models of the three CdSe morphologies.

	$\mathrm{Var}(\eta_n)$
Nanosaws	$= 0.9385398 - 0.00185031\mu_T + 0.00000131\mu^2_T - 0.00281948\mu_P + 0.00000016\mu^2_P - 0.03526263\mu_D + 0.00108425\mu^2_D + 0.00000401\mu_T\mu_P + 0.000162130\mu_P\mu_D - 0.00000023\mu_T\mu_P\mu_D$
Nanobelts	$= -0.02514759 + 0.00007998\mu_T + 0.00008992\mu_P + 0.00000024\mu^2_P - 0.00157033\mu_D - 0.00000045\mu_T\mu_P + 0.00000841\mu_P\mu_D$
Nanowires	$= -0.02514759 + 0.00007998\mu_T + 0.00008992\mu_P + 0.00000024\mu^2_P - 0.00157033\mu_D - 0.00000045\mu_T\mu_P + 0.00000841\mu_P\mu_D$

Table B.27: Optimized growth values for statistical and variance analysis.

	Statistcal Analysis			*Variance Analysis*		
	T* (°C)	**P* (mbar)**	**D* (cm)**	**μ_T* (°C)**	**μ_P* (mbar)**	**μ_D* (cm)**
Nanosaws	630	400	13.7	630	405	13.7
Nanobelts	700	4	17.7	701	4	17.7
Nanowires	700	60	17.2	681	4	17.2

Table B.28: Time and temperature delays between inner and outer thermocouples for ramping up and cooling down a source temperature of 630˚C.

Ramp Up		Cool Down	
Minutes	Temperature (ºC)	Minutes	Temperature (ºC)
0	528	**0**	**630**
1	543	1	627
2	559	2	615
3	572	3	600
4	585	4	589
5	596	5	580
6	605		
7	610		
8	615		
9	617		
10	624		
11	626		
12	628		
13	629		
14	**630**		

Table B.29: Time and temperature delays between inner and outer thermocouples for ramping up and cooling down a source temperature of 700˚C.

Ramp Up		Cool Down	
Minutes	Temperature (ºC)	Minutes	Temperature (ºC)
0	608	0	700
1	624	1	686
2	**639**	2	669
3	652	3	652
4	665	**4**	**633**
5	668	5	614
6	672	6	593
7	679	7	581
8	684	8	577
9	689		
10	693		
11	699		
12	699		
13	700		

Table B.30: Time and temperature delays between inner and outer thermocouples for ramping up and cooling down a source temperature of 750˚C.

Ramp Up		Cool Down	
Minutes	Temperature (ºC)	Minutes	Temperature (ºC)
-2	624	0	750
-1	**644**	1	724
0	664	2	717
1	682	3	701
2	700	4	693
3	718	5	676
4	728	6	652
5	733	**7**	**631**
6	741	8	605
7	744	9	575
8	746		
9	748		
10	749		
11	750		

Table B.31: Time and temperature delays between inner and outer thermocouples for ramping up and cooling down a source temperature of 800˚C.

Ramp Up		Cool Down	
Minutes	Temperature (ºC)	Minutes	Temperature (ºC)
-4	**636**	0	800
-3	656	1	788
-2	676	2	765
-1	696	3	743
0	716	4	719
1	735	5	694
2	754	6	670
3	767	7	647
4	779	**8**	**624**
5	786	9	604
6	792	10	584
7	794	11	564
8	797	12	
9	800	13	
		14	

REFERENCES

[1] A.E. Rakhshani, *J. Appl. Phys.*, **81**, 7988 (1997).

[2] N.R. Pawaskar, S.D. Sathaye, M.M. Bhadhade, K.R. Patil, *Mater. Res. Bull.*, **37**, 1539 (2002).

[3] D.J. Norris, A. Sacra, C.B. Murray, and M.G. Bawendi, *Phys. Rev. Lett.*, **72**, 2612 (1994).

[4] S.H. Tolbert and A.P. Alvisatos, *Science*, **265**, 373 (1994).

[5] T. Matsunaga, Y. Okamura, and T. Tanaka, *J. Mater. Chem.*, **14**, 2099 (2004).

[6] K. Autumn, Y.A. Liang, S.T Hsieh, W. Zesch, W.P. Chan, T.W. Kenny, R. Fearing, R.J. Full, Nature, **405**, 681 (2000).

[7] C.D. Geddes, A. Parfenov, I. Gryczynski, J.R Lakowicz, *Chem. Phys. Lett.*, **380**, 269 (2003).

[8] Z.L. Wang, Z.C. Kang, *Functional and Smart Materials* (Plenum Press, New York, 1998).

9 M.G. Bawendi, P.J. Carroll, W.L. Wilson, L.E. Brus, *J. Chem. Phys.*, **96**, 946.

10 L.E. Brus, *J. Chem. Phys.*, **80**, 4403 (1984).

[11] A.P. Alivisatos, A.L. Harris, N.J. Steigerwald, and L.E. Brus, *J. Chem Phys.*, **89**, 4001 (1988).

[12] C.B. Murray, D.J. Norris, and M.G. Bawendi, *J. Am. Chem. Soc.*, **115**, 8706 (1993).

[13] M.G. Bawendi, P.J. Carroll, W.L. Wilson, and L.E. Brus, *J. Chem. Phys.*, **96**, 946 (1992).

[14] D.J. Norris and M.G. Bawendi, *J. Chem. Phys.*, **103**, 5260 (1995).

[15] A.P. Alivisatos, *J. Phys. Chem.*, **100**, 13226 (1996).

[16] X. Li, Y. Wu, D. Steel, D. Gammon, T.H. Stievater, D.S. Katzer, D. Park, C. Piermarcchi, L.J. Sham, *Science*, 3**01**, 809 (2003).

[17] M. Bruchez, M. Moronne, P. Gin, S. Weiss, and A.P. Alivisatos, *Science*, **281**, 2013 (1998).

[18] P.T. Tran, E.R. Goldman, G.P. Anderson, J.M Mauro, and H. Mattousi, *Phys. Stat. Sol. B*, **229**, 427 (2002).

[19] W. Chan and S. Nie, *Science*, **281**, 2016 (1998).

[20] X Gao, Y. Cui, R.M. Levenson, L. Chung, and S. Nie, *Nat. Biotechnol*., **22**, 969 (2004).

[21] A.M. Smith, X. Gao, and S. Nie, *Photochemistry and Photobiology*., **80**, 377 (2004).

[22] H. Jeong, A.M. Chang, and M.R. Melloch, *Science*, **293**, 2221 (2001).

[23] C. Kirchner, T. Liedl, S. Kudera, T. Pellegrino, A.M. Javier, H.E. Gaub, S. Stlözle, N. Fertig, W.J Parak, *Nano Lett*., **5**, 331 (2005).

[24] B. Dubertert, P. Skourides, D.J.Norris, V. Noireaux, A.H. Brivanlou, A. Libchaber, *Science*, **298**, 1759 (2002).

[25] M.E. Akerman, W.C. Chan, P. Laakkonen, S.N Bhatia, E. Ruoslahti, *Proc. Natl. Acad. Sci. USA*, **99**, 12617 (2002).

[26] X. Peng, J. Wickham, A.P Alivisatos, J. *Am Chem. Soc.,* **120**, 5343 (1998).

[27] M.S. Anwar, D. Blazina, H. Carteret, S.B. Duckett, T.K. Halstead, J.A. Jones, C.M. Kozak, and R.J.K. Taylor, *Phys. Rev. Lett*., **93**, 040501 (2004).

[28] L. Vandersypen, M. Steffen, G. Breyta, C.S. Yannoni, M.H. Sherwood, and I.L. Chuang, *Nature,* **414**, 883 (2001).

[29] E. Knill, R. Laflamme, and L. Viola, *Phys. Rev. Lett*., **84**, 2525 (2000).

[30] S. Iijima, *Nature*, **354**, 56 (1991).

[31] L. Zheng, M.J. O'Connell, S.K. Doorn, Z. Liao, Y. Zhao, E.A. Akhadov, M.A. Hoffbauer, B.J. Roop, Q. Jia, R.C. Dye, D.E. Peterson, S. Huang, J. Liu, and Y.T. Zhu, *Nature Materials*, **3**, 673(2004) .

[32] J.W.G. Wildöer, L.C. Venema, A.G. Rinzler, R.E. Smalley, C. Dekker, *Nature*, **391**, 59 (1998).

[33] T.W. Odom, J. Huang, P. Kim, C.M. Lieber, *Nature*, **391**, 62 (1998).

[34] L. Chico, L.X. Benedict, S.G. Louie, and M.L. Cohen, *Phys. Rev. B*, **54**, 2600 (1996).

[35] W. Tian and S. Datta, *Phys. Rev. B*, **51**, 7592 (1995).

[36] S. Datta, *Electronic Transport Properties in Mesoscopic Systems* (Cambridge Univ. Press, Cambridge, 1995).

[37] E. Dujardin, T.W. Ebbesen, A. Krishnan, P.N. Yianilos, and M. Treacy, *Phys. Rev. B*, **58**, 14013 (1998).

[38] M. Yu, B.S. Files, S. Arepalli, and R.S. Ruoff, *Phys. Rev. Lett*., **84**, 5552 (2000).

[39] T.L. Brown, B.E. Bursten, and H.E. Lemay, *Chemistry: The Central Science* (Prentice Hall PTR, 1999), 8th ed.

[40] E. Fitzer and W. Hüttner, *J. Phys. D*, **14**, 347 (1981).

[41] Q. Zhao, M.B. Nardelli, and J. Bernholc, *Phys. Rev. B*, **65**, 144105 (2002).

[42] B.I. Yakobson, *Appl. Phys. Lett*., **72**, 918 (1998).

[43] S. Iijima, C. Brabec, A. Maiti, and J. Bernholc, *J. Chem. Phys*., **104**, 2089 (1996).

[44] N. Chopra, L. Benedict, V. Crespi, M.L. Cohen, S.G. Louie, and D. Lorens, *Bull. Am. Phys. Soc*., **40**, 173 (1995).

[45] M.F. Yu, O. Lourie, M.J. Dyer, K. Moloni, T.F. Kelly, and R.S. Ruoff, *Science*, **287**, 637 (2000).

[46] N. Osakabe, K. Harada, M.I. Lutwyche, H. Kasai, and A. Tonomura, *Appl. Phys. Lett*., **70**, 940 (1997).

[47] E.W. Wong, P.E. Sheehan, and C.M. Lieber, *Science*, **277**, 1971 (1997).

[48] P. Poncharal, Z.L. Wang, D. Ugarte, and W.A. de Heer, *Science*, **283**, 1513 (1999).

[49] M.M Treacy, T.W. Ebbeson, J.M. Gibson, Nature, **38**, 678 (1996).

[50] M.R. Falvo, G.J. Clary, R.M. Taylor, V. Chi, F.P. Brooks Jr., S. Washburn, and R. Superfine, *Nature*, **389**, 582 (1997).

[51] J. Salvetat, A.J. Kulik, J. Bonard. G. Briggs, T. Stöckli, K. Méténier, S. Bonnamy, F. Béguin, N.A. Burnham, and L. Forró, *Adv. Mater*., **11**, 161 (1999).

[52] H.W.C. Postma, A. Sellmeijer, C. Dekker, *Adv. Mater.*, **12**, 1299 (2000)

[53] D. Qian, G.J. Wagner, W.K. Liu, M. Yu, and R.S. Ruoff, *Appl. Mech. Rev*., **55**, 495 (2002).

[54] R. Krupke, F. Hennrich, H. Löhneysen, and M.M. Kappes, *Science,* 3**01**, 344 (2003).

[55] X. Liu, L. Fu, S. Hong, V.P. Dravid, and C.A. Mirkin, *Adv. Mater*., **14**, 231 (2002).

[56] X.D. Wang, E. Graugnard, J.S. King, Z.L. Wang, C.J. Summers, *Nano Lett*., **4**, 2223 (2004).

[57] Y. Lei, L.D. Zhang, G.W. Meng, G.H. Li, X.Y. Zhang, C.H. Liang, W. Chen, and S.X. Wang, *Appl. Phys. Lett.*, **78**, 1125 (2001).

[58] P. Nyugen, H.T Ng, J. Kong, A.M. Cassell, R. Quinn, J. Li, J. Han, M. McNeil, and M. Meyyapapan, *Nano. Lett*., **3**, 925 (2003).

[59] T. Ono, S. Tsukamoto, and K. Hirose, *Appl. Phys. Lett*., **82**, 4570 (2003).

[60] H. Qi, C. Wang, and J. Liu, *Adv. Mater*., **15**, 411 (2003).

[61] D.P. Yu, Z.G. Bai, Y. Ding, Q.L. Hang, H.Z. Zhang, J.J. Wang, Y.H. Zou, W. Qian, G.C. Xiong, H.T. Zhou, and S.Q. Feng, *Appl. Phys. Lett*., **72**, 3458 (1998).

[62] N. Wang, Y.H. Tang, Y.F. Zhang, C.S. Lee, I. Bello, and S.T. Lee, *Chem. Phys. Lett*., **299**, 237 (1999).

[63] Y. Cui, C.M. Lieber, *Science*, **291**, 851 (2001).

[64] Y.F. Zhang, Y.H. Tang, C. Lam, N. Wang, C.S. Lee, I. Bello, and S.T. Lee, *J. Cryst. Growth*, **212**, 115 (2000).

[65] X. Zhang, L. Zhang, G. Meng, G. Li, N. Jin-Phillipp, and F. Phillipp, *Adv. Mater*., **13**, 1238 (2001).

[66] M.K. Sunkara, S. Sharma, and R. Miranda, G. Lian, and E.C. Dickey, *Appl. Phys. Lett*., **79**, 1546 (2001).

[67] J. Westwater, D.P. Gosain, S. Tomiya, and S. Usui, *J. Vac. Sci. Technol. B*, **15**, 554 (1997).

68 C.M. Lieber, *Sol. Stat. Comm*., **107**, 607 (1998).

[69] Y.Cui, L.J Lauhon, M.S. Gudiksen, J. Wang, C.M. Lieber, *Appl. Phys. Lett*., **78**, 2214 (2001).

[70] D.D.D. Ma, C.S. Lee, F.C.K. Au, S.Y. Tong, and T.S. Lee, *Science*, **299**, 1874 (2003).

[71] M.S. Gudiksen, C.M. Lieber, *J.Am. Chem. Soc.*, **122**, 8801 (2000).

[72] J.D. Holmes, K.P. Johnston, R.C. Doty, B.A. Korgel, *Science*, **287**, 1471 (2000).

[73] Y.F. Zhang, Y.H. Tang, N. Wang, D.P. Yu, C.S. Lee, I. Bell, S.T. Lee, *Appl. Phys. Lett*., **72**, 1835 (1998).

[74] Y. Cui, P. Wei, H. Park, C.M. Lieber, *Science*, **293**, 1289 (2001).

[75] R.G. Gordon, *Mater. Res. Soc. Bull.*, **25**, 52 (2000).

[76] B.G. Lewis, D.C. Paine, *Mater. Res. Soc. Bull*., **25**, 22 (2000).

[77] D.S. Ginley, C. Bright, *Mater. Res. Soc. Bull*., **25**, 15 (2000).

[78] Z.W. Pan, Z.R. Dai, Z.L. Wang, *Science*, **291**, 1947 (2001).

[79] *Science Watch*, July/August.

[80] J.A Zapien, Y. Jiang, X.M. Meng, W. Chen, F.C.K. Au, Y. Lifshitz, S.T. Lee, *Appl. Phys. Lett*., **84**, 1189 (2004).

[81] C. Yu, Q. Hao, S. Saha, L. Shi, X. Kong, Z.L. Wang, *Appl. Phys. Lett*., **86**, 063101 (2005).

[82] C. Ma, D. Moore, J. Li, Z.L. Wang, *Adv. Mater*., **15**, 228 (2003).

[83] C. Ma, Y. Ding, D. Moore, X. Wang, Z.L. Wang, *J. Am. Chem. Soc*., **126**, 708 (2004)

[84] Y. Jiang, X. Meng, W. Yiu, J. Liu, J. Ding, C. Lee, S. Lee, *J. Phys. Chem. B*, **108**, 2784 (2004).

[85] J. Westwater, D.P. Gosain, S. Tomiya, S. Usui, H. Ruda, *J. Vac. Sci. Technol. B*, **15**, 554 (1997).

[86] N. ang, Y.H. Tang, W.F. Zhang, C.S. Lee, I. Bello, S.T. Lee, *Chem. Phys. Lett*., **299**, 237 (1999).

[87] C. Ma, D. Moore, Y. Ding, J. Li, Z.L. Wang, *Intl. J. Nanotechnology*, **1**, 431 (2004).

[88] J. Gutowski, P. Michler, H.I. Ruckman, H.G. Brunig, M. Rowe, K. Sebald, T.Voss, *Phys. Sat. Sol. B*, **234**, 70 (2002).

[89] X. Jiang, Y. Xie, J. Lu, L. Zhu, W. He, Y. Qian, *Chem. Mater*., **13**, 1213 (2001).

[90] S. Yamaga, A. Yoshikawa, H. Kasai, *J. Cryst. Growth*, **86**, 252 (1998).

[91] B. Elidrissi, M. Addou, M. Regragui, A. Bougrine, A. Kachoune, J.C. Berncede, *Mater. Chem. Phys*., **68**, 175 (2001).

[92] C. Falcony, M. Garcia, A. Ortiz, J.C. Alfonso, *J. Appl. Phys*., *72*, 1525 (1992).

[93] T.V. Prevenslik, *J. Lumin*., **87-89**, 1210 (2000).

[94] C.N. Xu, T. Watannbe, M. Akiyama, X.G. Zheng, *Mater. Res. Bull*., **34**, 1491 (1999).

[95] W. Tang, D.C. Cameron, *Thin Solid Films*, **280**, 221 (1996).

[96] W. Chen, Z. Wang, Z. Lin, L. Lin, *Appl. Phys. Lett*., **70**, 1465 (1995).

[97] K. Lischka, *Phys. Stat. Sol. B*, **202**, 673 (1997).

[98] B.M. Basol, *Sol. Cells*, **23**, 69 (1988).

[99] K. Ando, H. Ishikura, Y. Fukunaga, T. Kubota, H. Maeta, T. Abe, H. Kasada, *Phys. Stat. Sol. B*, **229**, 1065 (2002).

[100] X. Duan, Y. Huang, R. Agarwal, C.M. Lieber, Nature, 421,241 (2003).

[101] W.C. Chen, S.M. Nie, *Science*, **281**, 2016 (1998).

[102] P.T. Tran, E.R. Goldman,G.P. Anderson, J.M Mauro, H. Mattousi, *Phys. Stat. Sol. B*, **229**, 427 (2002).

[103] J. Hu, L. Li, W. Yang, L. Manna, L.Wang, A.P. Alivisatos, *Science* , **292**, 2060 (2001).

[104] B. Ray, *II-VI Compounds* (Pergamon Press, Oxford, 1969).

[105] Z.L. Wang, *Annu. Rev. Phys. Chem*., **55**, 159 (2004).

[106] X.Y. Kong, Z.L. Wang, *Nano Lett*., **12**, 1625 (2003).

[107] Z.L. Wang, X.Y. Kong, Y. Ding, P. Gao, W.L. Hughes, R. Yang, and Y. Zhang, *Adv. Funct. Mater*., **14**, 943 (2004).

[108] M. Zhao, Z.L. Wang, S.X. Mao, *Nano Lett*., **4**, 587 (2004).

[109] M.H. Huang, S. Mao, H. Feick, H. Yan, Y. Wu, H. Kind, E. Weber, R. Russo, P. Yang, *Science*, **292**, 1897 (2001).

[110] P. Gao, Y. Ding, Z.L. Wang, *Nano Lett*., **3**, 1315 (2003).

[111] P. Yang, H. Yan, S. Mao, R. Russo, J. Johnson, R. Saykally, N. Morris, J. Pham, R. He, H. Coi., *Adv. Funct. Mater.*, **12**, 323 (2002).

[112] M. Law, D.J. Sirbuly, J.C. Johnson, J. Goldberger, R.J. Saykally, P. Yang, *Science*, **305**, 1269 (2004).

[113] J. Janata, *Principles of Chemical Sensors* (Plenum Press, New York, 1989).

[114] S.R. Whaley, D.S. English, E.L. Hu, P.F. Barbara, and A.M. Belcher, *Nature*, **405**, 665 (2000).

[115] J. Song, X.D> Wang, E. Riedo, Z.L. Wang, *J. Phys. Chem. B*, **109**, 9869 (2005).

[116] R.S. Wagner, W.C. Ellis, *Appl. Phys. Lett.*, **4,** 89 (1964).

[117] A.M. Morales, C.M. Lieber, *Science*, **279**, 208 (1998).

[118] Y. Wu, P. Yang, *J. Am. Chem. Soc*., **123**, 3165 (2001).

[119] N.R. Pawaskar, S.D. Sathaye, M.M Bhadbhade, K.R. Patil, J.C. Bernècde, *Mater. Chem. Phys*., **68**, 175 (2001).

[120] R.C. Sharma, Y. A. Chang, *J. Cryst. Growth,* **88**, 193 (1988).

[121] W. Wnag, l. Zhang, C. Liang, G. Wang, X. Peng, *Chem. Phys. Lett*., **357**, 314 (2002).

[122] S.H. Yu, M. Yoshimura, *Adv. Mater*., **14**, 296 (2002).

[123] J. Zhang, L. Sun, J. Yin, H. Su, C. Liao, C. Yan, *Chem. Mater*., **14**, 4172 (2002).

[124] J. Lao, J. Wen, Z. Ren, *Nano Lett.*, **2**, 1287 (2002).

[125] C.Y. Yeh, Z.W. Lu, S. Froyen, A. Zunger, *Phys. Rev. B*, **46**, 10086 (1992).

[126] C.B. Murray, C.R. Kagan, M.G. Bawendi, *Science*, **270**, 1335 (1995).

[127] V.L. Colvin, M.C. Schlamp, A.P. Alivisatos, *Nature*, **370**, 354 (1994).

[128] X.G. Peng, L. Manna, W.D. Yang, J. Wickham, E. A. Kadavanich, A.P. Alivisatos, *Nature*, **404**, 59 (2000).

[129] X.S. Peng, J. Zhang, X.F. Wang, Y.W. Wang, L.X. Zhao, G.W. Meng, L.D. Zhang, *Chem. Phys. Lett*., **343**, 470 (2001).

[130] X.C. Jiang, B. Mayers, T. Herricks, Y.N. Xia, *Adv. Mater*., **15**, 1740 (2003).

[131] Y.W. Wu, C.S. Wu, C.C. Chen, C.D. Chen, *Adv. Mater.*, **15**, 49 (2003).

[132] P.Ball, *Nature*, **427**, 497 (2004)

[133] J.C.H. Spence., J.M. Zuo, *Electron Microdiffraction* (Plenum Press, New York, 1992).

[134] Z.L. Wang, X.Y. Kong, J.M. Zuo, *Phys. Rev. Lett.*, **91**, 185502 (2003).

[135] D. Moore, C. Ronning, C. Ma, Z.L Wang, *Chem. Phys. Lett*., **385**, 8 (2004).

[136] J. Li, L. Wang, *Nano Lett*., **3**, 1357 (2003).